MAGNETIC PROPERTIES AND REACTIVITY STUDIES OF FAMILIES OF TRIGONAL BIPYRAMIDAL CYANIDE CLUSTERS AND THEIR EXTENDED STRUCTURES

A Dissertation

by

KRISTEN ELISE FUNCK

Submitted to the Office of Graduate Studies of
Texas A&M University
in partial fulfillment of the requirements for the degree of

DOCTOR OF PHILOSOPHY

December 2010

Major Subject: Chemistry

MAGNETIC PROPERTIES AND REACTIVITY STUDIES OF FAMILIES OF TRIGONAL BIPYRAMIDAL CYANIDE CLUSTERS AND THEIR EXTENDED STRUCTURES

A Dissertation

by

KRISTEN ELISE FUNCK

Submitted to the Office of Graduate Studies of
Texas A&M University
in partial fulfillment of the requirements for the degree of

DOCTOR OF PHILOSOPHY

Approved by:

Chair of Committee,	Kim R. Dunbar
Committee Members,	Timothy R. Hughbanks
	François P. Gabbaï
	Igor V. Roshchin
Head of Department,	David H. Russell

December 2010

Major Subject: Chemistry

ABSTRACT

Magnetic Properties and Reactivity Studies of Families of Trigonal Bipyramidal
Cyanide Clusters and Their Extended Structures. (December 2010)
Kristen Elise Funck, B.S, Mississippi State University
Chair of Advisory Committee: Dr. Kim R. Dunbar

Ferric ferrocyanide (Prussian blue) and its analogues are renowned for the variety of properties and applications associated with them. At the same time, however, they suffer from issues related to their variable composition and poor crystallinity. As a result, we are preparing discrete cyanide-bridged clusters both to mimic these materials and to search for properties unique to the molecule, such as single molecule magnetism. The work in this dissertation has focused on the expansion of series of trigonal bipyramidal (TBP) cyanide-bridged clusters, $[M(tmphen)_2]_3[M'(CN)_6]_2$, that exhibit a variety of properties including spin crossover, charge-transfer-induced spin transition, and photomagnetism.

One goal of the work was focused on the preparation of new paramagnetic TBP clusters incorporating various 3d metal ion combinations. Nine new clusters were prepared and characterized, including several “model compounds” with only one type of paramagnetic metal ion. The magnetic properties of these model compounds were combined to better explain the coupling through the cyanide ligands in clusters with two paramagnetic metal centers. An additional two clusters were also prepared that were found to exhibit a thermally induced LS Fe^{II} → HS Fe^{II} transition. The spin crossover event was confirmed by magnetic susceptibility and Mössbauer spectroscopy, and variable temperature X-ray crystallography revealed the transitions to be distinct for each Fe^{II} center and dependant on the interstitial solvent. Another major goal of the work was to investigate the TBP clusters for their potential to be used as building-blocks to prepare 1-D extended structures of linked clusters, such as a $\{[Co(tmphen)_2]_3[Fe(CN)_6]_2[Mn(MeOH)_4]\}_\infty(ClO_4)_3$ chain. A final research goal was a search for photomagnetic behavior, the change in magnetic properties with irradiation, related to spin transitions in several key TBP clusters. The Fe_3Fe_2 and Fe_3Co_2 TBP clusters were found to exhibit a light-induced excited spin state trapping (the LIESST effect) similar to that observed in mononuclear Fe^{II} compounds, and the photo-induced charge transfer that has been observed in Co-Fe Prussian blue materials is mimicked by the Co_3Fe_2 TBP molecular analogue.

DEDICATION

To my Edward:

- ♥ my husband
- ♥ my partner
- ♥ my fellow chemist
- ♥ my teacher
- ♥ my student
- ♥ my support
- ♥ my cheerleader (or should that be yell leader?)
- ♥ my strength
- ♥ my comfort
- ♥ my rock
- ♥ my love
- ♥ my everything

I can’t say that I couldn’t have done it without you . . . I just wouldn’t have wanted to.

ACKNOWLEDGEMENTS

First and foremost, none of this could have been possible without my advisor, Prof. Kim R. Dunbar. She initially accepted me into her group as an undergraduate, and onto a project to which she had already taken another student; I am grateful that she gave me this opportunity because I immediately came to love her group and her research. More importantly, I am glad that she took me back with open arms for my graduate career, despite the many qualified students that wanted my spot. Finally, I appreciate her advice, guidance, and particularly her patience with my work while in her group.

Next, I would like to thank the members of my committee, past and present, for all their help and advice in my graduate career. Thanks to Prof. Timothy R. Hughbanks, Prof. François P. Gabbaï, and Dr. Igor V. Roshchin for their hard work on correcting this dissertation and their comments on my defense. Also, thanks to Dr. Ray Schaak and Prof. Donald Naugle for their time on my committee during my literature seminar and preliminary exam. Thanks to the staff of Texas A&M for their help in my assorted measurements – Vanessa Santiago and Yohannes Rezenom for the measurements and advice on my seemingly-endless collection of mass spec samples and Dr. Joseph Reibenspies for all his help setting up unusually elaborate crystal data collections. Finally, I have to thank my collaborators who were indispensible to the success of this work. Thanks to Dr. Catalina Achim (Carnegie Mellon University) and her group for the Mössbauer measurements and analysis that were crucial to the study of the spin crossover compounds; thanks to Dr. Wolfgang Wernsdorfer for his microSQUID measurements; and thanks to Dr. Corine Mathonière, Dr. Rodolphe Clérac, and their groups (Université de Bordeaux) for all of their work measuring and interpreting the complicated photomagnetic properties of the tbp clusters.

I want to thank everyone who influenced my decision to pursue a graduate career in chemistry. Thanks to Mrs. Janet Sharp, my sixth grade science teacher who first introduced me to the concept of atoms and showed me that science was more than just animals and weather. Thanks to Mrs. Diana Turner, my high school chemistry teacher, who really fueled my interest in the subject of chemistry and spent many break periods discussing it with me. I am grateful to Dr. Philip Oldham for giving me my first research opportunity in his Mississippi State laboratory as a high school junior, and then again just before I entered college. I thank Sangeetha Shivaji, not only for being one of my best friends growing up, but for pointing out the should-have-been-obvious fact that I had much greater interest and abilities in chemistry than in architecture. I thank all of my chemistry professors at MSU for everything that they taught me. Finally, most of all, I thank Dr. William P. Henry (a.k.a. “Doc”) for taking a *sophomore* chemistry student onto his research project, giving me my first taste of real independent research, and helping me discover my love of inorganic chemistry.

I am extremely grateful to the current and former Dunbar group members who helped me the most over the years. Dr. Curtis Berlinguette was invaluable to me both as a secondary mentor in my undergraduate work and as a former student from whose work my dissertation research was inspired. Dr. Michael Shatruk was equally important to me as both a partner in lab in the tbp work and as another mentor teaching me so much about synthesis, x-ray crystallography, and magnometry. Dr. Andrey Prosvirin also taught me even more about magnetic measurements, and particularly the photomagnetic measurements. I also thank the former members of the Dunbar cyanide group – Dr. Ferdi Karadas, Dr. Matthew Hilfiger, Dr. Carolina Avendaño – for everything they taught me, and thanks to the current members – Dr. Xinyi Wang, Heather Southerland, Codi Sanders, Andrew Brown, and Mohammed Saber – for being a great group to work with. And thank you to the rest of the Dunbar group, past and present, for your friendship inside the lab and out – Dr. Brandi Schottel, Dr. Eric Reinheimer, Dr. Alfredo Angeles, Dr. Dafhne Aguirre, Dr. Nazario Lopez, Dr. Helen Chifotides, Dr. Akira Ota, Dr. Han Zhao, Sarah Lane, Zhongyue Zhang, Amanda David, Zhanyong Li, Bruno Peña-Maceda, and Maryfer Ballesteros Rivas.

I have to thank all of my friends who supported me during my time at A&M. Thanks to my fellow grad student chemistry friends outside the Dunbar group for lots of fun times. Thank you to all my church friends, both in Sunday school and in the handbell choir, and to my Wesley friends who helped me remember that there is life outside chemistry. Though they were far away, I am glad that I remained in contact with my high-school and college best friends, Allen Dollar (+ Jolie) and Jason Rohner (+ Heather), and their supportive words were very meaningful to me, even over the phone. Finally, I am grateful to my good friend Ian Giles, for *always* being around – in lab, in church, in Azeroth, and just hanging out (and glad Christina could join us later).

Finally, I want to thank both of my families for their unconditional love and support. I thank my brother-in-law, Scott, for helping me remember not to take life too seriously. I thank my sister-in-law, Carol, for putting up with *yet another* scientist in the family. I thank my mother-in-law, Jeanne, for her enthusiasm in and pride for my work, despite understanding little more than that an “emu” is not a flightless bird. I thank my father-in-law, Steven, for taking an active interest in my chemistry and for arranging an opportunity to present my work to his colleagues. I thank my sister, Cheryl (a.k.a. “Froggy”), for still being my best friend even 600 miles away and always being proud of everything I do; I was glad to teach her things over the years (including chemistry!), but she has also taught me many things about friendship, hard work, and what is really important in life. I thank my mother, Jan (“Mommy-dearest”), for six years of honest and helpful advice both personally and professionally; I have and will always look up to her as a shining example of the woman, professional, and mother that I want to be. I thank my father, Howard (“Daddy-dearest”), for being my eternal optimist and helping me hold onto my inner child; I am also grateful for always being able to talk to him, whether it’s ranting (or venting) about my chemistry of the day or talking about music when I need to talk about something else.

Finally, a list of acknowledgements would never be complete without a huge thank you to my husband, Edward. Few people get the opportunity to work with their spouse, and I feel lucky glad to have had that chance. I learned from you, you learned from me, we taught together, and we learned together – both in lab and in life. I am grateful for all the support that only you could give me in the times I needed it most. You are God’s blessing to me. My life . . . and my chemistry . . . are better for having known you.

NOMENCLATURE AND ABBREVIATIONS

acac	acetylacetonate
bpm	bis(1-pyrazolyl)methane
BEDT-TTF	bis(ethylenedithio)tetrathiafulvalene
bpy	2,2′-bipyridine
CTIST	charge-transfer-induced spin transition
cyclam	1,4,8,11-tetraazacyclotetradecane
diEt-DTC	N,N-diethyldithiocarbamate
dmdppz	11,12-dimethyldipyrido(3,2-a:2′,3′-c)phenazine
dppm	bis(diphenylphosphino)methane
dppz	dipyrido(3,2-a:2′,3′-c)phenazine
emu	electromagnetic unit (10^{-3} Am^2)
g	gyromagnetic factor
H	applied magnetic field
HS	high spin
IM2-py	2-(2-pyridyl)-4,4,5,5-tetramethyl-4,5-dihydro-1H-imidazolyl-1-oxy
J	magnetic exchange parameter
LS	low spin
M	magnetization (magnetic moment per unit volume)
Me$_3$tacn	N,N′,N″-trimethyl-1,4,7-triazacyclononane
Oe	oersted, unit of magnetic field strength (A/m, ~1 G)

OTf	trifluromethanesulfonate
ox	oxalate ($C_2O_4^{2-}$)
PB	Prussian blue
phen	1,10-phenanthroline
PPN	bis(triphenylphosphine)iminium
ptz	1-propyl-tetrazole
pz	pyrazolyl
$pzTp^-$	tetra(1-pyrazolyl)borate
R2	correlation value, $1 - \sqrt{\frac{\sum(\chi T_{obs} - \chi T_{calc})^2}{(n-p) \times \sum(\chi T_{obs})^2}}$
S	total ground state spin
SCO	spin crossover
SMM	single molecule magnet
SQUID	superconducting quantum interference device
tacn	1,4,7-triazacyclononane
TBA	tetrabutylammonium
TBP	trigonal bipyramid
T	temperature
T	Tesla, unit of magnetic field strength (10000 G)
T_c	Curie temperature or critical ordering temperature
TEA	tetraethylammonium
tetren	tetraethylenepentamine
TMA	tetramethylammonium

tmphen	3,4,7,8-tetramethyl-1,10-phenanthroline
Tp	hydrotris(1-pyrazolyl)borate
Tp*	hydrotris(3,5-dimethyl-1-pyrazolyl)borate
tpa	tris(2-pyridylmethyl)amine
trien	triethylenetetramine
χ	magnetic susceptibility (M/H)
χ_m	molar magnetic susceptibility
δ	isomer shift
ΔE_Q	quadrupole splitting
μ_B	Bohr magneton ($9.284*10^{-21}$ erg/Oe = $9.274*10^{-24}$ J/T)

TABLE OF CONTENTS

Page

CHAPTER

CHAPTER Page

III INVESTIGATION OF SPIN CROSSOVER TRIGONAL BIPYRAMIDAL CLUSTERS WITH **Fe_3Fe_2** AND **Fe_3Co_2** CORES . 71

IV INCORPORATION OF TRIGONAL BIPYRAMIDAL CLUSTERS INTO HIGHER NUCLEARITY CLUSTERS AND CHAINS 113

LIST OF FIGURES

FIGURE Page

FIGURE Page

FIGURE Page

FIGURE Page

FIGURE Page

LIST OF SCHEMES

SCHEME Page

LIST OF TABLES

TABLE Page

CHAPTER I

INTRODUCTION

GENERAL AND MOLECULAR MAGNETISM

Magnetic materials have long been fascinating to physicists and materials scientists and are important components in much of the current technology. In particular, the miniaturization of magnets is crucial to the improvement of this technology. Unfortunately, the “top-down” approach of making smaller and smaller particles of classical magnetic materials is fast approaching its limit. Instead, materials science is shifting focus to a “bottom-up” approach, in which materials are designed from molecular precursors. These materials, known as molecular magnets, were found to have many advantages over classical solid state magnets, such as lower temperature preparation, lower density, higher solubility, and the ability to tune the properties by variations in the syntheses and starting materials. Molecular magnets can serve as simple models for understanding the anisotropy and magnetic exchange interactions in magnetic systems, and they have great potential in applications, such as magnetic data storage, magneto-optical devices, spintronics, and quantum computing.

For any magnetic material, classical or molecular, to be useful, it is important to understand how the spin centers behave under a variety of conditions, particularly that there is an overall magnetic moment. If all of the magnetic moments in a material align in a single direction, such that the highest possible magnetization is attained, this

---

This dissertation follows the style of the *Journal of the American Chemical Society*.

situation is called ferromagnetic ordering. In contrast, antiferromagnetic ordering occurs when neighboring moments of equal size align antiparallel to each other, resulting in a magnetization of zero. If the neighboring moments have unequal size, a net magnetization results from the incompletely cancelled spins, an effect known as ferrimagnetic ordering (Figure 1).

In general, the most useful magnetic materials are those with some type of magnetic bistability – two different magnetic states attainable by variations in a physical stimulus. The most common case of bistability is the ability to magnetize a material in two opposing directions. Ferromagnets consist of magnetic domains, inside which all spins are aligned in a single direction. In a non-ordered, paramagnetic state, the magnetic moments are randomly oriented such that there is no net magnetization. In an applied magnetic field, the domain walls move and collapse allowing the domains which are aligned with the field to expand while the domains aligned in other directions are reduced, eventually magnetizing the entire material and saturating the magnetization. Below a certain temperature, called the critical ordering temperature or Curie temperature, (T_c), a remnant magnetization (M_r) is retained after the magnetic field is removed. Only an applied magnetic field in the opposite direction that is greater than a critical field, the coercitivity (H_c), can reverse the direction of the magnetization. This behavior is manifested as a hysteresis loop in the magnetization (M) vs. applied field (H) plot (Figure 2).

Molecular magnetism is considered to have originated in 1967 with Wickman's report of ferromagnetic ordering below 2.5 K for the Fe(diEt-DTC)$_2$Cl complex (Figure

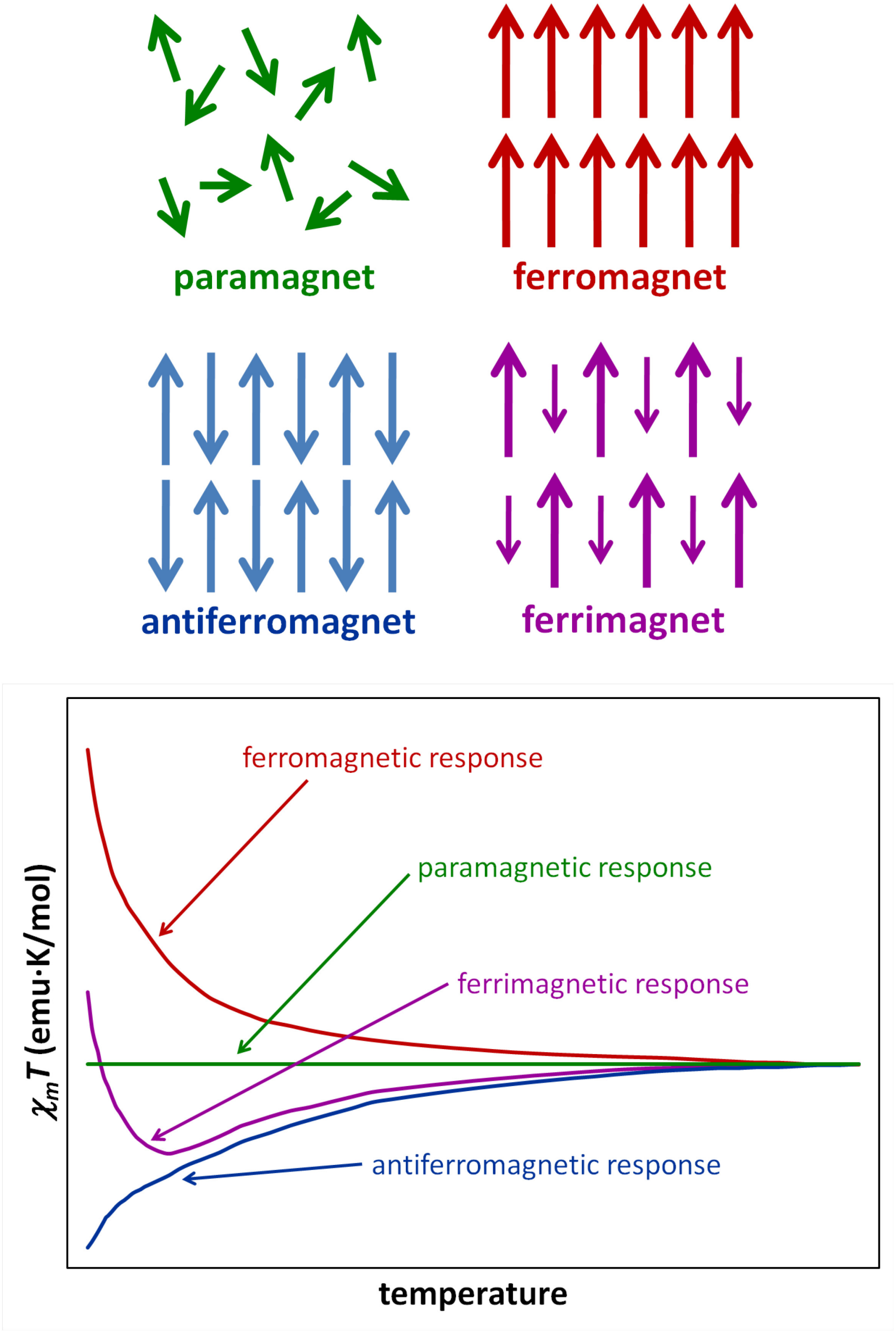

Figure 1: Types of magnetism and their magnetic susceptibility behavior ($\chi_m T$ vs. T).

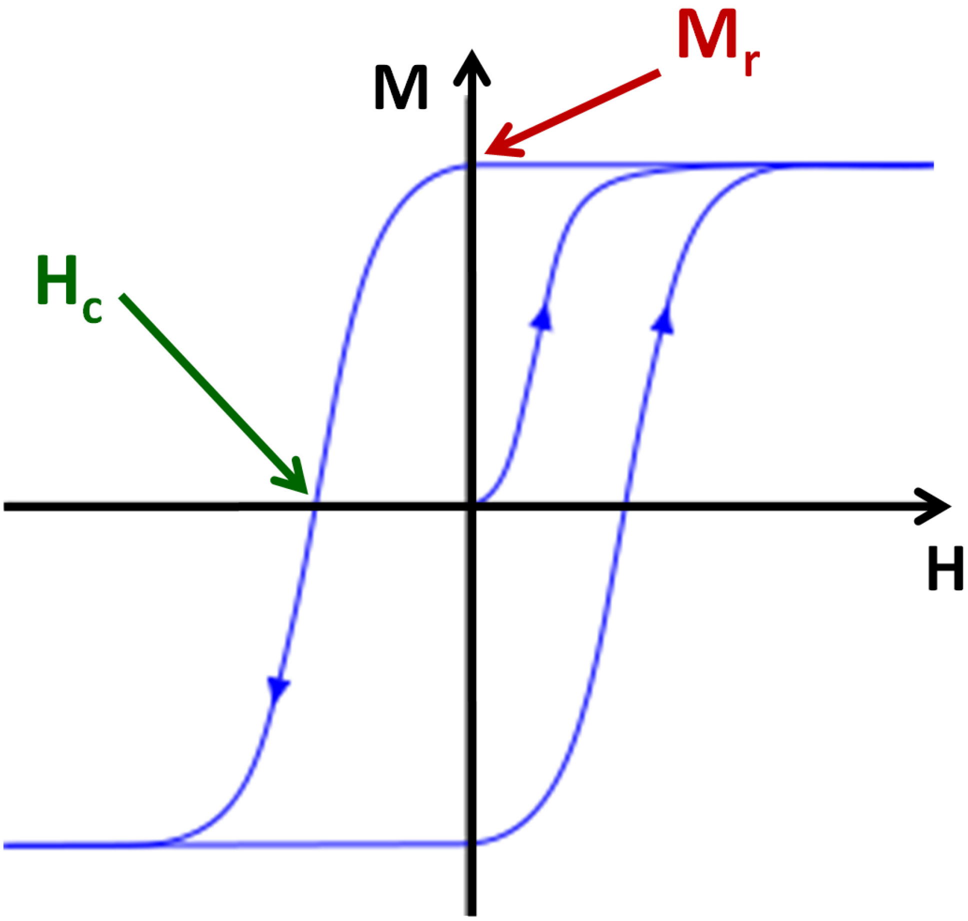

Figure 2: Magnetic hysteresis loop (blue) in magnetization vs. magnetic field, indicating the remnant magnetization (M_r) and coercitivity (H_c) of the system.[1]

3a);[2] this unexpected result was the first observation of magnetic ordering in a discrete complex. As the field of molecular magnetism developed, understandably, the focus was predominantly on the use of transition metal ions for large spin value materials. The organic ligands became a much higher priority, however, after the reports of the first organic ferromagnets by the Kinoshita group. The γ and β-phases of the crystals of *p*-nitrophenyl nitronyl nitroxide (*p*-NPNN, Figure 3b) exhibit ferromagnetic transitions at 0.65 and 0.60 K, respectively.[3,4] One of the most notable uses of the design aspect of molecular magnetism is to be able to combine two or more desired properties in a single material, a goal that is not easily attained with conventional solid state compounds. In 2000, Coronado *et al.* reported an important case of multi-functionality in [BEDT-TTF]$_3$[Mn^{II}Cr^{III}(ox)$_3$] (Figure 3c). The layers of BEDT-TTF radical cations impart a conductivity up to 250 S/cm at room temperature, and the [Mn^{II}Cr^{III}(ox)$_3$] network orders below 2.5 K.[5] Among the diverse array of molecular magnets reported today, cyanide-bridged compounds include some of the most fascinating examples and are known to exhibit a variety of properties.

CYANIDE CHEMISTRY AND PRUSSIAN BLUE ANALOGUES

Cyanide chemistry began serendipitously in 1704 when Heinrich Diesbach, a German artist, mixed iron sulfate and potash contaminated with animal blood to make a deep blue pigment.[6] This pigment became known as Prussian blue and was used extensively by artists for centuries. This intriguing coordination compound was finally revived in the mid-20th century when its structure (Figure 4) was determined to be

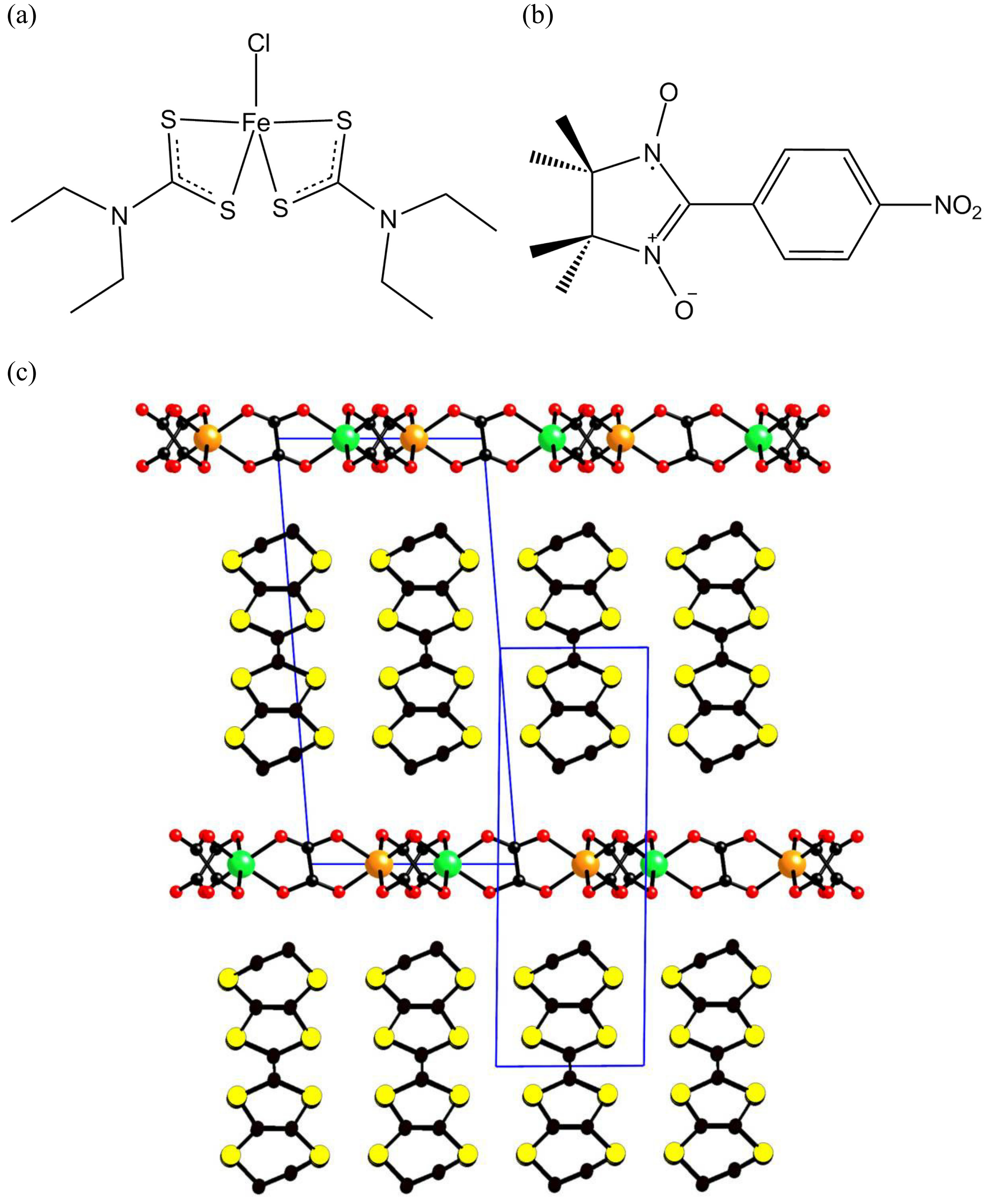

Figure 3: The first reported molecular magnet, Fe(diEt-DTC)$_2$Cl (a), the first reported organic ferromagnet, *p*-NPNN (b), and the first reported conducting magnet, [BEDT-TTF]$_3$[Mn^{II}Cr^{III}(ox)$_3$] (c, figure prepared by José R. Galán-Mascarós).

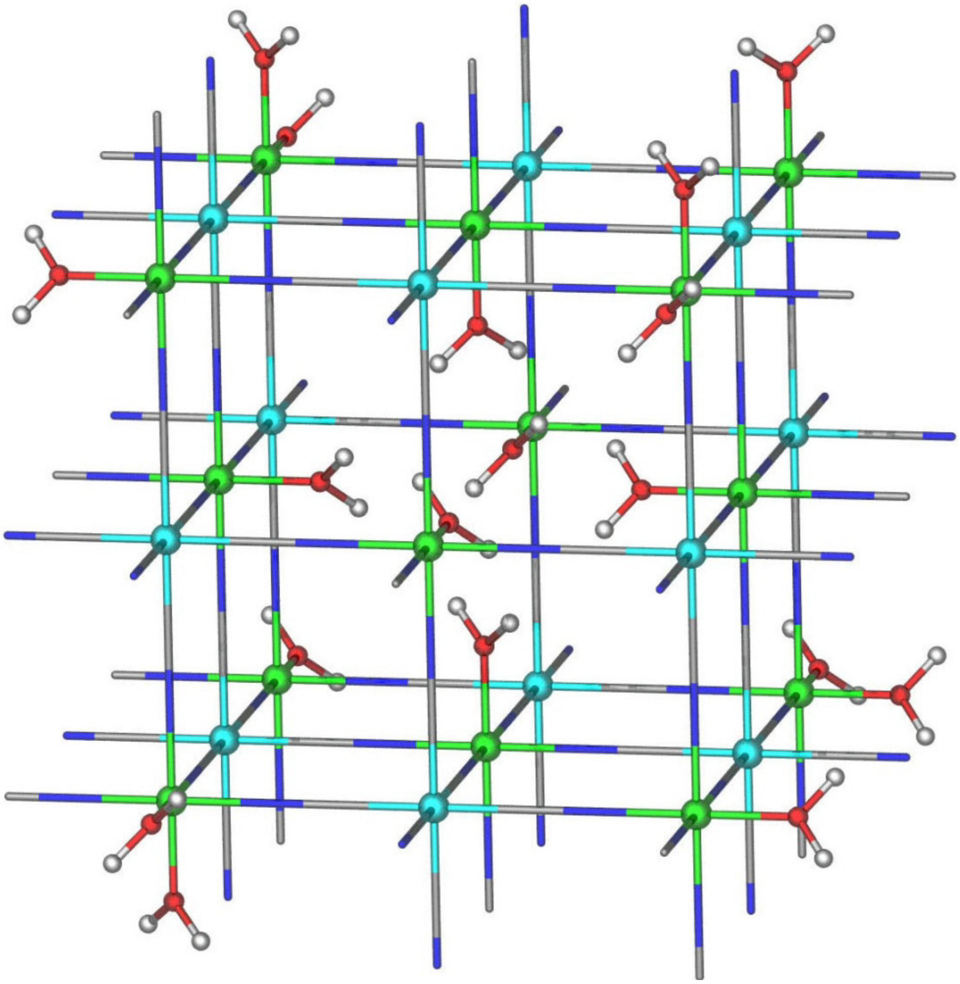

Figure 4: The general structure of a $M[M'(CN)_6]_y \cdot xH_2O$ Prussian Blue analogue, including coordinated water molecules filling $M'(CN)_6$ vacancies. (C, grey; H, white; N, blue; O, red; M, green; M′, light blue).

$Fe_4[Fe(CN)_6]_3 \cdot 14\text{-}16H_2O$.[7,8] Prussian blue has a 3D cubic framework of Fe^{II} and Fe^{III} ions connected by cyanide bridges. To create a neutral compound, every fourth $[Fe(CN)_6]^{4-}$ moiety is missing, and water molecules fill the vacant coordination sites on the Fe^{III} centers. The Fe^{III}—NC—Fe^{II} connectivity was confirmed by Mössbauer spectroscopy.[9,10] Although the Fe^{II} ions are diamagnetic from the strong ligand field of the cyanide ligands, Prussian blue actually exhibits ferromagnetic coupling ($T_C \approx 10K$) through mixed-valence delocalization of the Fe ions.[11] After these studies, cyanide chemistry slowly gained stature in the field of inorganic chemistry, but it has only been in the past 20 years that cyanide chemistry has really blossomed into a major topic in chemistry. This new interest was sparked by the discovery of Prussian blue (PB) analogues with high ordering temperatures,[12-14] as well as others that serve as molecular sieves,[15] antidotes for radioactive poisoning,[16] and hydrogen storage materials.[17,18] As evidence for the growth of the field, it is interesting to note that at the beginning of the renaissance in cyanide research, a review chapter published in the *Progress in Inorganic Chemistry* book series in 1997 by Dunbar and Heintz summarized most of the known topics in cyanide chemistry at that time.[19] By 2009, the field had grown such that a second review by Shatruk, Avendaño, and Dunbar had to be limited to the discussions of only discrete paramagnetic cyanide compounds.[20]

With a few exceptions, the superexchange between metal ions through a cyanide ligand is generally predictable by the Goodenough-Kanamori rules.[21-23] Two metal orbitals of the same symmetry (t_{2g}—t_{2g}, e_g—e_g) interact with the same types of orbitals on the bridging cyanide ligand, resulting in the stabilization of a bonding orbital, hence antiferromagnetic coupling of the two spins (Figure 5a). Conversely, two orbitals of different symmetries (t_{2g}—e_g) interact with different types of cyanide orbitals, leading to ferromagnetic coupling of the spins (Figure 5b). Antiferromagnetic and ferromagnetic coupling are observed in the PB analogues $KV^{II}[Cr^{III}(CN)_6]\cdot 2H_2O$[14] ($t_{2g}^3$—$t_{2g}^3$) and $Ni^{II}_3[Cr^{III}(CN)_6]_2\cdot 9H_2O$[24] ($e_g^2$—$t_{2g}^3$) respectively. Finally, since antiferromagnetic interactions are significantly stronger in cyanide compounds than those of the ferromagnetic type, a combination of both types of interactions typically leads to overall antiferromagnetic coupling between the metal centers, although the coupling is weaker than a system with only antiferromagnetic interactions. This situation is observed in compounds such as $Mn^{II}_3[Mn^{III}(CN)_6]_2$ ($t_{2g}^3e_g^2$—t_{2g}^4).[25]

The synthesis of PB analogues is straightforward. An aqueous solution of a metal salt, $[M(L)_6]^{x+}$ (where L is a labile ligand or solvent molecule), is mixed with a solution of a hexacyanometallate, $[M'(CN)_6]^{y-}$ which leads to the instantaneous precipitation of products. In many cases, an alkali metal salt is added for charge balance. Although they can exhibit many interesting properties, as previously mentioned, these materials consistently pose certain problems. PB materials are generally amorphous or poorly crystalline because they are formed so rapidly. Vacancies are formed because the requirement for charge balance usually prevents complete occupation of the metal sites, and they are typically randomly distributed though the material. These defect sites are occupied by varying amounts of water molecules which are known to influence the properties. The disorder causes inconsistencies in the metal ion ratio, the metal ion environments, and the solvent content between batches, and even

(a)

Antiferromagnetic coupling

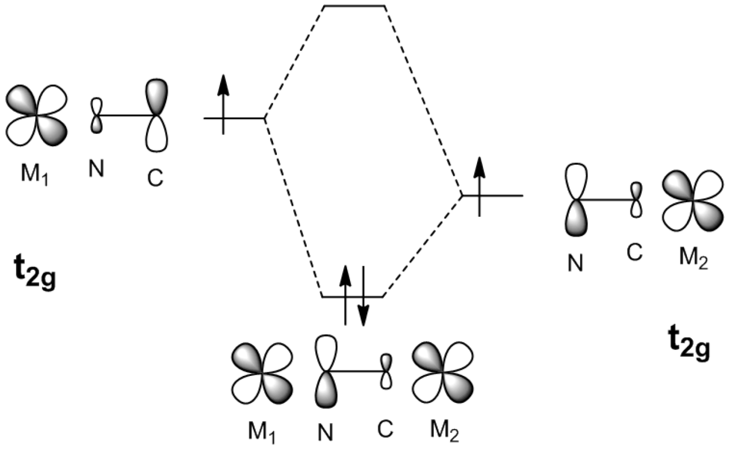

(b)

Ferromagnetic coupling

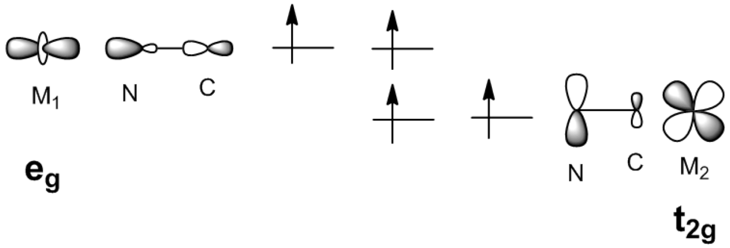

Figure 5: The interactions of metal orbitals with the orbitals of a bridging cyanide ligand. (a) Antiferromagnetic coupling results from metal orbitals of the same symmetry interacting with the same types of cyanide orbitals. (b) Ferromagnetic coupling results from orthogonal metal orbitals interacting with different types of cyanide orbitals.

within a single batch of product. With no way to predict or control the final composition, it is extremely difficult to determine precise relationships between the structure of a material and its properties.

To overcome this problem, many groups have turned to discrete cyanide compounds to model the properties of PB analogues, and even to find new properties unique to molecules. To circumvent the formation of extended networks, metal centers are capped with multidentate ligands to block some of the coordination sites. By combining convergent precursors or reacting a convergent with a divergent precursor (Figure 6), a building block or modular approach has been used to prepare cyanide clusters with well-defined structures and a variety of interesting magnetic properties.[20]

SINGLE MOLECULE MAGNETISM

Magnets used in computer and electronic applications are made from classical magnetic materials and are able to retain their ability to be magnetized at temperatures above the Curie temperature as the particle size is decreased, even down to the size of a single domain. For single domain particles, magnetic bistability is the result of an energy barrier (ΔE) between "up" and "down" spin states, a barrier that is dependent on the anisotropy and the volume of the particle. It was first observed by Néel[26] that for particles below a critical size regime, this energy barrier is decreased such that thermal effects will equally populate both spin states. The magnetic moment of the particle flips quickly between the two orientations and is unable to retain a permanent magnetization at zero field (*i.e.* the magnetization is zero). At temperatures below a critical blocking

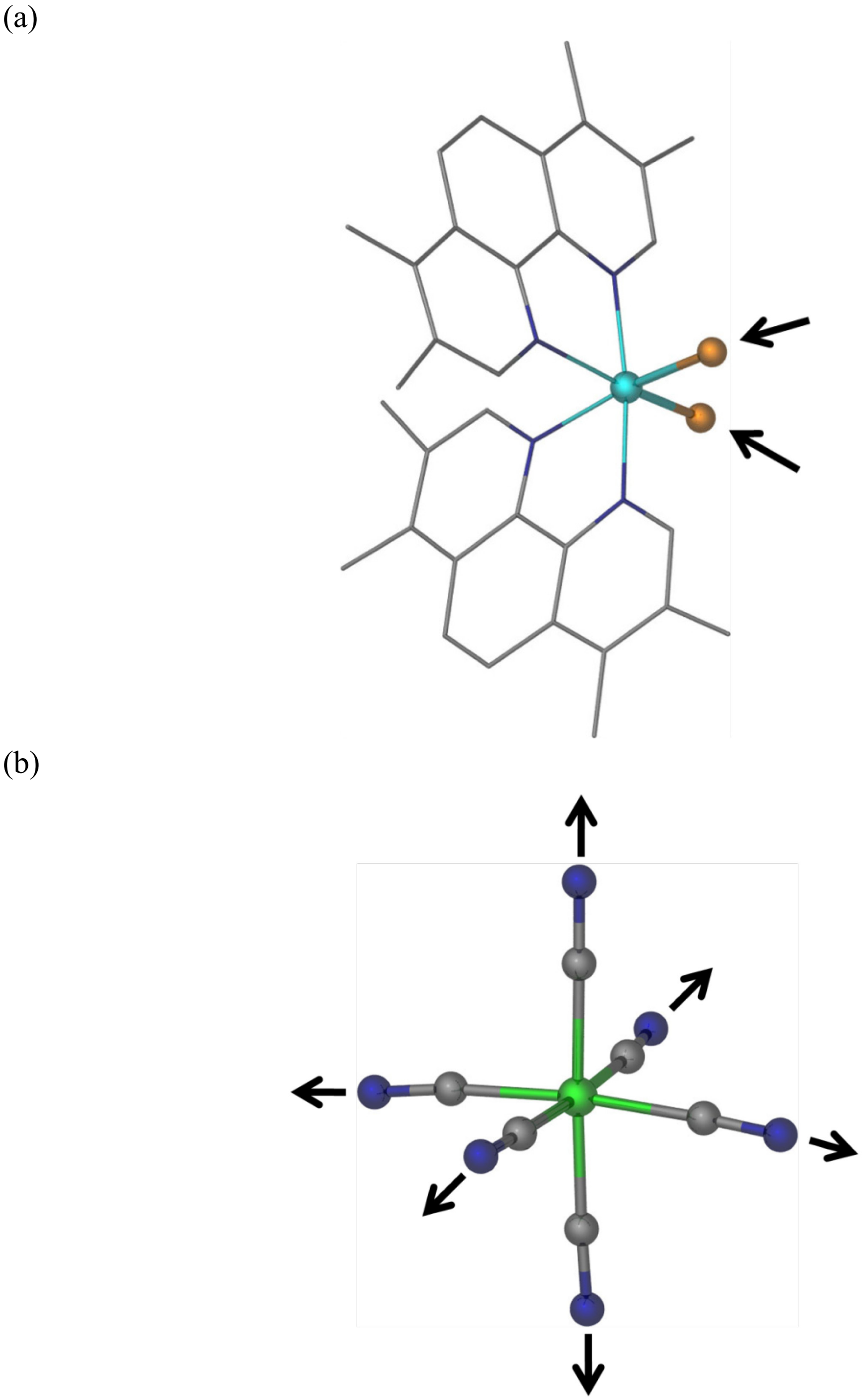

Figure 6: (a) An example of a convergent precursor with two labile ligands, indicated by arrows. (b) An example of a divergent precursor with six available binding sites, indicated by arrows.

temperature (T_b), however, the moment remains oriented in a single direction and therefore exhibits magnetization. Given that these particles still contain a large number of metal ions, it was would appear to be an impossible feat for a single molecule to behave as magnet – one property of materials that would seemingly never be modeled with molecular clusters. In 1980 however, unbeknownst to him, Lis prepared an oxo-bridged manganese cluster – $Mn_{12}O_{12}(O_2CCH_3)_{16}(H_2O)_4$[27] (Figure 7a) – which would soon open up a new field of magnetism.

In 1993, the Gatteschi group reported magnetic bistability for Lis's molecule now simply known as Mn_{12}-acetate or simply Mn_{12} – establishing the field of single molecule magnetism (SMM).[28] Although the bistability of SMM's is reminiscent of that of classical magnets, it is quantum, not classical, effects that bring about this behavior. The bistability is the result of two possible ground states (at zero field) at $M_s = \pm S$ (S is the ground state spin value) and an energy barrier between them (Figure 7b). One of the two states can be fully populated by applying a strong field at sufficiently low temperatures (Figure 8a). When the field is removed, the barrier "blocks" the equilibration of the spins if the molecule is maintained below the critical blocking temperature. The barrier height is defined as $S^2|D|$ for integer spin molecules and $(S^2-1/4)|D|$ for half-integer spin molecules, where S is the ground state spin value and D is the axial anisotropy of the molecule, which must be negative in order to have a double energy well and barrier. The slow relaxation of SMM's apprears in magnetic measurements as a frequency dependence of the out of phase AC magnetic susceptibility (χ_m'' vs. T, Figure 7c) and, more definitively, as a hysteresis loop (Figure 7d). Many

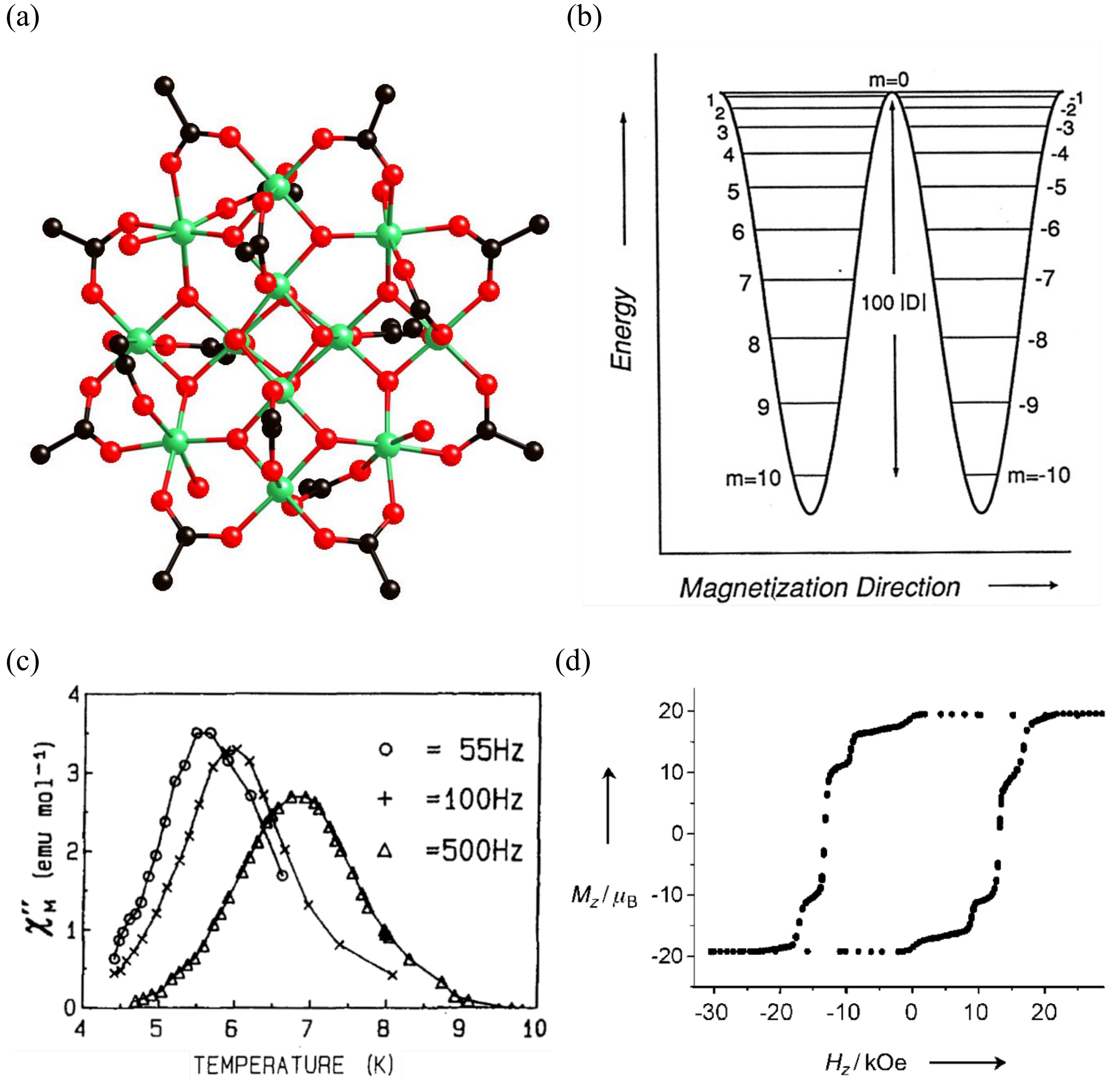

***Figure** 7*: (a) Molecular structure of $Mn_{12}O_{12}(O_2CCH_3)_{16}(H_2O)_4$ or Mn_{12}. (b) Energy well diagram for Mn_{12}. (c) Frequency dependence of the χ_m'' AC susceptibility vs. T for Mn_{12}. (d) Hysteresis loop for a single crystal of Mn_{12}, clearly indicating steps caused by quantum tunneling through the energy barrier. (Adapted with permission from Christou *et al.*,[29] Sessoli *et al.*,[30] and Gatteschi *et al.*[31] – Copyright Wiley-VCH Verlag GmbH & Co. KGaA).

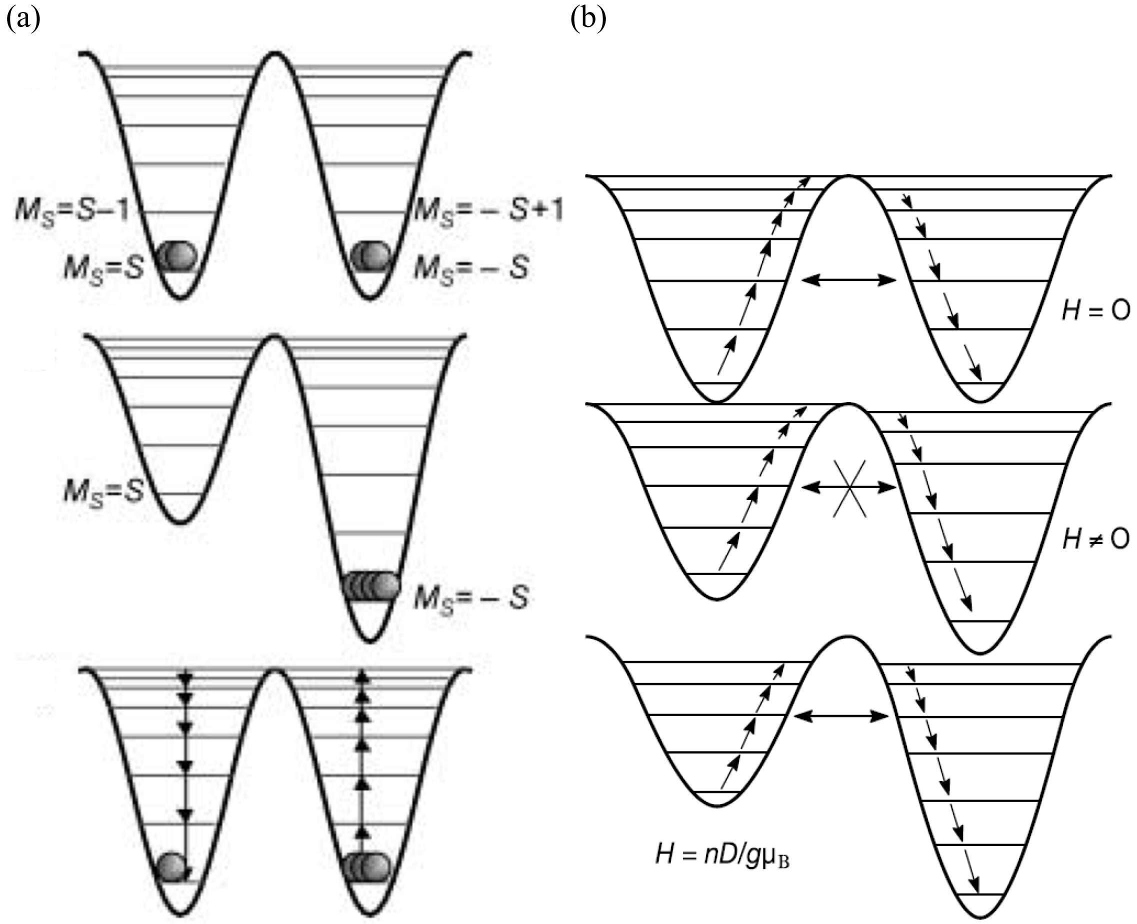

Figure 8: (a) Energy well diagrams indicating the equal population before applying a magnetic field, population of one well under a magnetic field, and the necessary steps to equilibrate after the field is removed. (b) Energy well diagrams indicating the possibility of quantum tunneling only at select magnetic fields, leading to steps in the hysteresis loop. (Adapted with permission from Gatteschi *et al.*[31] – Copyright Wiley-VCH Verlag GmbH & Co. KGaA – and Christou *et al.*[29]).

SMM's also exhibit quantum tunneling – the quantum transition of a system from one spin state to another, requiring less energy than overcoming the full energy of the barrier. Tunneling shows up as steps in a hysteresis loop, at points which the magnetic field allows the alignment of spin states (Figure 8b).

Despite being the first recognized SMM, Mn_{12} exhibits the highest known blocking temperature for a transition metal cluster – a value of 8 K (measured from the 1kHz AC signal).[32] One issue, however, with Mn_{12}, and its related SMM's, is the self assembly process that is used to prepare them. The assembly cannot be easily controlled and the final products are usually unpredictable.[33] For this reason, many researchers have turned to a building block approach in order to attempt to design SMM's. This method has led to the preparation of a number of cyanide-based SMM's in a variety of shapes[34-64] as small as linear[36] and bent[44] trinuclear complexes and as large as pentadecanuclear face-and-body-centered cubic clusters[41,43,46] (Figure 9).

SPIN CROSSOVER

By far, the most common type of spin transition is spin crossover (SCO). SCO is a property of d^4-d^7 ions in which the ligand field of the ion is close to the barrier between the low-spin (LS) and high-spin (HS) states. In this case, the two electronic states are very similar in energy, allowing a physical perturbation (temperature, pressure, or light) to convert between the two states. SCO was first observed in a series of Fe^{III}-dialkyldithiocarbamate complexes[65] by Cambi and coworkers. Since then, SCO has been observed in all d^4-d^7 ions, but it is by far the most common in Fe^{II} complexes. One

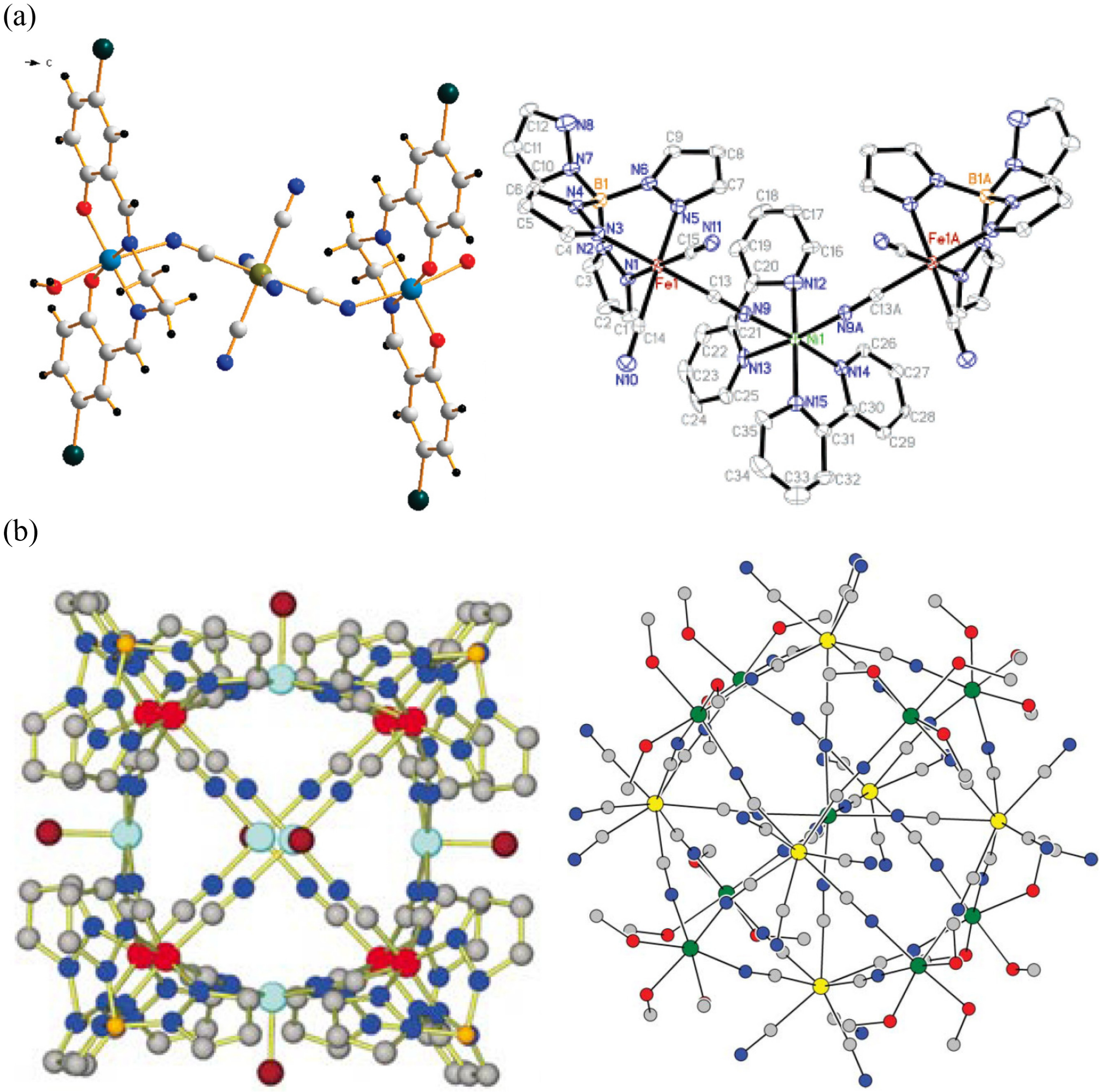

Figure 9: The smallest (a) and largest (b) reported geometries of cyanide-bridged single molecule magnets. (Adapted with permission from Tregenna-Piggott *et al.*,[61] Li *et al.*,[44] Wang *et al.*[39] – Copyright Wiley-VCH Verlag GmbH & Co. KGaA – and Freedman *et al.*[43] – Copyright The Royal Society of Chemistry).

of the most important SCO complexes is the $Fe(phen)_2(NCS)_2$ molecule first studied by König and Madeja.[66]

The SCO phenomenon can be detected in Fe^{II} complexes by three methods. The most obvious method is the determination of the magnetic properties, in which the SCO is typically evident as an S-shaped curve in $\chi_m T$ vs. T, representing the transition from the S = 0 (LS) state to the S = 2 (HS) state with increasing temperature. This transition can be gradual or abrupt, exhibit hysteresis, consist of multiple steps, and/or be incomplete depending on the particular compound (Figure 10). A second method for detecting SCO in Fe compounds is Mössbauer spectroscopy, a technique that measures nuclear transitions to determine the oxidation states and spin states present in the sample. By measuring a compound at different temperatures, the amount of each spin state can be observed to vary, characterizing the SCO behavior. Finally, variable temperature single crystal x-ray diffraction is very useful for documenting the spin crossover event. The Fe—L bond lengths vary significantly between the high spin and low spin states. In the HS state, the two electrons in the antibonding e_g orbitals cause significant electronic repulsion and a significantly longer bond length than in the LS state. For example, in a FeN_6 complex, Fe—N bond lengths typically range from 1.92-2.00 Å in LS complexes and 2.15-2.21 Å in HS complexes.[67] Since X-ray diffraction can distinguish different sites in a dinuclear or multinuclear cluster, it can be used to help lend insight into issues related to partial spin transitions.

Many mononuclear and dinuclear Fe^{II} SCO compounds have been reported, but higher nuclearity compounds are much less common,[68-85] and only four of which contain

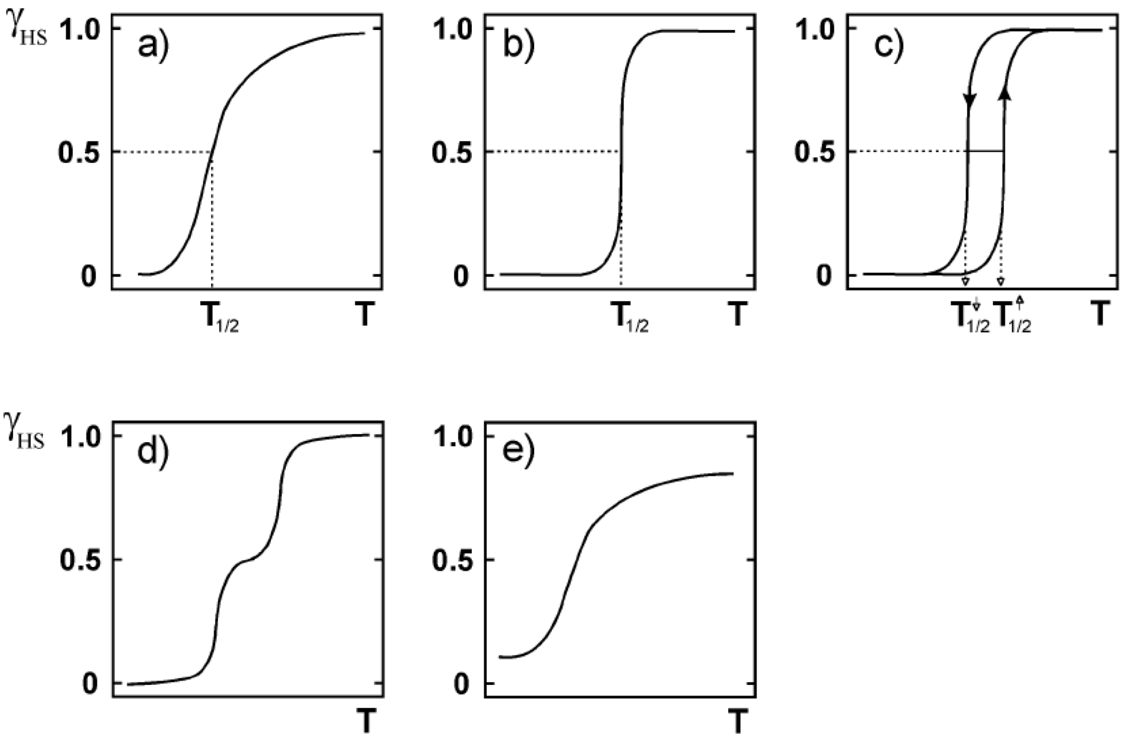

Figure 10: Examples of spin transition curves, plotted as HS fraction (γ_{HS}) vs. temperature: (a) gradual transition, (b) abrupt transition, (c) abrupt transition with hysteresis, (d) two step transition, and (e) incomplete transition. (Adapted with permission from Gutlich *et al.*[86] – Copyright Springer Science+Business Media). Curves (a)-(c) represent increasing cooperativity.

cyanide. The $[Fe(tpa)]_2[Fe(bpy)_2(CN)_2]_2$ square by Nihei *et al.* undergoes a two-step transition, each corresponding to one of the two $[Fe^{II}(tpa)(NC)_2]$ moieties.[77] Two related squares, $[Fe(tpa)]_2[Fe(phen)_2(CN)_2]_2$[79] and $\{[Fe(bpym)_2]_2[Fe(phen)_2(CN)_2]_2\}(PF_6)_4$,[82] reveal that simple changes in the ligands can result in a single-step transition. Finally, the mixed valence $[Fe^{III}(Tp^*)(CN)_3]_2[Fe^{II}(tpa)]$ cluster by Nihei *et al.* also shows SCO at only one of the Fe^{II} centers.[82]

PHOTOMAGNETISM

The two most common types of photomagnetic behavior in cyanide compounds are light-induced spin state trapping or LIESST effect and light-induced charge transfer. Photo-induced spin crossover was first observed in 1982 on a nanosecond timescale by McGarvey and Lawthers for three mononuclear Fe^{II} complexes.[87] In 1984, Decurtins and Gütlich *et al.*, were the first researchers to trap this photo-excited state, and they coined the term LIESST (light-induced excited spin state trapping) as a description for the behavior of $[Fe(ptz)_6](BF_4)_2$.[88] White light irradiation of the compound at low temperatures (<50 K) excites low-spin Fe^{II} centers to high-spin centers as revealed by Mössbauer spectroscopy. Since this discovery, LIESST has been observed in many spin-crossover compounds, including numerous $FeL_2(NCX)_2$ complexes (L = diimine ligand, X = S, Se).[89-97] As with SCO, although mononuclear and dinuclear Fe^{II} species and extended structures that show LIESST behavior are quite prevalent, to date, only four higher nuclearity clusters have been investigated for this behavior.[70,81,83,85] In particular, only one cyanide cluster has exhibited the LIESST effect – a tetranuclear cluster prepared by Oshio and coworkers.[83] One of the four Fe^{II} centers can be partially converted by green light (532 nm) or fully converted by red light (693 nm) (Figure 11).

Photo-induced charge-transfer was first observed in 1996 by Sato *et al.* for the Prussian blue analogue $K_{0.2}Co_{1.4}[Fe(CN)_6]\cdot 6.9H_2O$.[98] When the material is irradiated with red light (660 nm) at low temperatures (<20 K), a charge-transfer-induced spin transition occurs, converting Co^{III}_{LS}—NC—Fe^{II} states to Co^{II}_{HS}—NC—Fe^{III} states and increasing the magnetization of the sample (Figure 12a). The transition can be reversed using blue light (450 nm). Similarly, a photo-induced demagnetization is observed in $Rb_{0.91}Mn_{1.05}Fe(CN)_6\cdot 0.6H_2O$ upon irradiation of green laser light (532 nm) (Figure 12b).[99] In this case, the de-magnetization is caused by a charge-transfer-induced phase transition which involves a reversal of the Jahn-Teller distortion due to the conversion of Mn^{III}_{HS}—NC—Fe^{II} pairs to Mn^{II}_{HS}—NC—Fe^{III} states.

Several clusters have been reported exhibiting a photo-induced MM′CT, most of which are based on octacyanometallates. The $[Cu(bpy)_2]_2[Mo(CN)_8]$ cluster by Rombaut *et al.*[100] and the $\{[(Cu(tren)_2]_6[Mo(CN)_8]\}(ClO_4)_8$ cluster by Herrera *et al.*[101] undergo a $Cu^{II}/Mo^{IV} \rightarrow Cu^{I}/Mo^{V}$ transfer (Figure 13). Two additional clusters, $[Mn(bpy)_2]_4[M(CN)_8]_2$ (M = Mo, W) by Mathonière *et al.*,[102] undergo a similar transfer from $Mn^{II}/M^{IV} \rightarrow Mn^{I}/M^{V}$ (Figure 14). Only two photomagnetic clusters have been reported based on Prussian blue analogues, namely a Co_4Fe_4 octanuclear cluster[103] and a Co_2Fe_2 square[104] by Holmes and coworkers (Figure 15). No clusters have been described based on the Mn^{II}/Fe^{III} combination.

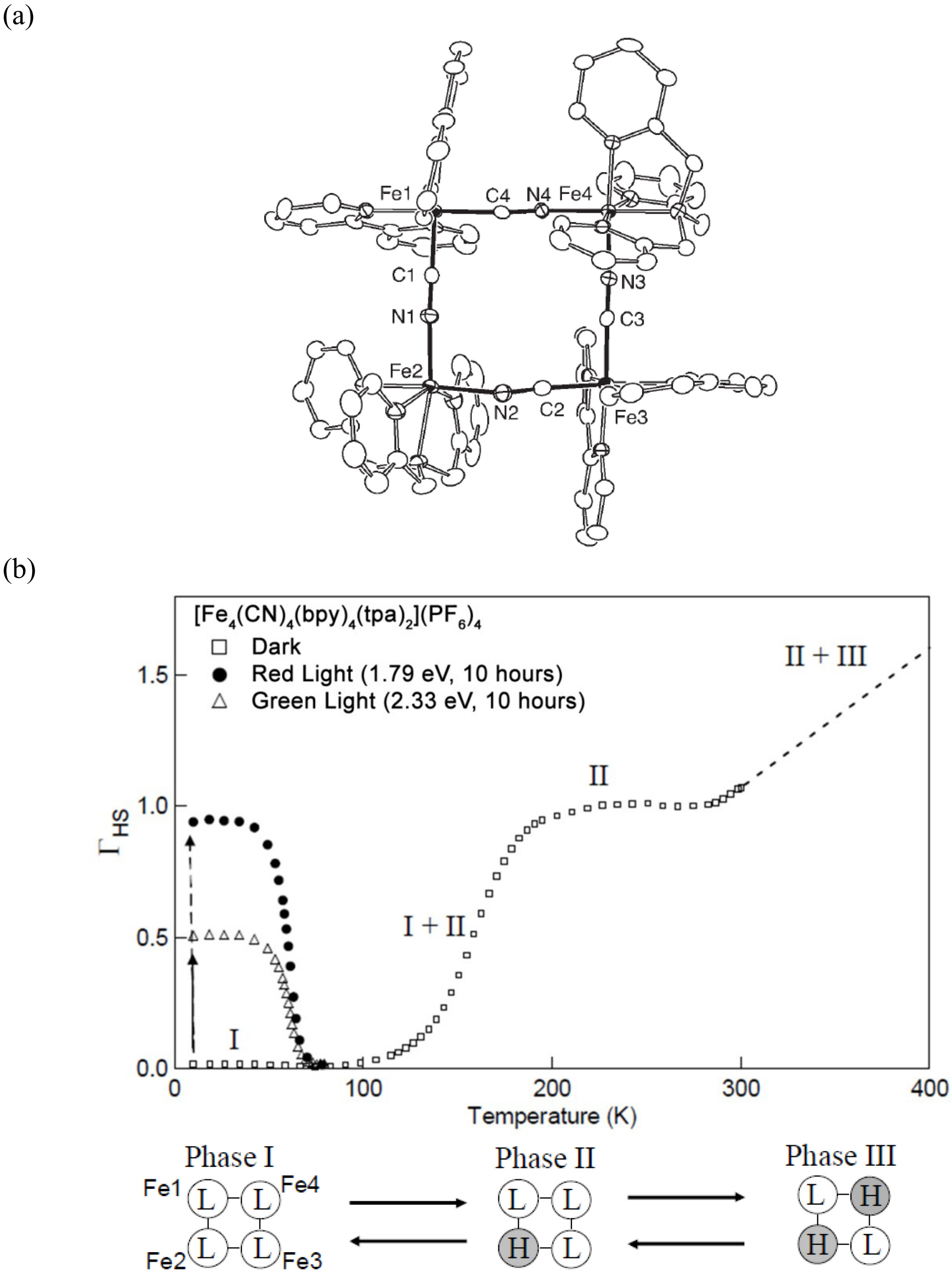

Figure 11: (a) The structure of the salt [$Fe_4(CN)_4(bpy)_4(tpa)_2](PF_6)$. (b) Data for the thermal spin crossover and LIESST effect of the Fe_4 cluster. (Adapted with permission from Nihei *et al.*[77] – Copyright Wiley-VCH Verlag GmbH & Co. KGaA – and Nishihara *et al.*[83] – Copyright IOP Publishing).

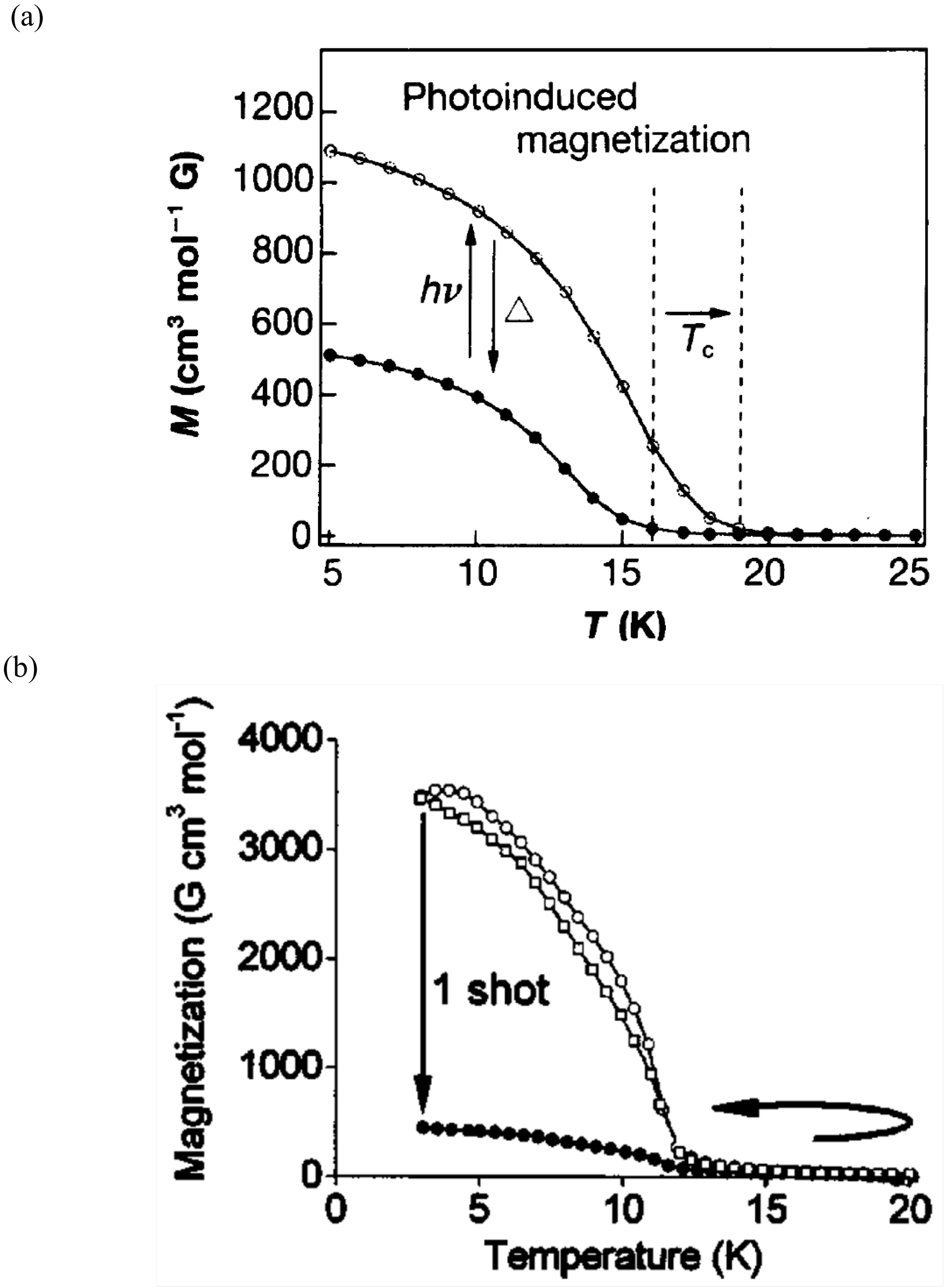

Figure 12: (a) The photoinduced magnetization data for $K_{0.2}Co_{1.4}[Fe(CN)_6]\cdot 6.9H_2O$. (b) The photoinduced de-magnetization data for $Rb_{0.91}Mn_{1.05}Fe(CN)_6\cdot 0.6H_2O$. (Adapted with permission from Sato *et al.*[98] and Tokoro *et al.*[99]).

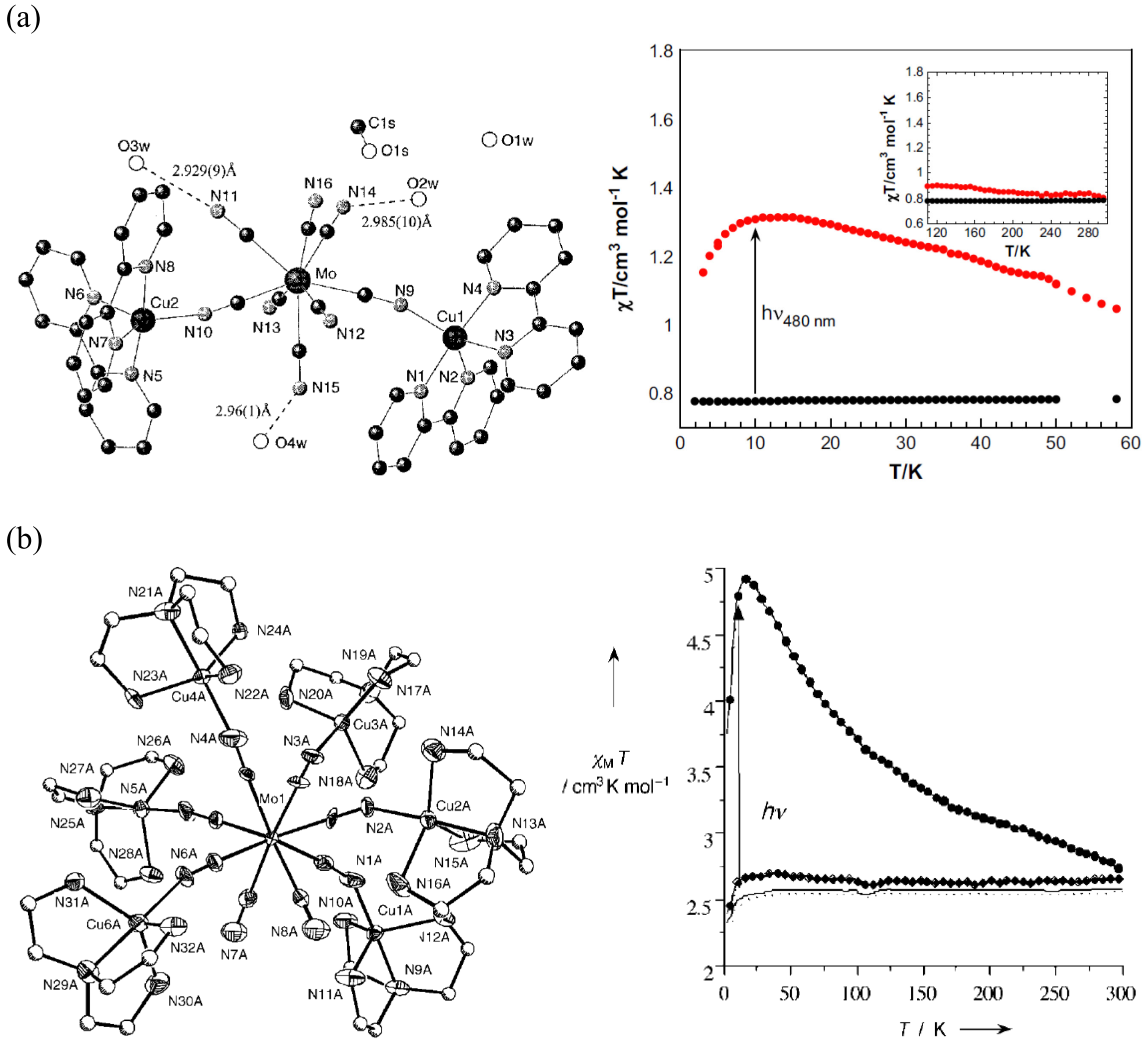

Figure 13: (a) The structure and photomagnetic behavior of $[Cu(bpy)_2]_2[Mo(CN)_8]\cdot xH_2O\cdot CH_3OH$. (b) The structure and photomagnetic behavior of $\{[(Cu(tren)_2]_6[Mo(CN)_8]\}(ClO_4)_8$. (Adapted with permission from Rombaut *et al.*,[100] Mathonière *et al.*[105] – Copyright Elsevier – and Herrera *et al.*[101] – Copyright Wiley-VCH Verlag GmbH & Co. KGaA).

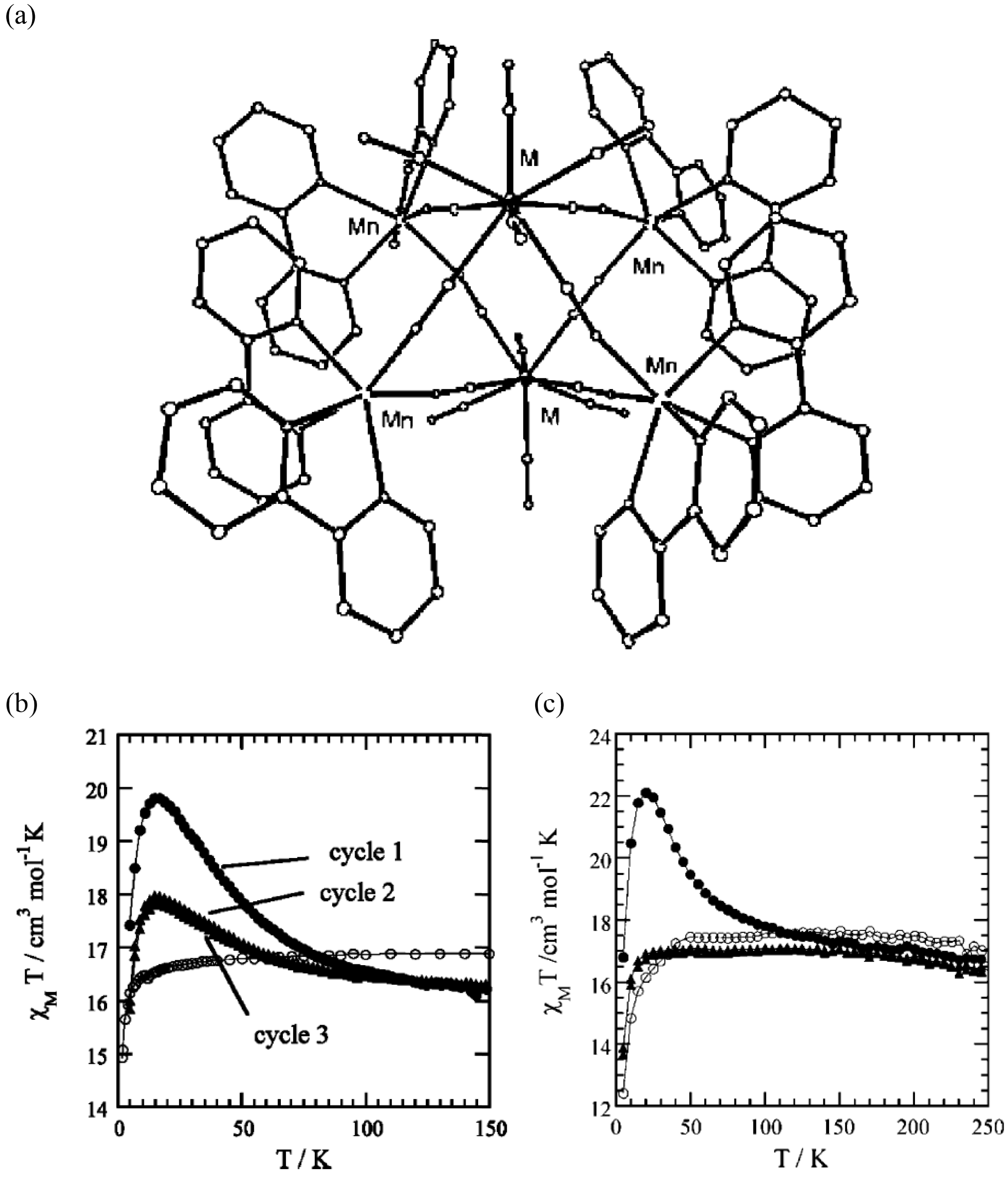

Figure 14: (a) The structure $[Mn(bpy)_2]_4[M(CN)_8]_2 \cdot xH_2O$ (M = Mo,W). (b) The photomagnetic behavior of $[Mn(bpy)_2]_4[Mo(CN)_8]_2 \cdot 14H_2O$. (c) The photomagnetic behavior of $[Mn(bpy)_2]_4[W(CN)_8]_2 \cdot 9H_2O$. (Adapted with permission from Mathoniere *et al.*[102]).

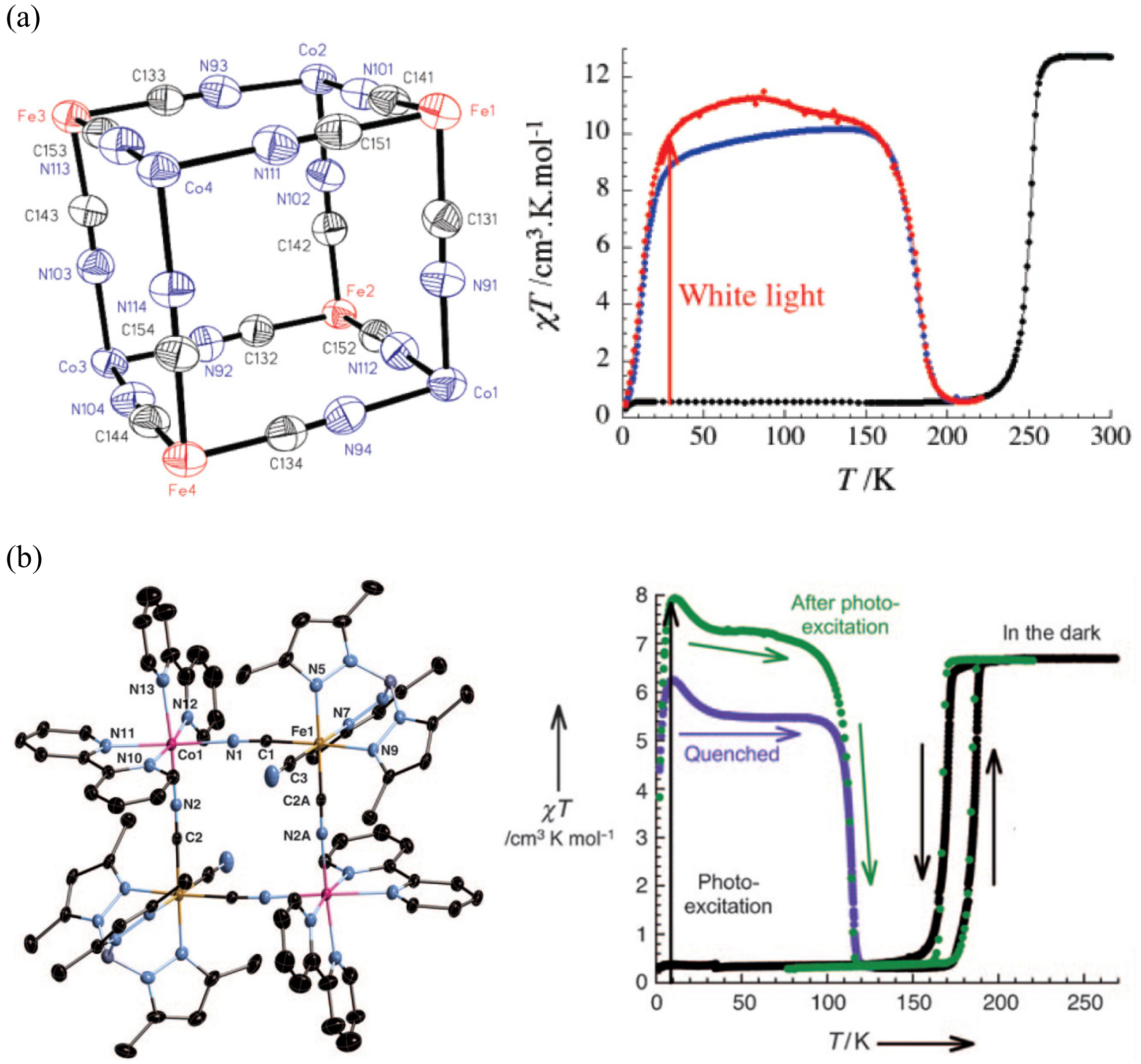

Figure 15: (a) The cubic core, photomagnetic behavior, and thermal charge transfer-induced spin transition of $\{[(pzTp)Fe(CN)_3]_4[Co(pz)_3CCH_2OH]_4[ClO_4]_4\}\cdot 13DMF\cdot 4H_2O$. (b) The structure, photomagnetic behavior, and thermal CTIST of $[\{(Tp^*)Fe(CN)_3\}_2\{Co(bpy)_2\}_2][OTf]_2\cdot 4DMF\cdot 2H_2O$. (Adapted with permission from Li *et al.*[103] and Zhang *et al.*[104] – Copyright Wiley-VCH Verlag GmbH & Co. KGaA).

TRIGONAL-BIPYRAMIDAL CYANIDE CLUSTERS

Cyanide clusters have been synthesized in a large range in sizes from dinuclear up to heptacosanuclear[106] compounds. One common cluster geometry that has been particularly interesting to the Dunbar group is the trigonal bipyramid or TBP. The TBP cyanide cluster type was first documented in 1997 by Murray *et al.*,[107] who reported a crystal structure of the ferromagnetically coupled cluster $\{[(Ni^{II}(bpm)_2]_3[Fe^{III}(CN)_6]_2\}$ with a ground-state spin value of $S = 4$. The group of Verdaguer et al. followed up on this theme with an interesting variation, viz., the isolation of $Ni^{II}{}_3Fe^{III}{}_2$ TBP clusters with ground-state spin values of $S = 7$ achieved by outfitting the Ni centers with paramagnetic $S = 1/2$ radical ligands (e.g., IM2-py).[108] Other metal combinations for the TBP core were reported in the same time frame by Dunbar *et al.* (i.e., $\{[Co(bpy)_2]_3[Fe(CN)_6]_2\}Cl$[109]) and Mallah *et al.* (i.e., $\{[Ni(IM2\text{-}py)_2]_3[Cr(CN)_6]_2\}$[110]). Over the next few years, a variety of similar clusters were isolated with various equatorial metal ions and hexacyanometallate anions (e.g., $\{[Cu(bpy)_2]_3[Fe(CN)_6]_2\}$[111] and $\{[Ni(bpm)_2]_3[Co(CN)_6]_2\}$[112]). Recently, Zuo *et al.* reported a new family of TBP clusters in which both equatorial and axial metal centers are capped by chelating ligands (e.g., $\{[Cu(Me_3tacn)]_3[Fe(Tp)(CN)_3]_2\}(ClO_4)_4$[49]). A number of related compounds have since been reported, including $\{[Fe(Tp)(CN)]_3[M(Tpm^{Me})(CN)_3]_2\}ClO_4$ (M = Ni, Co, Fe)[113] $\{[Ni(cyclen)]_3[Fe(Tp)(CN)_3]_2\}(BF_4)_4$, and $\{[Cu(Me_3tacn)]_3[Cr(Me_3tacn)(CN)_3]_2\}(ClO_4)_6$.[51]

Among the numerous reports of cyanide cluster compounds, there is a general lack of systematic data for a wide range of metal ion combinations for the same molecular geometry. One of the goals of the Dunbar group has been to develop a series of procedures to prepare structurally related molecules in order to determine the magnetic properties for different metal ion combinations and to understand the exchange interactions mediated by the cyanide ligand. The result is a family of trigonal bipyramid (TBP) clusters of the general formula $\{[M(tmphen)_2]_3[M'(CN)_6]_2\}$ (Figure 16), hereafter denoted as $M_3M'_2$ in which the metal centers form the vertices of the TBP and the cyanide bridges serve as the edges. Through the use of a building block approach, the preparation of trigonal-bipyramidal clusters can be accomplished by using a strategy that involves the reaction of divergent hexacyanometallate anions $[M'(CN)_6]^{3-}$ with convergent precursors in the form of mononuclear transition metal complexes $[M(tmphen)_2X_2]^{0/2+}$ which include two labile X ligands (X = Cl^-, Br^-, I^-, MeCN, MeOH, or H_2O) (Scheme 1). In previous work in the Dunbar laboratories, this synthetic approach led to the isolation of three pentanuclear complexes, namely $[Ni^{II}(tmphen)_2]_3[Fe^{III}(CN)_6]_2$,[114] $[Mn^{II}(tmphen)_2]_3[Mn^{III}(CN)_6]_2$,[35] and $[Co(tmphen)_2]_3[Fe(CN)_6]_2$,[115,116] which exhibit the properties of ferromagnetic coupling, single-molecule magnetism (Figure 17), and charge-transfer induced spin transition (Figure 18), respectively. Following these discoveries, three additional clusters were prepared at the same time as this work; these molecules are $[Cr(tmphen)_2]_3[Cr(CN)_6]_2$,[117] $[Fe(tmphen)_2]_3[Cr(CN)_6]_2$,[118] and $[Co(tmphen)_2]_3[Cr(CN)_6]_2$.[117,119] The latter two compounds were found to engage in cyanide-linkage isomerism.

The work described in this dissertation encompasses topics relating to TBP cyanide clusters, their magnetic properties, and the general use of a building block

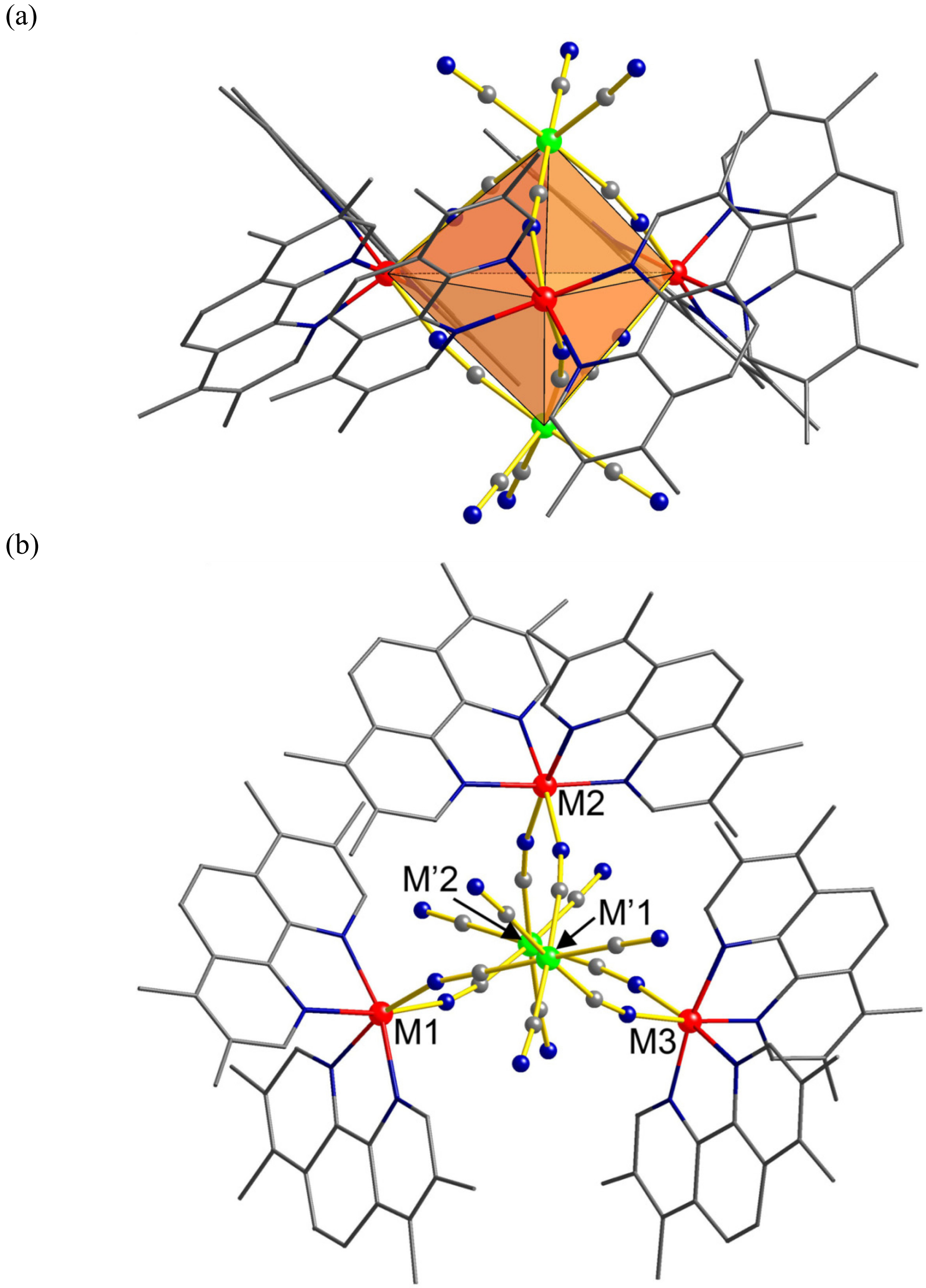

Figure 16: The side (a) and top (b) views (with respect to the pseudo-C_3 axis) of the structure of a typical $[M(tmphen)_2]_3[M'(CN)_6]_2$ TBP cluster. (C, grey; N, blue; O, red; M, red; M′, green). (H atoms and solvent molecules have been omitted for the sake of clarity.)

Scheme 1: General preparation of a $[M(tmphen)_2]_3[M'(CN)_6]_2$ TBP cluster from mononuclear precursors.

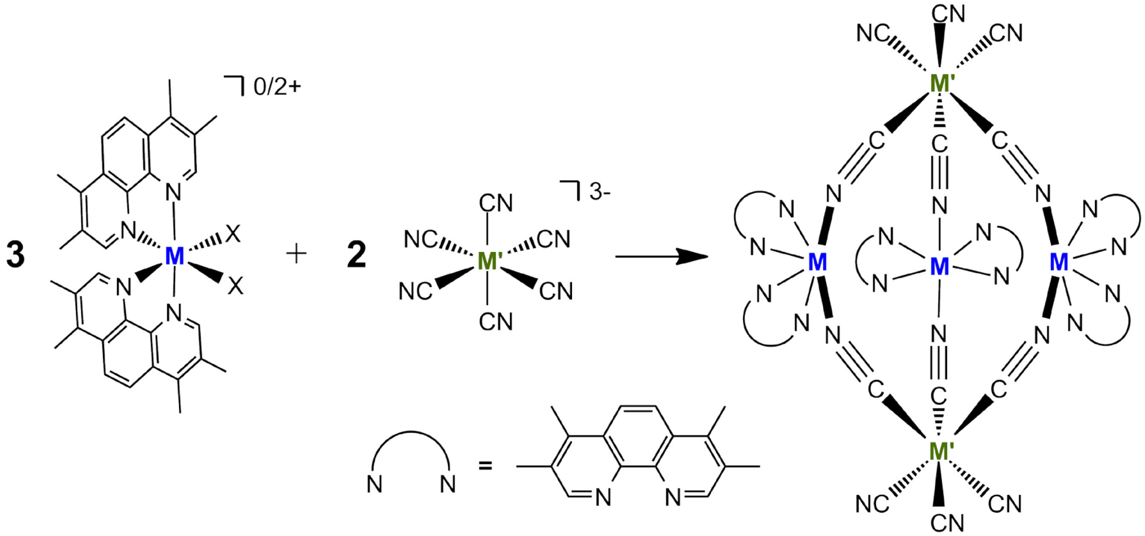

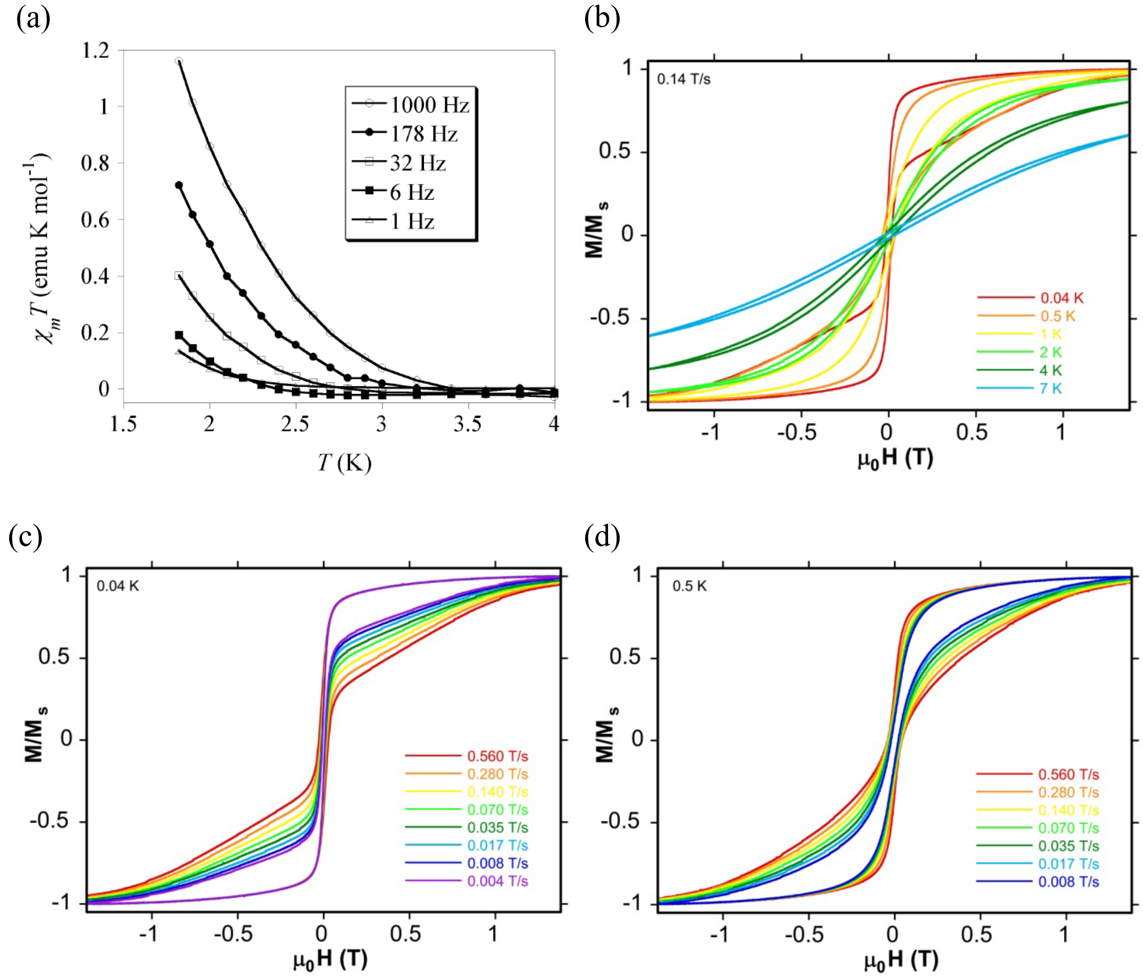

Figure 17: (a) Frequency dependence of the χ_m'' AC magnetic susceptibility vs. T for Mn_3Mn_2. (b) Temperature-dependent micro-SQUID scans collected at 0.14 T/s. (c) Micro-SQUID magnetization scans at variable sweep rates at 0.04 K. (d) Micro-SQUID magnetization scans at variable sweep rates at 0.5 K. (Adapted with permission from Berlinguette *et al.*[35] – Copyright Wiley-VCH Verlag GmbH & Co. KGaA – and Funck *et al.*[60]).

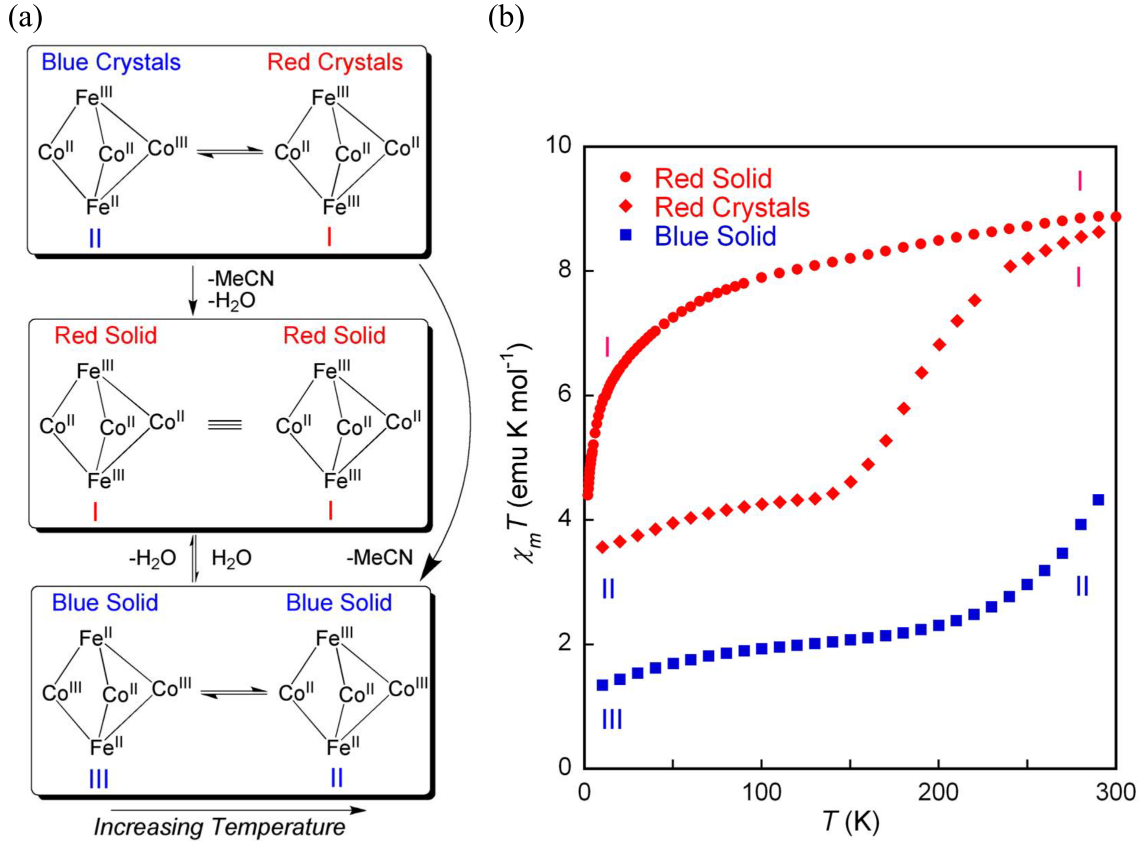

Figure 18: (a) The electronic configurations of the TBP core and (b) the temperature dependence of $\chi_m T$ of the different phases of Co_3Fe_2. (Adapted with permission from Funck *et al.*[60]).

approach. Chapter II describes the expansion of the known family of TBP clusters to include additional 3d transition metal combinations by the synthesis and characterization of nine new TBP clusters. Analyses of the magnetic properties include the use of "model" compounds, where one of the metal centers is examined as to its role in the magnetic coupling between the axial and equatorial paramagnetic metal centers. Chapter III describes the synthesis and characterization of two additional TBP clusters which were found to exhibit spin crossover behavior. In addition, a study to determine the relationship between interstitial solvent and the SCO properties, such as transition temperature and cooperativity was performed. Chapter IV describes the attempts to use soluble TBP clusters as building blocks to prepare 1-D chains of clusters. Chapter V is devoted to the search for photomagnetic properties – LIESST effect or light-induced spin transition – in four TBP clusters. This chapter also reports further work with a previously studied cluster, Co_3Fe_2, with the aim being to find a method to prepare crystals of the cluster without solvent and the determination of the resulting magnetic properties.

CHAPTER II

PREPARATION AND CHARACTERIZATION OF NEW MEMBERS OF THE FAMILY OF MAGNETIC TRIGONAL BIPYRAMIDAL CYANIDE CLUSTERS*

INTRODUCTION

The availability of cyanide-bridged clusters has been very useful for theoreticians working in the area molecular magnetism as simple model systems for testing the proposed theories concerning the properties of extended materials. Indeed, recent trends have indicated that the design of homologous series of molecules and the study of their magnetic properties is one of the most important challenges for the advancement of molecular magnetism.[42,47,120] At this stage, there have been relatively few *systematic* studies of cyanide-bridged clusters of transition metals restricted to a well-defined geometry.[121,122] This chapter provides details of research aimed at extending a synthetic procedure developed in our laboratories for the synthesis of trigonal bipyramidal (TBP) clusters to include new combinations of the first-row transition-metal ions. In particular, a series of model compounds was prepared with

---

*Parts of this chapter are reproduced with permission from:

1. "Systematic Investigation of Trigonal-Bipyramidal Cyanide-Bridged Clusters of the First Row Transition Metals" by Shatruk, M.; Chambers, K. E.; Prosvirin, A. V.; Dunbar, K. R., **2007**. *Inorg. Chem.*, *46*, 5155-5165, Copyright 2007 by ACS Publications.
2. "Properties of Prussian Blue Materials Manifested in Molecular Complexes: Observation of Cyanide Linkage Isomerism and Spin-Crossover Behavior in Pentanuclear Cyanide Clusters" by Shatruk, M.; Dragulescu-Andrasi, A.; Chambers, K. E.; Stoian, S. A.; Bominaar, E. L.; Achim, C.; Dunbar, K. R., **2007**. *J. Am. Chem. Soc.*, *129*, 6104-6116, Copyright 2007 by ACS Publications.

diamagnetic metal centers in either the equatorial or axial positions. By understanding the nature of the magnetic properties of the equatorial and axial metal ions individually we are in a position to properly analyze the magnetic coupling in clusters containing additional paramagnetic ions. The properties of these complexes are discussed and compared to the corresponding behavior of the related mixed-metal 3D Prussian blue materials.

EXPERIMENTAL

Materials

Commercially available tmphen (Alfa Aesar), 18-crown-6 (Aldrich, Acros), PPNCl (Aldrich), $K_3[Cr(CN)_6]$ (Aldrich), $K_3[Fe(CN)_6]$ (Fisher), $K_3[Co(CN)_6]$ (Pfaltz & Bauer), $(TBA)_3[Fe(CN)_6]$ (Fluka), $Mn(OAc)_2\cdot 4H_2O$ (Aldrich), $Mn(ClO_4)_2\cdot 6H_2O$ (Alfa Aesar), $Co(NO_3)_2\cdot 6H_2O$ (Strem), $Ni(OAc)_2\cdot 4H_2O$ (Fisher), $Zn(NO_3)_2\cdot 6H_2O$ (Fisher), and $Zn(OAc)_2\cdot 4H_2O$ (Fisher) were used as received. Acetonitrile and methanol are ACS reagent grade and were used as received (EMD Chemicals).

The compound $(PPN)_3[Fe(CN)_6]$ was prepared by a slight modification of the method of Predieri *et al.*, [123] in which the product was washed with diethyl ether prior to drying *in vacuo* at 50-60°C. Stock solutions (4mM) of $[(18\text{-crown-}6)K]_3[M(CN)_6]$ (M = Cr, Co) were prepared by stirring 150 mg (0.451 mmol) $K_3[M(CN)_6]$ and 318 mg (1.20 mmol) 18-crown-6 in 100 mL acetonitrile for 24 h (or 100 mL of methanol for 2 h) which were filtered to remove the excess $K_3[M(CN)_6]$.

Synthesis

Note: The concentrations typically yield the highest quality single crystals (for X-ray crystallography), but the reactions can be scaled up to obtain larger quantities of the products.

{[Mn(tmphen)$_2$]$_3$[Fe(CN)$_6$]} (1). Samples of $Mn(OAc)_2{\cdot}4H_2O$ 9.9 mg, (0.040 mmol) and tmphen (18.9 mg, 0.080 mmol) were combined in 10 mL acetonitrile and stirred for 30 minutes to obtain a clear, pale yellow solution. (If the mixture was not clear after 30 minutes, it was filtered through filter paper.) To this solution was quickly added a solution of 37.6 mg (0.040 mmol) of $(TBA)_3[Fe(CN)_6]$ or 73.1 mg (0.040 mmol) $(PPN)_3[Fe(CN)_6]$ in 10 mL of acetonitrile. The mixture was left to stand undisturbed for 2 days. After this time, yellow-brown needle-like crystals were observed to be present in the bottom of the vial. The crystals were collected by filtration, washed with acetonitrile (40 mL), and dried *in vacuo*. Yield – 9.5 mg (32%). Elemental analysis indicated the presence of interstitial water molecules. Calculated for $Mn_3Fe_2O_{12}N_{24}C_{108}H_{120}$ (**1**$\cdot 12H_2O$): O, 8.67; N, 15.18; C, 58.56; H, 5.46; Found: O, 8.61; N, 14.90; C, 57.92; H, 5.35%. Thermal gravimetric analysis (Figure 19) indicates an 8.3% mass loss which corresponds to 10 water molecules. IR (Nujol), ν(C≡N), cm^{-1}: 2147, 2141, 2135, 2117, 2112.

{[Zn(tmphen)$_2$]$_3$[Fe(CN)$_6$]} (2). A similar procedure was used as that described for **1** using a quantity of $Zn(NO_3)_2{\cdot}6H_2O$ (11.9 mg, 0.040 mmol) in place of $Mn(OAc)_2{\cdot}4H_2O$. Light brown needle-like crystals were formed. Yield – 87.2 mg (73%). Elemental analysis indicated the presence of interstitial water molecules. Calculated for

$Zn_3Fe_2O_{12}N_{24}C_{108}H_{120}$ (**2**·12H_2O): O, 8.52; N, 14.91; C, 57.55; H, 5.37; Found: O, 8.39; N, 14.66; C, 56.71; H, 4.97%. Thermal gravimetric analysis (Figure 19) indicates a 7.6% mass loss which corresponds to 9 water molecules. IR (Nujol), $\nu(C\equiv N)$, cm $^{-1}$: 2165, 2156, 2154, 2117, 2112.

{[Mn(tmphen)$_2$]$_3$[Cr(CN)$_6$]} (3). A sample of $Mn(ClO_4)_2 \cdot 6H_2O$ (14.5 mg, 0.040 mmol) and tmphen (18.9 mg, 0.080 mmol) were combined in 10 mL of acetonitrile and stirred for 30 minutes to obtain a clear, pale yellow solution. To this solution was added 10 mL of the [(18-crown-6)K]$_3$[Cr(CN)$_6$] stock solution (acetonitrile) The mixture was left to stand undisturbed for 3 days during which time pale yellow needle-like crystals formed at the bottom of the vial which were collected by filtration, washed with acetonitrile (40 mL), and dried *in vacuo*. Yield – 9.9 mg (33%). Elemental analysis indicated the presence of interstitial water molecules. Calculated for $Mn_3Cr_2O_{14}N_{24}C_{108}H_{124}$ (**3**·14H_2O): O, 9.95; N, 14.93; C, 57.62; H, 5.55; Found: O, 10.26; N, 15.01; C, 57.70; H, 5.22%. Thermal gravimetric analysis (Figure 19) indicates a 12.8% mass loss which corresponds to 16 water molecules. IR (Nujol), $\nu(C\equiv N)$, cm^{-1}: 2153, 2144, 2127.

{[Ni(tmphen)$_2$]$_3$[Cr(CN)$_6$]} (4). A similar procedure was used as that described for **3** using a quantity of $Ni(OAc)_2 \cdot 6H_2O$ (10.0 mg, 0.040 mmol) in place of $Mn(ClO_4)_2 \cdot 6H_2O$ and methanol solutions of all compounds. Light pink needle-like crystals were formed. Yield – 10.1 mg (34%). Elemental analysis indicated the presence of interstitial water molecules. Calculated for $Ni_3Cr_2O_{12}N_{24}C_{108}H_{120}$ (**4**·12H_2O): O, 8.62; N, 15.09; C, 58.25; H, 5.43; Found: O, 8.51; N, 14.73; C, 58.81; H, 5.46%. Thermal gravimetric analysis (Figure 19) indicates an 8.3% mass loss which corresponds to 10 water molecules. IR (Nujol), ν(C≡N), cm^{-1}: 2160, 2150, 2127.

{[Zn(tmphen)$_2$]$_3$[Cr(CN)$_6$]} (5). A similar procedure was used as that described for **3** using a quantity of $Zn(NO_3)_2 \cdot 6H_2O$ (11.9 mg, 0.040 mmol) in place of $Mn(ClO_4)_2 \cdot 6H_2O$. Pale yellow needle-like crystals were formed. Yield – 96.3 mg (82%). Elemental analysis indicated the presence of interstitial water molecules. Calculated for $Zn_3Cr_2O_{11}N_{24}C_{108}H_{118}$ (**4**·11H_2O): O, 7.90; N, 15.09; C, 58.21; H, 5.34; Found: O, 7.47; N, 14.83; C, 57.09; H, 5.28%. Thermal gravimetric analysis (Figure 19) indicates a 10.4% mass loss which corresponds to 13 water molecules. IR (Nujol), ν(C≡N), cm^{-1}: 2172, 2162, 2152, 2125.

{[Mn(tmphen)$_2$]$_3$[Co(CN)$_6$]} (6). **Samples** of $Mn(ClO_4)_2 \cdot 6H_2O$ (14.5 mg, 0.040 mmol) and tmphen (18.9 mg, 0.080 mmol) were combined in 10 mL of acetonitrile and stirred for 30 minutes to obtain a clear, pale yellow solution. To this solution was added 10 mL of [(18-crown-6)K]$_3$[Co(CN)$_6$] stock solution (acetonitrile) and the mixture was left to stand undisturbed for 5 days. After this time, clear light yellow needle-like crystals had formed at the bottom of the vial which were collected by filtration, washed with acetonitrile (40 mL), and dried *in vacuo*. Yield – 9.8 mg (33%). Elemental analysis indicated the presence of interstitial water molecules. Calculated for $Mn_3Co_2O_{13}N_{24}C_{108}H_{122}$ (**5**·13H_2O): O, 9.26; N, 14.97; C, 57.71; H, 5.48; Found: O, 9.27; N, 14.78; C, 57.74; H, 5.04%. Thermal gravimetric analysis (Figure 19) indicates a 9.7% mass loss which corresponds to 12 water molecules. IR (Nujol), ν(C≡N), cm^{-1}: 2165, 2154, 2145, 2131.

{[Co(tmphen)$_2$]$_3$[Co(CN)$_6$]} (7). A similar procedure was used as that described for **6** using a quantity of $Co(NO_3)_2\cdot6H_2O$ (11.7 mg, 0.040 mmol) in place of $Mn(ClO_4)_2\cdot6H_2O$ and methanol solutions of all compounds. Clear orange needle-like crystals were formed. Yield – 27.5 mg (83%). Elemental analysis indicated the presence of interstitial water molecules. Calculated for $Co_5O_{19}N_{24}C_{108}H_{124}$ (**6**$\cdot$19H_2O): O, 12.84; N, 14.20, C, 54.80; H, 5.71; Found: O, 13.74; N, 14.22, C, 55.12; H, 5.19%. Thermal gravimetric analysis (Figure 19) indicates a 12.5% mass loss which corresponds to 16 water molecules. IR (Nujol), $\nu(C\equiv N)$, cm^{-1}: 2167, 2157, 2148, 2130, 2125.

{[Ni(tmphen)$_2$]$_3$[Co(CN)$_6$]} (8). A similar procedure was used as that described for **3** using a quantity of $Ni(OAc)_2\cdot4H_2O$ (10.3 mg, 0.040 mmol) in place of $Mn(ClO_4)_2\cdot6H_2O$. Clear purple block-shaped crystals were formed. Yield – 17.0 mg (52%). Elemental analysis indicated the presence of interstitial water molecules. Calculated for $Ni_3Co_2O_{23}N_{24}C_{108}H_{142}$ (**7**$\cdot$23H_2O): O, 15.11; N, 13.80; C, 53.23; H, 5.88; Found: O, 15.16; N, 13.79; C, 53.77; H, 5.38%. Thermal gravimetric analysis (Figure 19) indicates a 16.0% mass loss which corresponds to 21 water molecules. IR (Nujol), $\nu(C\equiv N)$, cm^{-1}: 2174, 2164, 2154, 2127, 2123.

{[Zn(tmphen)$_2$]$_3$[Co(CN)$_6$]} (9). A similar procedure was used as that described for **3** using a quantity of $Zn(OAc)_2\cdot2H_2O$ (8.8 mg, 0.040 mmol) in place of $Mn(ClO_4)_2\cdot6H_2O$. Clear colorless block-shaped crystals were formed. Yield – 14.5 mg (46%). Elemental analysis indicated the presence of interstitial water molecules. Calculated for $Zn_3Co_2O_{18}N_{24}C_{108}H_{132}$ (**8**$\cdot$18H_2O): O, 12.19; N, 14.22; C, 54.85; H, 5.63; Found: O, 12.02; N, 13.85; C, 54.21; H, 4.91%. Thermal gravimetric analysis (Figure 19) indicates a 13.8% mass loss which corresponds to 18 water molecules. IR (Nujol), ν(C≡N), cm^{-1}: 2173, 2164, 2155, 2130.

Single Crystal X-ray Studies

In a typical experiment, a crystal selected for study was suspended in polybutene oil (Aldrich) and mounted on a cryoloop, which was placed in an N_2 cold stream. Single-crystal X-ray data were collected at 120 or 150 K on a Bruker APEX diffractometer equipped with a CCD detector. The data sets were recorded as three ω-scans of 606 frames each, at 0.3° step width, and integrated with the Bruker SAINT[124] software package. The absorption correction (SADABS[125]) was based on fitting a function to the empirical transmission surface as sampled by multiple equivalent measurements (intentional redundancy in the data collection). Solution and refinement of the crystal structures was carried out using the SHELX[126] suite of programs and the graphical interface X-SEED.[127] Preliminary indexing of the data sets established similar monoclinic unit cells for all of the studied compounds. Systematic extinctions indicated the space group $P2_1/c$ (No. 14). All of the structures were solved by direct methods that resolved the positions of the metal atoms and most of the C and N atoms. The remaining non-hydrogen atoms were located by alternating cycles of least-squares refinements and difference Fourier maps. Hydrogen atoms were placed at calculated positions. In all structures, a large number of interstitial solvent molecules were present, most of which are heavily disordered. Only for structures **1** and **7** was it possible to obtain a satisfactory model of the disorder. Given the fact that the refinement of the TBP clusters is essentially uninfluenced by the presence of the disordered solvents, the SQUEEZE

(a)

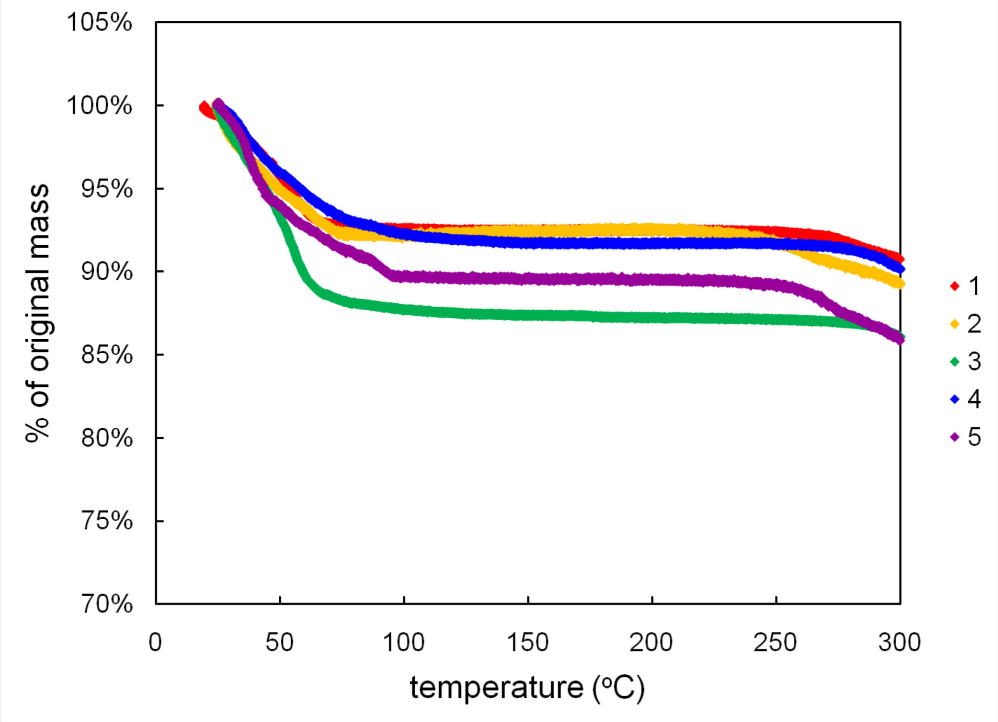

(b)

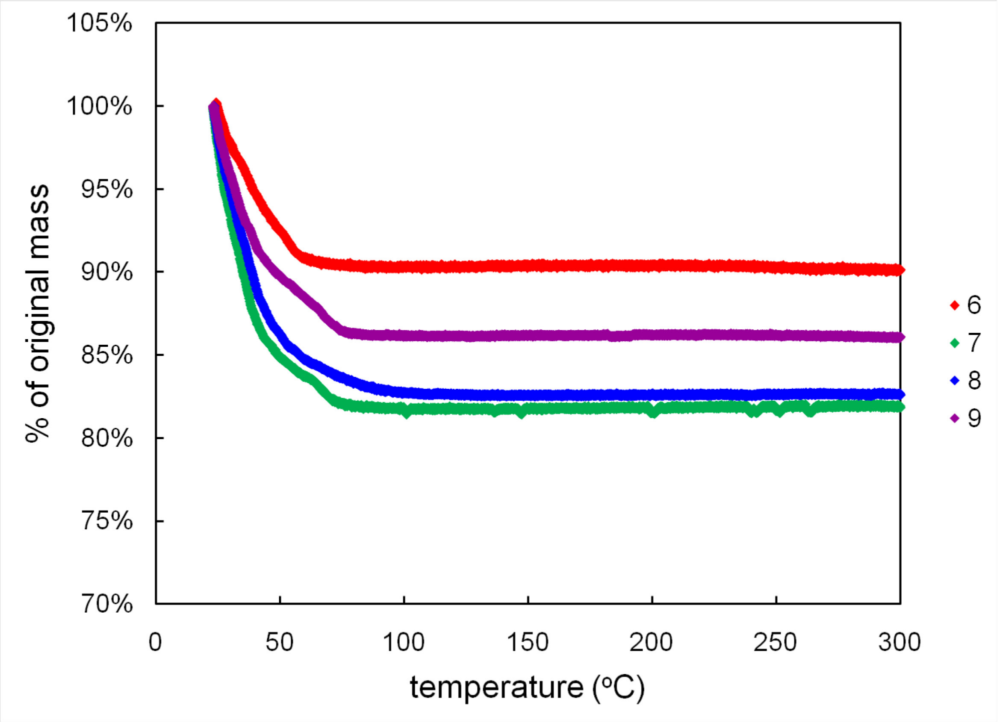

Figure 19: The weight loss observed for (a) compounds **1-5** and (b) compounds **6-9** in the temperature range of 25-300°C.

routine[128] was applied to subtract the diffraction contribution from the disordered solvents and to evaluate the number of solvent molecules present in the interstices of **2**,**4-6**, **8**, and **9**. The final refinement was carried out with anisotropic thermal parameters for all non-hydrogen atoms of the TBP unit and isotropic thermal parameters for the disordered solvent molecules; the latter were refined only for **1** and **7**. All attempts to grow a single crystal of **3** of satisfactory quality for an X-ray crystal structure determination were unsuccessful. Some crystals, however, were sufficiently large to allow for unit cell parameters to be obtained (primitive monoclinic cell with a = 19.313(4), b = 25.167(5), c = 24.316(5) Å, β = 99.42(3)°), which confirmed that **3** is isostructural with the other structurally characterized compounds presented in this chapter.

RESULTS

Syntheses

The combination of a divergent hexacyanometallate anion $[M'(CN)_6]^{3-}$ with a convergent mononuclear precursor, in this case an octahedral divalent 3d metal ion in which four coordination sites are capped by two bis-chelating tmphen ligands, results in the precipitation of crystalline solids of general formula $[M(tmphen)_2]_3[M'(CN)_6]_2 \cdot x(solvent)$. The preparation methods are similar to previously prepared TBP's of this family[35,114-116] and were used to prepare new clusters with various combinations of the first-row transition-metal ions. The facile crystallization of pure samples of **1-9** is attributed to the fact that the clusters are neutral and essentially insoluble in most common solvents. Except for the exchange of the interstitial solvent with ambient water, the products are air-stable and can be stored without specific precautions for prolonged periods of time, as there is no observed change in the magnetic properties with time.

It should be noted that crystalline forms of **1-9** contain large and varying amounts of interstitial solvents as a result of the poor packing of the molecules. Examination of the compounds by TGA revealed that they gradually lose the interstitial solvent when heated to ~120°C. Above this temperature, the clusters remain stable to 250-300°C, after which temperature they decompose with further heating. The significance of the interstitial solvent is explored further in Chapter III.

Single-Crystal X-ray Structures

Summaries of pertinent information relating to unit cell parameters, data collection, and refinement statistics are provided in Tables 1-3. Single-crystal X-ray studies revealed that **1-9** are isostructural and crystallize in the monoclinic space group $P2_1/c$. The molecular structures consist of a pentanuclear core composed of CN-bridged M^{II} and M'^{III} ions (Figures 20). The latter belong to $[M'(CN)_6]^{3-}$ moieties that occupy the axial positions of the TBP core. Three CN^- ligands of each hexacyanometallate unit act as bridges, and the other three terminal CN^- ligands point toward the exterior of the cluster. The three equatorial M^{II} ions are in pseudo-octahedral coordination environments that consist of two bidentate tmphen molecules and two N-bound CN^- ligands. The tmphen ligands are involved in intra- and intermolecular π-π interactions.

Table 1: Crystallographic data and structural refinement parameters for compounds **1**, **2**, and **4**.

	(**1**)·5.5MeCN·2.5H_2O	(**2**)·16MeCN[a]	(**4**)·14.5MeOH[a]
chemical formula	$C_{119}H_{117.5}N_{29.5}O_{2.5}Mn_3Fe_2$	$C_{140}H_{144}N_{40}Zn_3Fe_2$	$C_{122.5}H_{125}N_{41}O_{14.5}Ni_3Cr_2$
formula weight	2277.46	2694.89	2683.69
space group	$P2_1/c$ (No. 14)	$P2_1/c$ (No. 14)	$P2_1/c$ (No. 14)
a	19.57(3) Å	19.425(3) Å	19.50(1) Å
b	25.36(4) Å	25.331(4) Å	25.12(2) Å
c	24.57(2) Å	24.729(4) Å	24.67(2) Å
α	90°	90°	90°
β	99.11(5)°	98.142(3)°	98.17 (3)°
γ	90°	90°	90°
volume	12042(29) Å^3	12045(3) Å^3	11962(16) Å^3
Z	4	4	4
temperature	120 K	150 K	110 K
density (calc)	1.244 g/cm^3	1.124 g/cm^3	1.116 g/cm^3
abs coeff (μ)	0.602 mm^{-1}	0.874 mm^{-1}	0.690 mm^{-1}
crystal color and habit	yellow-brown needle	yellow needle	pink needle
crystal size (mm^3)	0.48 × 0.07 × 0.07	0.80 × 0.06 × 0.06	0.50 × 0.09 × 0.06
radiation	Mo Kα, 0.71073 Å	Mo Kα, 0.71073 Å	Mo Kα, 0.71073 Å
θ range	1.05-26.37°	1.06-23.26°	1.16-26.37°
reflections collected	96698 [R_{int} = 0.1500]	74253 [R_{int} = 0.1438]	127053 [R_{int} = 0.1327]
data/parameters/restraints	24596/1383/27	17320/1258/0	24463/1258/0
R_1	0.099	0.0727	0.069
wR_2	0.252	0.1582	0.135
GOF (F^2)	0.984	1.072	1.059
max./min. residual densities (e·Å^{-3})	1.138, -0.849	0.520, -0.450	0.599, -0.340

[a] The solvent content was estimated from the electron density attributed to the disordered solvent contribution by SQUEEZE.

Table 2: Crystallographic data and structural refinement parameters for compounds **5**, **6**, and **7**.

	(**5**)·17MeCN[a]	(**6**)·13MeCN[a]	(**7**)·7.25MeOH·3.75H_2O
chemical formula	$C_{142}H_{147}N_{41}Zn_3Cr_2$	$C_{134}H_{135}N_{37}Mn_3Co_2$	$C_{115.25}H_{132.5}N_{24}O_{11}Co_5$
formula weight	2728.24	2546.49	2324.65
space group	*P*2$_1$/c (No. 14)	*P*2$_1$/c (No. 14)	*P*2$_1$/c (No. 14)
a	19.420(3) Å	19.449(2) Å	19.494(2) Å
b	25.613(4) Å	25.589(2) Å	25.075(3) Å
c	24.874(4) Å	25.047(2) Å	24.727(3) Å
α	90°	90°	90°
β	97.498(3)°	98.153(2)°	98.979 (2)°
γ	90°	90°	90°
volume	12267(3) Å^3	12339(2) Å^3	11939(2) Å^3
Z	4	4	4
temperature	150 K	150 K	150 K
density (calc)	1.099 g/cm^3	1.084 g/cm^3	1.233 g/cm^3
abs coeff (μ)	0.602 mm^{-1}	0.611 mm^{-1}	0.746 mm^{-1}
crystal color and habit	colorless needle	colorless needle	orange needle
crystal size (mm^3)	0.97 × 0.07 × 0.06	1.20 × 0.16 × 0.16	0.82 × 0.14 × 0.05
radiation	Mo Kα, 0.71073 Å	Mo Kα, 0.71073 Å	Mo Kα, 0.71073 Å
θ range	1.15-23.26°	1.14-28.46°	1.06-26.37°
reflections collected	75346 [R_{int} = 0.1471]	106600 [R_{int} = 0.0550]	95915 [R_{int} = 0.0855]
data/parameters/restraints	17615/1258/0	28986/1258/0	24413/1442/21
R_1	0.0630	0.054	0.078
wR_2	0.1312	0.117	0.218
GOF (F^2)	1.000	1.054	1.029
max./min. residual densities (e·Å^{-3})	0.430, -0.575	0.696, -0.273	0.891, -0.476

[a] The solvent content was estimated from the electron density attributed to the disordered solvent contribution by SQUEEZE.

Table 3: Crystallographic data and structural refinement parameters for compounds **8** and **9**.

	(**8**)· 14MeCN[a]	(**9**)·21MeCN[a]
chemical formula	$C_{136}H_{138}N_{38}Ni_3Fe_2$	$C_{150}H_{159}N_{45}Zn_3Co_2$
formula weight	2598.81	2906.33
space group	$P2_1/c$ (No. 14)	$P2_1/c$ (No. 14)
a	19.225(2) Å	19.348(5) Å
b	25.009(3) Å	25.480(7) Å
c	24.716(3) Å	25.186(7) Å
α	90°	90°
β	98.031 (2)°	97.888(4)°
γ	90°	90°
volume	11767(2) $Å^3$	12299(6) $Å^3$
Z	4	4
temperature	150 K	150 K
density (calc)	1.143 g/cm^3	1.104 g/cm^3
abs coeff (μ)	0.799 mm^{-1}	0.890 mm^{-1}
crystal color and habit	purple block	colorless needle
crystal size (mm^3)	0.50 × 0.31 × 0.15	0.90 × 0.08 × 0.08
radiation	Mo Kα, 0.71073 Å	Mo Kα, 0.71073 Å
θ range	1.07-28.29°	1.33-26.37°
reflections collected	44651 [R_{int} = 0.0519]	64919 [R_{int} = 0.1772]
data/parameters/restraints	24395/1259/0	25057/708/30
R_1	0.070	0.107
wR_2	0.174	0.215
GOF (F^2)	0.820	1.104
max./min. residual densities ($e\cdot Å^{-3}$)	1.871, -0.574	1.162, -1.977

[a] The solvent content was estimated from the electron density attributed to the disordered solvent contribution by SQUEEZE.

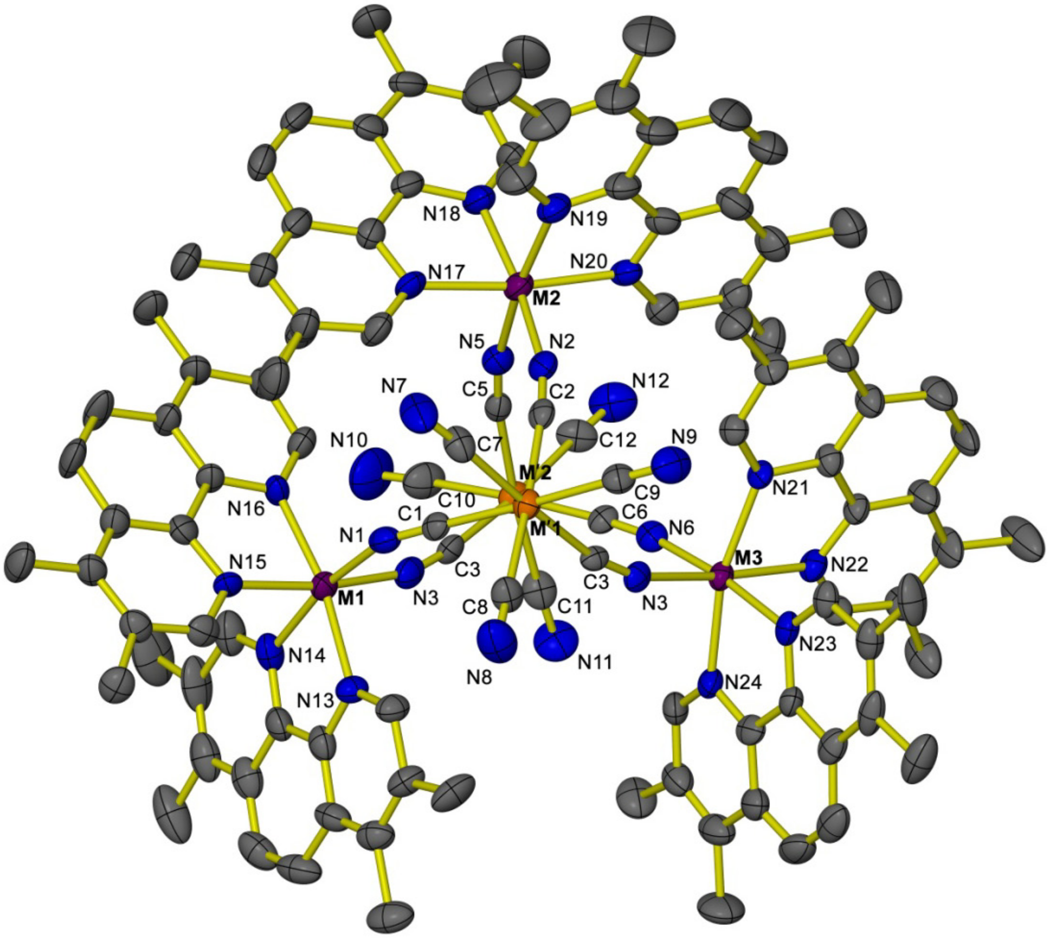

Figure 20: Thermal ellipsoid plot of a typical tbp cluster ($M_3M'_2$), drawn at the 50% probability level. (H atoms have been omitted for the sake of clarity).

Both tmphen ligands bound to the M(2) center engage in intramolecular π-π contacts with tmphen ligands from neighboring M(1)/M(3) centers (Figure 21a). In contrast, only one tmphen ligand from the M(1) and M(3) centers is involved in an intramolecular π-π interaction with a tmphen ligand bound to the M(2) site. The large separation between the remaining non-interacting tmphen ligands affords sufficient space for the corresponding tmphen ligands from a second cluster to interact to form a dimer held together by the π-π stacking of the four ligands (Figure 21b). In thisarrangement, one of the tmphen ligands on each M(1) center is engaged in *two* intermolecular π-π contacts, whereas the ligands coordinated to the M(3) center exhibit only one such contact.[60] The three equatorial metal sites in one TBP cluster exhibit the same chirality (Δ or Λ), and each dimer contains both enantiomers, resulting in the centrosymmetric space group.

Mass Spectrometry

Compounds **1-9** are slightly soluble in 1:1 v/v methanol-dichloromethane – from ~0.05 mM for **3** and **5** to over 1 mM for **7** and **8**. Mass spectrometry for **1**-**9** indicated some fragmentation of the clusters under the conditions of nano-electrospray ionization, which led to the mononuclear fragments $[M(tmphen)_2]^{2+}$ (m/z = 264-268) and $[M(tmphen)_3]^{2+}$ (m/z = 382-386), as well as free, protonated tmphen (m/z = 237) (Table 4). Whole clusters have been also observed, taking various forms such as $[M_3M'_2 + 2Na]^{2+}$, $[M_3M'_2 + M(tmphen)_2]^{2+}$, and $[M_3M'_2 + Na + M(tmphen)_3]^{3+}$ (Table 4, Figures 22-23), suggesting that the clusters remain intact when dissolved.

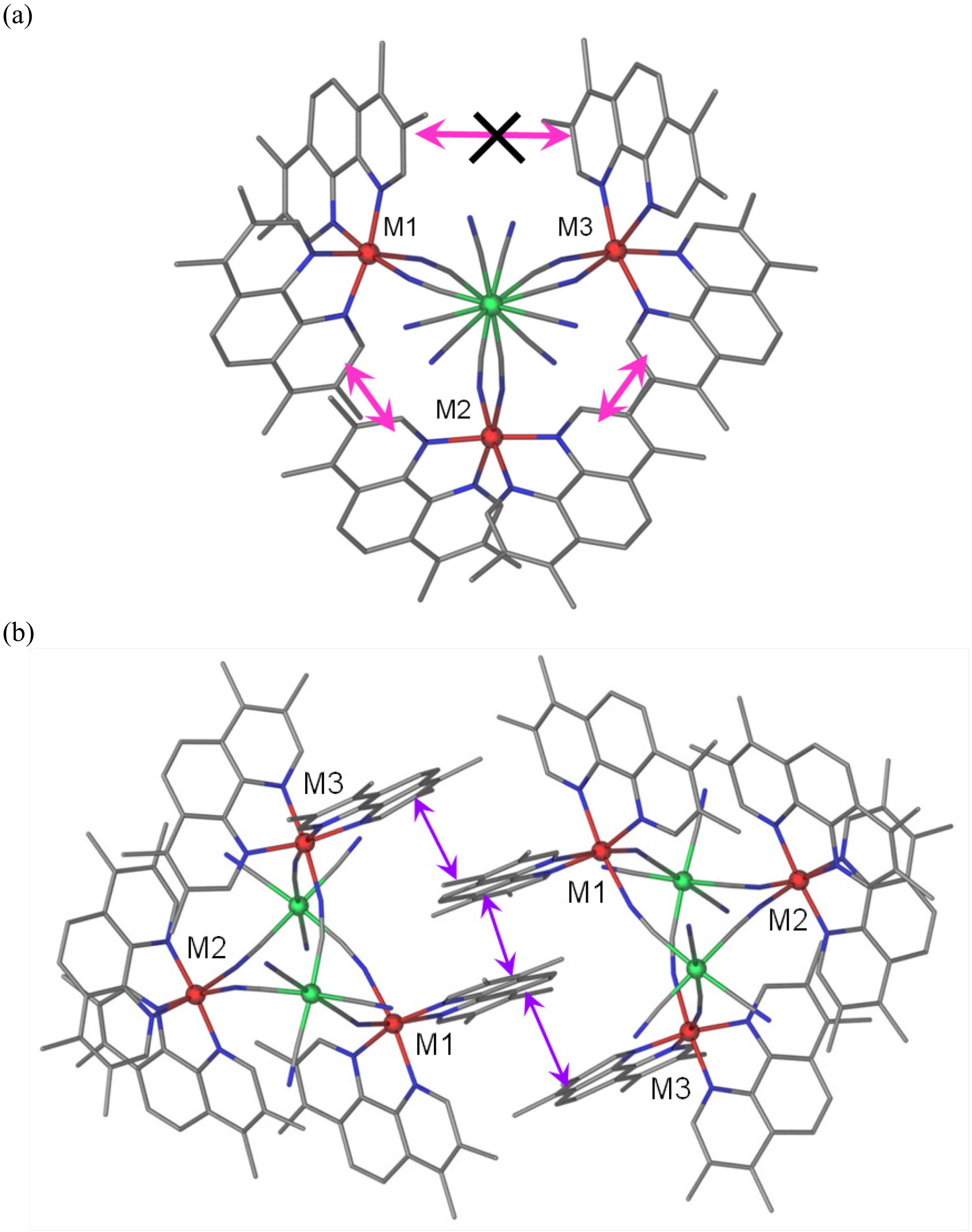

Figure 21: (a) The intramolecular π-π interactions in TBP compounds. (b) The intermolecular π-π interactions between two clusters in the π-stacked dimer.

Table 4: Mass spectral peaks (m/z) observed for compounds **1-9** (dissolved in 1:1 methanol/dichloromethane).

fragment	1	2	3	4	5	6	7	8	9
$[\text{tmphen} + \text{H}]^{+}$	237.1	237.1	237.1	237.1	237.1	237.1	237.1	237.1	237.1
$[\text{M(tmphen)}_2]^{2+}$	263.6	268.1	263.6	265.1	268.1	263.6	263.6	263.6	268.1
$[\text{M(tmphen)}_3]^{2+}$	382.2	386.1	382.1	383.1	386.1	382.1	382.1	382.1	386.2
$[\text{M}_3\text{M}'_2 + \text{Na} + \text{M(tmphen)}_2]^{3+}$		865.9		854.9	864.2				868.5
$[\text{M}_3\text{M}'_2 + \text{Na} + \text{M(tmphen)}_3]^{3+}$		944.6		933.3	942.6				
$[\text{M}_3\text{M}'_2 + 2\text{Na}]^{2+}$	1026.2	1042.3	1022.2	1027.7	1037.7	1029.2	1035.2	1034.2	1044.7
$[\text{M}_3\text{M}'_2 + \text{M(tmphen)}_2]^{2+}$	1266.8	1288.4		1269.8	1284.3				1290.2

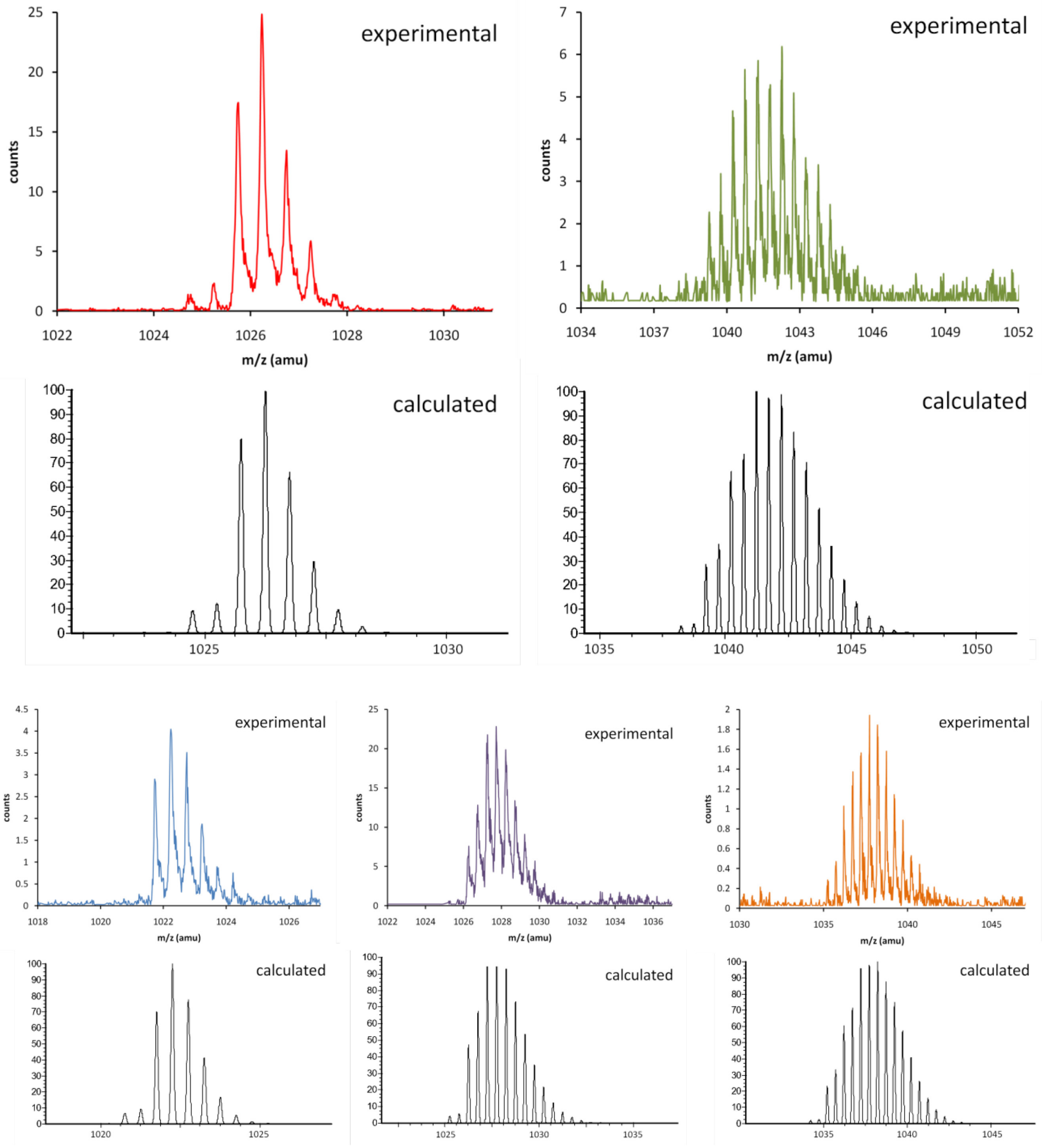

Figure 22: Experimental and calculated (plotted as relative isotopic abundance vs. mass to charge ratio, m/z) "$[M_3Co_2 + 2Na]^{2+}$" MS peaks for **1** (red), **2** (green), **3** (blue), 4 (purple), and **5** (orange).

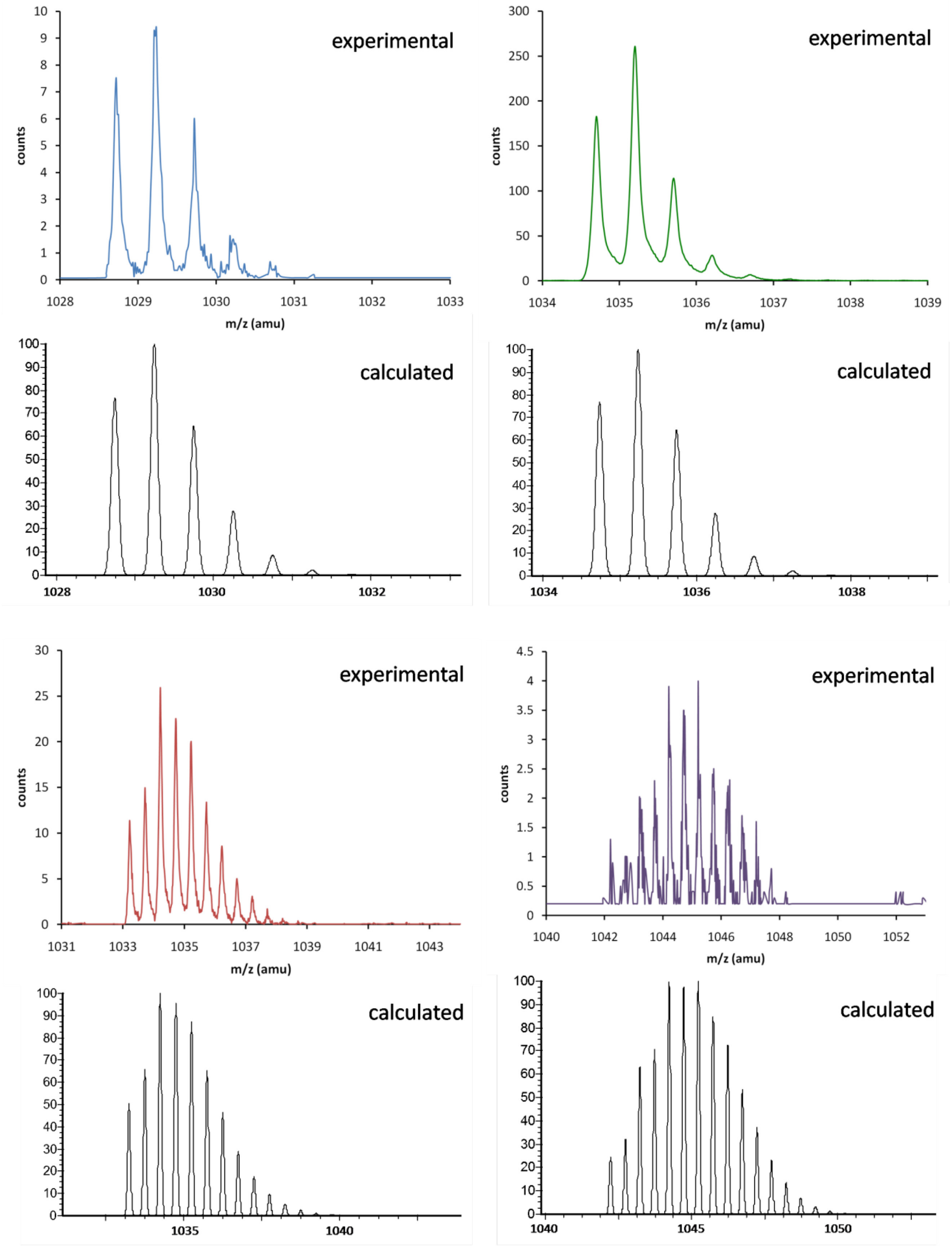

Figure 23: Experimental and calculated “[M_3Co_2 + 2Na]$^{2+}$” MS peaks for **6** (blue), **7** (green), **8** (red), and **9** (purple).

Infrared Spectroscopy

Compounds **1-9** exhibit characteristic bands in the region of the C≡N stretching frequencies. These bands can be assigned to bridging or terminal cyanide ligands by comparing the cluster IR data to the *v*(C≡N) stretches observed for the corresponding extended Prussian blue phases and the free hexacyanometallate anions. As indicated by the data in Table 5, the IR spectra of **1-9** exhibit lower frequency stretches that are comparable to the corresponding modes of the $[M'(CN)_6]^{3-}$ ions and, therefore, are reasonably assigned to the terminal cyanide ligands. Upon formation of the M'^{III}-C≡N-M^{II} bridge, the CN stretching frequency increases as a result of kinematic coupling.[129] This is clearly reflected in the data for the PB materials, in which nearly all cyanide ligands are bridging. **1-9** also exhibit similar higher energy CN stretching vibrations that appear 20-60 cm^{-1} higher than the *v*(C≡N) stretches of the free $[M'(CN)_6]^{3-}$ ions. These features are assigned to the bridging CN^- ligands.

Optical Absorption Spectroscopy

Compounds **1-9** were dissolved in 1:1 v/v methanol-dichloromethane for electronic spectroscopy measurements. Spectra were also measured for tmphen and the $(PPN)_3M(CN)_6$ salts for reference; no soluble compounds were found to serve as references for the M^{II} d-d transitions. Five strong absorbance bands were observed in the ultraviolet region for all nine compounds, at approximately 241, 278, 300, 330, and 344nm (Table 6a). Four of these bands (excluding 300nm) were also observed in the tmphen spectrum (Table 6a), and the 241 and 278nm peaks were assigned to $\pi \rightarrow \pi^*$ transitions.[130]

Table 5: IR data in the $\nu(\mathrm{C{\equiv}N})$ region (cm^{-1}) for complexes **1**-**9**, the corresponding PB analogues, and the free hexacyanometallate anions.

cluster	M	M′	3D PB analogue	bridging	terminal	$[\mathrm{M'(CN)_6}]^{3-}$ anion[a]
1	Mn$^{\mathrm{II}}$	Fe$^{\mathrm{III}}$	2148[131]	2147, 2141, 2135	2117, 2112	2101
2	Zn$^{\mathrm{II}}$	Fe$^{\mathrm{III}}$	2175[131]	2165, 2156, 2142	2117, 2112	2101
3	Mn$^{\mathrm{II}}$	Cr$^{\mathrm{III}}$	2170[132]	2153, 2144	2127	2114
4	Ni$^{\mathrm{II}}$	Cr$^{\mathrm{III}}$	2150[133]	2160, 2150	2127	2114
5	Zn$^{\mathrm{II}}$	Cr$^{\mathrm{III}}$	2165[132]	2165, 2156, 2142	2125	2114
6	Mn$^{\mathrm{II}}$	Co$^{\mathrm{III}}$	2160[131]	2165, 2154, 2145	2131	2126
7	Co$^{\mathrm{II}}$	Co$^{\mathrm{III}}$	2170[131]	2167, 2157, 2148	2130, 2125	2126
8	Ni$^{\mathrm{II}}$	Co$^{\mathrm{III}}$	2176[131]	2174, 2164, 2154	2127, 2123	2126
9	Zn$^{\mathrm{II}}$	Co$^{\mathrm{III}}$	2175[131]	2173, 2164, 2155	2130	2126

[a] The $\nu(\mathrm{C{\equiv}N})$ stretches of free $[\mathrm{M(CN)_6}]^{3-}$ anions were measured for $(\mathrm{TMA})_3[\mathrm{Fe(CN)_6}]$, $(\mathrm{TEA})_3[\mathrm{Cr(CN)_6}]$, and $[18\text{-crown-6})\mathrm{K}]_3[\mathrm{Co(CN)_6}]$.

Table 6a: Absorbance maxima in the ultraviolet region for tmphen and compounds **1-9**.

tmphen	**1**	**2**	**3**	**4**
344.5 nm (1200 cm^{-1}M^{-1})	343.5 nm	344.5 nm	344 nm	345 nm
329.5 nm (620 cm^{-1}M^{-1})	330 nm	330 nm	330 nm	331 nm
	302.5 nm	299.5 nm	300 nm	300.5 nm
278.5 nm (30000 cm^{-1}M^{-1})	278 nm	278.5 nm	278 nm	278.5 nm
243 nm (30000 cm^{-1}M^{-1})	241.5 nm	240.5 nm	241 nm	240 nm
5	**6**	**7**	**8**	**9**
344 nm	344 nm		345.5 nm	344.5 nm
329.5 nm	330 nm		331 nm	330 nm
299.5 nm	302.5 nm		300.5 nm	299.5 nm
278.5 nm	278.5 nm	277 nm	279 nm	279 nm
240 nm	241 nm	242 nm	240 nm	240 nm

Table 6b: Absorbance maxima in the visible region for compounds **1**, **2**, **4**, **7**, and **8**.

1	**2**	**4**	**7**	**8**
408.5 nm (Fe^{III}: $^{2}T_{2g} \rightarrow {}^{2}T_{1u}$)	424 nm (Fe^{III}: $^{2}T_{2g} \rightarrow {}^{2}T_{1u}$)	910 nm (Ni^{II}: $^{3}A_{2} \rightarrow {}^{3}T_{2}$)	962 nm (Co^{II}: $^{4}T_{1} \rightarrow {}^{4}T_{2}$)	879.5 nm (Ni^{II}: $^{3}A_{2} \rightarrow {}^{3}T_{2}$)
		532 nm (Ni^{II}: $^{3}A_{2} \rightarrow {}^{3}T_{1}$)	485 nm (Co^{II}: $^{4}T_{1} \rightarrow {}^{4}T_{1}$)	543 nm (Ni^{II}: $^{3}A_{2} \rightarrow {}^{3}T_{1}$)

Absorbance bands in the visible region, corresponding to d-d transitions, were only observed for compounds **1**, **2**, **4**, **7**, and **8** (Table 6b). The bands in **1** (408nm) and **2** (424nm) are quite similar to the 420nm band observed in $(PPN)_3Fe(CN)_6$, corresponding to a $^2T_{2g} \rightarrow {}^2T_{1u}$ transition in Fe^{III}.[134] For both **4** and **8**, two bands are observed, likely corresponding to d-d transitions for Ni^{II} – $^3A_2 \rightarrow {}^3T_2$ (~900nm) and $^3A_2 \rightarrow {}^3T_1$ (~540nm). The two bands observed for **7** are attributed to d-d transitions for Co^{II} – $^4T_1 \rightarrow {}^4T_2$ centers (**6-9**) because the d-d transitions fall entirely in the ultraviolet region and are obscured by the much stronger tmphen absorptions. No features were observed for Mn^{II} centers (**1**, **3**, **6**) because the clusters are not soluble to the extent necessary to observe the spin forbidden bands.

Magnetic Properties

The dc magnetic properties of **1-8** were measured in the 2-300 K temperature range at an applied magnetic field of 1000 Oe; compound **9** was confirmed to be diamagnetic at room temperature. Compounds **2** and **5-8** were prepared as model compounds to act as references for the magnetic properties of the more complex clusters. Compounds **2** and **5** contain diamagnetic Zn^{II} ions (d^{10} configuration) in the equatorial positions and serve to establish the magnetic behavior of the paramagnetic Fe^{III} and Cr^{III} ions situated in the axial positions of the clusters. For compounds **6-8**, the strong ligand field of the cyanide ligands on the Co^{III} ions (d^6) leads to a low-spin, diamagnetic configuration in the axial sites; this situation allows for the evaluation of the magnetic behavior of the paramagnetic metal centers in the equatorial positions of the TBP core. These characteristic magnetic parameters for the equatorial and axial atoms separately can be applied to modeling the behavior of the magnetically coupled clusters containing paramagnetic ions in all positions, compounds **1**, **3**, and **4**.

For clusters with magnetic exchange, the magnetic susceptibility data are modeled using the MAGPACK simulation program. The spins of the individual metal centers are specified, and the Hamiltonian is defined by the assignment of the exchange parameters. The g-values and J parameters are then varied to correlate the calculated susceptibility data to the experimental data. The field-dependant magnetization data, measured at 1.8 K, were simulated using the equation,

$$\mathrm{M} = Ng\beta SB_S(\mathrm{y}) \tag{1}$$

where $B_S(y)$ is the Brillouin function,

$$B_S(y) = \frac{2S+1}{2S}\coth\left(\frac{2S+1}{2S}y\right) - \frac{1}{2S}\coth\left(\frac{1}{2S}y\right) \qquad y = \frac{g\mu_B S\mathrm{H}}{kT} \tag{2}$$

Assuming the expected S values for the clusters (with the appropriate magnetic coupling taken into account), the g values are adjusted to best simulate the experimental magnetization data.

[Zn(tmphen)$_2$]$_3$[M'(CN)$_6$]$_2$ (M' = Fe (2) or Cr (5))

With diamagnetic equatorial positions, their magnetic properties of clusters **2** and **5** are determined entirely by the axial paramagnetic $\mathrm{Fe^{III}}$ and $\mathrm{Cr^{III}}$ ions, respectively. For compound **2**, the $\chi_m T$ value of 1.33 emu·K/mol at room temperature (Figure 24) is higher than the spin-only value of 0.75 emu·K/mol expected for two magnetically isolated LS $\mathrm{Fe^{III}}$ ions (S = 1/2, g = 2.0). Similar deviations are known in LS $\mathrm{Fe^{III}}$ complexes and are attributed to the strong orbital contribution and spin-orbit coupling.[135-137]

For compound **5**, the $\chi_m T$ product is constant above 10 K and its high-temperature value agrees well with the spin-only value of 3.75 emu·K/mol expected for two isolated $\mathrm{Cr^{III}}$ centers. The decrease in $\chi_m T$ observed below 10 K (Figure 24) can most likely be attributed to weak antiferromagnetic coupling between the $\mathrm{Cr^{III}}$ ions mediated by the diamagnetic $\mathrm{Zn^{II}}$ centers.[138] This exchange interaction are determined using MAGPACK, applying the Heisenberg-Dirac-Van Vleck Hamiltonian:[139]

$$\hat{H} = -2J\hat{S}_{\mathrm{Cr(1)}}\hat{S}_{\mathrm{Cr(2)}} \tag{3}$$

The simulation results in a best-fit value of $J = -0.08\ \mathrm{cm^{-1}}$. Zero field splitting is another possible explanation for the decrease in $\chi_m T$. If the data are modeled with no exchange coupling using a Hamiltonian that includes an axial zero field splitting at $\mathrm{Cr^{III}}$,

$$\hat{H} = D[\hat{S}_z^{\ 2} - S(S + 1)/3] \tag{4}$$

a value of $D = 2.4\ \mathrm{cm^{-1}}$ is obtained. This value is high for the $\mathrm{Cr^{III}}$ ion, which typically has a ZFS less than 1 $\mathrm{cm^{-1}}$, and therefore this hypothesis is unlikely.[140,141]

[M(tmphen)$_2$]$_3$[Co(CN)$_6$]$_2$ (M = Mn (6), Co (7), Ni (8))

For cluster **6**, the room temperature value of $\chi_m T$ of 13.1 emu·K/mol corresponds well to the value of 13.13 emu·K/mol expected for three isolated $\mathrm{Mn^{II}}$ ions ($S = 5/2$, $g = 2.0$). The $\chi_m T$ value is essentially constant over the entire temperature range from 300 to 2 K (Figure 24), which indicates the absence of magnetic interactions between the equatorial $\mathrm{Mn^{II}}$ centers. The magnetization data of **6** are in excellent agreement with the Brillouin function for three non-interacting $S = 5/2$ ions with g = 2.03 (Figure 25).

At 300 K, the value of $\chi_m T$ for cluster **7** is 9.68 emu·K/mol, which is much higher than the value expected for a spin-only case which is 5.625 emu·K/mol for three isolated

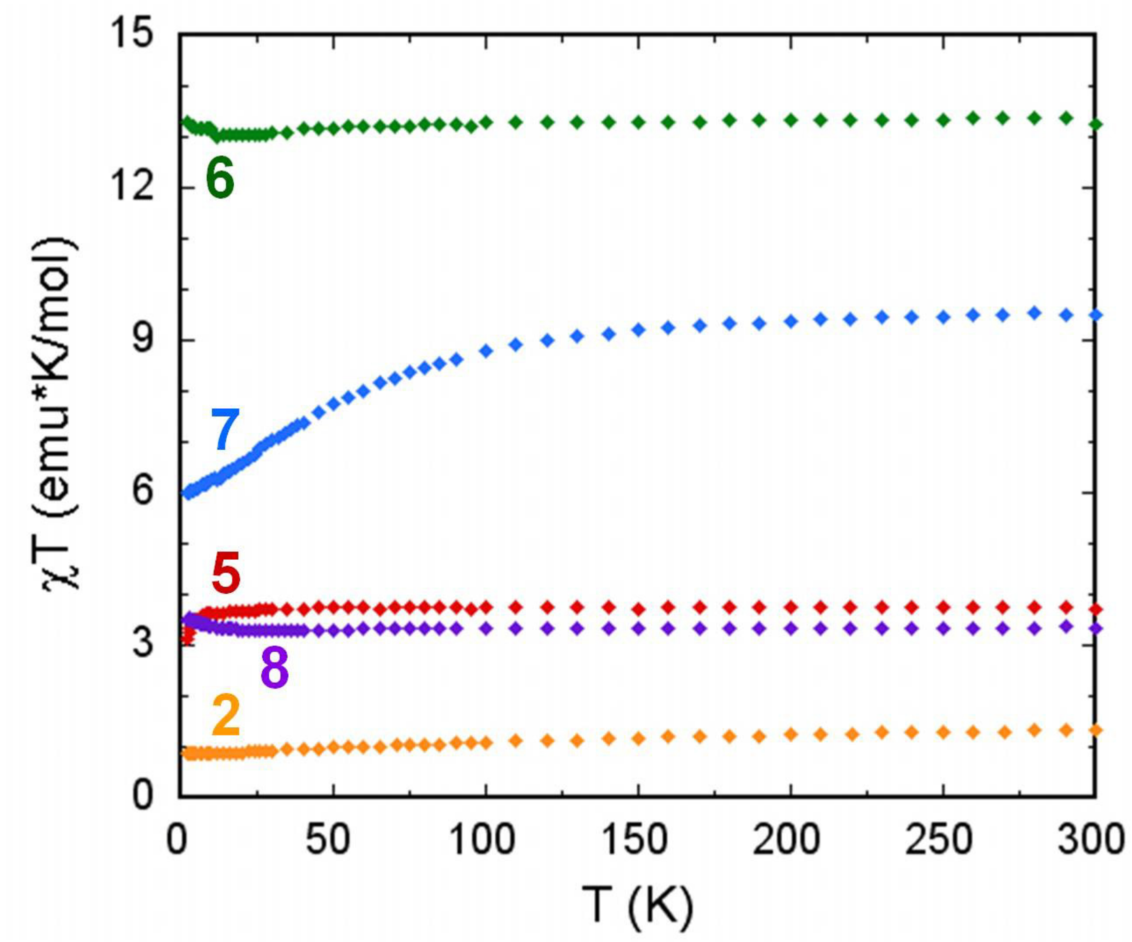

Figure 24: Thermal variation of the $\chi_m T$ product for the model TBP compounds – **2** (Zn_3Fe_2), orange; **5** (Zn_3Cr_2), red; **6** (Mn_3Co_2), green; **7** (Co_3Co_2), blue; **8** (Ni_3Co_2), purple.

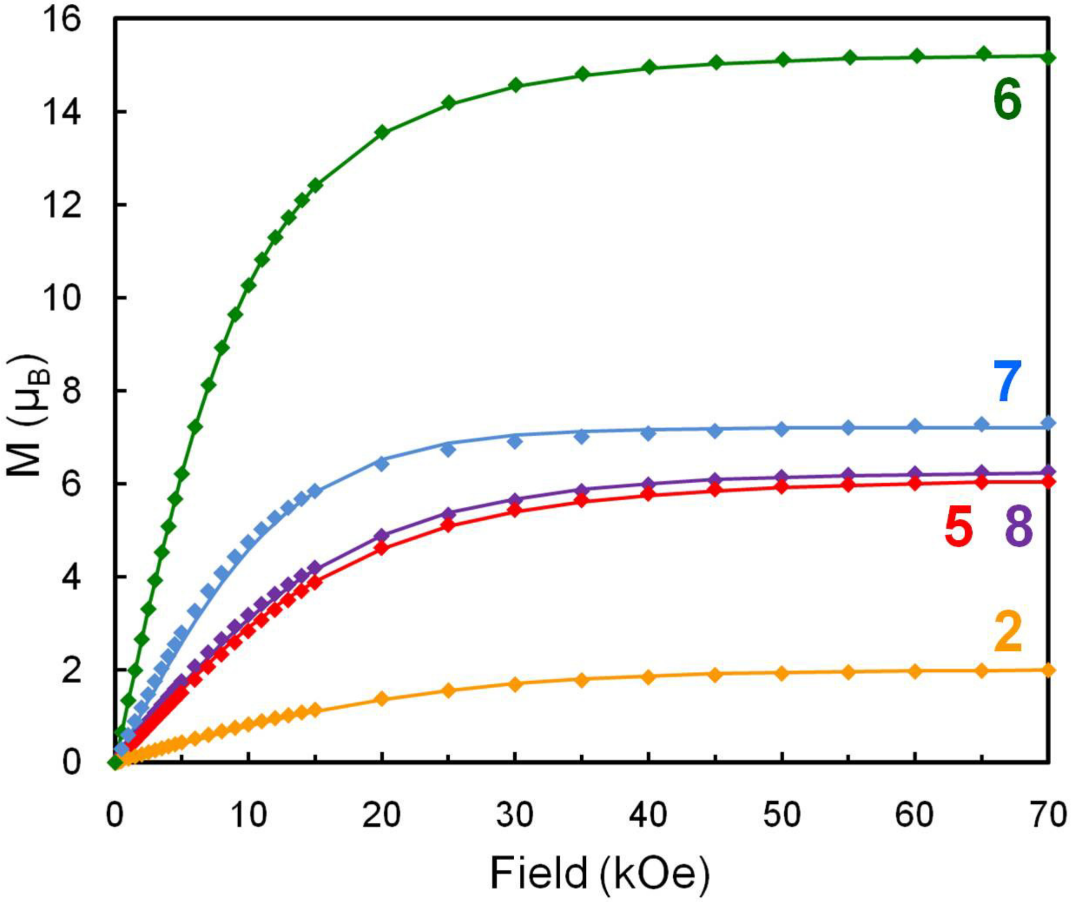

Figure 25. Field dependence of the magnetization measured at 1.8 K – **2** (Zn_3Fe_2), orange; **5** (Zn_3Cr_2), red; **6** (Mn_3Co_2), green; **7** (Co_3Co_2), blue; **8** (Ni_3Co_2), purple. The solid lines correspond to the best fit to the Brillouin functions.

Co^{II} ions ($S = 3/2$, $g = 2.0$). This difference is easily explained by the significant orbital contributions from the high-spin Co^{II} centers. The strong spin-orbit coupling combined with the crystal field distortion splits the ${}^4T_1$ term of the octahedral Co^{II} ion and stabilizes a ground-state Kramers doublet.[142] Therefore, as the temperature is lowered, the $\chi_m T$ value decreases as a result of the depopulation of the excited states and reaches a minimum of 6.0 emu·K/mol at 2 K (Figure 24). At low temperatures, each Co^{II} ion behaves as an effective $S' = 1/2$ center. The magnetization data were modeled by the Brillouin function as three non-interacting Co^{II} centers with effective $S' = 1/2$ and $g = 4.8$ (Figure 25).

The room temperature $\chi_m T$ value for **8** of 3.42 emu·K/mol is slightly higher than the expected spin-only value of 3.00 emu·K/mol for three isolated Ni^{II} ions ($S = 1$, $g = 2.0$) as expected for an orbital contribution. The value of $\chi_m T$ remains constant over the entire temperature interval (Figure 24). The magnetization data were fitted to the Brillouin function for three noninteracting Ni^{II} ions with $S = 1$ and $g = 2.08$ (Figure 25). The lack of significant zero-field splitting, usually observed for Ni^{II} complexes,[139] may be due to the substantial distortion of the octahedral geometry caused by the bite angle of tmphen ligands or by the cancellation of the individual zero-field contributions from Ni^{II} centers due to the high overall symmetry of the cluster.

For **6** and **8,** there is a slight increase of the $\chi_m T$ value at very low temperatures, These observations suggest weak ferromagnetic coupling between the equatorial metal centers, most likely mediated by the diamagnetic Co^{III} axial sites. Such an interaction was previously reported by Chen *et al.* for the trigonal bipyramidal cluster

$[Ni(bpm)_2]_3[Co(CN)_6]_2$,[112] in which equatorial Ni^{II} ion spins are said to be interacting via N≡C-Co-C≡N bridges involving axial Co^{III} ions. In this case, however, the magnetic coupling is significantly stronger (isotropic $J = 4.06$ cm^{-1}) than in compounds **6** and **8**. One possible explanation for this strong coupling is a magnetic impurity in Chen's compound.

$[Mn(tmphen)_2]_3[Fe(CN)_6]_2$ (1)

For **1**, the room temperature value of $\chi_m T$ of 14.54 emu·K/mol is somewhat higher than the spin-only value of 13.88 emu·K/mol, expected for three high-spin Mn^{II} ($S = 5/2$) and two low-spin Fe^{III} ($S = 1/2$) ions without magnetic interactions. This value compares satisfactorily, however, to 14.43 emu·K/mol, the sum of the $\chi_m T$ values for model clusters **2** and **6**. The deviation from the spin-only case is the result of the significant orbital contribution from the Fe^{III} ions, which is also observed in compound **2**. The value of $\chi_m T$ for **1** gradually decreases with decreasing temperature (Figure 26a) and reaches a minimum of 7.42 emu·K/mol at 2 K, suggesting antiferromagnetic coupling between the Mn^{II} and Fe^{III} ions. Antiferromagnetic exchange should, however, result in the stabilization of a ground-state spin value of $S = 13/2$ and a maximum $\chi_m T$ value of ~24 emu·K/mol at low temperatures, which is not observed for cluster **1**. The magnetization (at 1.8 K) reaches a maximum of 12.6 μ_B at 7 T, which is less than the value of 13.0 μ_B expected for the ground state $S = 13/2$, (Figure 26b). This incomplete saturation suggests that low-lying excited states, which are due to zero-field splitting and spin orbit coupling in the Fe^{III} ions, are populated even at low temperatures and high applied fields. Field-dependent magnetization measurements performed at different

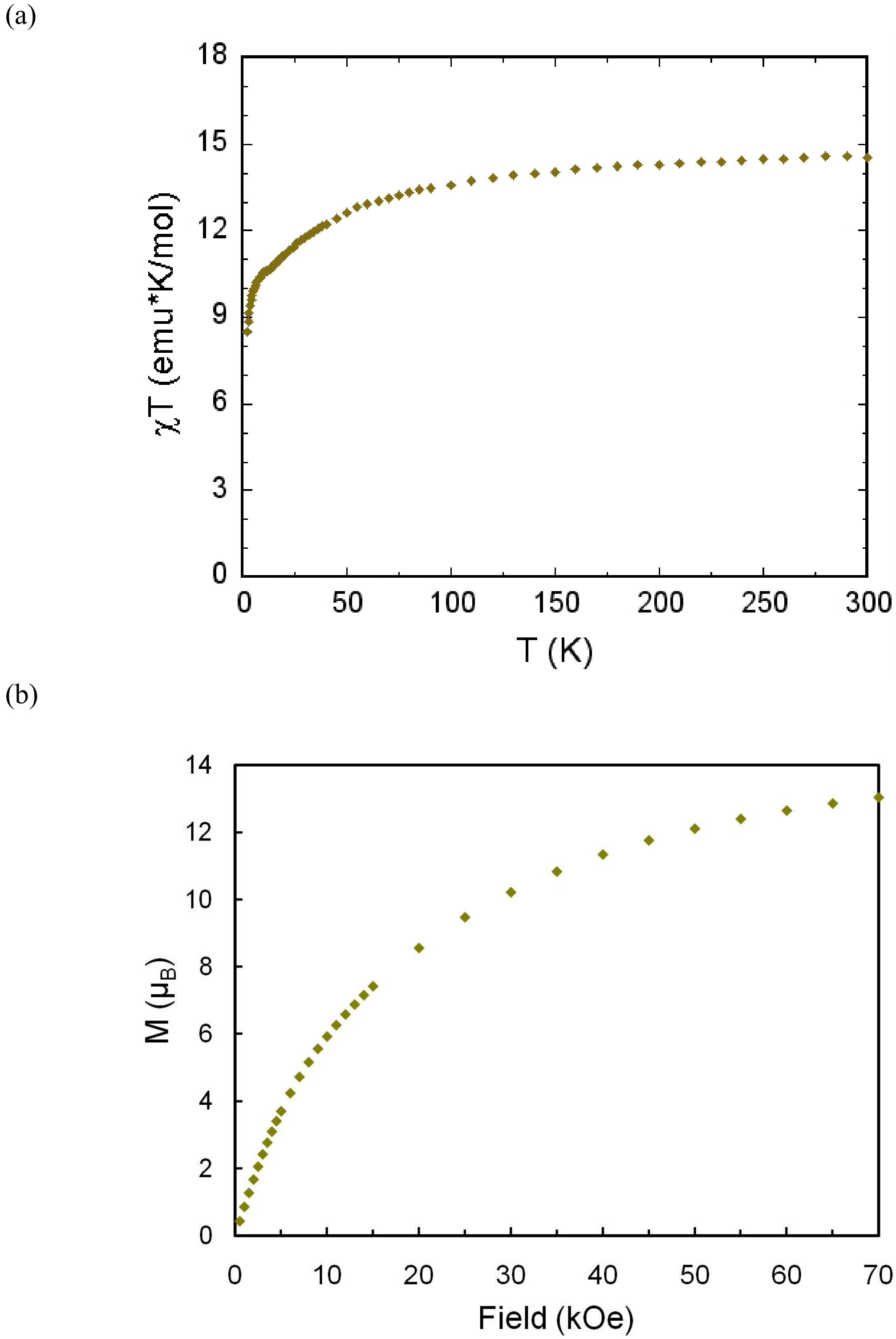

Figure 26: (a) Thermal variation of $\chi_m T$ for compound **1**. (b) Field dependent magnetization data for compound **1** at 1.8 K.

temperatures (1.8-3.9 K) revealed a separation of the field lines (Figure 27), an indication that the cluster exhibits considerable magnetic anisotropy, as expected from the LS $\mathrm{Fe^{III}}$ ions. A thorough treatment of the magnetic behavior requires the application of more advanced physical models which are not available.

$[\mathrm{Mn(tmphen)_2}]_3[\mathrm{Cr(CN)_6}]_2$ (3)

The room-temperature $\chi_m T$ value for **3** is 14.50 emu·K/mol, notably less than expected for a spin only case of uncoupled $\mathrm{Mn^{II}}$ ($S = 5/2$) and $\mathrm{Cr^{III}}$ ($S = 3/2$) ions ($\chi_m T =$ 16.88 emu·K/mol). The $\chi_m T$ value decreases continuously from the room temperature value and reaches a minimum of 10.50 emu·K/mol at 50 K, indicating antiferromagnetic coupling between the $\mathrm{Mn^{II}}$ and $\mathrm{Cr^{III}}$ centers (Figure 28a). Below 50 K, the $\chi_m T$ value increases to reach a maximum of 13.08 emu·K/mol at 2 K. The MAGPACK simulation of the susceptibility data was based on the Hamiltonian,

$$\hat{H} = -2J(\hat{S}_{\mathrm{M1'}} + \hat{S}_{\mathrm{M2'}})(\hat{S}_{\mathrm{M1}} + \hat{S}_{\mathrm{M2}} + \hat{S}_{\mathrm{M3}}) \tag{5}$$

where M′ and M correspond to $\mathrm{Cr^{III}}$ and $\mathrm{Mn^{II}}$ ions, respectively. Assuming $g_{\mathrm{Cr}} = g_{\mathrm{Mn}} = g_{\mathrm{av}} = 2.02$, the best agreement was achieved with the magnetic exchange constant $J = -4.7\ \mathrm{cm^{-1}}$. This value is comparable to the values of -6.2 and -3.1 $\mathrm{cm^{-1}}$ reported for $\{[\mathrm{Cr^{III}(bpy)(CN)_4}]_2[\mathrm{Mn^{II}(H_2O)_4}]\}$[143] and $\mathrm{K}\{[(\mathrm{Me_3tacn})\mathrm{Cr^{III}(CN)_3}]_6\mathrm{Mn^{II}}\}(\mathrm{ClO_4})_3$, respectively.[144] The maximum in $\chi_m T$ is indicative of the stabilization of a high spin ground state, which, according to the antiferromagnetic coupling scheme, is $S_{\mathrm{total}} = 3S_{\mathrm{Mn}} - 2S_{\mathrm{Cr}} = 9/2$. The Brillouin function calculated for $S_{\mathrm{total}} = 9/2$ and $g = 2.02$ fits well with the experimental magnetization data (Figure 28b).

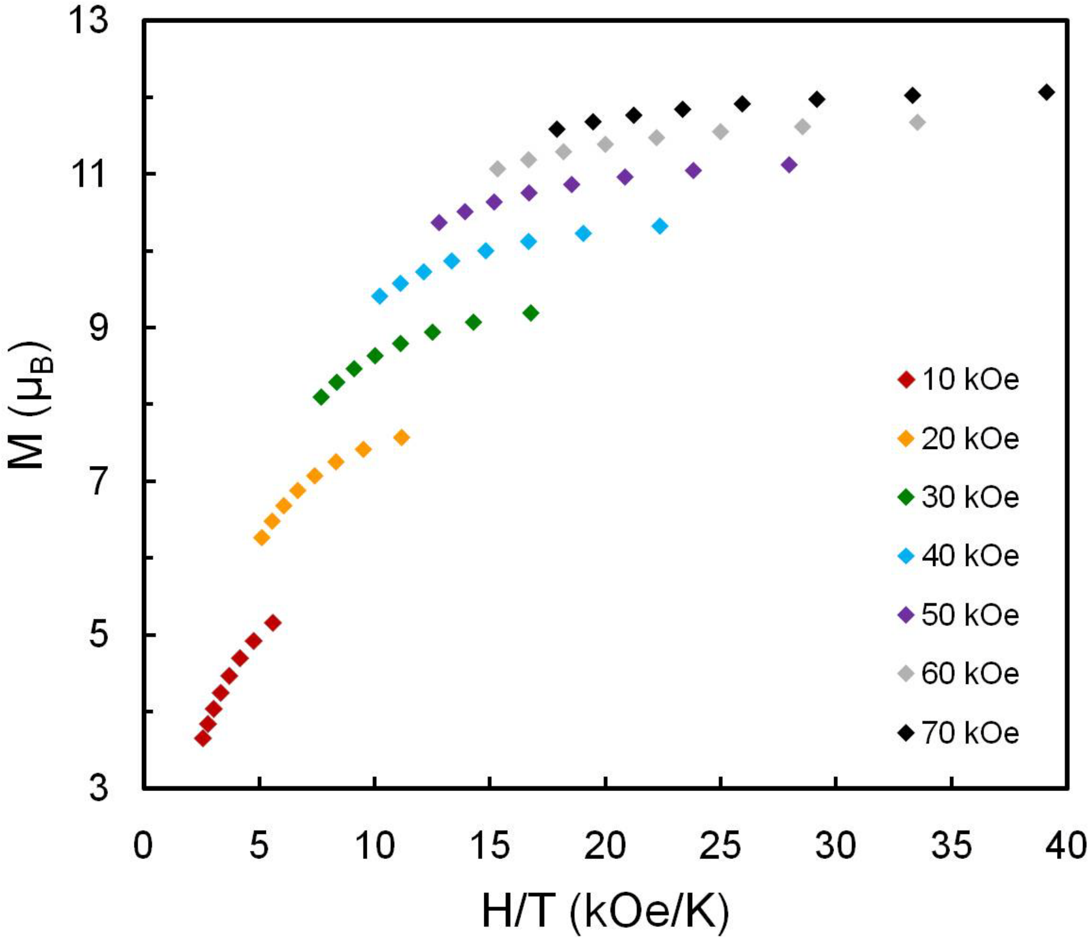

Figure 27: Reduced magnetization data for compound **1**.

(a)

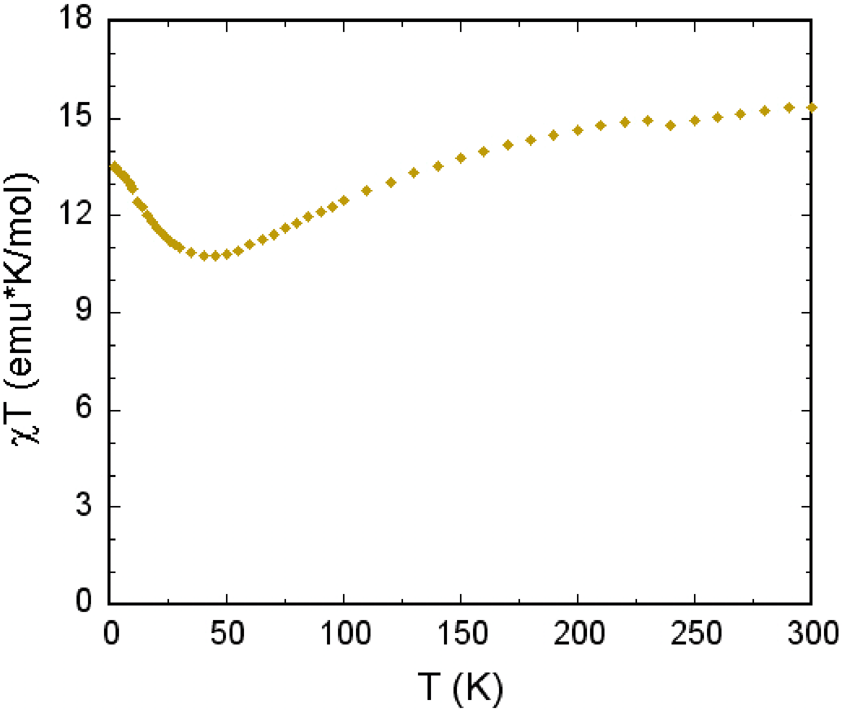

(b)

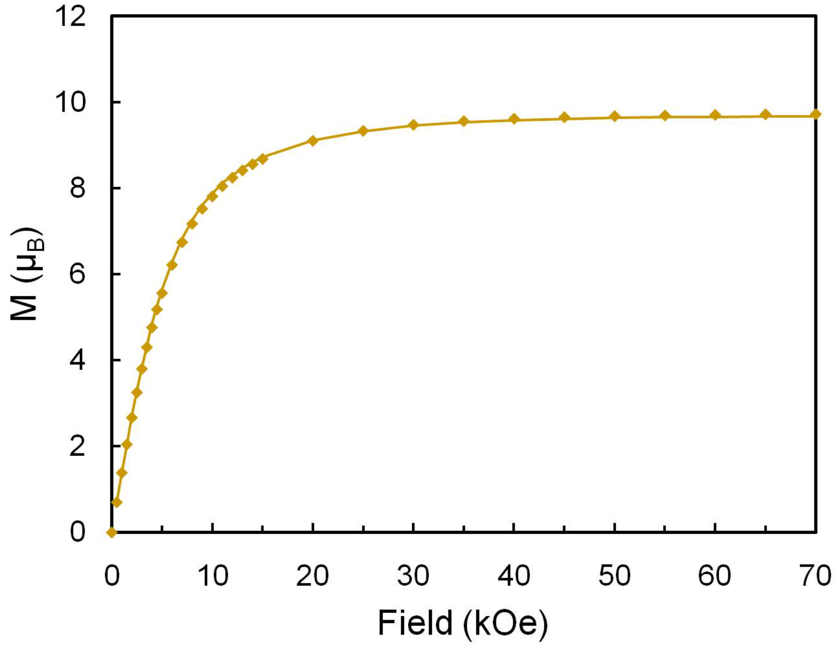

Figure 28: (a) Thermal variation of $\chi_m T$ for compound **3**. (b) Field dependent magnetization data for compound **3** at 1.8 K. The solid line corresponds to the best fit to the Brillouin function for S = 9/2 (g = 2.02, R2 = 0.9999).

[Ni(tmphen)$_2$]$_3$[Cr(CN)$_6$]$_2$ (4)

At room temperature, the value of $\chi_m T$ for **4** of 8.64 emu·K/mol, which is higher than expected for a spin only case ($\chi_m T$ = 6.75 emu·K/mol). The $\chi_m T$ value continuously increases from that at room temperature (Figure 29a), indicating the existence of ferromagnetic coupling between Ni^{II} and Cr^{III} ions, which is expected given that the unpaired electrons are located in the e_g and t_{2g} orbitals, respectively. Defining g_{Cr} = 2.00, the MAGPACK simulation of the $\chi_m T$ versus T data based on the Hamiltonian (eq. 5) calculated g_{Ni} = 2.15 and the isotropic J = 8.5 cm^{-1}. The J value is comparable to the values of 10.9 and 8.7 cm^{-1} reported for {[Ni(cyclam)][(Me$_3$tacn)Cr(CN)$_3$]$_2$}(ClO$_4$)$_2$[145] and {[Ni(tetren)]$_6$[Cr(CN)$_6$]}(ClO$_4$)$_9$,[121] respectively. The maximum value of $\chi_m T$ of 22.7 emu·K/mol reached at 6 K is indicative of the stabilization of a high spin ground state with S = 6. The magnetization data was fitted to the Brillouin function for S = 6 and g_{av} = 2.10 (Figure 29b).

DISCUSSION

The TBP clusters constitute simple assemblies of magnetically coupled transition metal ions. Although the magnetism of the Mn$_3$Fe$_2$ (**1**) cluster is complicated by spin-orbit coupling, the magnetic behavior of Mn$_3$Cr$_2$ (**3**) and Ni$_3$Cr$_2$ (**4**) were interpreted in a straightforward fashion by the use of the isotropic magnetic exchange Hamiltonian (eq. 3). Model clusters Zn$_3$Fe$_2$ (**2**), Zn$_3$Cr$_2$ (**5**), Mn$_3$Co$_2$ (**6**), and Ni$_3$Co$_2$ (**8**) were used for an accurate estimation of the individual ion magnetic parameters for use in modeling the magnetic properties of clusters **1**, **3**, and **4**. The application of the isotropic exchange

(a)

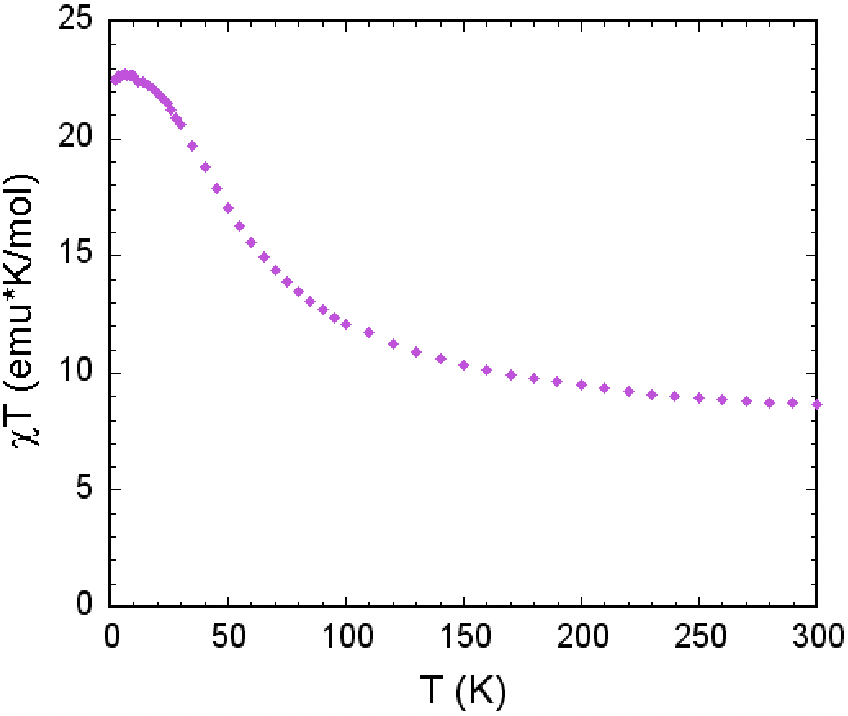

(b)

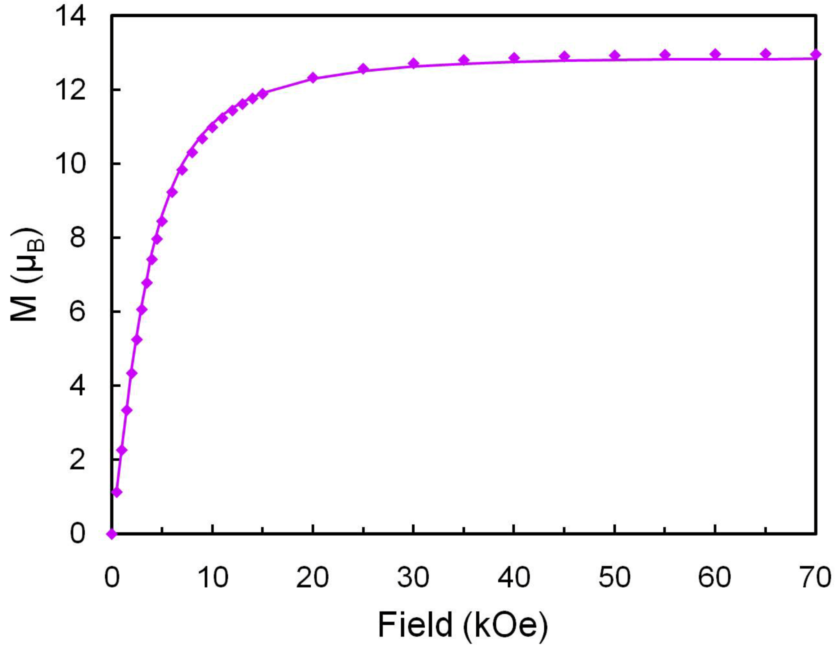

Figure 29: (a) Thermal variation of $\chi_m T$ for compound **4**. (b) Field dependent magnetization data for compound **4** at 1.8 K. The solid line corresponds to the best fit to the Brillouin function for S = 6 (g = 2.10, R2 = 0.9994).

model to Mn_3Cr_2 (**3**) and Ni_3Cr_2 (**4**) resulted in J values of -4.7 and +8.5 cm^{-1}, respectively.

Since it has been our plan to use the TBP clusters will be able to serve as simple models for studying the magnetic interactions in extended cyanide systems, it is important to compare these J values observed in the clusters to the magnitude of the magnetic exchange interactions through the cyanide bridges in the corresponding Prussian blue-type solids, $NaMn^{II}[Cr^{III}(CN)_6]$[146] and $CsNi^{II}[Cr^{III}(CN)_6]$[24]. These J values of the solids can be estimated using the mean-field expression derived by Langevin, Weiss, and Néel[147]

$$T_C = \frac{2|J|}{3k_B}\left[xZ_M\hat{S}_M\left(\hat{S}_M+1\right)\cdot Z_{M'}\hat{S}_{M'}\left(\hat{S}_{M'}+1\right)\right]^{1/2} \tag{6}$$

where $\hat{S}_M$ and $\hat{S}_{M'}$ are spin values of individual M and M′ ions, Z_M and $Z_{M'}$ are the numbers of nearest metal centers connected to M and M′ via CN^- bridges, x is the stoichiometry of the PB-type compound, and k_B is the Boltzmann constant. The estimated J values of -1.8cm^{-1} (Mn^{II}/Cr^{III}) and +5.7cm^{-1} (Ni^{II}/Cr^{III}) are in good agreement with the values found for **3** and **4**, helping to support the hypothesis that these pentanuclear molecules can serve as useful models.

Molecular cyanide clusters provide the obvious advantage of being more readily crystallized than PB materials, which provides precise metrical parameters from the crystal structure determination. Moreover, in the few reported single-crystal structures, the PB materials are characterized by the presence of statistically disordered vacancies in the positions of the $[M'(CN)_6]^{n-}$ anions or the linkage disorder of the CN^- bridges, which leads to the description of the geometries around the metal centers as statistically averaged coordination environments.[7,146,148] The TBP clusters presented herein do not exhibit any disorder with regard to both metal ions and CN^- ligands and allow for direct synthetic control over the identity of metal ions in equatorial and axial positions of the trigonal bypiramid.

CONCLUSIONS

A homologous family of new pentanuclear cyanide-bridged clusters based on the trigonal bipyramidal geometry was prepared and fully characterized by X-ray crystallography, mass spectrometry, infrared spectroscopy, electronic spectroscopy, and SQUID magnetometry. The magnitude of the exchange interactions between the transition-metal ions observed for these clusters correlates well with the values found for the respective mixed-metal Prussian blue-type phases that have been reported in the recent literature. The TBP clusters are excellent targets for advanced theoretical modeling of magnetically coupled systems because of their small size and relatively high symmetry.

CHAPTER III

INVESTIGATION OF SPIN CROSSOVER TRIGONAL BIPYRAMIDAL CYANIDE CLUSTERS WITH Fe_3Fe_2 AND Fe_3Co_2 CORES *

INTRODUCTION

The trigonal bipyramidal molecules under investigation contain equatorial metal ions that are in an all nitrogen ligand environment, namely two chelating diimine type ligands and two N-bound cyanide ligands (Scheme 1 in Chapter I).[35,114-117] Given that Fe^{II} complexes with N donor ligands often exhibit spin crossover behavior,[66,149-151] Fe^{II} ions were introduced into the equatorial position of TBP clusters. The spin crossover phenomenon has been studied extensively over the last 50 years,[86] and it is generally known that interactions between individual spin crossover molecules in crystals mediated by hydrogen bonding or π-π interactions lead to cooperative behavior, abrupt spin transitions, and thermal hysteresis or bistability within a finite temperature range.[152] The latter property renders spin crossover compounds attractive materials for the development of magnetic sensors and memory devices. Multinuclear spin crossover

---

*Portions of this chapter are reproduced with permission from:

1. "Properties of Prussian Blue Materials Manifested in Molecular Complexes: Observation of Cyanide Linkage Isomerism and Spin-Crossover Behavior in Pentanuclear Cyanide Clusters" by Shatruk, M.; Dragulescu-Andrasi, A.; Chambers, K. E.; Stoian, S. A.; Bominaar, E. L.; Achim, C.; Dunbar, K. R., **2007**. *J. Am. Chem. Soc.*, *129*, 6104-6116, Copyright 2007 by ACS Publications.
2. "Trigonal-Bipyramidal Metal Cyanide Complexes: A Versatile Platform for the Systematic Assessment of the Magnetic Properties of Prussian Blue Materials" by Funck, K. E.; Hilfiger, M. G.; Berlinguette, C. P.; Shatruk, M.; Wernsdorfer, W.; Dunbar, K. R., **2009**. *Inorg. Chem.*, *48*, 3438-3452. Copyright 2009 by ACS Publications.

clusters fall naturally into the regime intermediate between mononuclear complexes and extended solids and can be used to understand the factors that govern cooperativity in spin transitions in solids. Although various dinuclear spin crossover complexes have been described in the literature over the years,[153] there are few reports of spin crossover behavior for clusters of higher nuclearity.[68-85] This chapter describes the preparation and characterization of two TBP clusters containing Fe^{II} ions in the equatorial positions. The physical properties of these clusters were found to mimic the behavior of the corresponding PB analogues, namely a thermally induced transition between the low spin (LS) and the high spin (HS) states of Fe^{II}. Attempts to improve the cooperativity of the spin crossover by varying the diimine ligands on the Fe^{II} centers to increase π-π stacking between the clusters are also described. Finally, a solvent study is reported whose aim is to determine the effects of the interstitial solvent identity and content on the SCO behavior of the Fe_3Co_2 cluster.

EXPERIMENTAL

Materials

Commercially available tmphen (Alfa Aesar), 18-crown-6 (Aldrich), bis(triphenylphosphine)iminium chloride (PPNCl, Aldrich), $K_3[Cr(CN)_6$ (Aldrich), $K_3[Fe(CN)_6$ (Fisher), $K_3[Co(CN)_6]$ (Pfaltz & Bauer), $(TBA)_3[Fe(CN)_6$ (Fluka), $Fe(BF_4)_2{\cdot}6H_2O$ (Aldrich), and anhydrous $FeCl_2$ (Strem) were used as received. ACS reagent grade acetonitrile and methanol (EMD Chemicals) were used as received, or acetonitrile was dried over 3Å molecular sieves and distilled prior to use.

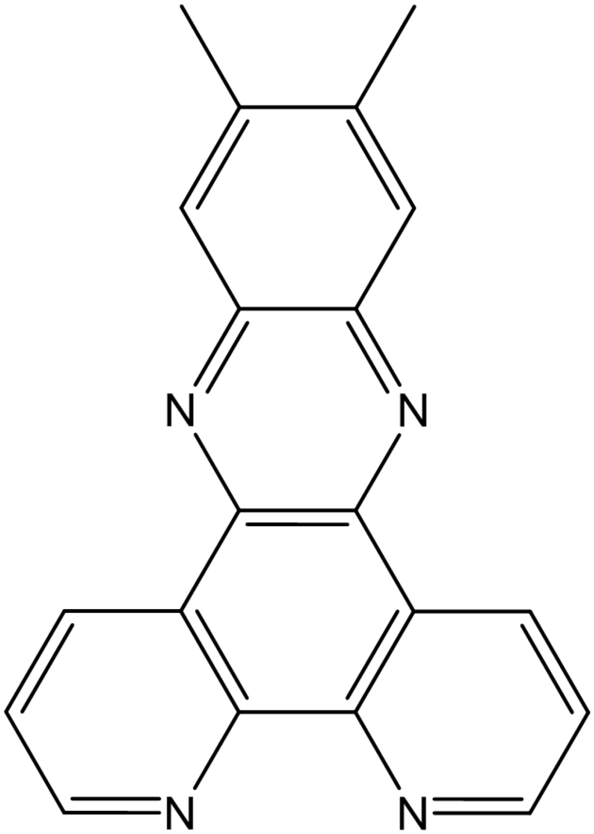

Scheme 2: The dmdppz ligand (11,12-dimethyldipyrido(3,2-a:2′,3′-c)phenazine).

The starting material $Fe_4Cl_8(THF)_6$ was prepared by a slight modification of the method of Cotton *et al.*,[154] in which hexanes was added to the filtered reaction solution to obtain a bulk product. The salts $(PPN)_3[M(CN)_6]$ (M = Fe, Co) were prepared by slight modification of the methods of Predieri *et al.*,[123] in which the products were washed with diethyl ether prior to drying *in vacuo* at 50-60°C. The dmdppz ligand (11,12-dimethyldipyrido(3,2-a:2′,3′-c)phenazine, Scheme 2) was prepared by the method of Mattay *et al.*[155] Stock solutions of $[(18\text{-crown-}6)K]_3[Co(CN)_6]$ were prepared by stirring 150 mg (0.451 mmol) of $K_3[Co(CN)_6]$ and 318 mg (1.20 mmol) of 18-crown-6 in 100 mL of dry acetonitrile under nitrogen for 24 h and filtering the mixture to remove the excess $K_3[M(CN)_6]$.

For magnetic and Mössbauer measurements, the crystalline products are used in two forms. In one case, the mother liquor is decanted from the crystals and washed with acetonitrile until the supernatant is colorless while keeping the crystals covered with solvent at all times; these crystals will be referred to hereafter as "acetonitrile-wet" crystals. For the other type of samples, the crystals collected by filtration, washed with acetonitrile, dried *in vacuo*, and exposed to the ambient laboratory atmosphere which results in the exchange of interstitial acetonitrile with water; these crystals are referred to as "water-containing" crystals.

Synthesis

Note: All reactions were performed in a N_2-filled drybox using dried solvents. The concentrations used typically yield the highest quality single crystals (for X-ray crystallography), but the reactions can be scaled up to obtain larger quantities of the products.

{[Fe(tmphen)$_2$]$_3$[Fe(CN)$_6$]} (10). Samples of $FeCl_2$ (20.3 mg, 0.160 mmol) and tmphen (79.4 mg, 0.336 mmol) were dissolved in 40 mL of dry acetonitrile and stirred for 30 minutes to obtain a clear, dark red solution. An alternate preparation is to use $Fe_4Cl_8(THF)_6$ (37.6 mg, 0.040mmol) in place of the $FeCl_2$. (If the solution became cloudy from precipitated $Fe(tmphen)_2Cl_2$, it was filtered through filter paper.) To this solution was quickly added a solution of $(TBA)_3[Fe(CN)_6$ (150 mg, 0.160 mmol) or $(PPN)_3[Fe(CN)_6]$ (292 mg, 0.160 mmol) in 40 mL of dry acetonitrile. The mixture was left to stand undisturbed for 5 days. After this time, burgundy-red block-shaped crystals formed at the bottom of the container. The crystals were collected by filtration, washed with acetonitrile (100 mL), and dried *in vacuo*. Yield – 41.1 mg (35%). Elemental analysis indicated the presence of interstitial water molecules after exposure to air. Calculated for $Fe_5O_{14}N_{24}C_{108}H_{124}$ (**10**$\cdot 14H_2O$): O, 9.90; N, 14.86; C, 57.36; H, 5.53; Found: O, 10.10; N, 14.79; C, 56.89; H, 5.48%. Thermal gravimetric analysis indicates a 14.8% mass loss which corresponds to 19 water molecules. IR (Nujol), $\nu(C{\equiv}N)$, cm^{-1}: 2131, 2109.

{[Fe(tmphen)$_2$]$_3$[Co(CN)$_6$]} (11). Compound **11** was prepared by a similar method as the one described for compound **10**, by using 40 mL of a 4mM $[Co(CN)_6]^{3-}$ stock solution or a solution of $(PPN)_3[Co(CN)_6]$ (293 mg, 0.160 mmol) in 40 mL of dry acetonitrile. Yield – 38.4 mg (32%). Elemental analysis indicated the presence of interstitial water molecules after exposure to air. Calculated for $Fe_3Co_2O_{12}N_{24}C_{108}H_{120}$

(**8**·13H_2O): O, 9.25; N, 14.94; C, 57.66; H, 5.47; Found: O, 9.13; N, 14.84; C, 57.60; H, 5.33%. Thermal gravimetric analysis indicates a 10.6% mass loss which corresponds to 13 water molecules. IR (Nujol), ν(C≡N), cm^{-1}: 2167, 2156, 2147, 2127.

Solvent Exchange Properties for Fe_3Co_2 Crystals

1. Dry solvent exchange: Crystals of **11** were separated from the mother liquor and washed with dry acetonitrile until no color was observed in the supernatant. In a nitrogen atmosphere, crystals (10-20 mg) were transferred using minimal (~0.1mL) acetonitrile to 20 mL of dry solvent – benzene, toluene, or hexanes.
2. Wet solvent exchange: Crystals of **11** were separated from the mother liquor, washed with dry acetonitrile until no color was observed in the supernatant, and removed to an air atmosphere. Crystals (10-20 mg) were transferred using minimal (~0.1mL) acetonitrile to 20 mL of ordinary solvent – distilled water, methanol, or ethanol.

Attempts to Vary the Bidentate Ligands on the TBP Clusters

<u>Note</u>: These attempts are performed in air using ACS grade solvents as received.

1. ***Attempt to prepare {[Fe(dmppz)$_2$]$_3$[Fe(CN)$_6$]$_2$}.*** Samples of $Fe(BF_4)_2 \cdot 6H_2O$ (14.9 mg, 0.044 mmol) and dmdppz (28.7 mg, 0.092 mmol) were dissolved in 11 mL of acetonitrile and stirred for 15 minutes to obtain a clear, dark red solution. To this solution was quickly added a solution of $(TBA)_3[Fe(CN)_6]$ (47.0 mg, 0.040 mmol) in 10 mL acetonitrile. A dull maroon powder which was observed to precipitate instantaneously was collected by filtration, washed with acetonitrile (45 mL), and dried *in vacuo*. Yield – 32.4 mg. IR (Nujol), ν(C≡N), cm^{-1}: 2136, 2106, 2079, 2014.

Attempts to grow single crystals by layering the two starting solutions were unsuccessful, and produced only powder or glassy materials. Additional attempts using (1) a 1:1 v/v acetonitrile-methanol solvent system (2) three equivalents of dmdppz ligand per Fe were also unsuccessful.

2. ***Attempt to prepare {[Fe(dmdppz)$_2$]$_3$[Co(CN)$_6$]$_2$}.*** This reaction was performed in an analogous fashion to the previously described method by using 10 mL of a 4mM $[Co(CN)_6]^{3-}$ stock solution in acetonitrile. Yield – 27.0 mg. IR (Nujol), ν(C≡N), cm^{-1}: 2152, 2127. Attempts to grow single crystals by the methods above were unsuccessful.

Single Crystal X-ray Diffraction Studies

In a typical experiment, the crystal selected for study was suspended in polybutene oil (Aldrich), mounted on a cryoloop, and placed in an N_2 cold stream. In the low-temperature experiment at ~30 K, a single crystal of **11** was mounted on a glass fiber attached to a rigid brass pin and cooled in a stream of He. Since single crystals of TBP compounds rapidly lose interstitial solvent at room temperature and disintegrate when removed from the mother liquor, for a room-temperature experiment, a crystal was drawn into a capillary and covered with mother liquor. The capillary was sealed on both ends with epoxy cement in such a way that the crystal was made to adhere to one of the ends. Single-crystal X-ray data were collected on a Bruker SMART 1000 or Bruker APEX II diffractometer equipped with a CCD detector. The data sets were recorded as three ω-scans of 606 frames each, at 0.3° step width, and integrated with the Bruker SAINT[124] software package. The absorption correction (SADABS[125]) was based on fitting a function to the empirical transmission surface as sampled by multiple equivalent measurements. Solution and refinement of the crystal structures was carried out using the SHELX[126] suite of programs and the graphical interface X-SEED.[127] Preliminary indexing of the data sets established similar monoclinic unit cells for both compounds at all temperatures and solvent contents, and systematic extinctions indicated that they belonged to the space group $P2_1/c$ (No. 14). The structures were solved by direct methods, which resolved the positions of all metal atoms and most of the C and N atoms. The remaining non-hydrogen atoms were located by alternating cycles of least-squares refinements and difference Fourier maps. All hydrogen atoms were placed in calculated positions. All of the structures contain a large number of interstitial solvent molecules most of which were heavily disordered and could not be satisfactorily refined to a reasonable disorder model. Since the refinement of the basic TBP unit and the coordination geometries of metal ions are essentially uninfluenced by the presence of the disordered solvent, the SQUEEZE routine[128] was applied to the structures of crystals taken from acetonitrile to subtract the diffraction contribution from the latter and to evaluate the number of solvent molecules present in the interstices. The final refinements were carried out with anisotropic thermal parameters for all non-hydrogen atoms.

RESULTS

{[Fe(tmphen)$_2$]$_3$[M′(CN)$_6$]} (10, 11).

Syntheses

By using the same general procedure as compounds **1-9** in the previous chapter, the reactions of the divergent [Fe^{III}(CN)$_6$]$^{3-}$ and [Co^{III}(CN)$_6$]$^{3-}$ anions and the convergent Fe^{II}(tmphen)$_2$Cl$_2$ precursor produce TBP compounds. The synthesis is greatly reproducible and can be easily scaled up. Compounds **10** and **11** were prepared under a nitrogen atmosphere, but they are stable in solid form in air for an indefinite time. TGA analyses were performed to determine the number of interstitial solvent molecules in water-containing samples of **10** and **11** and the thermal stability of the complexes. Gradual solvent loss occurred when the compounds were heated from room temperature to ~120 °C. The compounds are stable until ~250 °C. The typical solvent mass lost (10-15%) corresponds to 12-19 molecules of water per molecule of complex, which is in agreement with the elemental analyses. These analyses indicate that the interstitial acetonitrile molecules in the original crystals are replaced with water molecules when the compounds are stored in air.

Single-Crystal X-ray Structures

Summaries of pertinent information relating to unit cell parameters, data collection, and refinement statistics are provided in Tables 7-8. Single-crystal X-ray studies revealed that compounds **10** and **11** are isostructural to the TBP clusters described in Chapter II (Figures 30-31).

Table 7: Crystallographic data and structural refinement parameters for compounds **10** and **11** (30 K). The solvent content was estimated from the electron density attributed to the disordered solvent contribution by SQUEEZE.

	(**10**)·14MeCN	(**11**)·7.7MeCN
chemical formula	$C_{136}H_{138}N_{36}Fe_5$	$C_{123.4}H_{119.1}N_{31.7}Fe_3Co_2$
formula weight	2556.08	2331.63
space group	*P*2$_1$/c (No. 14)	*P*2$_1$/c (No. 14)
a	18.967(5) Å	19.113(4) Å
b	24.818(7) Å	24.925(4) Å
c	24.440(6) Å	24.674(5) Å
α	90°	90°
β	97.682 (6)°	98.108(5)°
γ	90°	90°
volume	11401(5) Å^3	11637(4) Å^3
Z	4	4
temperature	110 K	30 K
density (calc)	1.171 g/cm^3	1.150 g/cm^3
abs coeff (μ)	0.674 mm^{-1}	0.697 mm^{-1}
crystal color and habit	burgundy red block	burgundy red block
crystal size (mm^3)	0.31 × 0.18 × 0.10	0.31 × 0.13 × 0.11
radiation	Mo Kα, 0.71073 Å	Mo Kα, 0.71073 Å
θ range	1.17-28.43°	1.08-23.26°
reflections collected	117450 [R_{int} = 0.1358]	21869 [R_{int} = 0.0630]
independent reflections	26681	14754
data/parameters/restraints	26681/1259/0	14754/1234/48
R_1	0.0877	0.1019
wR_2	0.1870	0.2354
GOF (F^2)	0.981	0.889
max./min. residual densities (e·Å^{-3})	0.623, -0.776	0.721, -0.893

Table 8: Crystallographic data and structural refinement parameters for compounds **11** (110, 200, and 298 K). The solvent content was estimated from the electron density attributed to the disordered solvent contribution by SQUEEZE.

	(**11**)·18MeCN	(**11**)·11MeCN	(**11**)·7.6MeCN
chemical formula	$C_{144}H_{150}N_{42}Fe_3Co_2$	$C_{130}H_{129}N_{42}Fe_3Co_2$	$C_{123.2}H_{116.8}N_{31.6}Fe_3Co_2$
formula weight	2754.48	2467.11	2325.51
space group	$P2_1/c$ (No. 14)	$P2_1/c$ (No. 14)	$P2_1/c$ (No. 14)
a	19.159(4) Å	19.24(2) Å	19.49(1) Å
b	25.952(5) Å	25.10(3) Å	25.33(2) Å
c	24.709(5) Å	24.89(3) Å	24.15(2) Å
α	90°	90°	90°
β	97.938(4)°	98.11(3)°	98.26 (1)°
γ	90°	90°	90°
volume	11699(4) Å^3	11900(20) Å^3	12309(16) Å^3
Z	4	4	4
temperature	110 K	200 K	298 K
density (calc)	1.144 g/cm^3	1.125 g/cm^3	1.088 g/cm^3
abs coeff (μ)	0.693 mm^{-1}	0.681 mm^{-1}	0.658 mm^{-1}
crystal color and habit	burgundy red block	burgundy red block	burgundy red block
crystal size (mm^3)	0.45 × 0.22 × 0.08	0.45 × 0.22 × 0.12	0.47 × 0.33 × 0.15
radiation	Mo Kα, 0.71073 Å	Mo Kα, 0.71073 Å	Mo Kα, 0.71073 Å
θ range	1.17-23.26°	1.07-28.49°	1.61-23.47°
reflections collected	76232 [R_{int} = 0.1639]	98257 [R_{int} = 0.1311]	47425 [R_{int} = 0.2009]
independent reflections	16757	28940	17339
data/parameters/restraints	16757/1259/0	28940/1259/0	17339/1198/0
R_1	0.0798	0.0826	0.0933
wR_2	0.1758	0.1721	0.2187
GOF (F^2)	1.003	0.988	0.685
max./min. residual densities (e·Å^{-3})	0.648, -0.782	0.860, -1.312	0.796, -0.404

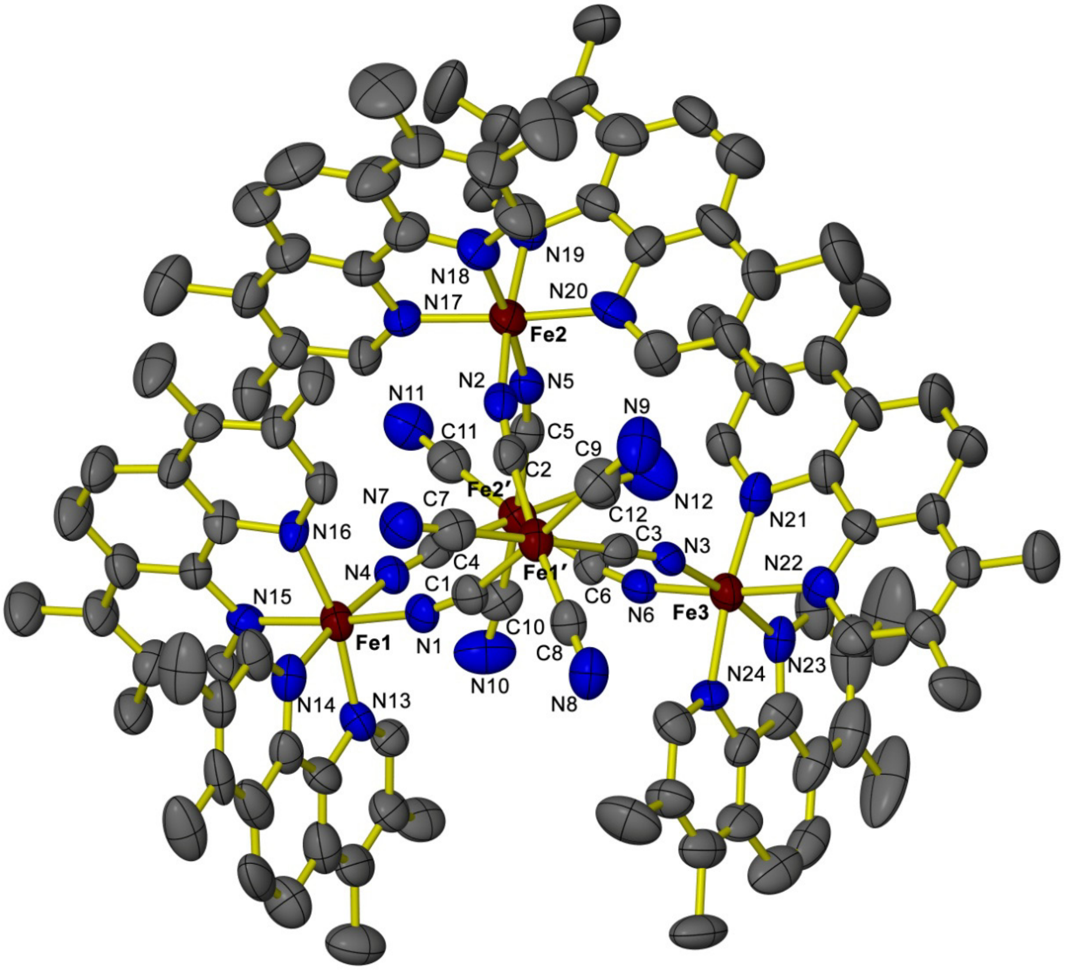

Figure 30: Thermal ellipsoid plot of **10** (Fe_3Fe_2), drawn at the 50% probability level. (H atoms and solvent molecules have been omitted for the sake of clarity.).

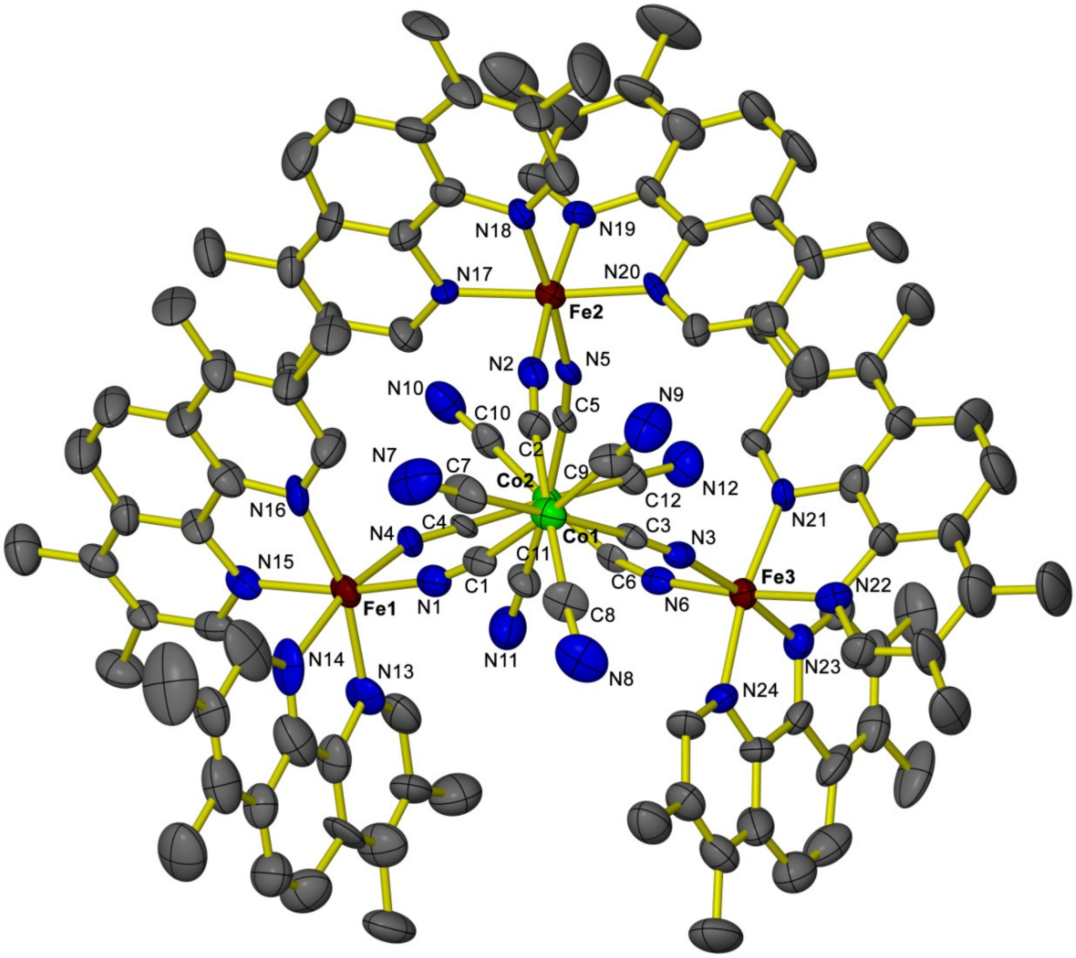

Figure 31: Thermal ellipsoid plot of **11** (Fe_3Co_2), drawn at the 50% probability level. (This structure was determined at 110K from a crystal in acetonitrile, but the structures from other temperatures and solvents were labeled in the same way. H atoms and solvent molecules have been omitted for the sake of clarity.).

Mass Spectrometry

Compounds **10** and **11** are sparingly soluble in acetonitrile and slightly more soluble in 1:1 v/v acetonitrile-methanol. ESI mass spectrometry for these compounds showed some fragmentation of the clusters, resulting in the mononuclear fragments [Fe(tmphen)$_2$]$^{2+}$ (*m*/*z* = 264) and [Fe(tmphen)$_3$]$^{2+}$ (*m*/*z* = 382). Intact clusters were also observed in the forms of [Fe$_3$M′$_2$ + Fe(tmphen)$_2$]$^{2+}$ (*m*/*z* = 1269-1272) and [Fe$_3$M′$_2$ + Fe(tmphen)$_3$]$^{2+}$ (*m*/*z* = 1387-1390) (Figure 32).

Infrared Spectroscopy

The CN$^-$ stretching frequencies in IR spectra can be very helpful by providing information about the oxidation state of the metal ions involved. The energy of the *v*(C≡N) stretch increases with the metal oxidation state and typically shifts to higher energies when the cyanide acts as a bridging ligand.[19] For example, the *v*(C≡N) modes of K$_4$[Fe(CN)$_6$] and K$_3$[Fe(CN)$_6$] are located at ~2040 and ~2115 cm^{-1} respectively, and those of M^{II}-C≡N-M′^{III} are found at 2100-2165 cm^{-1}.[131,156] Complexes **10** and **11** contain terminal cyanide ligands coordinated to M′^{III} ions and bridging cyanide ligands that are expected to be of either the Fe^{II}-N≡C-M′^{III} or Fe^{II}-C≡N-M′^{III} type. (Studies of Fe^{II}-Cr^{III} Prussian blue analogues[157,158] and [Fe(phen)$_2$(CNBH$_3$)$_2$]/[Fe(phen)$_2$(NCBH$_3$)$_2$] compounds[159] have shown that IR frequencies can distinguish the two bridging modes, but the stability of [Fe(CN)$_6$]$^{3-}$ and [Co(CN)$_6$]$^{3-}$ suggests that only Fe^{II}-N≡C-M′^{III} modes will be observed in **10** and **11**.) The lower energy *v*(C≡N) stretches for complexes **10** and **11**, 2109 and 2127 cm^{-1} respectively, fall in the same range as those measured for (TMA)$_3$[Fe^{III}(CN)$_6$] (2101 cm^{-1}) and (18-crown-6-K)$_3$[Co^{III}(CN)$_6$] (2126 cm^{-1})

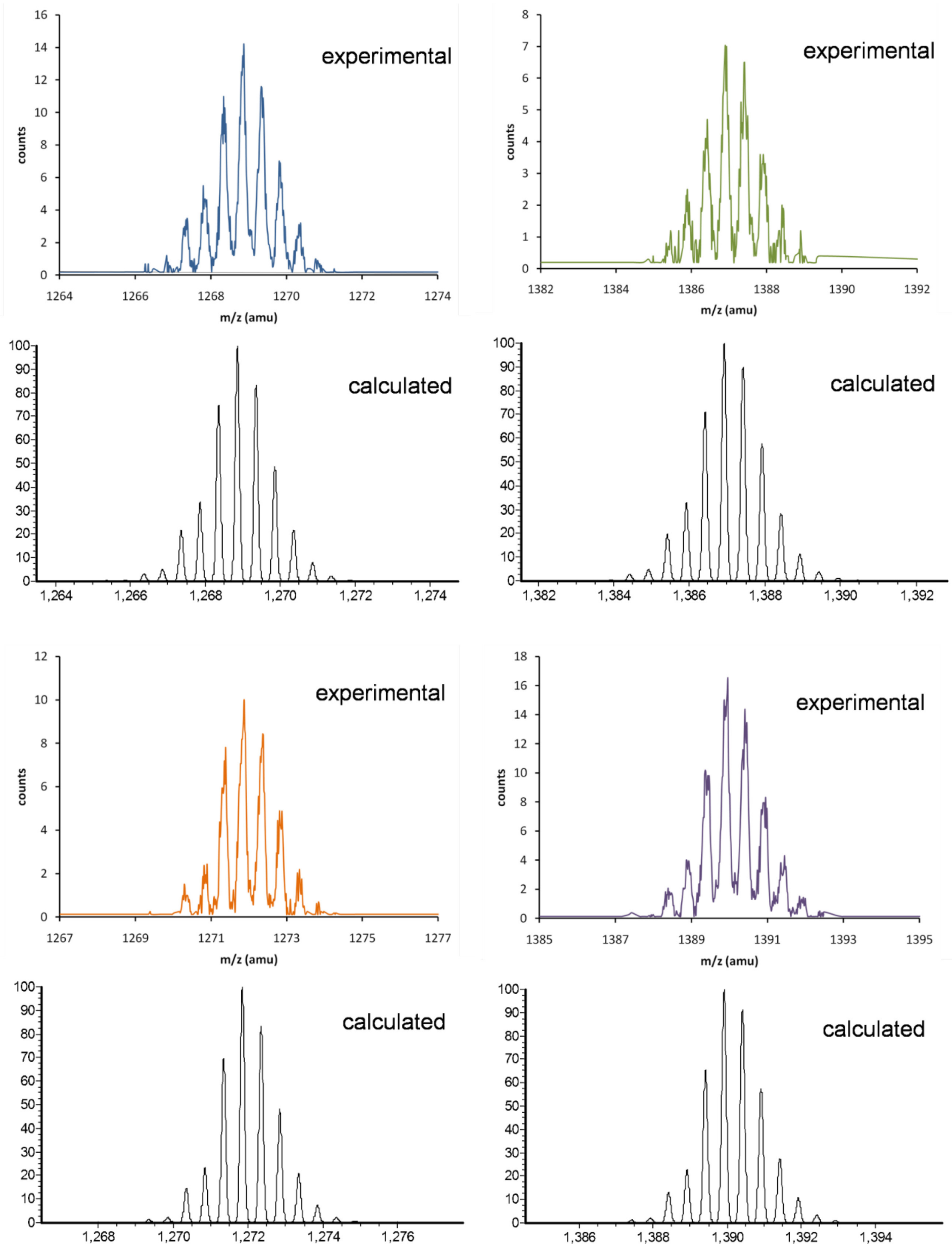

Figure 32: Experimental and calculated (plotted as relative isotopic abundance vs. mass to charge ratio, m/z) "$[Fe_3M_2 + Fe(tmphen)_2]^{2+}$" (**10**, blue; **11**, orange) and "$[Fe_3M_2 + Fe(tmphen)_3]^{2+}$" (**10**, green; **11**, dark purple) mass spectral data.

compunds. Therefore, these modes can be reasonably assigned to the terminal CN^- ligands. Compound **11** displays higher energy *v*(C≡N) stretches at 2167, 2156, and 2147 cm^{-1}. The observed stretch of 2165 cm^{-1} in the $Fe^{II}_3[Co^{III}(CN)_6]_2$ Prussian blue analogue[131] supports the assignment of these bands to the Fe^{II}-N≡C-Co^{III} bridging mode. Compound **10** also exhibits a higher frequency feature at 2131 cm^{-1}, but in this case, there is no PB analogue containing the Fe^{II}-N≡C-Fe^{III} connectivity that can be used for comparison. The stretch, however, can still reasonably be assigned to the Fe^{II}-N≡C-Fe^{III} bridging mode, as it is ~20 cm^{-1} higher in energy than the Fe^{III}-CN terminal mode. The considerable difference in this stretch from the *v*(C≡N) frequency of Prussian blue (2080cm^{-1})[160] is strong evidence against the possibility of a Fe^{III}-N≡C-Fe^{II} bridging mode.

^{57}*Fe Mössbauer Spectroscopy*

Unlike TBP's such as Zn_3Cr_2 which are unambiguous in the assignment of the oxidation states, the assignment of oxidation states in the Fe_3Fe_2 and Fe_3Co_2 cores is not trivial since the divalent and trivalent oxidation states are common for both Fe and Co. Fortunately, since both compounds **10** and **11** contain Fe ions, ^{57}Fe Mössbauer spectroscopy, performed by the group of Catalina Achim, can be used to obtain direct information about these ions.

At 4.2 K and 0.05 T, the Mössbauer spectrum of a sample of acetonitrile-wet crystals of **10** exhibits a doublet characteristic of LS Fe^{II} (Table 9, Figure 33a) which accounted for 55% of the Fe in the sample. Accounting for another 42%, a second doublet is observed with identical Mössbauer parameters to the LS Fe^{III} sites in **2**

Table 9: Mössbauer parameters (0.05 T) for the Fe ions in compounds **10** and **11**.

compound, phase	T(K)	δ (mm/s)	ΔE_Q (mm/s)	% (±2%)	assignment
10, water-containing crystals	300	0.36	0.27	40	LS Fe^{II}
		0.98	2.06	22	HS Fe^{II}
		-0.14	0.7	39	LS Fe^{III}
	220	0.38	0.4	54	LS Fe^{II}
		0.99	2.56	8	HS Fe^{II}
		-0.11	0.82	38	LS Fe^{III}
	50	0.43	0.44	56	LS Fe^{II}
		1.11	2.91	3	HS Fe^{II}
		-0.04	0.96	41	LS Fe^{III}
	4.2	0.44	0.44	60	LS Fe^{II}
				< 3[a]	HS Fe^{II}
			broad		LS Fe^{III}
10, acetonitrile-wet crystals	220	0.39	0.40	41	LS Fe^{II}
		0.90	2.9	22	HS Fe^{II}
		-0.01	0.90	37	LS Fe^{III}
	4.2	0.44	0.47	55	LS Fe^{II}
		1.16	2.9	3	HS Fe^{II}
		-0.02	0.9	42	LS Fe^{III}
11, water-containing crystals	300	0.38	0.27	40	LS Fe^{II}
		0.99	2.06	22	HS Fe^{II}
	220	0.38	0.4	54	LS Fe^{II}
		0.99	2.56	8	HS Fe^{II}
	4.2	0.44	0.44	60	LS Fe^{II}
				< 3	HS Fe^{II}
11, acetonitrile-wet crystals	220	0.36	0.27	40	LS Fe^{II}
		0.98	2.06	22	HS Fe^{II}
	4.2	0.38	0.4	54	LS Fe^{II}
		0.99	2.56	8	HS Fe^{II}

[a] Only an upper limit can be determined due to the broad feature assigned to LS Fe^{II}.

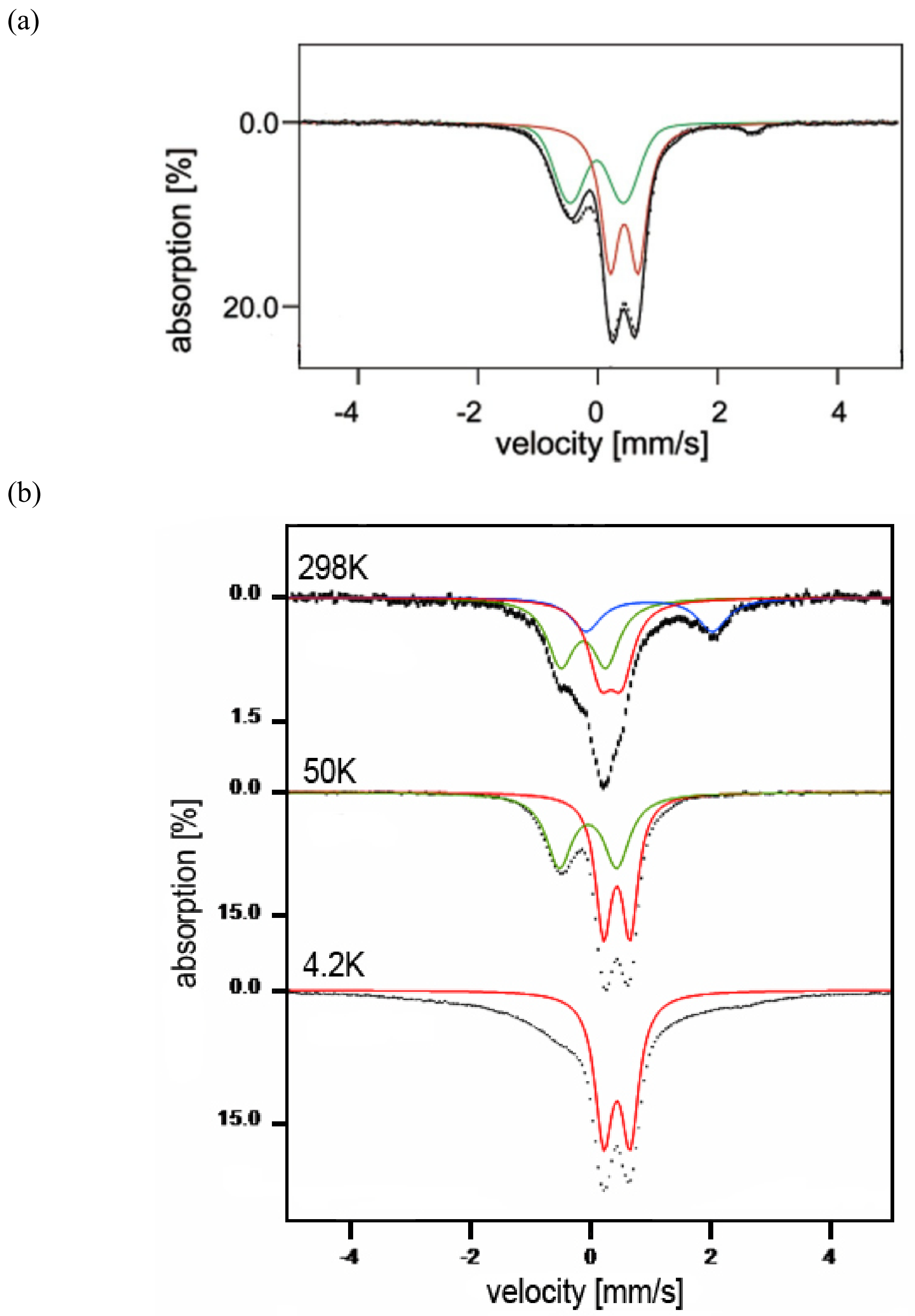

Figure 33: (a) The 4.2 K Mössbauer spectrum (0.05 T) of acetonitrile-wet crystals of **10**. (b) Variable temperature Mössbauer spectra (0.05 T) for a water-containing sample of compound **10**. Contributions from LS Fe^{II} are shown in red, HS Fe^{II} in blue, and LS Fe^{III} in green.

(Zn_3Fe_2). The 4.2 K Mössbauer spectrum of water-containing crystals of **10** showed a similar doublet for LS Fe^{II} representing ~60% of Fe in the sample, as well as a broad spectral feature, which collapsed at 50 K into a quadrupole doublet (41% Fe) very similar to the LS Fe^{III} signal observed at 4.2 K for the acetonitrile-wet crystals (Figure 33b). Therefore, it is clear that compound **10** contains an $(Fe^{II}{}_{LS})_3Fe^{III}{}_2$ core at 4.2 K, and the interstitial solvent has no effect on the spin states.

The 298 K Mössbauer spectrum of a sample of water-containing crystals of **10** shows an absorption band at +2.1 mm/s, which confirms the presence of 20% HS Fe^{II} (Figure 33b), significantly more than the≤ 3% identified at 4.2 K. The increase of the amount of HS Fe^{II} in the sample of water-containing crystals from ≤3% at 4.2-50 K to 8% at 220 K and 20% at room temperature is characteristic for a gradual LS Fe^{II} to HS Fe^{II} transition. The transition for acetonitrile-wet crystals of **10** starts at temperatures lower than that for water-containing crystals and leads to 22% of the Fe^{II} in the sample being HS at 220 K.

The 4.2 K, 0.05 T Mössbauer spectra for samples of both acetonitrile-wet and water-containing crystals (prepared in air or under nitrogen) of **11** showed the presence of only two types of Fe atoms (Figure 34-35). The first type (80-90% of the Fe in the samples) had Mössbauer parameters suggestive of LS Fe^{II}, and the second type (the other 10-20%) had parameters characteristic of HS Fe^{II} (Table 3). A 4.2 K, 8T spectrum of the water-containing crystals (Figure 35a), with 90% of the first type of Fe, confirmed that the majority of the Fe is diamagnetic, and therefore LS Fe^{II}. The variable amount of HS Fe^{II} present in the samples at 4.2 K (10% found in the samples of water-containing

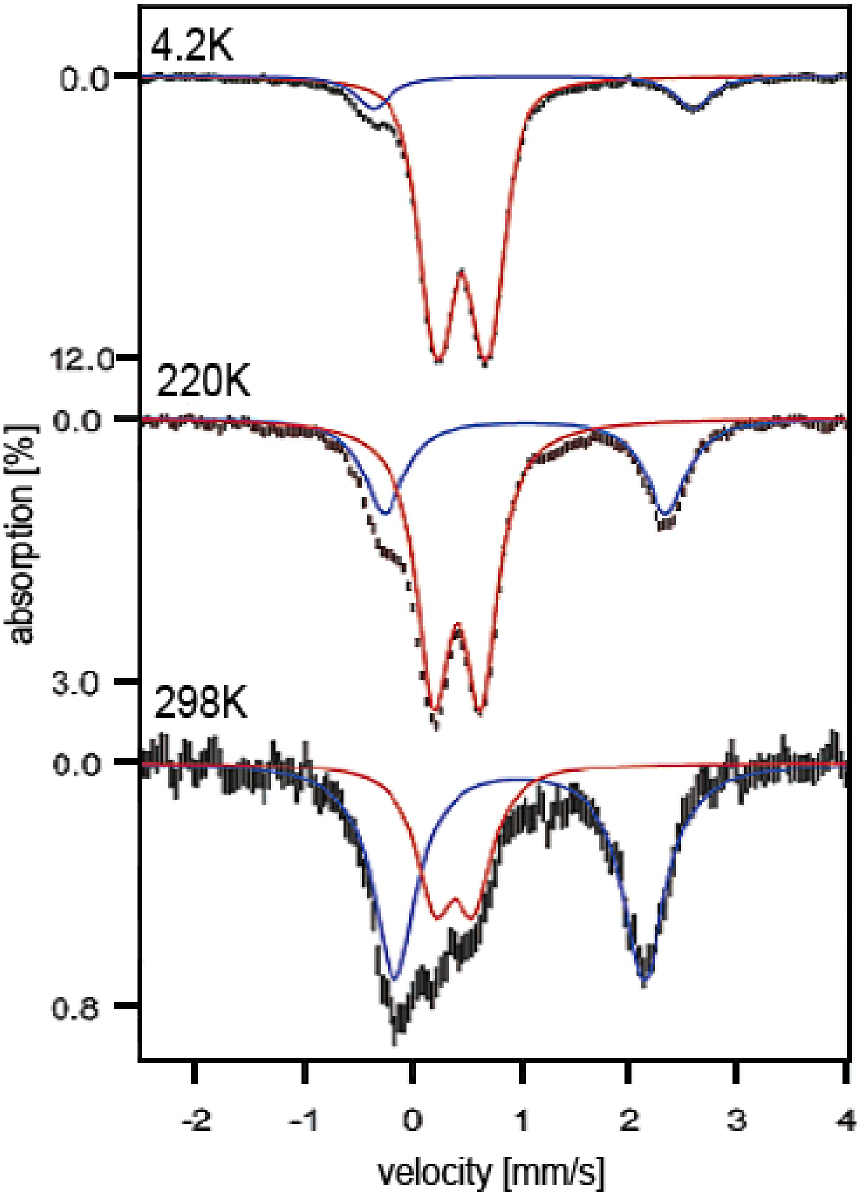

Figure 34: Variable temperature Mössbauer spectra (0.05 T) for a water-containing sample of compound **11**. Contributions from LS Fe^{II} are shown in red and HS Fe^{II} in blue.

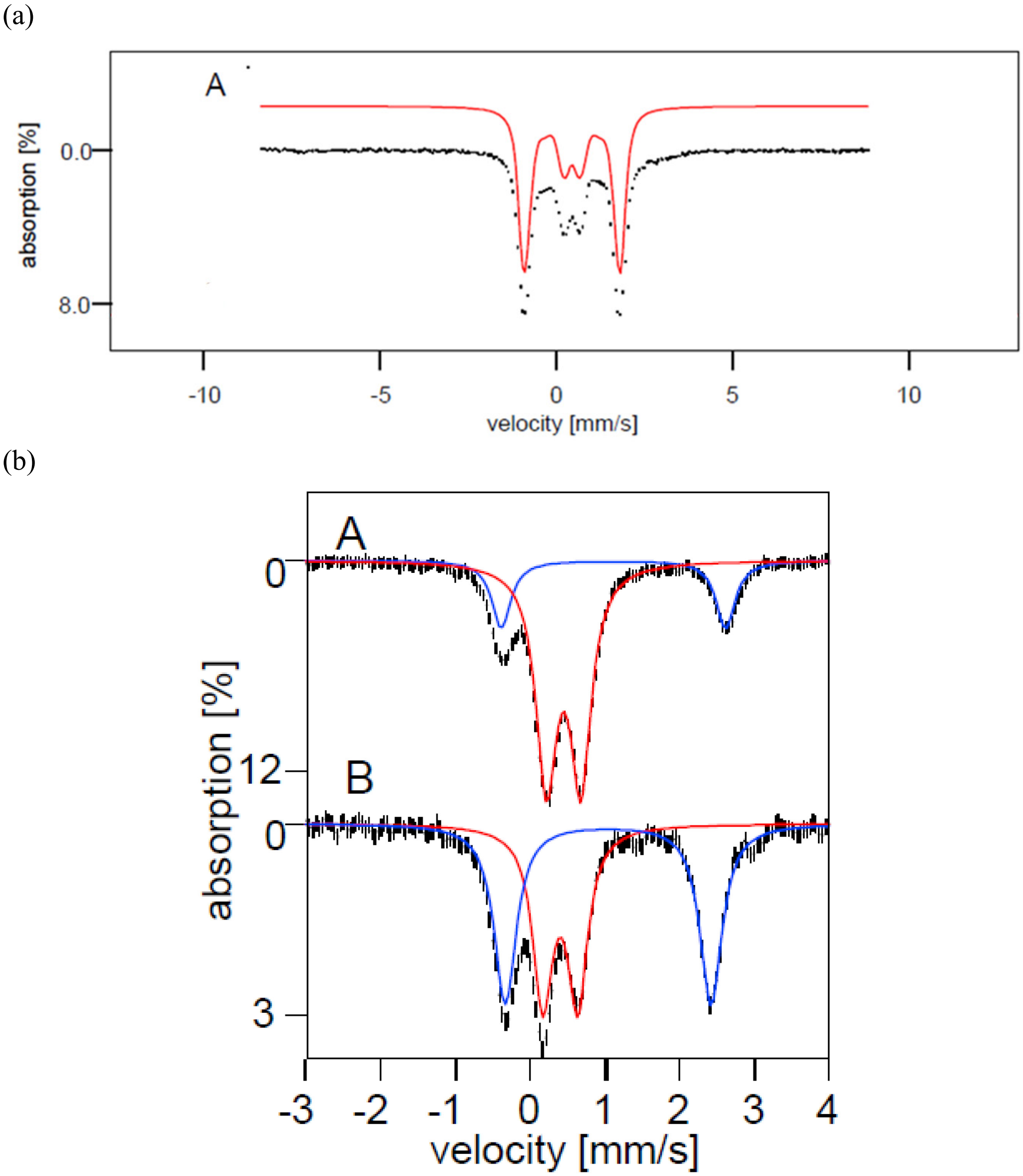

Figure 35: (a) 4.2 K Mössbauer spectra of water-containing crystals of **11** recorded in a parallel external field of 8 T. The continuous red line is a simulation assuming diamagnetic Fe^{II} sites. (b) Variable temperature Mössbauer spectra (0.05 T) of acetonitrile-wet crystals of **11** recorded at 4.2 (A), and 220 K (B). Contributions from LS Fe^{II} are shown in red and HS Fe^{II} in blue.

crystals and 10-20% in acetonitrile-wet crystals) is suggestive of an incomplete spin transition at low temperatures. These spectra have also confirmed, by the lack of Fe^{III} absorption peaks, that the clusters in **11** have an $[Fe^{II}_3Co^{III}_2]$ core independent of the solvent content of the crystals and exposure to air. A variable temperature Mössbauer study of **11** shows that increasing temperature leads to a major change in the cluster electronic structure (Figure 34). There was no noticeable increase in the amount of HS Fe^{II} from 4.2 K to 50 K for any of the samples, but at room temperature two-thirds of the Fe ions in the water-containing crystals exhibit the HS Fe^{II} Mössbauer parameters, while the rest remain LS (Table 9). Despite the similarity of **11** to the Co_3Fe_2 TBP cluster,[115,116] the same charge-transfer-induced spin transition is not possible since there is no evidence for Fe^{III} in the 220 and 298 K spectra (Figures 34). Instead, from 4.2 K to room temperature, a "classical" spin transition at the equatorial $[Fe^{II}(tmphen)_2(NC)_2]$ sites converts every TBP cluster from $[(Fe^{II}_{LS})_3Co^{III}_2]$ to $[(Fe^{II}_{LS})(Fe^{II}_{HS})_2Co^{III}_2]$; a conversion of 2/3 of the clusters in the sample from $[(Fe^{II}_{LS})_3Co^{III}_2]$ to $[(Fe^{II}_{HS})_3Co^{III}_2]$ is equally possible. Similar to **10**, variable temperature Mössbauer spectra for the acetonitrile-wet crystals of **11** reveal that the spin transition also takes place in this material at a lower temperature than for the water-containing crystals (Table 9 and Figure 35b).

Magnetic Properties

Compounds **10** and **11** both contain Fe^{II} ions in the equatorial positions of the TBP core and exhibit magnetic properties similar to each other. For the water-containing crystals of **10**, the $\chi_m T$ value measured below 100 K (~1.2 emu·K/mol) is comparable to that measured for compound **2** ($Zn^{II}_3Fe^{III}_2$) (Figure 36). Therefore, the three Fe^{II} sites of the cluster **10** must be in the diamagnetic LS state up to 100 K, in agreement with the Mössbauer spectra. The $\chi_m T$ observed for the water-containing crystals of **11** below 100 K (~0.8 emu·K/mol, Figure 37) is assigned to paramagnetic HS Fe^{II} from an incomplete spin crossover at low temperatures, which was also revealed in the Mössbauer results. The axial diamagnetic Co^{III} ions are estimated to have only a very small temperature-independent paramagnetic contribution of $\sim 3 \times 10^{-4}$ emu/mol.[139]

For both **10** and **11**, the $\chi_m T$ product for water-containing crystals gradually increases to ~9 emu·K/mol in the temperature range of 100-375 K (Figure 8-9). This value corresponds to the spin only value for 3 $S = 2$ centers. Therefore, the increase in $\chi_m T$ is assigned to the LS to HS transition at all three Fe^{II} sites of the clusters. The $\chi_m T$ value for samples of acetonitrile-wet crystals of **10** and **11** exhibit a similar increase with temperature, but the rise is more gradual and the onset is at lower temperatures than the water-containing samples (Figure 36-37). This finding is also in agreement with the observations made by Mössbauer spectroscopy.

Variable Temperature X-ray Diffraction

The LS to HS states of Fe^{II} ions are typically quite different in terms of the metal-ligand bond lengths and their octahedral coordination geometry (nearness to a perfect octahedron). The average Fe-N distances in LS and HS complexes of the $[FeN_6]$ type are 1.92-2.00 and 2.16-2.21 Å, respectively.[67] The deformation of the octahedral geometry can be quantified by the change in the parameter Σ, defined as the sum of the deviations from 90° of the 12 *cis* N-Fe-N angles. While Σ is 0 for an ideal octahedron,

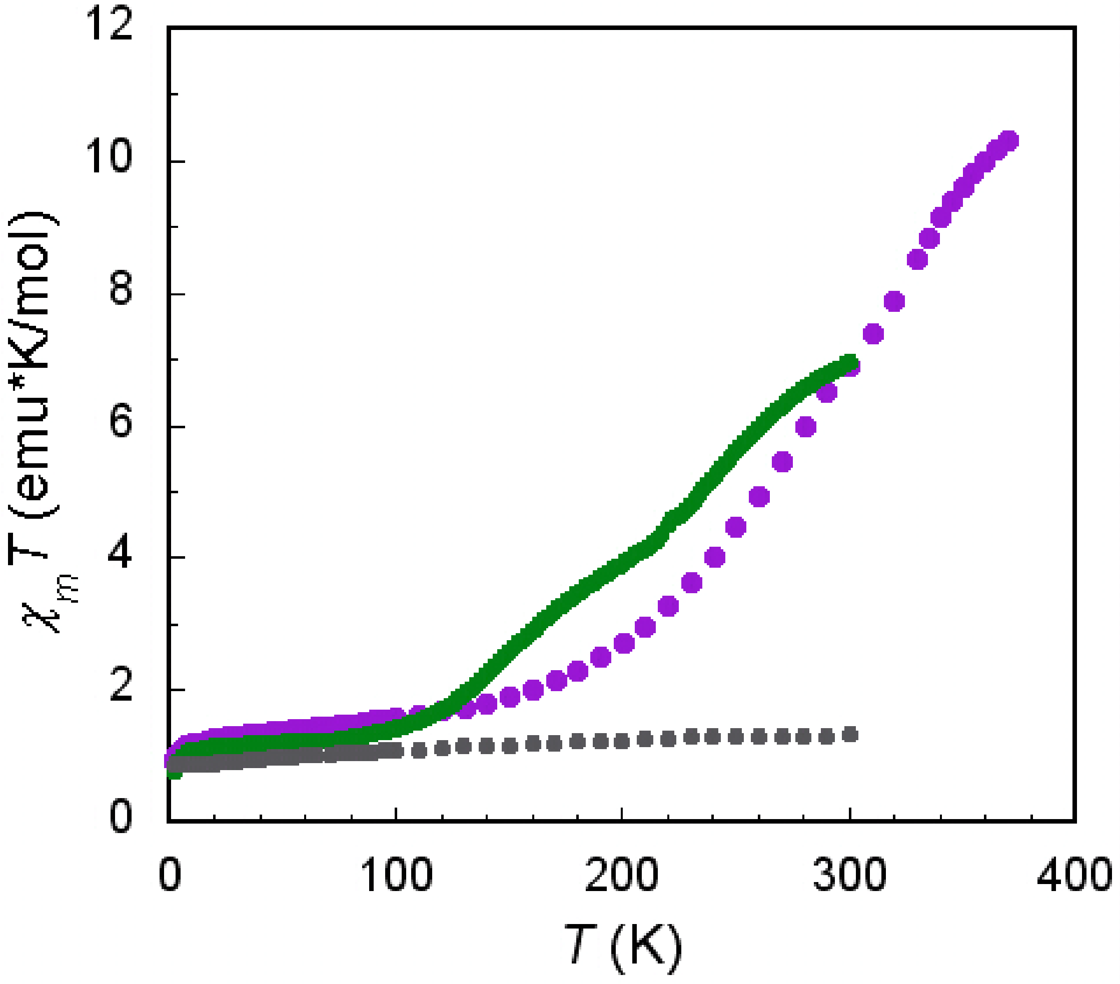

Figure 36: Thermal variation of $\chi_m T$ for water containing crystals of compound **10** (purple), acetonitrile-wet crystals of compound **10** (green), and compound **2** (Zn_3Fe_2, grey).

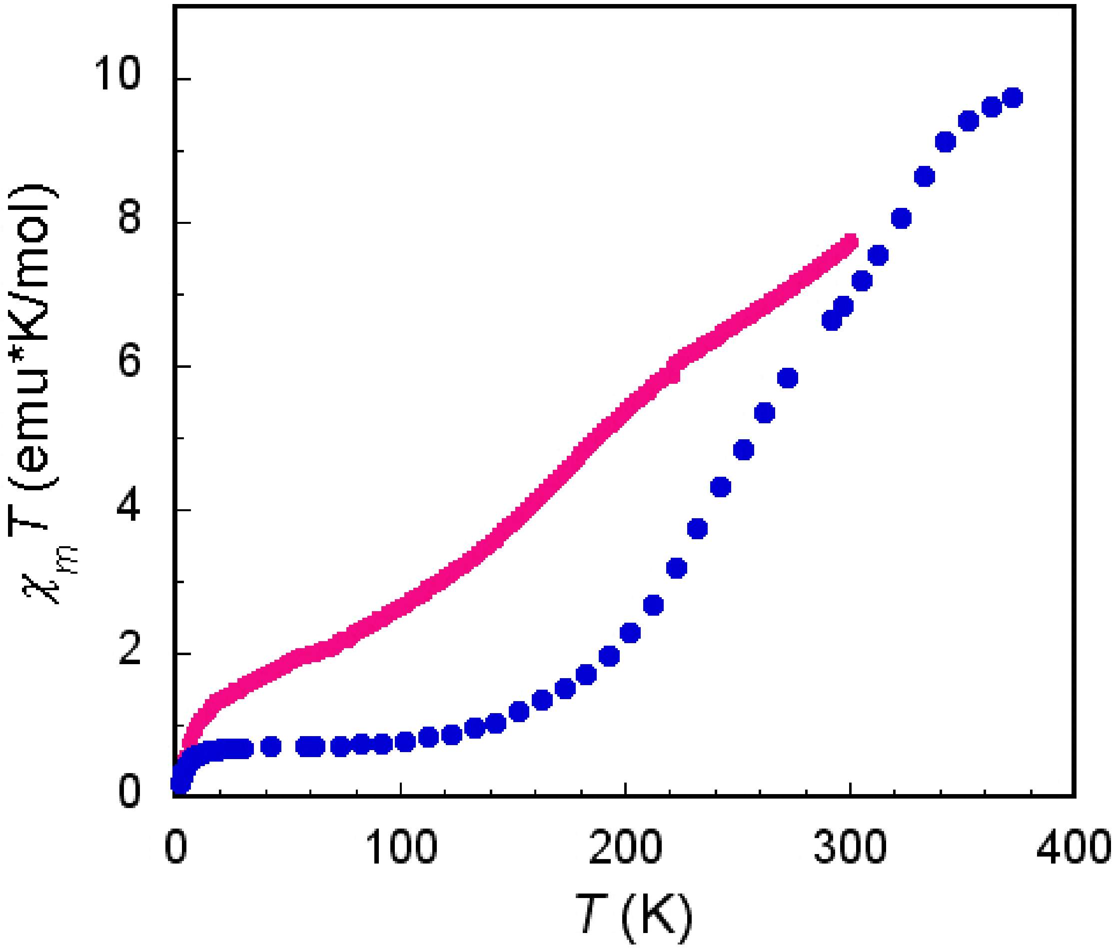

Figure 37: Thermal variation of $\chi_m T$ for water containing crystals (blue) and acetonitrile-wet crystals (pink) of compound **11**.

and, this parameter is ~30 to 50° for LS [FeN_6] complexes and ~70 to 90° for HS complexes. To study these changes, the crystal structure of complex **11**, which undergoes a spin transition, was determined at several temperatures between 30 and 298 K, and the structural parameters for the cluster at these temperatures were compared to those measured for the Fe sites in complex **10** (Table 10).

At 110 K, the average Fe^{II}—N distances for the three equatorial [Fe(tmphen)$_2$(NC)$_2$] units in the structure of **10** are 1.94, 1.95, and 1.95 Å, which are typical for LS Fe^{II} in this type of coordination environment.[67] These bond lengths are comparable to those observed in the LS forms of the [Fe(phen)$_2$(NCX)$_2$] complexes (X = S, Se);[96,161] these distances are 1.990(3)-2.007(2) and 1.971(2)-1.997(2) Å, respectively. The Σ parameters for the three Fe sites of **10** are between 38° and 44° and are also indicative of LS Fe^{II}.

At 30 and 110 K, the average bond lengths and Σ for the equatorial Fe(2) and Fe(3) ions in complex **11** are characteristic of LS Fe^{II} (Table 10). The corresponding parameters for Fe(1) are significantly higher than for the other two Fe sites suggesting significant HS Fe^{II} character, although they are lower than the values typically reported for HS Fe^{II} sites. Typically the bond lengths determined for a compound by X-ray crystallography at multiple temperatures show a small decrease with the increasing temperature due to an increase in the amplitude of the atom vibrations. This is the case above 110 K for the average Co-N bond lengths in **11** but not for the Fe-N bonds, which show a systematic increase. At room temperature, both the Fe-N bond lengths and Σ for Fe(1) and Fe(3) are typical of HS Fe^{II}. These parameters also increase for Fe(2), but to a

Table 10: Metal-ligand bond distances (Å) and the Σ parameter obtained from single crystal structures of compounds **10** and **11** at different temperatures.

	equatorial			axial	
	Fe1—N	Fe2—N	Fe3—N	M′1—C	M′2—C
10, 110K	*1.853(5)*	*1.923(5)*	*1.895(5)*	*1.874(8)*	*1.925(7)*
	1.943(6)	*1.939(6)*	*1.928(6)*	*1.913(7)*	*1.945(7)*
	1.910(5)	1.954(5)	1.943(6)	*1.952(7)*	*1.950(7)*
	1.961(4)	1.954(6)	1.947(5)	1.900(8)	1.900(7)
	1.966(5)	1.960(5)	1.966(5)	1.910(8)	1.909(8)
	1.986(5)	1.968(6)	1.968(5)	1.933(7)	1.931(8)
average M—L	1.94	1.95	1.94	1.91	1.93
Σ	44.5°	38.9°	42.6°		
11, 30K	*2.026(3)*	*1.924(3)*	*1.946(4)*	*1.852(4)*	*1.870(3)*
	2.084(3)	*1.927(4)*	*1.958(3)*	*1.891(4)*	*1.917(4)*
	2.115(4)	1.917(3)	1.936(3)	*1.895(4)*	*1.925(5)*
	2.133(3)	1.929(3)	1.943(3)	1.814(5)	1.886(5)
	2.139(3)	1.955(3)	1.961(3)	1.836(5)	1.890(3)
	2.187(4)	1.992(4)	1.985(4)	1.909(4)	1.909(4)
average M—L	2.11	1.94	1.95	1.87	1.90
Σ	72.2°	39.8°	41.3°		
11, 110K	*2.024(2)*	*1.944(2)*	*1.945(2)*	*1.880(3)*	*1.859(3)*
	2.054(3)	*1.956(2)*	*1.961(2)*	*1.897(3)*	*1.872(3)*
	2.080(3)	1.954(2)	1.948(3)	*1.925(3)*	*1.892(3)*
	2.093(3)	1.961(2)	1.960(2)	1.831(3)	1.823(3)
	2.100(3)	1.962(2)	1.963(2)	1.887(3)	1.869(3)
	2.129(3)	1.977(2)	1.971(2)	1.921(3)	1.900(3)
average M—L	2.08	1.96	1.96	1.87	1.87
Σ	71.8°	40.6°	43.9°		
11, 200K	*2.070(4)*	*1.938(5)*	*1.972(5)*	*1.881(6)*	*1.861(5)*
	2.106(6)	*1.939(5)*	*2.002(6)*	*1.884(7)*	*1.885(7)*
	2.168(5)	1.955(5)	1.996(5)	*1.903(5)*	*1.885(7)*
	2.179(5)	1.958(5)	2.007(4)	1.853(7)	1.858(7)
	2.184(5)	1.976(5)	2.007(5)	1.879(8)	1.890(7)
	2.200(5)	1.976(5)	2.012(5)	1.901(6)	1.902(5)
average M—L	2.15	1.96	2.00	1.90	1.88
Σ	77.1°	40.6°	52.0°		
11, 298K	*2.120(6)*	*1.954(7)*	*2.087(7)*	*1.821(9)*	*1.824(8)*
	2.123(6)	*1.989(8)*	*2.116(7)*	*1.899(8)*	*1.854(8)*
	2.181(7)	1.954(7)	2.138(6)	*1.918(9)*	*1.864(9)*
	2.196(7)	1.959(7)	2.160(7)	1.86(1)	1.799(8)
	2.201(6)	1.979(8)	2.194(7)	1.893(9)	1.82(1)
	2.225(7)	1.998(6)	2.233(6)	1.920(9)	1.88(1)
average M—L	2.17	1.97	2.15	1.89	1.84
Σ	78.5°	45.5°	80.0°		

much smaller extent. The temperature-induced changes in the cluster geometry indicate that a spin transition occurs at the Fe^{II} sites. For Fe(2), the transition is not complete at room temperature, which is the highest temperature at which we have collected Mössbauer spectra and single-crystal diffraction data. The different behavior of the three Fe centers can be explained by the differences π-π interactions of the tmphen ligands on each of the Fe centers (see discussion).

Solvent-Exchanged Variable Temperature X-ray Diffraction

The previously discussed Mössbauer and magnetic properties of compound **11** revealed that the interstitial solvent in the crystals (acetonitrile or water) has a significant influence on the properties of the spin transition, namely the transition temperature ($T_{1/2}$), the cooperativity, and the completeness of the transition. Although most crystals will disintegrate when their original solvent is lost, the TBP clusters are surprisingly robust in that they will typically retain their crystalline form when removed from their mother liquor. In fact, preliminary experiments by Matthew Hilfiger showed that crystals of the Fe_3Os_2 TBP can be filtered and dried and then re-soaked in water with no loss of integrity as determined by single crystal X-ray diffraction.[162]

To study the solvent dependence more thoroughly, the interstitial acetonitrile molecules in crystals of **11** were exchanged with six other solvents. Structures were determined (Tables 11-14) at two different temperatures, 110K and 200K, for crystals from each solvent except hexanes, for which only a 110 K structure has been obtained thus far. The influence of the solvent on the spin crossover behavior was evaluated, as in the previous section, by the measurement of the Fe—N bond lengths and Σ parameters

Table 11: Crystallographic data and structural refinement parameters for compound **11** solvent-exchanged with benzene, toluene, and hexanes (110 K).

	(**11**)$\cdot$2.5C_6H_6 $\cdot$3$H_2O$$\cdot$1MeCN	(**11**)$\cdot$3$C_7H_8$$\cdot$1MeCN	(**11**)$\cdot$2$C_6H_{14}$$\cdot$6$H_2O$
chemical formula	$C_{125}H_{120}N_{25}O_3Fe_3Co_2$	$C_{131}H_{123}N_{25}Fe_3Co_2$	$C_{120}H_{142}N_{24}O_6Fe_3Co_2$
formula weight	2305.90	2333.00	2302.02
space group	$P2_1/c$ (No. 14)	$P2_1/c$ (No. 14)	$P2_1/c$ (No. 14)
a	19.084(4) Å	19.175(2) Å	18.975(2) Å
b	24.684(5) Å	24.775(3) Å	24.794(3) Å
c	24.383(5) Å	24.563(3) Å	24.242(3) Å
α	90°	90°	90°
β	97.837(2)°	97.628(2)°	97.722(2)°
γ	90°	90°	90°
volume	11379(4) $Å^3$	11565(4) $Å^3$	11301(4) $Å^3$
Z	4	4	4
temperature	110 K	110 K	110 K
density (calc)	1.346 g/cm^3	1.334 g/cm^3	1.353 g/cm^3
abs coeff (μ)	0.724 mm^{-1}	0.72 mm^{-1}	0.74 mm^{-1}
crystal color and habit	burgundy red block	burgundy red block	burgundy red block
crystal size (mm^3)	0.57 × 0.17 × 0.14	0.48 × 0.32 × 0.18	0.51 × 0.24 × 0.21
radiation	Mo Kα, 0.71073 Å	Mo Kα, 0.71073 Å	Mo Kα, 0.71073 Å
θ range	1.65-27.71°	2.19-26.15°	2.17-19.44°
reflections collected	130140 [R_{int} = 0.1256]	132546 [R_{int} = 0.0602]	130325 [R_{int} = 0.1174]
independent reflections	26118	26506	26079
data/parameters/restraints	26118/1369/0	26506/1478/0	26079/1385/0
R_1	0.1002	0.0748	0.1064
wR_2	0.3674	0.2554	0.3976
GOF (F^2)	1.038	1.067	1.078
max./min. residual densities ($e\cdot Å^{-3}$)	1.725, -0.777	1.795, -0.694	1.229, -0.950

Table 12: Crystallographic data and structural refinement parameters for compound **11** solvent-exchanged with water, methanol, and ethanol (110 K).

	(**11**)$\cdot 24H_2O$	(**11**)$\cdot 7CH_4O\cdot 7H_2O$	(**11**)$\cdot 5C_2H_5O$ $\cdot 3H_2O\cdot 1MeCN$
chemical formula	$C_{108}H_{144}N_{24}O_{24}Fe_3Co_2$	$C_{115}H_{138}N_{42}O_{14}Fe_3Co_2$	$C_{120}H_{126}N_{25}O_{14}Fe_3Co_2$
formula weight	2347.09	2365.92	2331.89
space group	*P*2$_1$/c (No. 14)	*P*2$_1$/c (No. 14)	*P*2$_1$/c (No. 14)
a	19.459(3) Å	19.253(6) Å	18.904(2) Å
b	24.705(3) Å	24.623(8) Å	24.787(3) Å
c	24.803(3) Å	24.144(8) Å	24.471(3) Å
α	90°	90°	90°
β	98.290(2)°	98.189°	97.892(2)°
γ	90°	90°	90°
volume	11798(5) Å^3	11329(11) Å^3	11358(4) Å^3
Z	4	4	4
temperature	110 K	110 K	110 K
density (calc)	1.321 g/cm^3	1.387 g/cm^3	1.364 g/cm^3
abs coeff (μ)	0.71 mm^{-1}	0.72 mm^{-1}	0.72 mm^{-1}
crystal color and habit	burgundy red block	burgundy red block	burgundy red block
crystal size (mm^3)	0.51 × 0.25 × 0.25	0.55 × 0.22 × 0.22	0.53 × 0.22 × 0.21
radiation	Mo Kα, 0.71073 Å	Mo Kα, 0.71073 Å	Mo Kα, 0.71073 Å
θ range	2.25-22.10°	2.21-23.79°	2.28-22.8°
reflections collected	134302 [R_{int} = 0.0804]	129117 [R_{int} = 0.0916]	130244 [R_{int} = 0.0778]
independent reflections	26901	25749	26074
data/parameters/restraints	26901/1354/0	25749/1434/0	26074/1342/0
R_1	0.0918	0.1074	0.0983
wR_2	0.3302	0.3847	0.3105
GOF (F^2)	1.023	1.158	1.655
max./min. residual densities (e·Å^{-3})	1.918, -0.840	1.098, -0.717	3.416, -0.755

Table 13 Crystallographic data and structural refinement parameters for compound **11** solvent-exchanged with benzene and toluene (200 K).

	(**11**)·3.5C_6H_6·3H_2O	(**11**)·3C_7H_8·5H_2O
chemical formula	$C_{129}H_{123}N_{24}O_3Fe_3Co_2$	$C_{129}H_{130}N_{24}O_5Fe_3Co_2$
formula weight	2342.97	2382.02
space group	$P2_1/c$ (No. 14)	$P2_1/c$ (No. 14)
a	19.301(5) Å	19.367(6) Å
b	24.966(7) Å	24.846(8) Å
c	24.717(7) Å	24.812(8) Å
α	90°	90°
β	97.919(4)°	97.498(4) °
γ	90°	90°
volume	11796(10) $Å^3$	11837(11) $Å^3$
Z	4	4
temperature	200 K	200 K
density (calc)	1.319 g/cm^3	1.336g/cm^3
abs coeff (μ)	0.70 mm^{-1}	0.71 mm^{-1}
crystal color and habit	burgundy red block	burgundy red block
crystal size (mm^3)	0.34 × 0.11 × 0.08	0.65 × 0.27 × 0.22
radiation	Mo Kα, 0.71073 Å	Mo Kα, 0.71073 Å
θ range	2.18-20.79°	2.17-23.40°
reflections collected	134501 [R_{int} = 0.0817]	135548 [R_{int} = 0.0664]
independent reflections	26916	27172
data/parameters/restraints	26916/1354/13	27172/1268/0
R_1	0.0836	0.0814
wR_2	0.3093	0.2919
GOF (F^2)	1.027	1.011
max./min. residual densities ($e·Å^{-3}$)	1.117, -0.678	2.360, -1.015

Table 14: Crystallographic data and structural refinement parameters for compound **11** solvent-exchanged with water, methanol, and ethanol (200 K).

	$(\mathbf{11})\cdot 24H_2O$	$(\mathbf{11})\cdot 6CH_4O\cdot 8H_2O$	$(\mathbf{11})\cdot 2C_2H_5O\cdot 5H_2O$
chemical formula	$C_{108}H_{144}N_{24}O_{24}Fe_3Co_2$	$C_{114}H_{136}N_{24}O_{14}Fe_3Co_2$	$C_{112}H_{118}N_{24}O_5Fe_3Co_2$
formula weight	2447.89	2355.93	2165.74
space group	$P2_1/c$ (No. 14)	$P2_1/c$ (No. 14)	$P2_1/c$ (No. 14)
a	19.78(1) Å	19.428(4) Å	19.195(4) Å
b	24.84(1) Å	24.902(4) Å	24.935(5) Å
c	24.93(1) Å	24.482(4) Å	24.759(5) Å
α	90°	90°	90°
β	98.681(6)°	98.233(3)°	98.023(3)°
γ	90°	90°	90°
volume	12106(17) Å^3	11722(6) Å^3	11734(7) Å^3
Z	4	4	4
temperature	200 K	200 K	200 K
density (calc)	1.679 g/cm^3	1.335 g/cm^3	g/cm^3
abs coeff (μ)	0.85 mm^{-1}	0.70 mm^{-1}	0.70 mm^{-1}
crystal color and habit	burgundy red block	burgundy red block	burgundy red block
crystal size (mm^3)	0.54 × 0.35 × 0.18	0.46 × 0.28 × 0.18	0.49 × 0.25 × 0.22
radiation	Mo Kα, 0.71073 Å	Mo Kα, 0.71073 Å	Mo Kα, 0.71073 Å
θ range	2.24-23.90°	2.18-20.53°	2.14-20.90°
reflections collected	136448 [R_{int} = 0.0733]	134392 [R_{int} = 0.0798]	133409 [R_{int} = 0.0926]
independent reflections	27512	26732	26805
data/parameters/restraints	27512/1354/0	26732/1346/0	26805/1302/0
R_1	0.0796	0.0835	0.0905
wR_2	0.2991	0.3258	0.3027
GOF (F^2)	1.042	1.030	1.527
max./min. residual densities (e·Å^{-3})	1.936, -0.737	0.986, -0.703	1.982, -0.718

for each Fe center to determine the spin state (Table 15-16). At 110 K, the Fe(2) and Fe(3) centers exhibited very similar parameters for all seven solvents, including the original acetonitrile-containing crystal (Table 15-16). The Fe(2) centers have average Fe—N bond lengths of 1.95-1.96 Å and Σ parameters of 36.5-41.8°, and these parameters for the Fe(3) centers are 1.95-1.97 Å and 40.8-46.1°, respectively. In both cases, it is clear that the Fe centers are LS for all solvents. The Fe(1) centers, however, show a much greater variation, with Fe—N bond lengths ranging 1.95-2.16 Å and Σ parameters of 46.2-81.1°. This variation is solvent dependent. The crystals containing small, polar solvent molecules (water and methanol) have shorter bond lengths and lower Σ parameters, which corresponds to the Fe(1) center being LS in these cases. On the other hand, crystals containing planar aromatic molecules (benzene and toluene), exhibit larger bond lengths and higher Σ parameters, leading to a HS Fe(1) center. Crystals containing ethanol and hexanes are similar to acetonitrile in that the Fe(1) center is intermediate between the two states. At 200 K, all three Fe centers were found to have parameters consistent for all interstitial solvents. Fe(2) (1.95-1.97 Å, 37.5-40.6°) and Fe(3) (1.97-2.00 Å, 40.2-52.0°) were observed to be consistently LS, and Fe(1) (2.15-2.17 Å, 77.1-84.9°) was consistently HS (Table 15-16).

Attempts to Vary the Bidentate Ligands on the TBP Clusters

The addition of $[Fe(CN)_6]^{3-}$ or $[Co(CN)_6]^{3-}$ anions to a $[Fe(dmdppz)_2]^{2+}$ solution instantaneously produces a maroon or red powder which are insoluble in common solvents. An IR spectrum of the Fe product contains four overlapping bands in the cyanide region. The two highest energy stretches, 2136 and 2106 cm^{-1}, correspond very

Table 15: Fe-N bond distances (Å) in the crystal structure of compound **11** at different temperatures after being soaked in other solvents for ~1 month.

interstitial solvent	110K			200K		
	Fe1—N	Fe2—N	Fe3—N	Fe1—N	Fe2—N	Fe3—N
benzene	*2.045*	*1.920*	*1.916*	*2.075*	*1.947*	*1.933*
	2.086	*1.944*	*1.958*	*2.117*	*1.948*	*1.965*
	2.138	1.954	1.949	2.188	1.968	1.972
	2.173	1.966	1.953	2.192	1.978	1.974
	2.184	1.969	1.953	2.201	1.978	1.981
	2.186	1.970	1.983	2.219	1.983	1.999
toluene	*2.074*	*1.939*	*1.943*	*2.087*	*1.944*	*1.943*
	2.105	*1.940*	*1.961*	*2.118*	*1.950*	*1.967*
	2.169	1.962	1.963	2.191	1.971	1.985
	2.193	1.971	1.973	2.202	1.977	1.985
	2.196	1.972	1.974	2.21	1.988	1.986
	2.213	1.985	1.983	2.229	1.989	1.997
hexanes	*2.025*	*1.943*	*1.909*	------	------	------
	2.061	*1.947*	*1.961*	------	------	------
	2.104	1.947	1.952	------	------	------
	2.144	1.970	1.954	------	------	------
	2.161	1.976	1.957	------	------	------
	2.187	1.980	1.970	------	------	------
water	*1.957*	*1.935*	*1.933*	*2.088*	*1.944*	*1.942*
	1.974	*1.939*	*1.970*	*2.117*	*1.948*	*1.958*
	1.949	1.970	1.940	2.156	1.980	1.974
	1.999	1.972	1.947	2.174	1.981	1.982
	2.003	1.972	1.965	2.202	1.985	1.991
	2.006	1.987	1.978	2.204	1.988	1.997
methanol	*1.915*	*1.928*	*1.947*	*2.064*	*1.935*	*1.948*
	1.972	*1.946*	*1.981*	*2.113*	*1.938*	*1.969*
	1.971	1.946	1.973	2.171	1.971	1.970
	1.973	1.978	1.987	2.182	1.973	1.973
	1.978	1.979	2.006	2.194	1.982	1.985
	1.981	1.991	2.015	2.202	1.992	1.998
ethanol	*1.983*	*1.932*	*1.922*	*2.060*	*1.938*	*1.949*
	2.026	*1.934*	*1.962*	*2.115*	*1.953*	*1.966*
	2.026	1.969	1.958	2.161	1.971	1.966
	2.058	1.971	1.968	2.194	1.976	1.981
	2.074	1.979	1.974	2.194	1.98	1.995
	2.086	1.985	1.981	2.205	1.994	1.996

Table 16: Average Fe-N bond distances and Σ parameter in the structures of solvent-exchanged crystals of compound **11** at different temperatures. (The pink, blue, and purple color-coding indicates that the Fe center is LS, HS, or intermediate, respectively.)

interstitial solvent	110K			220K		
	Fe1—N	Fe2—N	Fe3—N	Fe1—N	Fe2—N	Fe3—N
water	1.98 Å 48.9° LS Fe$^{\mathrm{II}}$	1.96 Å 38.1° LS Fe$^{\mathrm{II}}$	1.96 Å 40.9° LS Fe$^{\mathrm{II}}$	2.16 Å 80.7° HS Fe$^{\mathrm{II}}$	1.95 Å 37.5° LS Fe$^{\mathrm{II}}$	1.97 Å 40.2° LS Fe$^{\mathrm{II}}$
methanol	1.96 Å 46.2° LS Fe$^{\mathrm{II}}$	1.96 Å 41.8° LS Fe$^{\mathrm{II}}$	1.98 Å 46.1° LS Fe$^{\mathrm{II}}$	2.15 Å 78.7° HS Fe$^{\mathrm{II}}$	1.96 Å 38.7° LS Fe$^{\mathrm{II}}$	1.97 Å 42.9° LS Fe$^{\mathrm{II}}$
ethanol	2.04 Å 58.5° intermediate	1.96 Å 36.9° LS Fe$^{\mathrm{II}}$	1.96 Å 43.4° LS Fe$^{\mathrm{II}}$	2.16 Å 77.1° HS Fe$^{\mathrm{II}}$	1.97 Å 38.9° LS Fe$^{\mathrm{II}}$	1.98 Å 43.1° LS Fe$^{\mathrm{II}}$
acetonitrile	2.08 Å 71.8° intermediate	1.96 Å 40.6° LS Fe$^{\mathrm{II}}$	1.96 Å 43.9° LS Fe$^{\mathrm{II}}$	2.15 Å 77.1° HS Fe$^{\mathrm{II}}$	1.96 Å 40.6° LS Fe$^{\mathrm{II}}$	2.00 Å 52.0° LS Fe$^{\mathrm{II}}$
hexanes	2.11 Å 74.6° intermediate	1.96 Å 36.5° LS Fe$^{\mathrm{II}}$	1.95 Å 41.3° LS Fe$^{\mathrm{II}}$	------ ------ ------	------ ------ ------	------ ------ ------
benzene	2.14 Å 81.1° HS Fe$^{\mathrm{II}}$	1.95 Å 38.7° LS Fe$^{\mathrm{II}}$	1.95 Å 40.8° LS Fe$^{\mathrm{II}}$	2.16 Å 82.8° HS Fe$^{\mathrm{II}}$	1.97 Å 39.4° LS Fe$^{\mathrm{II}}$	1.97 Å 42.4° LS Fe$^{\mathrm{II}}$
toluene	2.16 Å 79.9° HS Fe$^{\mathrm{II}}$	1.96 Å 38.2° LS Fe$^{\mathrm{II}}$	1.97 Å 41.4° LS Fe$^{\mathrm{II}}$	2.17 Å 84.9° HS Fe$^{\mathrm{II}}$	1.97 Å 39.8° LS Fe$^{\mathrm{II}}$	1.98 Å 42.9° LS Fe$^{\mathrm{II}}$

closely to the two modes observed for **10**. These two bands are therefore assigned to bridging Fe^{II}-NC-Fe^{III} and terminal Fe^{III}-CN cyanide stretching frequencies, respectively. The band at 2079 cm^{-1} is nearly similar to the 2080 cm^{-1} stretch of Prussian Blue,[160] suggesting that the Fe^{III}-NC-Fe^{II} bridge is also present in the sample. The lowest energy absorption at 2014 cm^{-1} is unusually low for known cyanide compounds and remains unassigned. Magnetic susceptibility measurements were measured and analyzed assuming the molecular weight of the proposed TBP cluster – $[Fe(dmdppz)_2]_3[Fe(CN)_6]_2$. The room temperature value of $\chi_m T$ is 7.3 emu·K/mol and slowly decreases down to 5.9 emu·K/mol at ~40 K. Below 10-15 K, ferromagnetic coupling is observed, reaching a maximum of 21.8 emu·K/mol at 3 K. This coupling is reminiscent of Prussian Blue,[11] and the combination of IR and magnetism data suggest that there is a Prussian Blue impurity in this compound. Small scale reactions using 3 equivalents of ligand produced a red compound similar to the $[Co(CN)_6]^{3-}$ product; this observation is further evidence that the maroon compound is likely to be a mixture of the desired red product and the Prussian blue impurity.

IR spectral data for the Co product reveal only two bands in the cyanide region located at 2152 and 2127 cm^{-1}. As in the case of the Fe product, these frequencies correspond very closely to the two bands exhibited by **11** and can be reasonably assigned to bridging Fe^{II}-NC-Co^{III} and terminal Co^{III}-CN cyanide stretching modes, respectively. Magnetic susceptibility data for the sample were analyzed assuming the molecular weight of the theoretical $[Fe(dmdppz)_2]_3[Co(CN)_6]_2$ cluster. The room temperature $\chi_m T$ value is 21.5 emu·K/mol and continuously decreases down to 3.8 emu·K/mol at 10 K

(Figure 38), behavior suggestive of a large ferromagnetic (iron or iron oxide) impurity. Below this temperature, $\chi_m T$ decreases more quickly down to 1.9 emu·K/mol at 2 K.

DISCUSSION

The existence of the Fe^{II}—NC—Fe^{III} connectivity observed in **10** is unprecedented in the PB family. In 1962, Robin demonstrated that Turnbull blue (the product of Fe^{II} with $[Fe(CN)_6]^{3-}$) undergoes an electron transfer producing $Fe^{III}_4[Fe^{II}(CN)_6]_3$ (Prussian blue).[163] The “Ukrainian red” compound was reported as the first Turnbull blue prototype,[164] but the compound contains a complex Fe^{II} cation that is isolated from the $[Fe^{III}(CN)_6]^{3-}$ counterion. The **10** cluster is the first molecular analogue of the theoretical $Fe^{II}_3[Fe^{III}(CN)_6]_2$ “Turnbull blue” material in which the $[Fe^{III}(CN)_6]^{3-}$ fragment is directly bound to Fe^{II} centers.

The $[FeN_6]$ coordination environment of the equatorial Fe^{II} ions in clusters **10** and **11** produces a ligand field appropriate for thermally-induced spin crossover behavior. This transition was established by: (1) an increase in the magnetic susceptibility of the clusters with temperature, (2) larger relative amounts of HS Fe^{II} ions in the clusters with increasing temperature as determined by Mössbauer spectroscopy, and (3) an Fe-N bond length elongation of ~0.20 Å with increasing temperature as determined by X-ray crystallography. The last method revealed that the spin transitions occur at specific Fe sites in each cluster in the crystal and do not occur with intramolecular cooperativity, which would have led to the observation of $[(Fe^{II}_{HS})_3Co_2]$ cores.

(a)

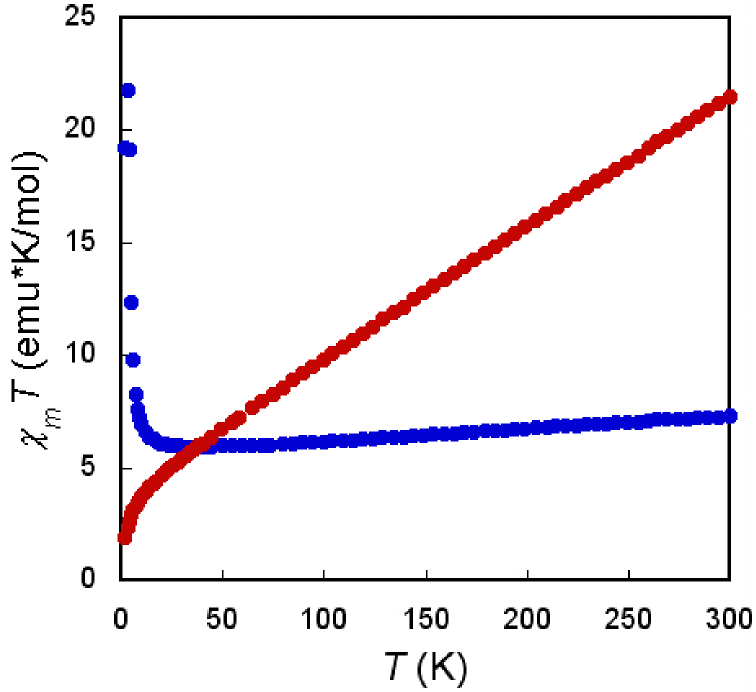

(b)

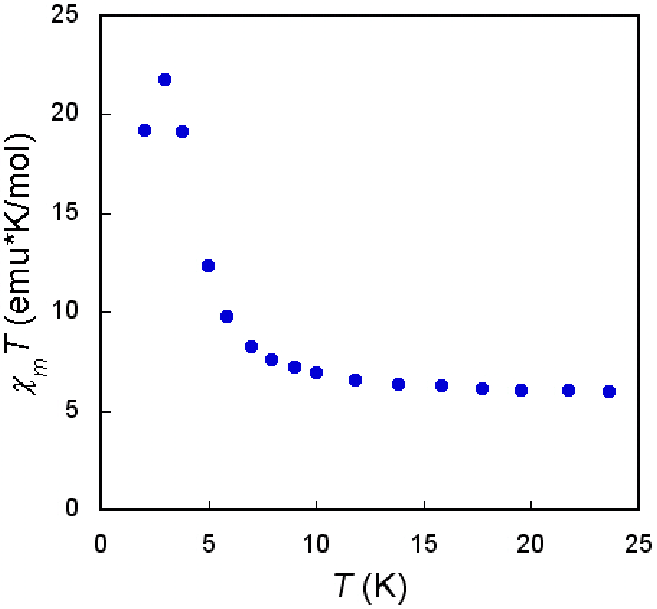

Figure 38: (a) Thermal variation of $\chi_m T$ for the products of the reactions of $[Fe(dmdppz)_2]^{2+}$ with $[Fe(CN)_6]^{3-}$ (blue) and $[Co(CN)_6]^{3-}$ (red) anions. The data assume the formula is $[Fe(dmdppz)_2]_3[M'(CN)_6]_2$. (b) A view of the ferromagnetic coupling apparent in the low temperature region for the $[Fe(CN)_6]^{3-}$ product.

The magnetic data of water-containing crystals of **10** reveal a room temperature $\chi_m T$ value of 6.9 emu·K/mol. If the contribution of Fe^{III} to $\chi_m T$ is the same as that measured for cluster **2** at the same temperature, and the TIP of the equatorial Fe^{II} ions is taken into account, the contribution of the Fe^{II} centers is 5.2 emu·K/mol. The magnetic moment of a HS Fe^{II} ion is affected by the orbital contribution, with reported $\chi_m T$ values up to 3.9 emu·K/mol.[165] Using the $\chi_m T$ value of the model *cis*-$[Fe(phen)_2(NCS)_2]$ complex (3.4 emu·K/mol) leads to 1.5 HS Fe^{II} centers per cluster at room temperature, which is 50% higher than the value determined by Mössbauer spectroscopy. A reason for the discrepancy between the magnetic and Mössbauer estimates may be slight differences in sample composition. Although the samples for both measurements were taken from the same synthetic batch, samples are exposed to vacuum in the SQUID cavity while Mössbauer samples are not; the sample handling differences will lead to higher solvent contents in the Mossbauer samples.

The crystal structure determination carried out at 30 and 110 K on single crystals of **11** revealed that one of the three equatorial Fe^{II} ions is different from the other two and has noticeably longer bond lengths. Low-temperature Mössbauer and magnetic susceptibility of acetonitrile-wet and water-containing crystals confirmed the presence of HS and LS Fe^{II} ions in the clusters and showed that the content of HS Fe^{II} is 10-20% in the former and ~10% in the latter. These measurements indicate that the clusters contain the $[Fe^{II}_3Co^{III}_2]$ core and that the spin state of the Fe^{II} ions is sensitive to the crystallization solvent, with acetonitrile favoring the HS state more so than water. Variable temperature magnetic measurements and Mössbauer spectroscopy studies have shown that, irrespective of the solvent, the LS to HS transition occurs at the Fe^{II} sites, and that, in the case of acetonitrile-wet crystals, the transition starts at lower temperatures and is less abrupt. The spin transition observed at the Fe^{II} sites in both clusters **10** and **11** is gradual, irrespective of the solvent present in the crystals, a fact which is indicative of weak cooperativity and consequently weak intermolecular interactions between the TBP molecules. These same weak intermolecular interactions are also a factor in the single molecule magnet behavior in the Mn_3Mn_2 TBP.[35]

The change in the Fe-N bond distances for the equatorial Fe^{II} atoms (Table 10) supports a stepwise nature for the spin transition. With increasing temperature, the Fe(1) centers are the first sites to undergo the LS → HS transition, followed by the conversion of the Fe(3) centers. X-ray crystallographic data support the conclusion that the Fe(2) sites remain LS up to 298 K; these centers eventually convert at higher temperatures as indicated by a further increase in $\chi_m T$ above 300 K. This behavior is rationalized by considering the intra- and intermolecular π-π interactions between the tmphen ligands (Figure 23). Recall that the tmphen ligands coordinated to the Fe(1) center engages in one *intra*molecular and two *inter*molecular π-π contacts. The tmphen ligands of the Fe(3) site participate in one of each interaction, and the ligands of the Fe(2) center have only intramolecular π–π contacts. It appears that the number and types of these interactions affect the ligand field of the corresponding Fe^{II} ions. The results indicate that π-π interactions weaken the ligand field and stabilize the HS state, with the intermolecular contacts exerting a more pronounced effect than the intramolecular ones. Thus, the HS state is more favorable, and the transition temperature lowest, for the Fe(1) center with three π-π contacts (two of them intermolecular) tmphen ligands. At the other extreme, the Fe(2) site has only two π-π interactions (both *intra*molecular), favors the LS state, and has the highest transition temperature. The Fe(3) site represents an intermediate case.

The characteristics of the spin transition of **10** and **11**, that is, abruptness and transition temperature, depend on the amount and/or type of solvent present in the crystals. Such differences in solvent content have been shown to influence significantly the spin crossover behavior of Fe^{II} complexes.[166-168] For example, the hydrated complex $\{Fe(pyrazine)[Pt(CN)_4]\}\cdot nH_2O$ (n = 2,3) undergoes a gradual transition centered at 230 K with $\chi_m T$ changeing by ~3 emu·K/mol, whereas the dehydrated complex (n = 0) exhibits a more abrupt spin crossover behavior centered at room temperature with $\chi_m T$ changing by ~3.65 emu·K/mol.[168]

The spin crossover of the Fe(1) center in acetonitrile-solvated crystals of **11** is incomplete at low temperatures. This transition is completed when the acetonitrile is replaced with small, polar molecules, but there is no transition at all for Fe(1) when aromatic molecules are present in the interstices. Since increased intermolecular π-π interactions seem to favor the HS state, it appears that the aromatic solvent molecules are contributing to these interactions. This influence does not extend to higher temperatures or to the other two Fe centers, however, since all structures have the same spin configuration at 200 K – HS Fe(1), LS Fe(2), LS Fe(3). The determination of the room temperature structures and the magnetic properties of solvent exchanged crystals are in progress and will help to resolve additional issues regarding the solvent influence.

CONCLUSIONS

Two new Fe^{II} containing TBP compounds have been prepared and fully characterized by X-ray crystallography, mass spectrometry, infrared spectroscopy, ^{57}Fe Mössbauer spectroscopy, and SQUID magnetometry. Both of these compounds were found to exhibit a thermally-induced LS to HS transition of their equatorial Fe^{II} site, adding valuable data to the family of $[M(tmphen)_2]_3[M'(CN)_6]_2$ TBP clusters. Variable temperature single crystal X-ray diffraction studies were used to directly probe the differences in metrical parameters for the three Fe centers which convert at different temperatures depending on the number and types of π-π interactions of the tmphen ligands. The nature of the interstitial solvent in the crystals was clearly shown to influence the spin crossover behavior.

CHAPTER IV

INCORPORATION OF TRIGONAL BIPYRAMIDAL CLUSTERS INTO HIGHER NUCLEARITY CLUSTERS AND CHAINS*

INTRODUCTION

Previous work in the Dunbar labs to use trigonal bipyramidal clusters as building blocks for extended structures led to the discovery that the $Co^{III}_2Co^{II}Fe^{II}_2$ (blue) form of the Co_3Fe_2 cluster can be linked by $[Mn(H_2O)_6]^{2+}$ to form two different one-dimensional compounds in which Mn^{II} centers serve as linkers for the oxidized clusters (Figure 39). In the first structure type, $\{[Co^{III}(tmphen)_2]_3[Fe^{II}(CN)_6]_2[Mn^{II}(MeOH)_4]\}_\infty(ClO_4)_3 \cdot xMeOH$, which we denoted as “type A”, the chain is composed of oxidized $Co_3Fe_2^+$ clusters linked by single $[Mn(CH_3OH)_4]^{2+}$ bridges. In the second structure type, $\{[Co^{III}(tmphen)_2]_3[Fe^{II}(CN)_6]_2[Mn^{II}(MeOH)_4]_{0.5}[Mn^{II}(MeOH)_3(MeO)]\}_\infty(ClO_4)_3 \cdot xMeOH$, or “type B”, the $Co_3Fe_2^+$ units are connected into a chain by alternating single $[Mn(MeOH)_4]^{2+}$ bridges and pairs of $[Mn(MeOH)_3(MeO)]^+$ bridges. Unfortunately, the two chain compounds were found to crystallize simultaneously under the same reaction conditions. The mixture of products prevented further characterization beyond single crystal X-ray diffraction studies.

---

*Parts of this chapter are reproduced with permission from “Trigonal-Bipyramidal Metal Cyanide Complexes: A Versatile Platform for the Systematic Assessment of the Magnetic Properties of Prussian Blue Materials” by Funck, K. E.; Hilfiger, M. G.; Berlinguette, C. P.; Shatruk, M.; Wernsdorfer, W.; Dunbar, K. R., **2009**. *Inorg. Chem.*, *48*, 3438-3452. Copyright 2009 by ACS Publications.

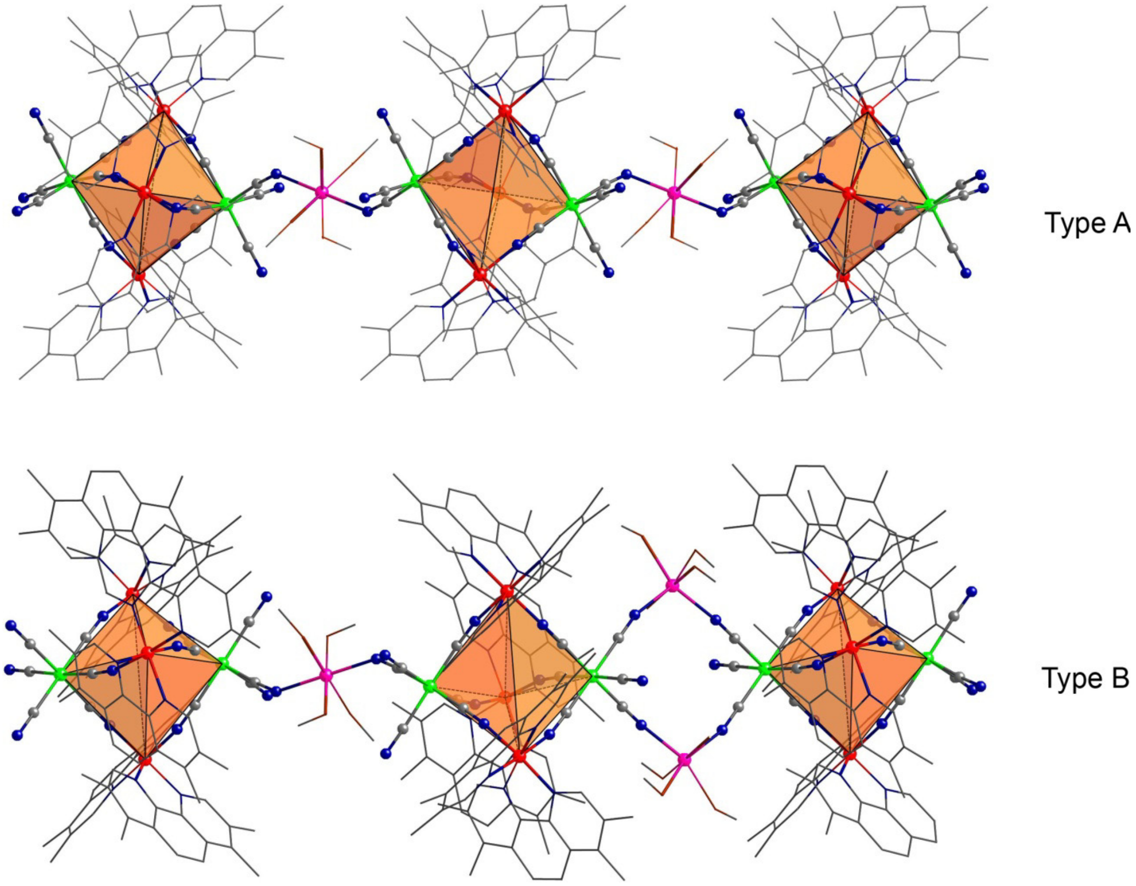

Figure 39: Fragments of infinite chains of Mn^{II}-bridged Co_3Fe_2 clusters in the crystal structures of $\{[Co^{III}(tmphen)_2]_3[Fe^{II}(CN)_6]_2[Mn^{II}(MeOH)_4]\}_\infty(ClO_4)_3 \cdot 10MeOH$ (Type A) and $\{[Co^{III}(tmphen)_2]_3[Fe^{II}(CN)_6]_2[Mn^{II}(MeOH)_4]_{0.5}[Mn^{II}(MeOH)_3(MeO)]\}_\infty(ClO_4)_3 \cdot 8MeOH$ (type B). (C, grey; N, blue; O, brown; Co, red; Fe, green; Mn, pink). (H atoms and solvent molecules have been omitted for the sake of clarity.).

To overcome the problem of multiple, inseparable phases of the $Co_3Fe_2Mn_x$ chain compounds and to be able to characterize each individually, it was necessary to find a way to control the reaction by using different mononuclear precursors. It was observed that the bridging CN^- ligands are always coordinated in a *trans* orientation to the Mn^{II} ions in the type A chain and in a *cis* arrangement in the double bridges of the type B chain (Figure 40). It was reasoned that if the bridging interaction could be restricted to a *trans* arrangement, the formation of the product would be limited to the type A chain. This restriction can be accomplished by the use of a metal precursor in which the four equatorial sites are blocked by a planar tetradentate ligand (or two *trans* bidentate ligands) with the remaining *trans* axial sites being occupied by labile ligands.

EXPERIMENTAL

Materials

Commercially available 3,4,7,8-tetramethyl-1,10-phenanthroline (tmphen; Alfa Aesar), 18-crown-6 (Aldrich, Acros), cyclam (Alfa Aesar), $K_3[Fe(CN)_6$ (Fisher), and $Co(NO_3)_2\cdot 6H_2O$ (Strem) were used as received. Acetonitrile and methanol were of the ACS reagent grade and were used as received (EMD Chemicals). The starting materials $[Mn(acac)_2(H_2O)_2]ClO_4$,[169] $[Mn(cyclam)Cl_2]Cl$,[170] $Ni(cyclam)Cl_2$,[171] and $[Cr(cyclam)Cl_2]Cl$,[172] were prepared according to literature methods. Stock solutions of $[(18\text{-crown-}6)K]_3[Fe(CN)_6]$ were prepared by stirring a mixture of $K_3[Fe(CN)_6]$ (700 mg, 2.13 mmol) and 18-crown-6 (1.63 g, 6.18 mmol) in 200 mL acetonitrile for 24 h and filtering the mixture to remove the excess $K_3[Fe(CN)_6]$.

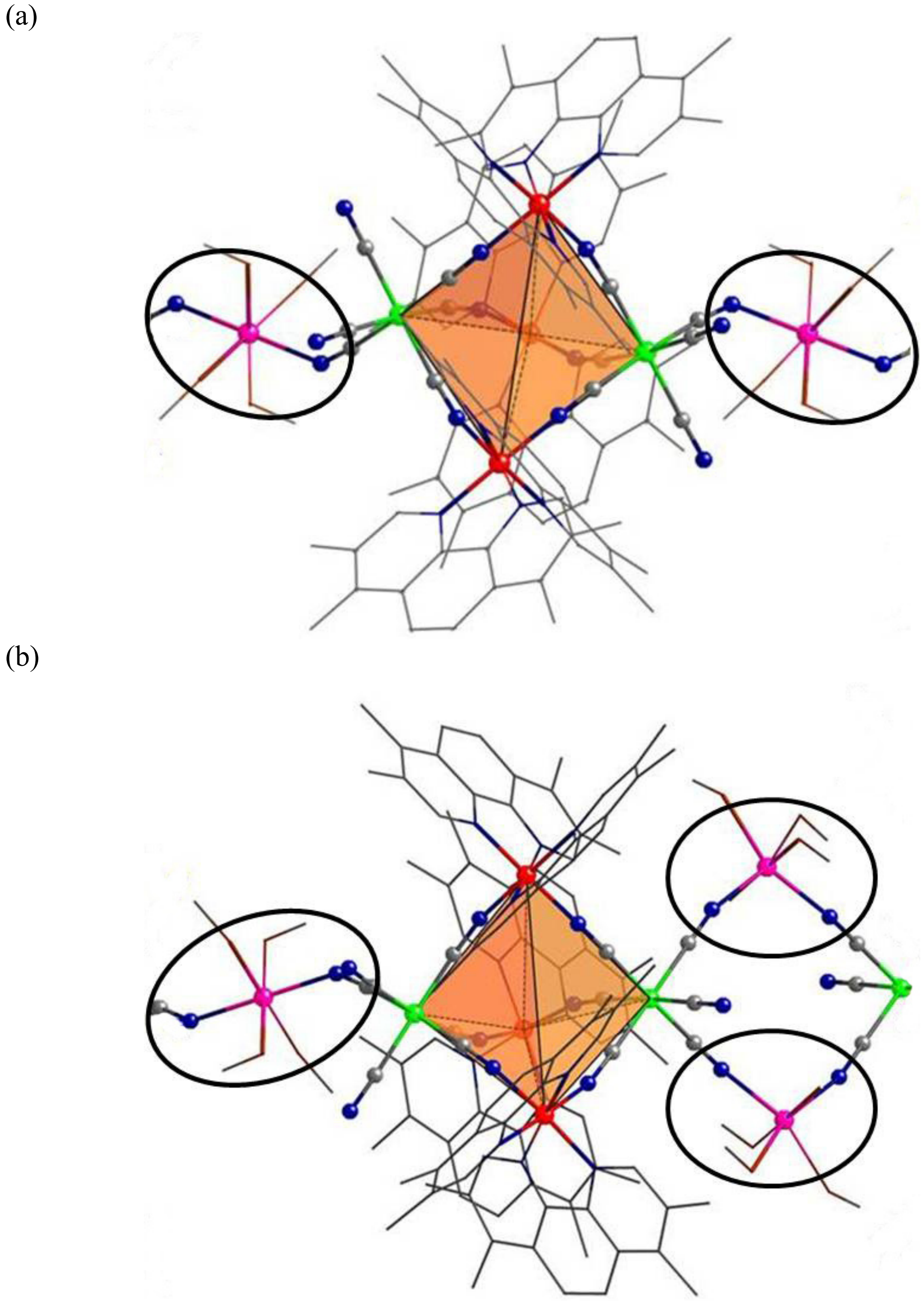

Figure 40: (a) View of the building blocks in the type A $Co_3Fe_2Mn_1$ chain emphasizing the *trans* coordination of the bridging cyanide ligands. (b) Close up view of the type B $Co_3Fe_2Mn_{1.5}$ chain emphasizing the alternating *trans* and *cis* coordination of the bridging cyanide ligands.

Synthesis

$\{[Co(tmphen)_2]_3[Fe(CN)_6]\}$ (12). This procedure is a variation of our previously reported synthesis.[116] Samples of $Co(NO_3)_2{\cdot}6H_2O$ (300 mg, 1.03 mmol) and tmphen (609 mg, 2.58 mmol) were combined in 150 mL of acetonitrile and stirred for 30 minutes to obtain a clear, yellow-orange solution. To this solution was slowly added 50 mL of $(18\text{-}C\text{-}6\text{-}K)_3[Fe(CN)_6]$ stock solution. The mixture was left to stand undisturbed for 3 days. After this time, red crystals had formed at the bottom of the flask. The crystals were collected by filtration, washed with acetonitrile (45 mL) and diethyl ether (30mL), and dried *in vacuo*. Yield – 477 mg (75%). IR (Nujol), ν(€N), cm^{-1}: 2133, 2109, 2057.

$\{[Co(tmphen)_2]_3[Fe(CN)_6]_2[Mn(CH_3OH)_4]\}_\infty(ClO_4)_3$ (13). The solutions were prepared by dissolving **12** (49 mg, 0.020mmol) in 40 mL of methanol and $[Mn(acac)_2(H_2O)_2]ClO_4$ (244 mg, 0.600 mmol) in another 40 mL of methanol. For bulk reactions, the Co_3Fe_2 solution was layered on the Mn^{III} solution in 4mL/4mL portions in glass vials and left to stand for one week. The dark blue crystals were harvested, washed with methanol, and dried *in vacuo*. Yield – 43.3 mg (81%). IR (Nujol), ν(C≡N), cm^{-1}: 2140, 2103, and 2061. Thermal gravimetric analysis indicates a 14% mass loss, corresponding to 23 water molecules. X-ray quality crystals were grown by layering the two solutions in 2mL/2mL portions in 5mm i.d. Pyrex glass tubes.

Additional Attempts to Synthesize Linked Co_3Fe_2 Clusters

1. **Co_3Fe_2 + $Mn(cyclam)Cl_3$**. A sample of **12** (245 mg, 0.10 mmol) was dissolved in 100 mL of methanol. To this was added a solution of $[Mn(cyclam)Cl_2]Cl{\cdot}5H_2O$

(90 mg, 0.20 mmol) in 25 mL of methanol. After stirring the solution for 30 minutes, a large excess of $NaClO_4 \cdot H_2O$ (400 mg, 2.85 mmol) in 2 mL methanol was added. After another 90 minutes of stirring, a dull blue precipitate was isolated, washed with diethyl ether, and dried *in vacuo*. Yield – 246 mg. IR (Nujol), ν(C≡N), cm^{-1}: 2140, 2109, 2070, and 2036. Attempts to grow crystals by layering the **12**/Mn(cyclam)Cl_3 solution over a 50mg/mL solution of $NaClO_4$ in methanol in a 5mm i.d. Pyrex glass tube produced crystals of **13** after a month.

2. **Co_3Fe_2 + Ni(cyclam)Cl_2**. A solution of **12** (98 mg, 0.040 mmol) was prepared in 40 mL of methanol. A second solution of Ni(cyclam)Cl_2 (26 mg, 0.080 mmol) was prepared in 10 mL of methanol and added to the first solution. After stirring the mixture for 45 minutes, a large excess of $NaClO_4 \cdot H_2O$ (150 mg, 1.07 mmol) in 1 mL methanol was added. After one hour of additional stirring, the resulting dull blue precipitate was isolated, washed with diethyl ether, and dried *in vacuo*. Yield – 103 mg. IR (Nujol), ν(C≡N), cm^{-1}: 2135, 2102, and 2069. Attempts to grow crystals were unsuccessful.
3. **Co_3Fe_2 + Cr(cyclam)Cl_3**. This reaction was performed in an analogous fashion to reaction 2 above with a sample of [Cr(cyclam)Cl_2]Cl (29 mg, 0.080 mmol) in 10 mL of methanol in place of the Ni(cyclam)Cl_2 solution. A grey precipitate was isolated. Yield - 23 mg. IR (Nujol), ν(C≡N), cm^{-1}: 2134, 2104, and 2063. Attempts to grow crystals were unsuccessful.

Attempts to Synthesize Linked Fe_3M_2 Clusters (M = Fe, Co)

4. **Fe_3Co_2 + $Mn(ClO_4)_2$**. The solutions were prepared by dissolving **11** (33 mg, 0.015 mmol) in 15 mL of 1:1 v/v methanol/dichloromethane and $Mn(ClO_4)_2 \cdot 6H_2O$ (181 mg, 0.500 mmol) in 5 mL of methanol. The two solutions were mixed and, after 3 days, red-orange fiber-like needles were harvested, washed with methanol, and dried *in vacuo*. Yield – 31 mg. IR (Nujol), ν(C≡N), cm^{-1}: 2163 and 2014. Attempts to grow larger, X-ray quality crystals were unsuccessful.
5. **Fe_3Fe_2 + $Mn(cyclam)Cl_3$**. A sample of **10** (33 mg, 0.015 mmol) was dissolved in 15 mL of 1:1 v/v methanol/dichloromethane. To this was added a solution of $[Mn(cyclam)Cl_2]Cl$ (14 mg, 0.060 mmol) in 4 mL of methanol. After stirring the solution for 1 hour, a large excess of $NaClO_4 \cdot H_2O$ (0.060 g, 0.43 mmol) in methanol was added. After 30 minutes of stirring, an orange precipitate was collected, washed with a small volume of methanol, and dried *in vacuo*. Yield – 30 mg. IR (Nujol), ν(C≡N), cm^{-1}: 2108 and 2038. When the filtrate was left to stand overnight, red-orange fibers form as was observed in the previous reaction.
6. **Fe_3Co_2 + $[Mn(cyclam)Cl_2]Cl$**. This reaction was performed in a manner akin to to the previous reaction but with a sample of **11** (45 mg, 0.020 mmol) dissolved in 20 mL of 1:1 v/v methanol/dichloromethane and with all the other reagents being scaled appropriately. A red-orange precipitate was isolated. Yield – 60 mg. IR (Nujol), ν(C≡N), cm^{-1}: 2165 and 2130.

Single Crystal X-ray Diffraction Studies

In a typical experiment, a crystal selected for study was suspended in polybutene oil (Aldrich) and mounted on a cryoloop, which was placed in an N_2 cold stream. Single-crystal X-ray data were collected on a Bruker APEX II diffractometer equipped with a CCD detector. The data sets were recorded as three ω-scans of 606 frames each, at 0.3° step width, and integrated with the Bruker SAINT[124] software package. The absorption correction (SADABS[125]) was based on fitting a function to the empirical transmission surface as sampled by multiple equivalent measurements. Solution and refinement of the crystal structures was carried out using the SHELX[126] suite of programs and the graphical interface X-SEED.[127] Preliminary indexing of the data sets established a monoclinic unit cell for **13**. Systematic extinctions indicated that the compound crystallizes in the space group *C*2/*c* (No. 15). The structure was solved by direct methods, which resolved the positions of all metal atoms and most of the C and N atoms. The remaining non-H atoms were located by alternating cycles of least-squares refinements and difference Fourier maps. All H atoms were placed in calculated positions. A large number of disordered interstitial solvent molecules are present in the crystal. The final refinement was carried out with anisotropic thermal parameters for all non-H atoms. A summary of pertinent information relating to unit cell parameters, data collection, and refinement statistics is provided in Table 17.

RESULTS AND DISCUSSION

{[Co(tmphen)$_2$]$_3$[Fe(CN)$_6$]$_2$[Mn(CH$_3$OH)$_4$]}$_\infty$(ClO$_4$)$_3$ (13)

Synthesis

The use of the precursor [Mn^{III}(acac)$_2$(H$_2$O)$_2$]$^+$, in which the *trans* acac ligands block the equatorial positions, was predicated on the idea that it would lead to the exclusive formation of a "type A" chain bridged by [Mn^{III}(acac)$_2$]$^+$ moieties. Surprisingly, the crystals that were obtained were the previously solved type A structure with [Mn^{II}(MeOH)$_4$]$^{2+}$ bridging moieties and with no acac ligands present. In addition, the determination of the unit cells of many crystals from the same batch confirmed that this is the sole product of the reaction. The formation of the known chain with methanol ligands demonstrates that the acac$^-$ ligands are sufficiently labile to be easily replaced by solvent molecules. At the same time, however, the selectivity in the synthesis suggests that the *trans* starting material does help to direct the assembly of the chain structure to a single product before the ligands are removed. As was found for Berlinguette's Co$_3$Fe$_2$Ni$_6$ complex,[173] all of the Co ions in the chain compound exhibits short M—L bonds (~1.92 Å) characteristic of the LS Co^{III} state. These data confirm the oxidation of TBP core[86] with simultaneous reduction of the Mn^{III} ions.

As with the TBP clusters, **13** contains a large amount of interstitial solvent (methanol under mother liquor or water upon exposure to humid air) found primarily in the channels between chains (Figure 41a). Examination of the compounds by TGA revealed that they gradually lose the interstitial solvent when heated to 140-150°C. The chains begin to lose coordinated methanol at ~170°C and they decompose above ~230°C.

Single-Crystal X-ray Structure

A summary of pertinent information relating to unit cell parameters, data collection, and refinement statistics is provided in Table 17. Single-crystal X-ray studies revealed that **13** is the same compound as previously described by Berlinguette,[174] except for slight differences in the amount of interstitial methanol. Compound **13** crystallizes in the monoclinic space group *C*2/*c* (Figure 42). The structure consists of CN-bridged $[Co^{III}_3Fe^{II}_2]^+$ TBP cores bridged by $[Mn(MeOH)_4]^{2+}$ moieties. The Mn^{II} ions are in an N_2O_4 environment with the four methanol molecules in *trans* positions and the remaining sites occupied by N-bound CN^- ligands from the exteriors of two TBP cores. Unlike typical TBP's, the TBP cores of the chains have nearly C_3 symmetry through the Fe centers (Figure 43). The three equatorial metal sites in one TBP exhibit the same chirality (Δ or Λ), and the neighboring TBP cores in the chain are of the opposite chirality, resulting in a centrosymmetric space group. The alternating chiralities lead to zig-zag type chains, which extend parallel to the (**a** + **c**) direction of the unit cell (translated from the origin by ¼) (Figure 41b). Neighboring chains are offset slightly which allows the chains to pack tightly (Figure 44), but there are no interchain π-π interactions between tmphen ligands.

Infrared Spectroscopy and Magnetic Properties

The IR stretches observed for **12** are comparable with those measured previously for the cluster.[116] As with the TBP clusters, compound **13** exhibits characteristic C≡N

Table 17: Crystallographic data and structural refinement parameters for compound **13**.

	(**13**)·10MeOH
chemical formula	$C_{122}H_{152}N_{24}O_{26}Cl_3Co_3Fe_2Mn_1$
formula weight	2598.81
space group	*C*2/c (No. 15)
a	20.791(2) Å
b	27.834 (3) Å
c	25.938(3) Å
α	90°
β	108.387 (2)°
γ	90°
volume	14244(2) Å^3
Z	4
temperature	110 K
density (calc)	1.315 g/cm^3
abs coeff (μ)	0.755 mm^{-1}
crystal color and habit	dark blue block
crystal size (mm^3)	not measured
radiation	Mo Kα, 0.71073 Å
θ range	1.27-28.33°
reflections collected	65472 [R_{int} = 0.1302]
data/parameters/restraints	17277/813/16
R_1	0.1261
wR_2	0.2888
GOF (F^2)	1.071
max./min. residual densities (e·Å^{-3})	1.421, -0.986

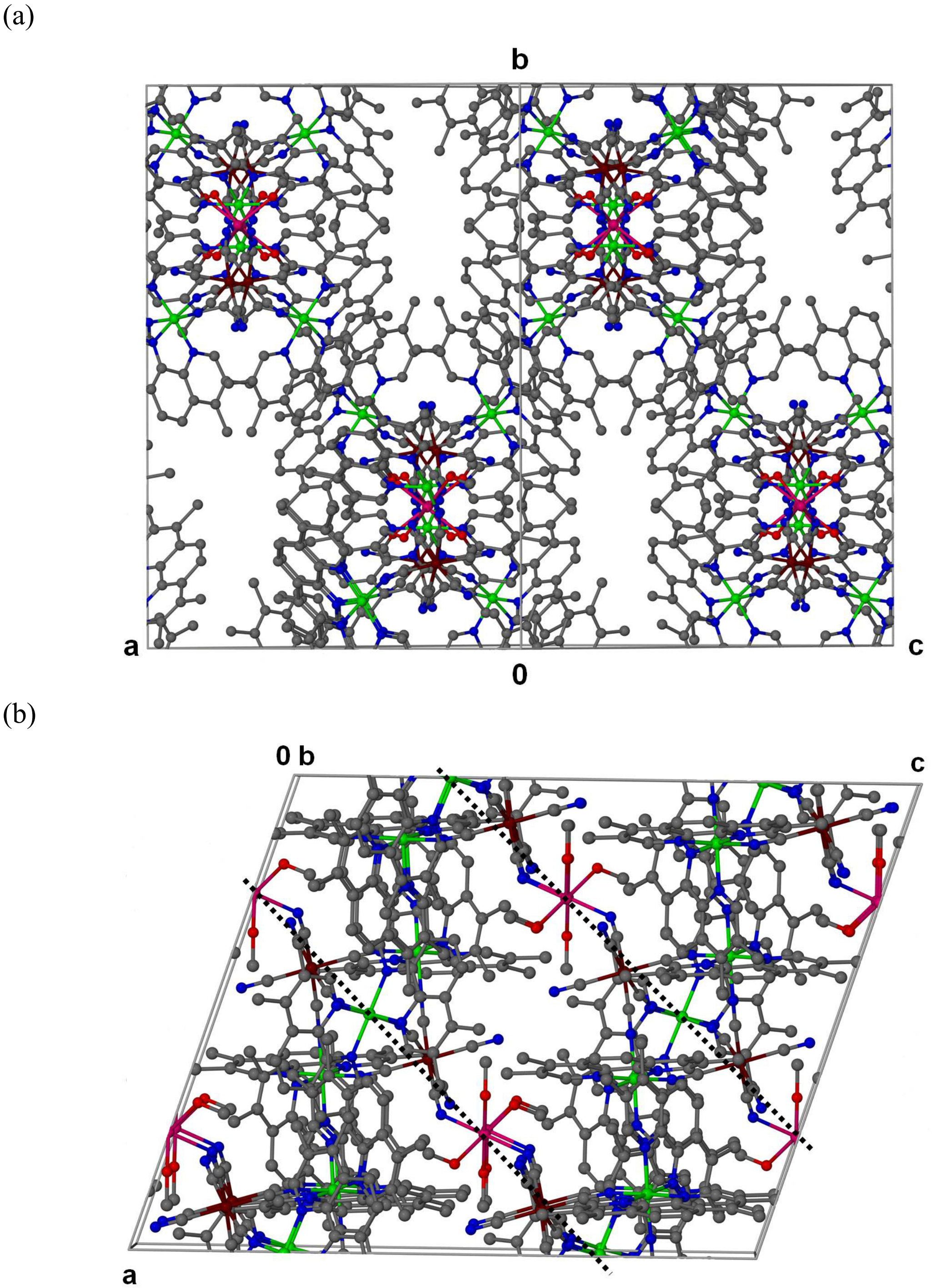

Figure 41: (a) Packing diagram of **13**, viewed along the (**a** + **c**) axis, which shows the packing of the chains. (b) Packing diagram of **13** viewed along the **b**-axis. The dotted lines indicate the alignment of the chains. (H atoms, ClO_4^- ions, and solvent molecules have been omitted for the sake of clarity.)

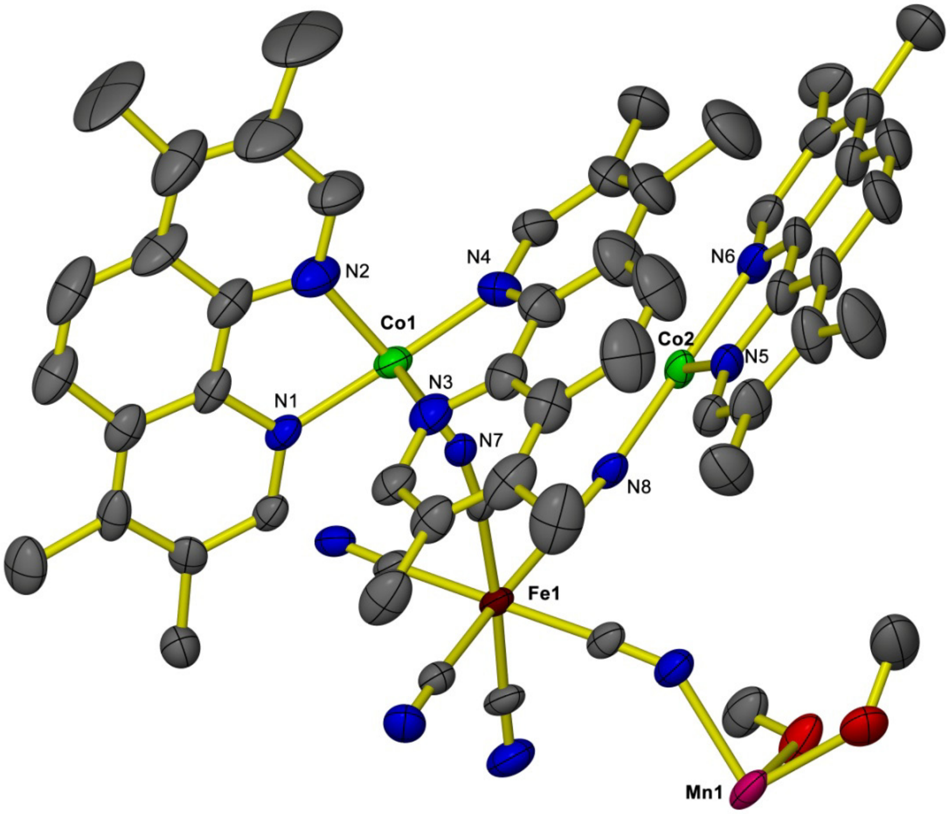

Figure 42: Thermal ellipsoid plot of the asymmetric unit of **13**, ($Co_{1.5}Fe_{1}Mn_{0.5}$), drawn at the 50% probability level. (H atoms and solvent molecules have been omitted for the sake of clarity.)

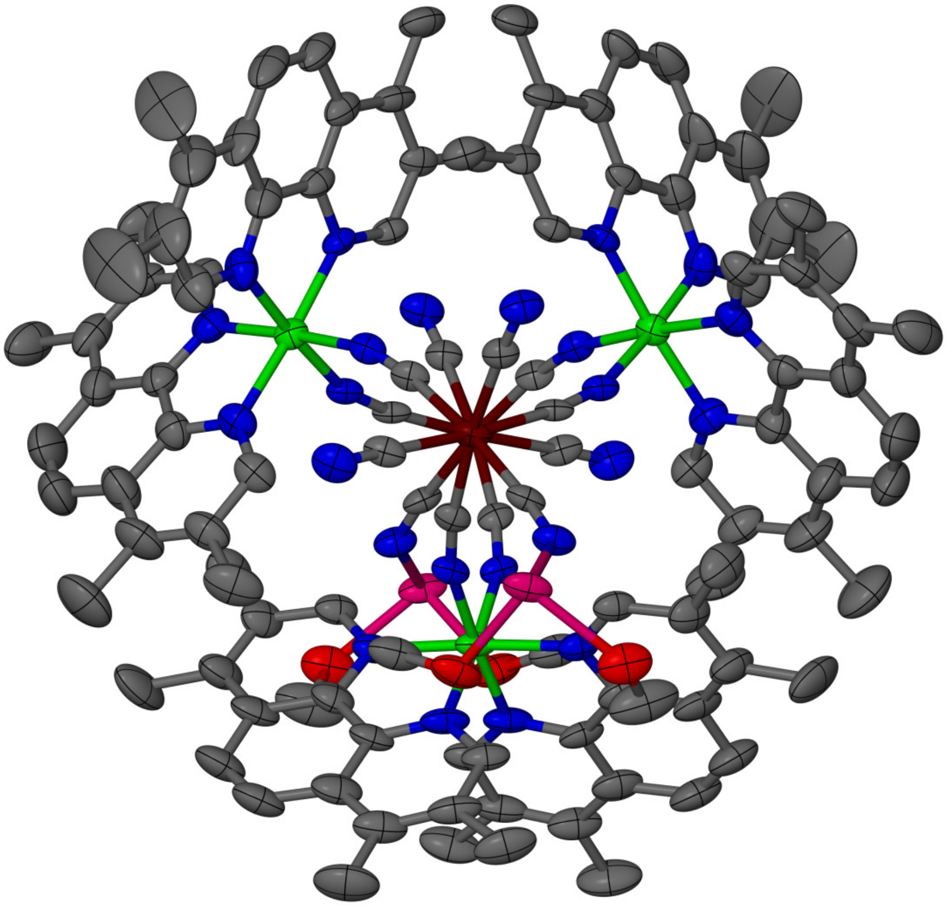

Figure 43: Thermal ellipsoid plot of two asymmetric units of **13** ($Co_3Fe_2Mn_1$), drawn at the 50% probability level, emphasizing the nearly C_3 axis of the TBP cores. (H atoms and solvent molecules have been omitted for the sake of clarity.)

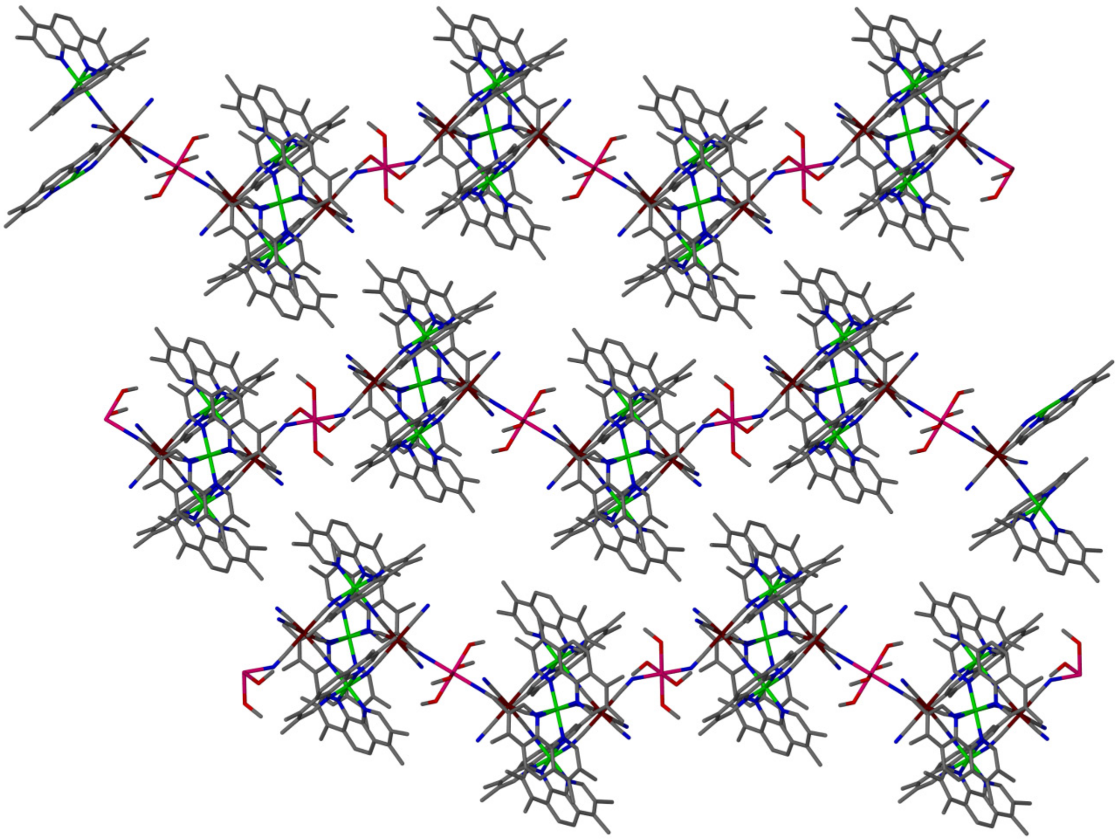

Figure 44: Packing of three chains in compound **13** (H atoms and solvent molecules have been omitted for the sake of clarity).

stretching modes. The lowest frequency stretch at 2061 cm^{-1} is comparable to the 2057 cm^{-1} band observed for **12** and is assigned to the terminal cyanide ligands. Since this stretch is also in the range expected for Fe^{II}—CN—Mn^{II}_{HS} bridging modes,[20,156] however, this band is likely a superposition of both modes. The highest energy stretch, 2140 cm^{-1}, falls close to the range of frequencies expected for Fe^{II}—CN—Co^{III}_{LS} bridging modes (2116-2137 cm^{-1}).[20,116] Similar bands to these two are also observed in the IR data for **12** (2057 and 2133 cm^{-1}), corresponding to the same modes. The third stretch in **13**, 2103 cm^{-1}, falls in the range of expected Fe^{II}—CN—Co^{II}_{HS} modes (2085-2103 cm^{-1}),[116] but this assignment is not appropriate in this case since the cluster contains only Co^{III}_{LS} centers. An analogous band is also observed in the spectrum of $Na\{[Co(tmphen)_2]_3[Fe(CN)_6]_2\}(ClO_4)_2$[116] but is not accounted for. One hypothesis for this feature is that it is due to a splitting of one of the other bands due to distortions in the chain. This hypothesis will require a more thorough investigation.

Since **13** consists of Mn^{II} ions connected by diamagnetic TBP building blocks, it should behave magnetically as isolated Mn^{II} ions, which have an expected spin-only value of 4.375 emu·K/mol at room temperature. Indeed, **13** was found to exhibit simple paramagnetism over the entire temperature range (300-2 K) with a susceptibility per $Co_3Fe_2Mn_1$ unit of 4.30 emu·K/mol (Figure 45), which is in good agreement with the spin only value (4.30 emu·K/mol).

Mass Spectrometry and Optical Absorption Spectroscopy

When **13** is placed into acetonitrile (or 1:1 acetonitrile/methanol), a dark blue solution is formed. Since **13** is a 1-D structure, however, it is highly unlikely that it

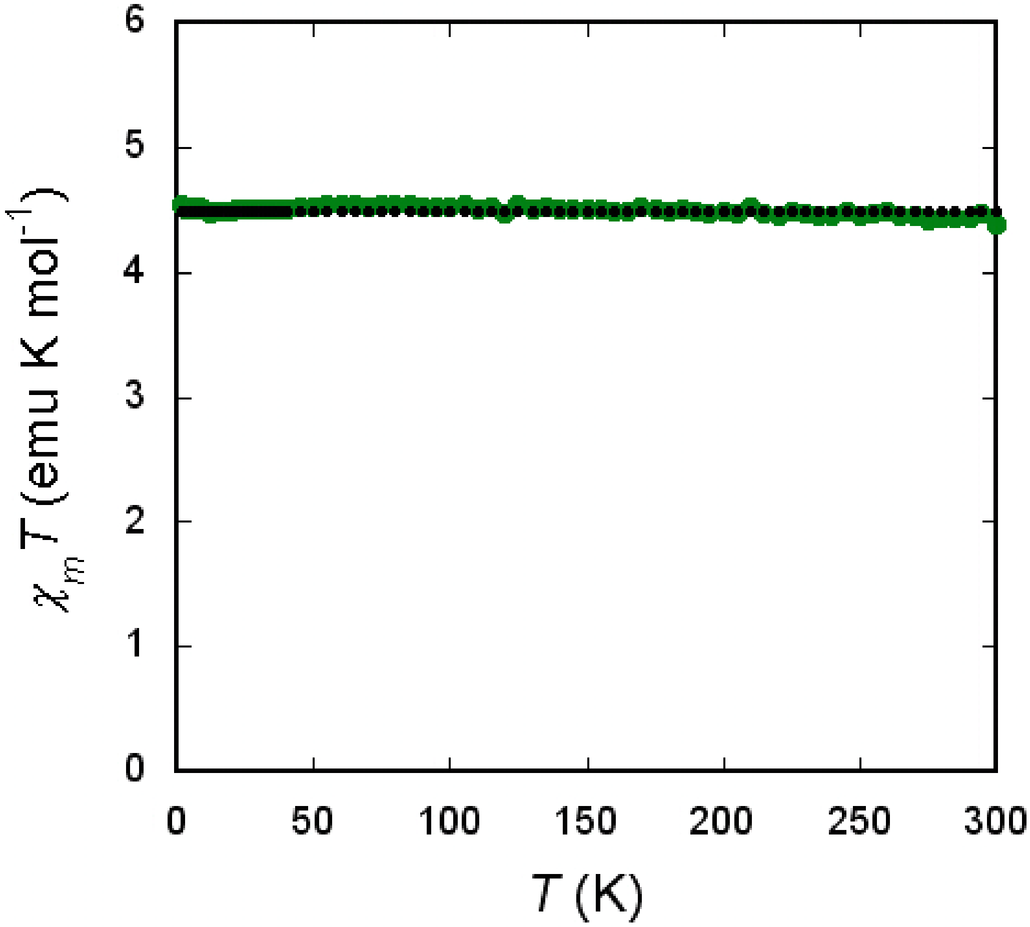

Figure 45: Thermal variation of the $\chi_m T$ product for compound **13** (green) and theoretical fit (black, g = 2.03).

would dissolve without decomposing. Nevertheless, mass spectrometry and UV-visible spectroscopy can still be used to gain further insights into the properties of fragments of the compound.

ESI mass spectroscopy of **13** (in acetonitrile) exhibit mass peaks indicative of portions of the original chain. Peaks were observed for an intact cluster, $[Co_3Fe_2]^{2+}$ (*m/z* = 1009), as well as a hexanuclear portion of a chain, $[Co_3Fe_2 + Mn]^{3+}$ (*m/z* = 691) (Figure 46). Moreover a very large undecanuclear fragment was observed, $[2Co_3Fe_2 + Mn]^{4+}$ (*m/z* = 1023), suggesting the likelihood that the solubility of large molecules are possible in solution.

As for the TBP clusters (Chapter II), the solution electronic absorption spectrum of **13** (in acetonitrile) is dominated by the very strong $\pi \rightarrow \pi^*$ transitions of the tmphen ligand in the UV region. The visible spectrum reveals a very broad absorption at 688 nm (5800 L/mol·cm), which corresponds to the $Co^{III}/Fe^{II} \rightarrow Co^{II}/Fe^{III}$ MM′CT (Figure 47). This band is very similar to the 698 nm (6100 L/mol·cm) feature observed for the compound $Na(Co_3Fe_2)(ClO_4)_2$. These two spectra are noticeably different from that of **12** whose spectrum exhibits a lower energy MMCT band (736 nm), as well as a feature assigned to the d-d transition of the Co^{II} ion (473nm). These comparisons provide further evidence that the Co_3Fe_2 core is oxidized.

Additional Studies Aimed to Bridge Co_3Fe_2 Clusters

The addition of excess $[ClO_4]^-$ ion to a solution of **12** with a $M(cyclam)Cl_x$ complex ($[Mn(cyclam)Cl_2]Cl$, $Ni(cyclam)Cl_2$, or $[Cr(cyclam)Cl_2]Cl$ results in the instantaneous precipitation of a powder. ESI mass spectrometry on solutions of these

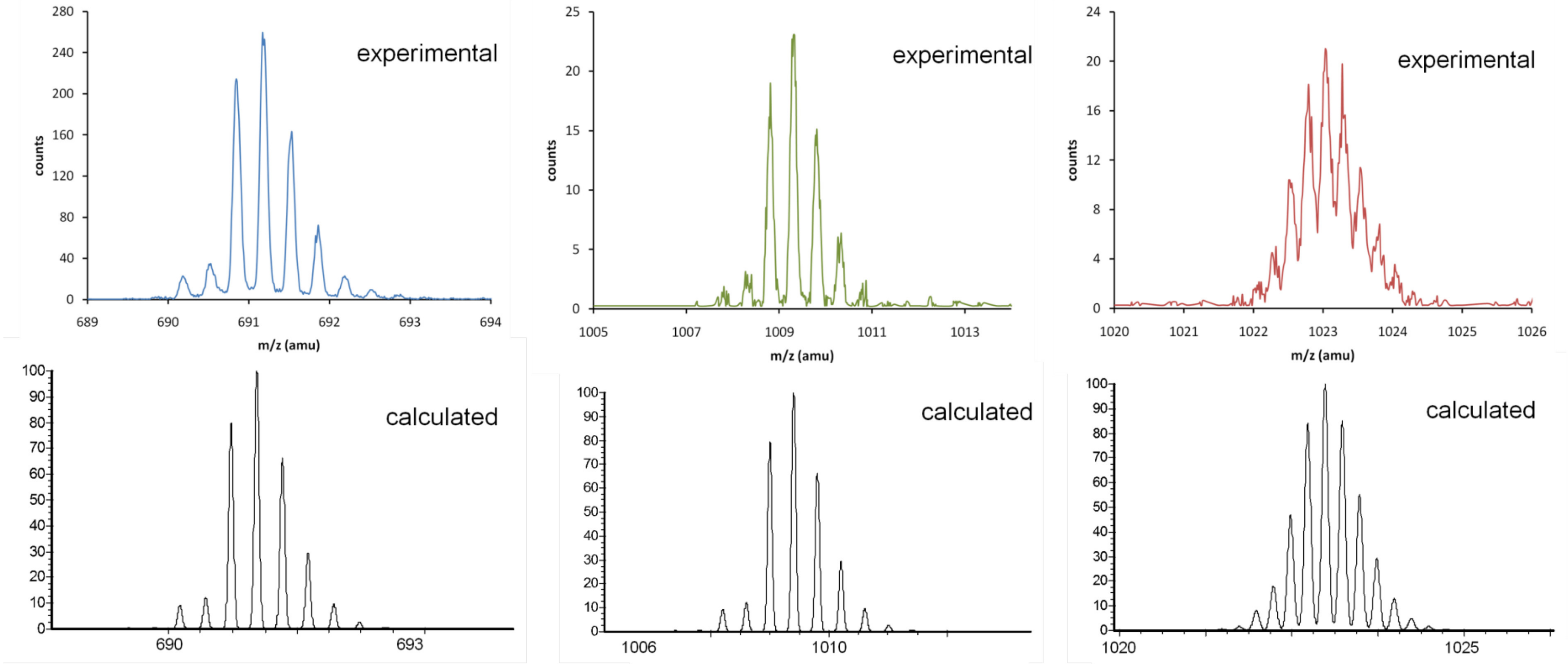

Figure 46: Experimental and calculated (plotted as relative isotopic abundance vs. mass to charge ratio, m/z) “$[Co_3Fe_2 + Mn]^{3+}$” (blue), “$[Co_3Fe_2]^{2+}$” (green), and “$[2Co_3Fe_2 + Mn]^{4+}$” (red) mass spectral peaks for **13**.

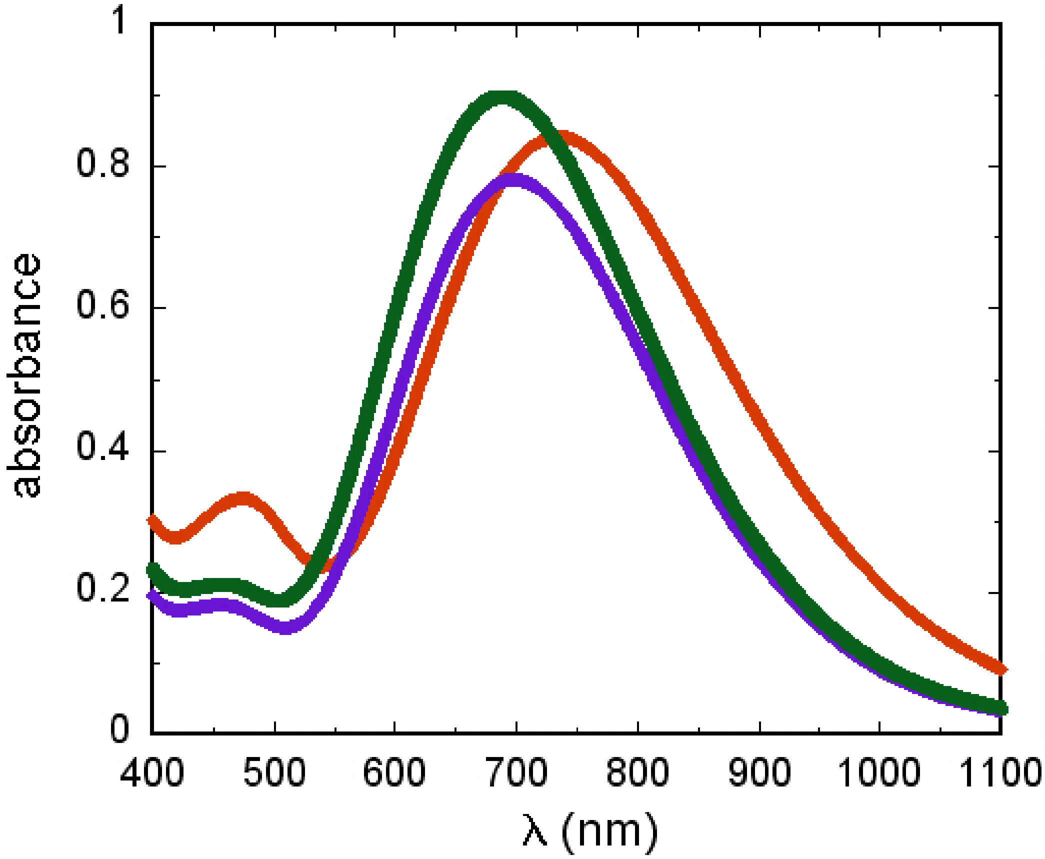

Figure 47: The $Co^{III}/Fe^{II} \rightarrow Co^{II}/Fe^{III}$ MM′CT band in the electronic absorption spectra of **12** (orange), $Na(Co_3Fe_2(ClO_4)_2$ (purple), and **13** (green).

products in 1:1 v/v acetonitrile/water yielded peaks for 1:1 combinations of the TBP and the M(cyclam) moiety – $[Co_3Fe_2 + Mn(cyclam)Cl]^{3+}$ (*m/z* = 770), $[Co_3Fe_2 + Ni(cyclam)]^{3+}$ (*m/z* = 759), and $[Co_3Fe_2 + Cr(cyclam)Cl_2]^{2+}$ (*m/z* = 1171). Although the structures of the powders were not able to be determined, the mass spectral data provide evidence that the M(cyclam) compounds do seem to be coordinating to the Co_3Fe_2 TBP. The charges of the fragments suggest that the Co_3Fe_2 cluster is oxidized <u>without</u> the concomitant reduction of the attached metal centers, but one cannot be certain of this because charges can be reduced or increased in the gas phase.

IR spectroscopy of the products reveals three similar bands for all three compounds. These features are similar to those observed for **13** as well as $Na\{[Co(tmphen)_2]_3[Fe(CN)_6]_2\}(ClO_4)_2$. The highest energy bands (2134-2140 cm^{-1}) are assigned to the Fe^{II}-CN-Co^{III}_{LS} bridging units in the TBP cluster, and the lowest energy bands (2063-2070 cm^{-1}) are attributed to the terminal cyanide ligands (Fe^{II}-CN_{term}). In the cases of the nickel and chromium reaction products, the intermediate energy bands, 2102 and 2104 cm^{-1} respectively are assigned to Fe^{II}-CN-Cr^{III} and Fe^{II}-CN—Ni^{II} bridging modes.[156] In the manganese compound, however, the appropriate Fe^{II}-CN-Mn^{III} band is expected at lower energy[20] and would likely overlap with the Fe^{II}-CN_{term} band.

Attempts to Bridge Fe_3M_2 Clusters

The addition of excess $[ClO_4]^-$ ion to a solution of **11** results in the formation of extremely thin red-orange needles/fibers. ESI mass spectrometry measured on a solution of the product in 1:5 v/v methanol/dichloromethane revealed no peaks large enough to contain a TBP cluster. The only peaks observed are assigned to $[Fe(tmphen)_3]^{2+}$ (*m/z* = 264), $[Fe(tmphen)_3]^{2+}$ (*m/z* = 382), $[Fe(tmphen)_2(ClO_4)]^+$ (*m/z* = 627), and $[Fe(tmphen)_3(ClO_4)]^+$ (*m/z* = 863). While IR stretches are observed in the cyanide region, they are quite weak and difficult to assign. The 2163 cm^{-1} band is at a higher energy than expected for either Co^{III}-C≡N-Fe^{II} or Co^{III}-C≡N-Mn^{II} bridging modes, and the 2014 cm^{-1} band is lower in energy than any reported cyanide cluster.[20] Most importantly, there is no feature corresponding to the Co^{III}-CN terminal cyanide ligands, a band which is usually the most intense stretch in the region. The magnetic susceptibility of the product revealed that there are no paramagnetic centers. Overall, the observed data, as well as the fact that similar thread-like solids are observed with **10**, suggest that the ClO_4^- anions are leading to decomposition of the cluster.

Inspired by the reactions of Co_3Fe_2 described previously, excess $NaClO_4$ was added to solutions of **10** or **11** mixed with $Mn(cyclam)Cl_3$ in an effort to precipitate a product before the TBP clusters are decomposed. Unfortunately, as in the case of the previously described reaction, ESI mass spectrometry on solutions of both products in acetonitrile showed no evidence of an intact cluster. Data for the Fe_3Fe_2 product contained only the same $Fe(tmphen)_x$ fragments as in the case of the aforementioned reaction. The Fe_3Co_2 product lead to these mass peaks as well along with peaks for the Mn complex itself, namely $[Mn(cyclam)Cl]^{2+}$ (*m/z* = 145) and $[Mn(cyclam)Cl_2]^+$ (*m/z* = 325). While the lack of intact TBP fragments does not exclude the possibility of an extended structure, experience suggests that these products are typically stable enough to be observed in the gas phase if they are present in solution. The IR stretches observed for a sample of the Fe_3Fe_2 product in the cyano stretching region are dominated by a very broad feature at 2038 cm^{-1}, which may conceal other absorptions at energies less than 2100 cm^{-1}. The only reasonable assignment for this peak is the terminal cyanide stretch for free $[Fe^{II}(CN)_6]^{4-}$.[156] A shoulder on this peak at ~2108 cm^{-1} suggests the presence of Fe^{III}-CN terminal cyanide groups, but the higher energy Fe^{III}-C≡N-Fe^{II} stretch is not observed. The two IR stretches in the Fe_3Co_2 product at 2165 and 2130 cm^{-1} can be assigned to Co^{III}-C≡N-Fe^{II} and Co^{III}-CN_{term} stretches respectively,[118] but the higher energy mode may also be from a Co^{III}-C≡N-Mn^{II} unit.[117] The magnetic susceptibilities for the two products were measured but they could not be analyzed because the structures of the powders are not known. The Fe_3Fe_2 product revealed ferromagnetic coupling and the Fe_3Co_2 product showed antiferromagnetic exchange interactions (Figure 48). This behavior has yet to be explained by any postulated structures, but the measurements do confirm that the products no longer exhibit spin crossover behavior. Overall, the data are inconclusive as to what the products are, but the evidence points to the fact that the desired extended structures are not being formed.

CONCLUSIONS

The previous work in the Dunbar group that led to two $Co_3Fe_2Mn_x$ chain compounds served as an excellent proof-of-concept for the use of the TBP clusters as building blocks. Unfortunately, there were two major problems with this these chains. First, the two chains were prepared by seemingly identical procedures and could not easily be separated. This problem was solved by the use of precursors that direct the

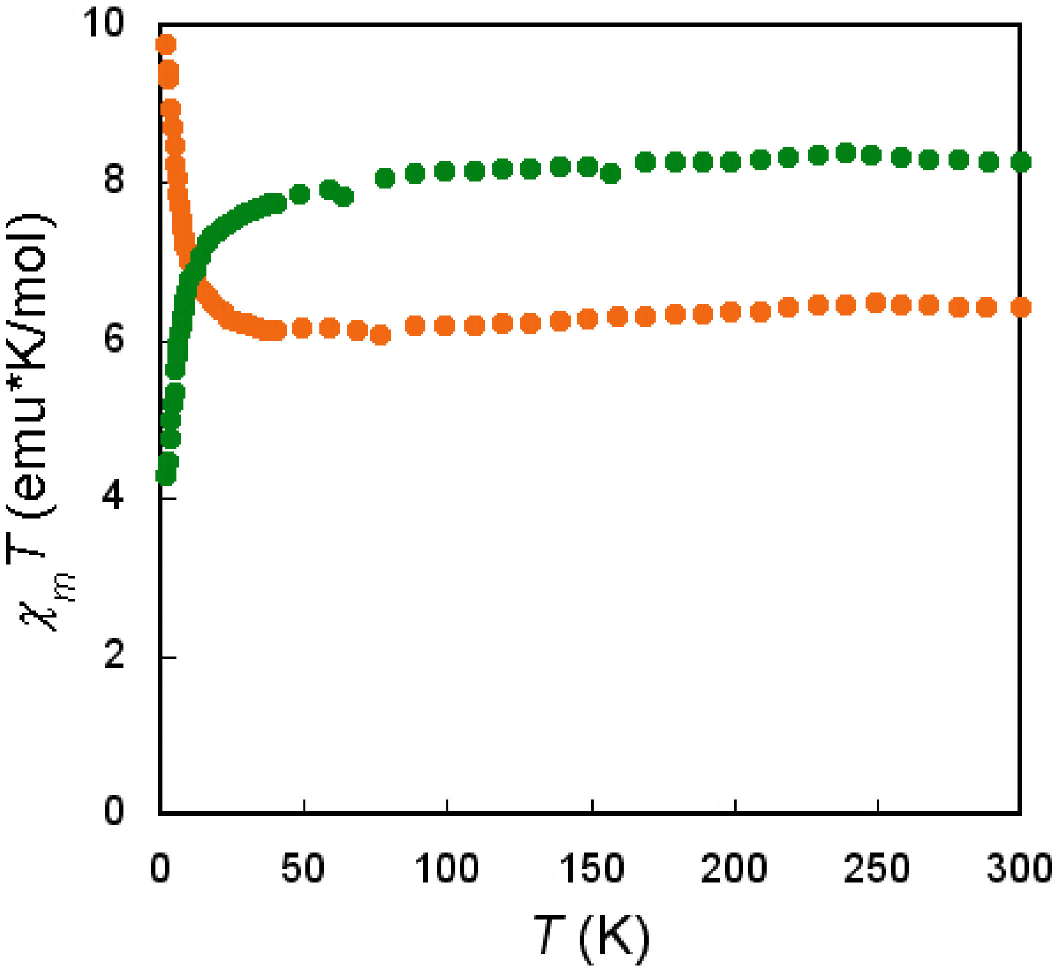

Figure 48: Thermal variation of the $\chi_m T$ product for the products from reactions of Mn(cyclam)Cl_3 with **10** (orange) and **11** (green). The data assumes a formula of [Fe_3M_2-Mn(cyclam)Cl]$ClO_4)_2 \cdot 10H_2O$.

coordination to a desired fashion. The use of [trans-Mn(acac)$_2$(H_2O)$_2$]ClO_4 to bridge Co_3Fe_2 clusters resulted in only “Type A” (or singly-bridged chains) to be produced. The second problem is the unfortunate lack of interesting properties for the chain. In both the original chains as well as the newly isolated product, the Co_3Fe_2 cluster is oxidized to a completely diamagnetic (Co^{III}/Fe^{II}) state, with no charge transfer or coupling observed. In principle, this obstacle can be overcome by the use of different TBP clusters with interesting properties. Bridging the spin crossover TBP’s, for example, may increase the cooperativity of the spin transitions or form chains whose coupling can be “turned on and off” by changes in temperature. Thus far, all attempts atachieving this goal have led to negative results. Other prospects for this building block approach are to link the Mn_3Mn_2 clusters into a single chain magnet, to bridge Co_3Fe_2 clusters without oxidation to retain the charge transfer properties, and, most importantly, to make multi-functional materials by combining the parent properties of the TBP cluster with magnetic linkers, especially those that have properties such as magnetic anisotropy.

CHAPTER V

PHOTOMAGNETIC BEHAVIOR OF TRIGONAL BIPYRAMIDAL MIXED METAL ION CLUSTERS

INTRODUCTION

The previous chapters in this dissertation and ongoing work in the Dunbar laboratories involves the properties of a family of $M_3M'_2$ TBP compounds, with a focus on DC susceptibility, magnetization, and AC susceptibility measurements. The combined data from magnetic and Mössbauer measurements provide evidence for spin crossover at the Fe^{II} sites in compounds **10** (Fe_3Fe_2) and **11** (Fe_3Co_2).[118] In these two compounds the ligand field environment of the equatorial Fe^{II} ions is similar to that of the $Fe(diimine)_2(NCS)_2$ complexes (Figure 49a). Therefore, it was postulated that a LIESST effect such as the one reported for $Fe(phen)_2(NCS)_2$[89] could be observed. Moreover, charge-transfer-induced spin transitions were found to occur for the Co_3Fe_2 cluster which is a discrete analog of the highly studied Co/Fe Prussian blue phases (Figure 49b).[98] Based on earlier studies, it appeared to be likely that a photo-induced MM′CT would be possible for the molecular analogue, compound **12** (Co_3Fe_2). The charge-transfer observed for $Rb_{0.91}Mn_{1.05}Fe(CN)_6 \cdot 0.6H_2O$[99] may also be possible for compound **1** (Mn_3Fe_2); this behavior, if observed, would be the first case of photo-induced magnetic changes for a $Mn^{II}/Fe^{III}(CN)_6$ cluster.

This chapter describes photomagnetic experiments on the four TBP compounds aimed at probing the LIESST effect and light-induced MM′CT. Also, the synthesis,

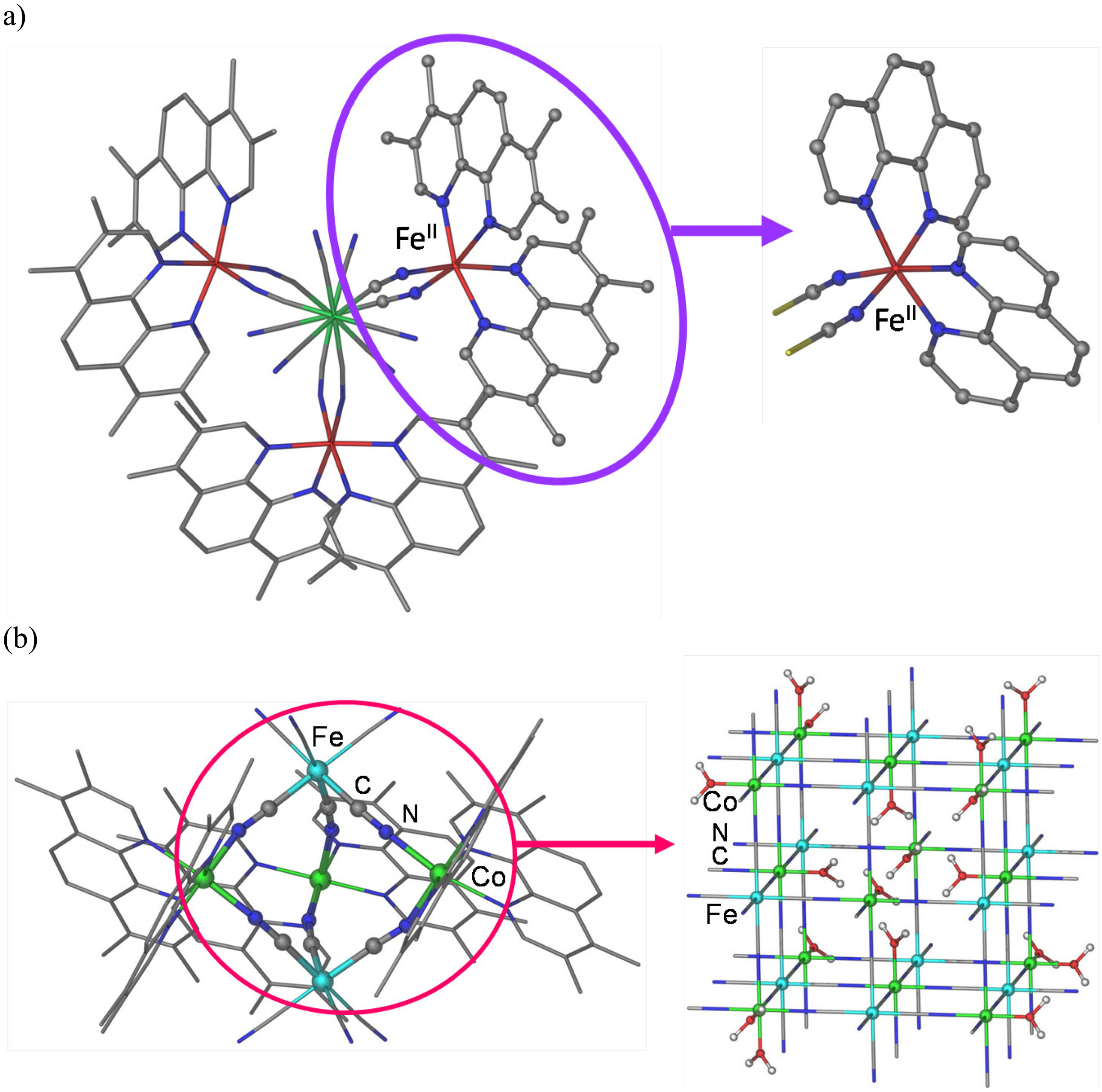

Figure 49: (a) Molecular structure (top view) of the Fe_3Co_2 TBP cluster with emphasis on the similarity of the equatorial sites to the $Fe(phen)_2(NCS)_2$ molecule. Color scheme: red, Fe; green, Co; grey, C; blue, N, yellow, S. (b) Crystal structure (side view) of the Co_3Fe_2 TBP cluster with emphasis on the similarity of the TBP core to a Co-Fe Prussian blue material. Color scheme: green, Co; light blue, Fe; grey, C; blue, N, red, O. Hydrogen atoms are omitted from the TBP cluster for the sake of clarity.

characterization, and magnetic properties are described for an anhydrous analogue of compound **12** in an attempt to understand the "SMM behavior" of the irradiated compound.

EXPERIMENTAL

Materials

The clusters in this study (**1**, **10**, **11**, and **12**) were prepared as previously reported in Chapters II-IV. Compound **1** was prepared by adding an acetonitrile solution of $(TBA)_3Fe(CN)_6$ (4mM) to an acetonitrile solution of $Mn(OAc)_2 \cdot 4H_2O$ (4mM) and tmphen (8 mM). Compounds **10** and **11** samples were prepared in a dry nitrogen atmosphere by combining an acetonitrile solution of $(TBA)_3Fe(CN)_6$ or $(18\text{-C-6-K})_3Co(CN)_6$ (4 mM) with an acetonitrile solution of $FeCl_2$ (4 mM) and tmphen (8.2 mM). Compound **12** (blue solid form) was prepared in air by slowly adding an acetonitrile solution of $(18\text{-C-6-K})_3Fe(CN)_6$ (~8.6 mM) to an acetonitrile solution of $Co(NO_3)_2 \cdot 6H_2O$ (~6.9 mM) and tmphen (~17.2 mM); the compound was kept in humid air for ~1 month before measurements to absorb water molecules. The compounds were characterized by infrared (IR) spectroscopy and magnetic susceptibility measurements to confirm their identity and purity.

Commercially available tmphen (Alfa Aesar), 18-crown-6 (Aldrich, Acros), PPNCl (Aldrich), $K_3[Fe(CN)_6$ (Fisher), cobalt powder (Alfa Aesar), and $(NO)(BF_4)$ (Strem) were used as received. Acetonitrile (EMD Chemicals) of the ACS reagent grade was dried over 3Å molecular sieves and distilled prior to use. $[Co(MeCN)_6](BF_4)_2$ was prepared by the method of Dunbar *et al.*[175] The salt $(PPN)_3[Fe(CN)_6]$ was prepared by a slight modification of the methods of Predieri *et al.*,[123] which involves washing the product with diethyl ether prior to drying *in vacuo* at 50-60°C.

Synthesis

<u>Note</u>: All reactions and manipulations were performed in a N_2-filled drybox or other dry nitrogen atmosphere.

Anhydrous $\{[Co(tmphen)_2]_3[Fe(CN)_6]\}$ (14). Samples of $[Co(MeCN)_6](BF_4)_2$ (172 mg, 0.360 mmol) and tmphen (213 mg, 0.900 mmol) were combined in 60 mL of dry acetonitrile and stirred for 30 minutes to obtain a clear, yellow-orange solution. To this solution was slowly added a solution of $(PPN)_3Fe(CN)_6$ (329 mg, 0.180 mmol) in dry acetonitrile. The mixture was left to stand undisturbed for 3 days. After this time, red crystals and microcrystals were present at the bottom of the container which were collected by filtration, washed with acetonitrile (20 mL), dried *in vacuo*, and stored in a dry atmosphere. Yield – 118 mg (~65%). IR (Nujol), $\nu(C\equiv N)$, cm^{-1}: 2143, 2113.

RESULTS AND DISCUSSION

Reflectivity and Photomagnetic Studies of Compound 11

To test the possibility for photomagnetic properties of the Fe_3Co_2 cluster, the optical properties were first investigated. The room temperature diffuse reflectance spectrum contains two absorbance bands located at 880 and 500 nm (Figure 50a). The optical reflectivity spectra were measured in order to determine the response of the sample to temperature changes and white light irradiation. As a sample was cooled under continuous low-power white light irradiation (0.05 mW/cm^2), the spectra revealed two broad bands as already observed in the absorbance spectrum – one centered at 540 nm that exhibited negligible variation with temperature and a second one at 880 nm that varied greatly with temperature (Figure 50b). An alternative way to visualize the thermal changes in the reflectivity spectra is presented in Figure 51a (cooling curve) by the thermal dependence of the absolute reflectivity at 880 nm (noted R_{880} hereafter). There is an increase in R_{880} (*i.e.* decrease in absorbance) from 295 K to 100 K. This change in reflectivity with temperature is reminiscent of the gradual spin crossover that is known to occur for this compound, as the 880 nm band corresponds to a d-d transition ($^5T_2 \rightarrow {}^5E$) in the high-spin state of the Fe^{II} ion which is similar to the 840 nm absorption reported for $Fe(phen)_2(SCN)_2$.[176] When the sample is further cooled to 10 K, there is a slight decrease in R_{880} that suggests a LIESST effect. To further study this photo-excitation, reflectivity spectra were measured on a sample that had been cooled to 5 K in the absence of light and then after being irradiated with a high power light (0.7 mW/cm^2) for 90 minutes (Figure 51b). The R_{880} response decreased continuously during irradiation (*i.e.* the absorbance increased) such that the spectrum was similar to the room temperature spectrum suggesting that the photo-conversion is nearly quantitative at the surface. (Note: It is theoretically possible that the incident light for the reflectivity measurement could cause some photo-excitation of the sample at low temperatures. Reason would suggest that, if this were this case, the relaxed sample would have a lower reflectivity than an externally-irradiated sample. In contrast, since the reflectivity of the sample actually decreases *after* the external radiation, it seems unlikely that excitation

(a)

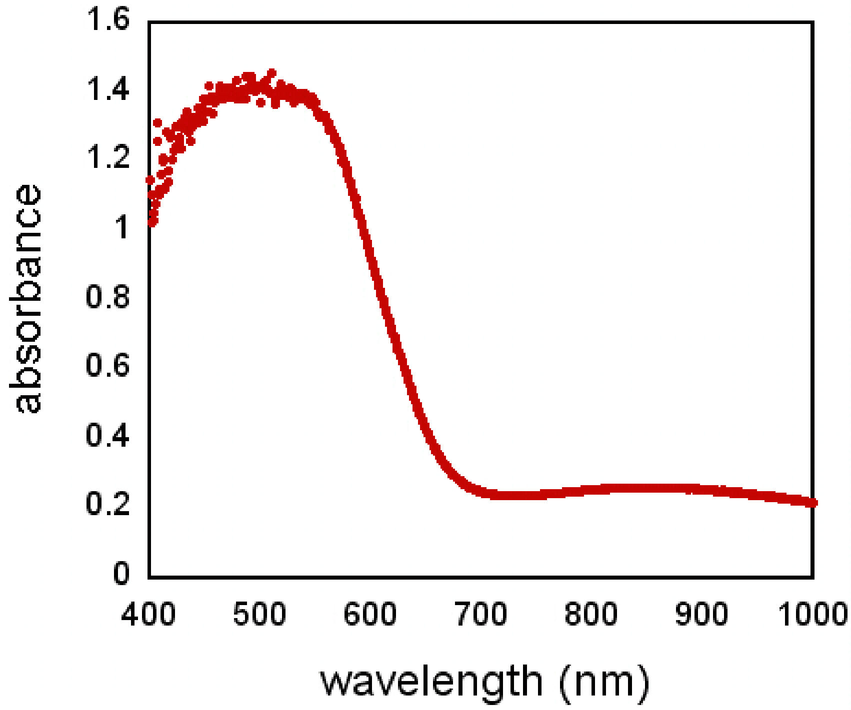

(b)

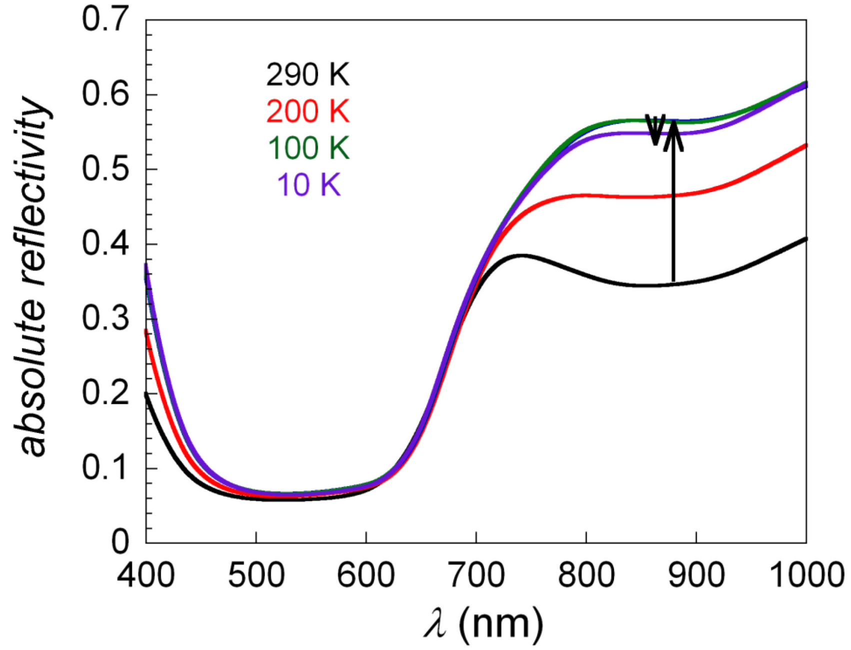

Figure 50: (a) Room temperature diffuse reflectance spectrum of **11**. (b) Variable temperature optical reflectivity spectra of **11** under continuous white light irradiation (0.05 mW/cm^2; black, 290 K; red, 200 K; green, 100 K; purple, 10 K).

(a)

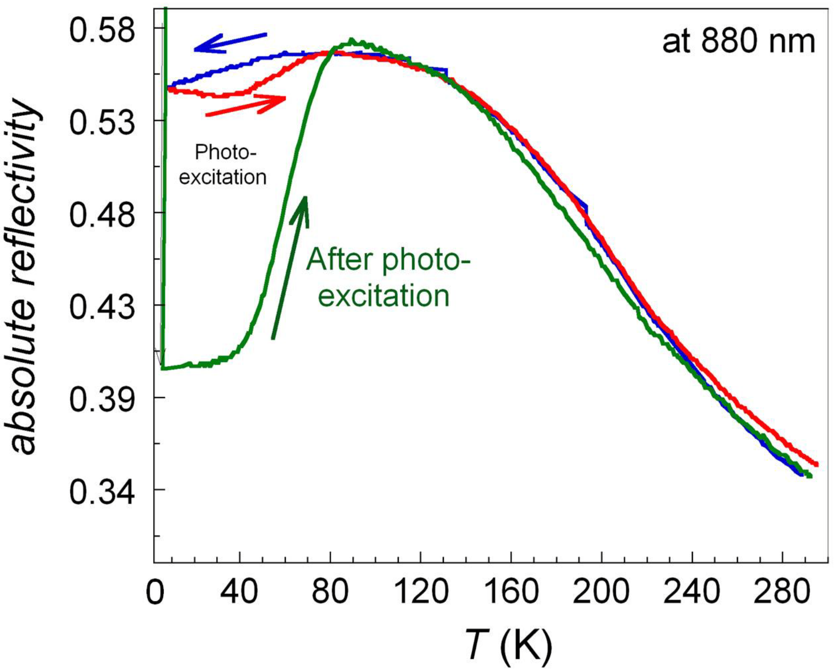

(b)

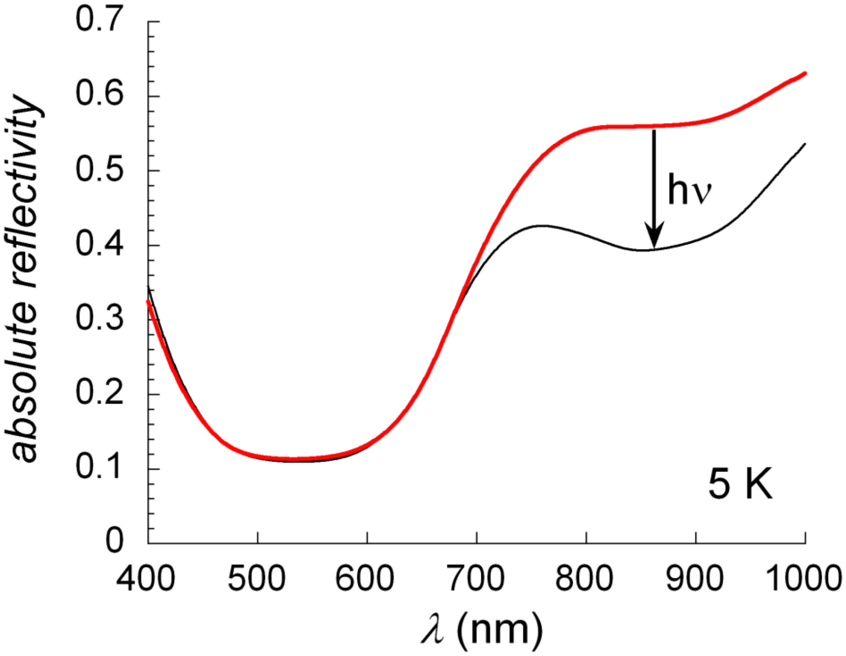

Figure 51: (a) Absolute reflectivity at 880 nm (with 0.05 mW/cm^2 white light irradiation) with cooling (blue), heating (red), and heating after 90 minutes of white light irradiation at 5 K (0.7 mW/cm^2 – green). (b) Optical reflectivity spectra of Fe_3Co_2 at 5 K before (red) and after (black) irradiation with white light (0.7 mW/cm^2).

from the incident light occurs to any significant extent.) The 880 nm absorbance corresponds to the formation of the high-spin $\mathrm{Fe^{II}}$ state and increases with both irradiation and increasing temperature. Finally, when the temperature dependence of the photo-induced reflectivity of 880 nm was measured (Figure 51a), three optical changes are apparent: a stable reflectivity signal up to 30 K (the photogenerated $\mathrm{Fe^{II}}_{\mathrm{HS}}$ is trapped) at low temperatures, a thermal relaxation ($\mathrm{Fe^{II}}_{\mathrm{HS}} \rightarrow \mathrm{Fe^{II}}_{\mathrm{LS}}$) from 30-80 K, and the known thermally-induced spin-crossover ($\mathrm{Fe^{II}}_{\mathrm{LS}} \rightarrow \mathrm{Fe^{II}}_{\mathrm{HS}}$) which occurs above 100 K.

Magnetic/photomagnetic measurements of $\mathrm{Fe_3Co_2}$ were performed to probe the possibility of recovering the high-spin $\mathrm{Fe^{II}}$ centers at low temperature using light irradiation. These measurements involved cooling the sample in the absence of light (“dark” measurements) followed by irradiation of the sample with white light for several hours at 5 K, and then re-heating of the sample without further irradiation (“irradiated” measurements). The heating rate is highly influential to the relaxation of the photo-excited state. A faster heating rate can artificially raise the maximum temperature at which the photo-excited state is observed if the sample does not heat as quickly as the surroundings. At the same time, a faster rate can also “stretch” the relaxation of this state over a larger temperature range. To minimize both of these effects, a slow sweep rate was used in this and all photomagnetic experiments.

White light irradiation (3 $\mathrm{mW/cm^2}$) at 5 K reveals significant photomagnetic activity in compound **11**, an increase in $\chi_m T$ from 0.8 emu·K/mol to 2.5 emu·K/mol over 16 hours (Figure 52a inset). Upon heating the sample from 2 K to 25 K, the $\chi_m T$ product increases from 1.09 to 2.9 emu·K/mol. This thermal behavior is likely the signature of

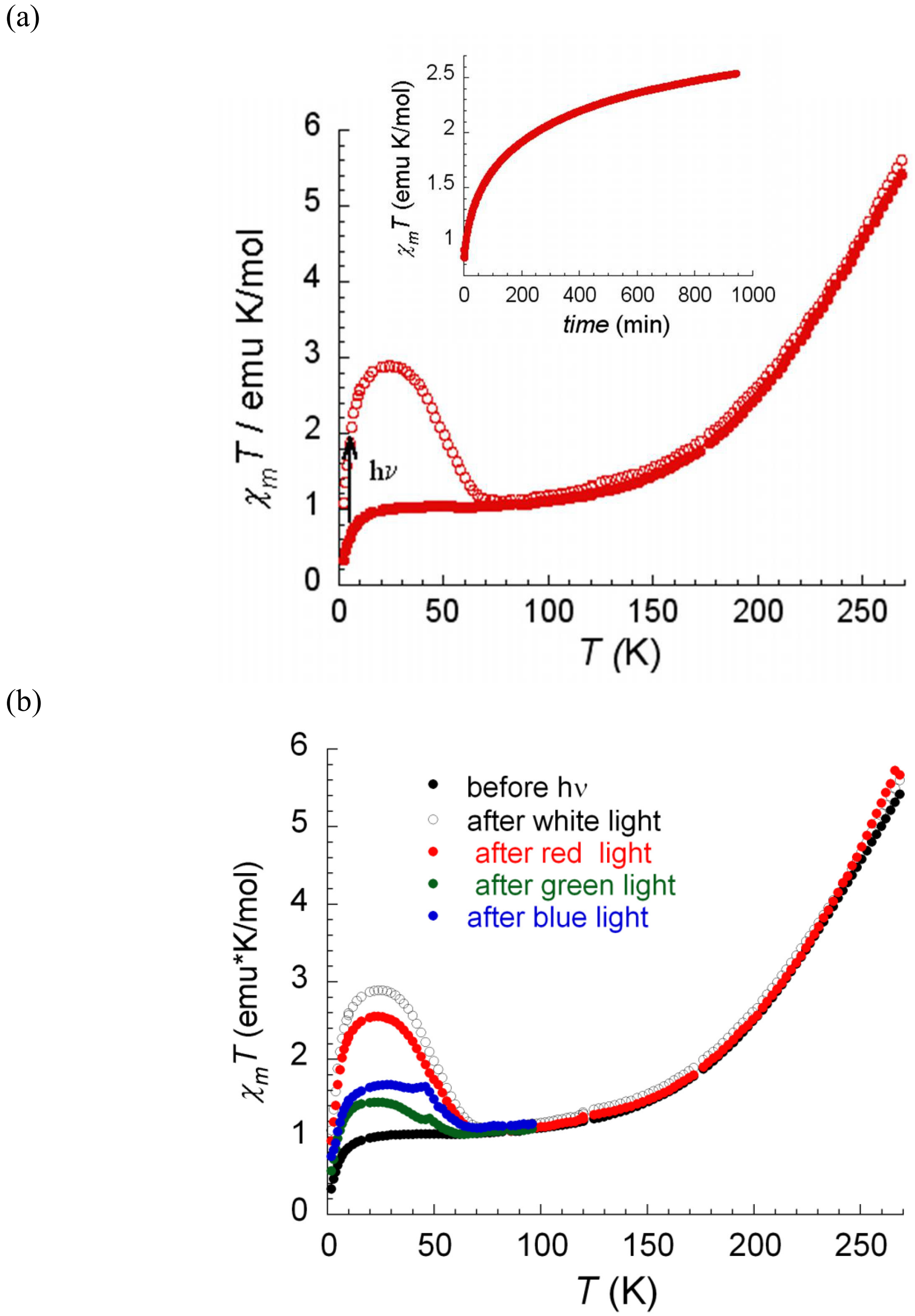

Figure 52: (a) Temperature dependence of $\chi_m T$ of Fe_3Co_2 at 1 T at a sweep rate of 0.5 K/min, before (filled) and after (open) irradiation with white light (3 mW/cm^2). Inset: time dependence of $\chi_m T$ under white light irradiation. (b) Temperature dependence of $\chi_m T$ of Fe_3Co_2 at 1 T at a sweep rate of 0.5 K/min, before (black) and after irradiation with white light (10 mW/cm^2; white) and several different wavelengths (red, 647 nm, 3 mW/cm^2; green 530 nm, 3 mW/cm^2; blue, 488 nm, 3 mW/cm^2).

the magnetic anisotropy of the HS Fe^{II} metal ions as observed in related Fe^{II} spin crossover systems,[177] though it could be related to weak antiferromagnetic interactions between HS Fe^{II} sites through diamagnetic Co^{III} centers within the TBP cluster. By increasing the temperature at a sweep rate of ~ 0.5 K/min, an abrupt decrease in the $\chi_m T$ product begins at 35 K, with a complete relaxation of the photo-induced metastable high-spin Fe^{II} centers by ~69 K. Thus, above ~70K, the two measurements are nearly identical (Figure 52a). As already noted in Chapter III, the dark measurements correspond to an incomplete gradual conversion between 140 K and 300 K which is attributed to a spin crossover of the Fe^{II} ion from LS (S = 0) to HS (S = 2) in agreement with the results of Mössbauer spectroscopy. Below 140 K, there is a residual $\chi_m T$ product due to remaining Fe$^{II}_{HS}$ sites as already reported in previous measurements. When specific energies of light (488 nm, 530 nm, and 647 nm; all 3 mW/cm^2) were used to irradiate the cluster, all wavelengths tested were found to excite the sample, with red light being the most efficient (Figure 52b). No wavelength, however, was found to relax the cluster. Although the reflectivity measurements indicated that the photo-excitation is nearly quantitative at the surface of the material, the susceptibility measurements suggested a much less efficient conversion, with a maximum photomagnetic susceptibility increase of 1.8 emu·K/mol (Figure 52a), corresponding to only 20% of Fe^{II} centers converted from low spin to high spin with the irradiation (36% of the amount of high spin Fe^{II} ions at room temperature in the compound, two centers per cluster). This low photomagnetic conversion, even with white light, is likely a combination of several factors. Firstly, the dark red color of the sample can significantly hinder light penetration, allowing for only the excitation of a small portion of the sample near the irradiated surface; the reflectivity measurements, which measure only surface properties, suggest that the excitation is efficient at the surface, but the photoactivity of the bulk sample can be significantly different. Secondly, previous work with the cluster reveals that the three Fe^{II} centers do not exhibit equivalent spin crossover behavior. Hence, the observed LIESST effect (with the light sources used) may involve only one or two of the three Fe^{II} centers. A third factor is the relaxation of the photo-induced high spin Fe^{II} centers over time in the dark.

Reflectivity and Photomagnetic Studies of Compound 10

As in the case of the Fe_3Co_2 TBP cluster, the photo-activity of the Fe_3Fe_2 cluster was first tested using optical techniques. First, the room temperature diffuse reflectance showed two absorbance bands (Figure 53a), one in the Near-Infrared Region (NIR) with a maximum above 1000 nm and the second one around 500 nm. It is pointed out that the two compounds present both two absorbance bands in the same wavelengths range, but not with the same intensity for the NIR band that is much bigger in more intense for the Fe_3Fe_2 compound which may be due to a charge transfer between Fe^{II} and Fe^{III}. Then, the optical reflectivity spectra were measured at various temperatures with concomitant white light irradiation. Spectra measured at different temperatures under continuous white irradiation (0.05 mW/cm^2) revealed two intense temperature independent bands, one at 520 nm which is analogous to the 540 nm peak observed for the Fe_3Co_2 compounds and one above 1000 nm (Figure 53b). Overall, no significant differences were observed with temperature changes or irradiation. The spectra did not show

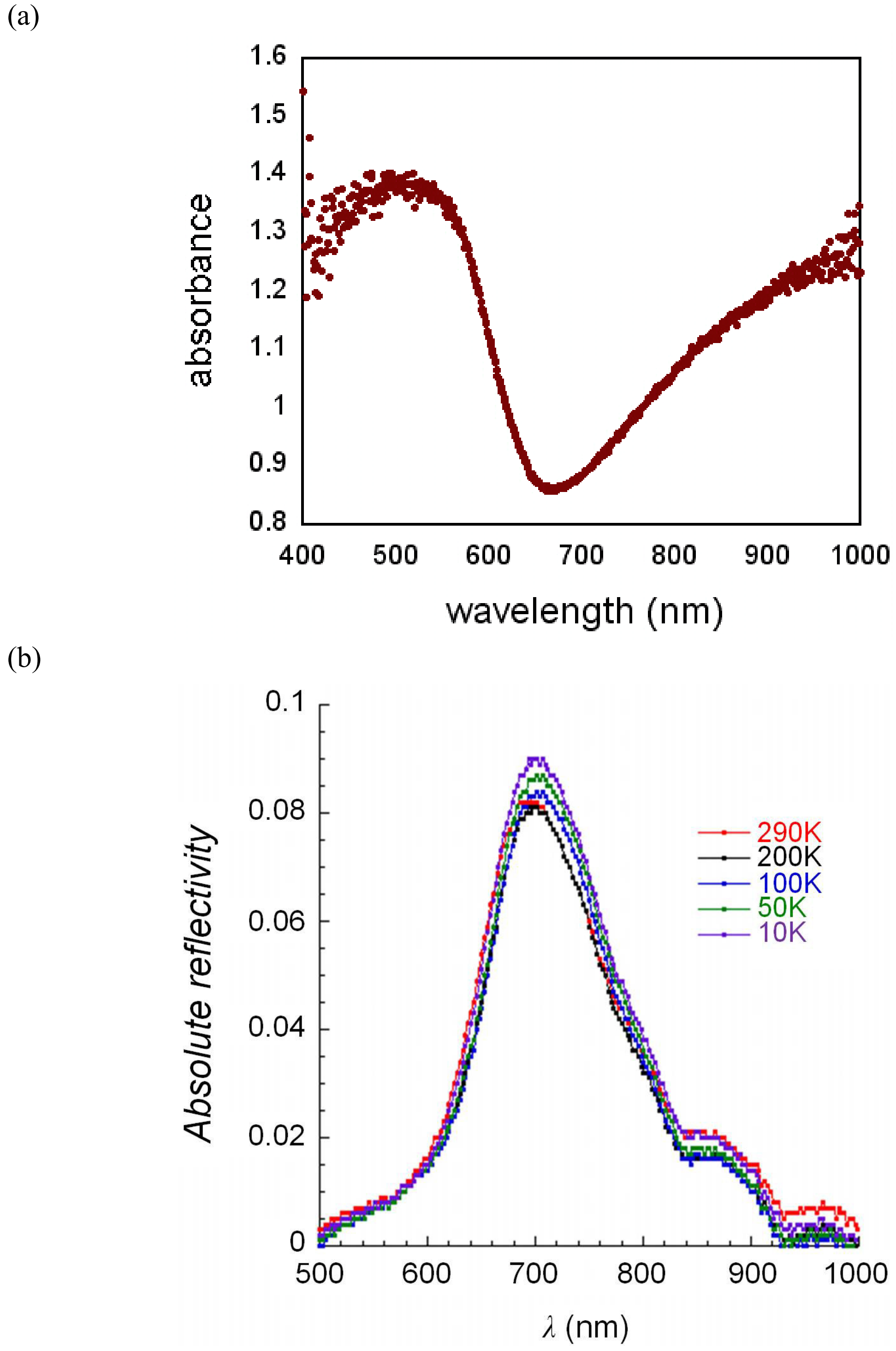

Figure 53: (a) Room temperature diffuse reflectance spectrum of **10**. (b) Variable temperature optical reflectivity spectra of **10** under continuous white light irradiation (0.05 mW/cm^2; red, 290 K; black, 200 K; blue, 100 K; green, 50K; purple, 10 K).

evidence for photo-induced behavior, but, surprisingly, they also did not indicate the thermal spin conversion which is known to occur and was observed in the dark magnetic susceptibility measurements. For this reason, the photomagnetic properties of Fe_3Fe_2 were tested by the same methods described for Fe_3Co_2. As in the case of Fe_3Co_2, the dark measurements were consistent between samples; and the photo-excited state was generated at 10 K when the sample is irradiated with white light. Because of the similarity of the compounds, photomagnetic results were expected to be analogous to the properties noted for Fe_3Co_2, but the average response for Fe_3Fe_2 was surprisingly small (Figure 54). The maximum photomagnetic response observed, 0.15 emu·K/mol, corresponds to only 2% of the Fe^{II} centers being converted from low spin to high spin configurations. This result suggests that the photo-conversion occurs only at the surface of the compound and does not propagate in the bulk of the sample.

Although factors such as sample amount and irradiation conditions are generally plausible explanations for differences in photomagnetic behavior, these issues are not the relevant ones in the comparison of the results for Fe_3Fe_2 and Fe_3Co_2 because they were intentionally kept as consistent as possible between the two compounds. Other factors, however, such as sample color (intensity of color), crystal size, and solvent content, are likely to be the reasons for the disparity in results between the two compounds. Although these factors may be considered to be minor in many cases, the spin conversions studied here occur between two states of very similar energy; hence, such factors can easily have significant effects. Also, crystal size and solvent content have already been shown to play important roles in the thermal spin conversions of our TBP compounds.[116,118] One

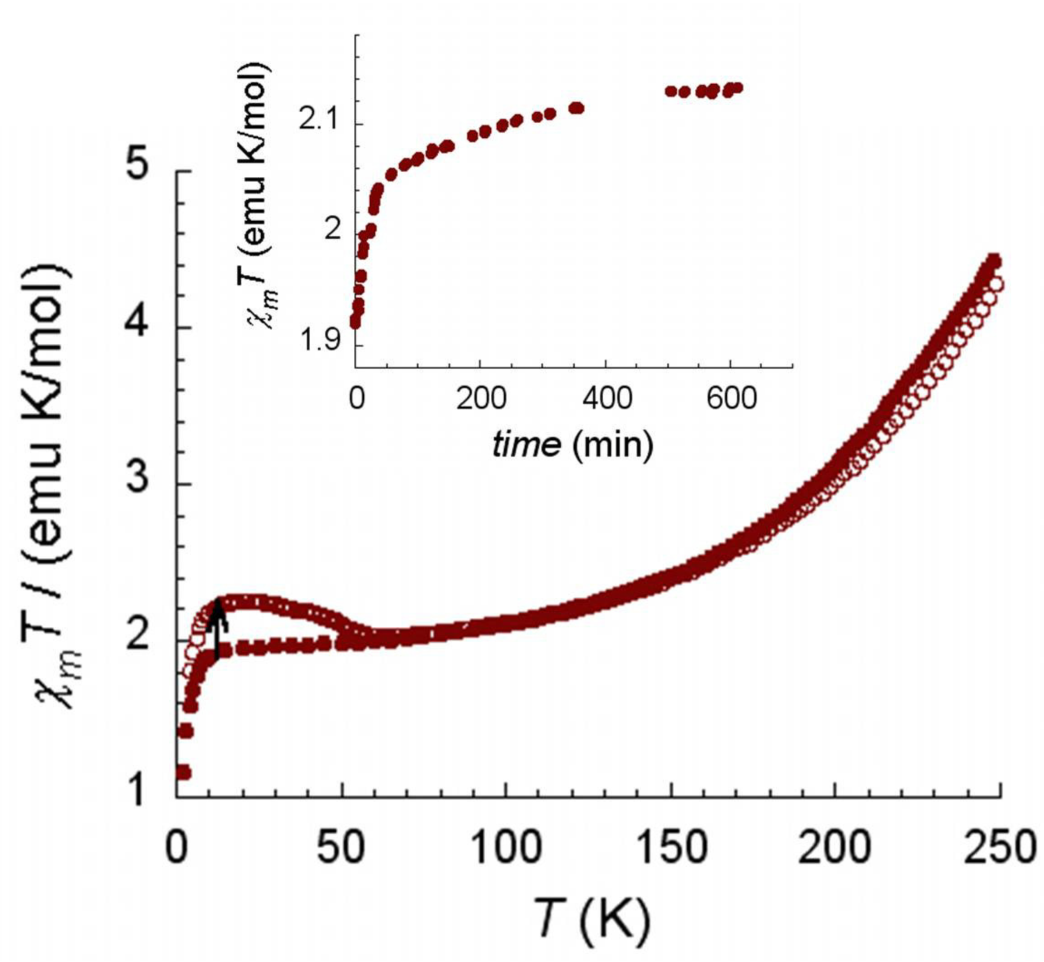

Figure 54: Temperature dependence of the $\chi_m T$ product of Fe_3Fe_2 at 0.1 T at a sweep rate of 0.5 K/min, before and after irradiation with white light (3 mW/cm^2). Inset: time dependence of $\chi_m T$ at 30 K of Fe_3Fe_2 upon irradiation with white light.

other possible explanation may be the darker color of the Fe_3Fe_2 compound compared to the Fe_3Co_2 compound that prevents the light penetration in the solid in the former compound. A definitive analysis of which factors are dominant is not possible, however, given the subtlety of the observed effects.

Reflectivity and Photomagnetic Studies of Compound 1

A previous analysis of the magnetic properties of the Mn_3Fe_2 compound revealed only antiferromagnetic coupling as evidenced by the decrease in $\chi_m T$ versus T at low temperatures.[117] The phenomenon of charge transfer,[99] as it exists in the Prussian blue analogue, however, was never considered as a possibility. As with the other compounds, the photo-activity of the Mn_3Fe_2 cluster was tested using optical reflectivity spectra at various temperatures with white light irradiation. The spectra show a gradual change with temperature between 500 and 950 nm (Figure 55a), but there is no reversal at 10 K as observed with the other TBP's. Also, the absolute reflectivity at 800 nm (Figure 55b) presents exactly same thermal dependence in cooling and heating modes. This monotonic variation suggests that the optical properties of Mn_3Fe_2 are only dependent on temperature, but not affected by light.

The photomagnetic properties of Mn_3Fe_2 were determined by magnetic susceptibility measurements. Initial measurements on the cluster revealed a very small increase of $\chi_m T$ upon irradiation with white light over time (Figure 56a). Further measurements, however, revealed only a very small increase with irradiation, only below ~15 K (Figure 56b). The response was not typical of the photomagnetism observed for the other clusters, and the $\chi_m T$ increase is likely not due to a photo-induced charge

(a)

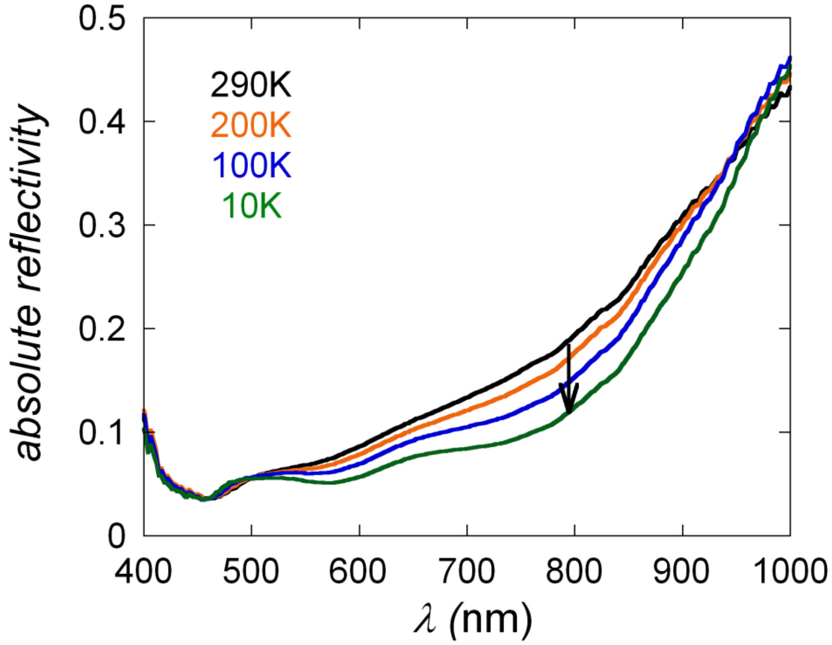

(b)

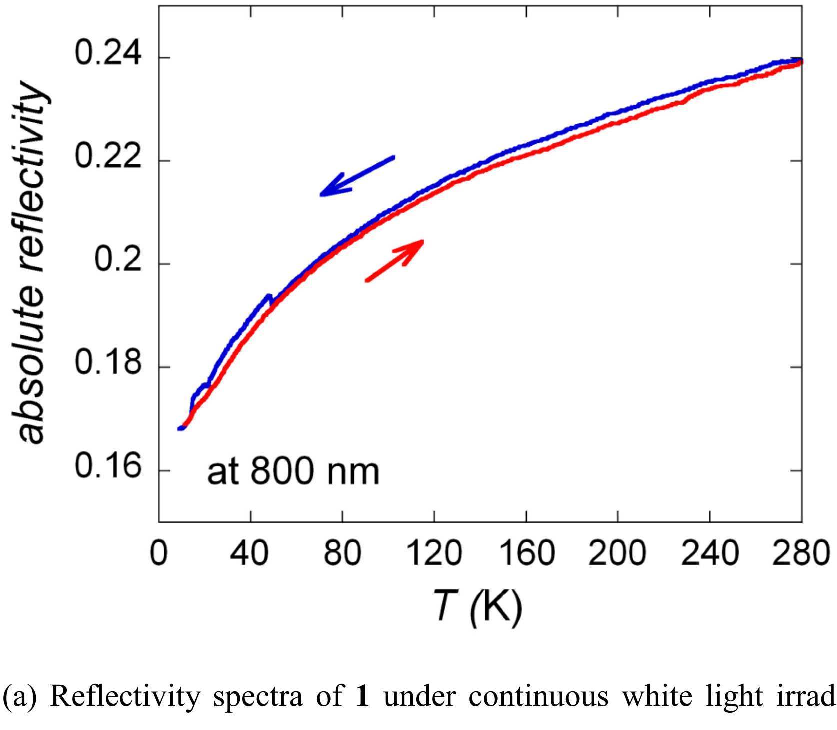

Figure 55: (a) Reflectivity spectra of **1** under continuous white light irradiation (0.05 mW/cm^2, black, 290K; red, 200K; green, 100K; purple, 10K). (b) Absolute reflectivity at 800 nm (with 0.05 mW/cm^2 white light irradiation) with cooling (blue) heating (red).

(a)

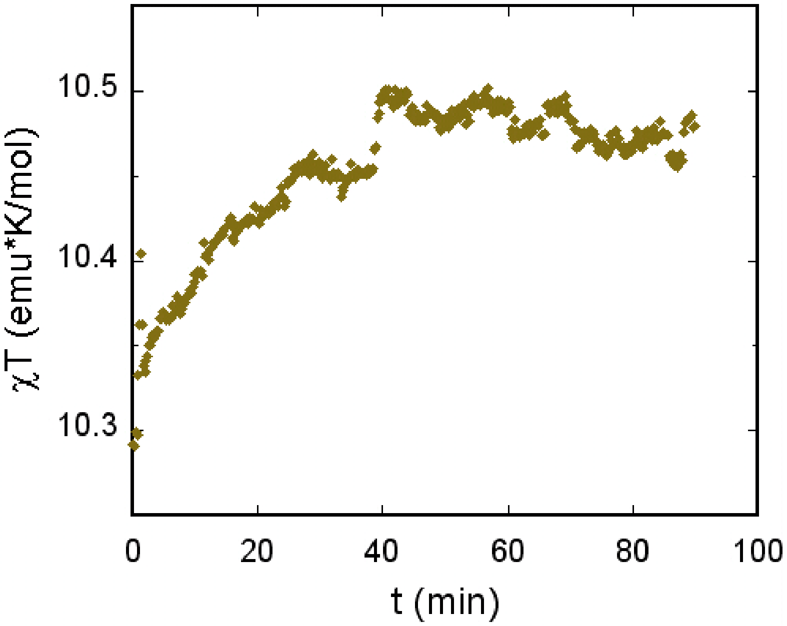

(b)

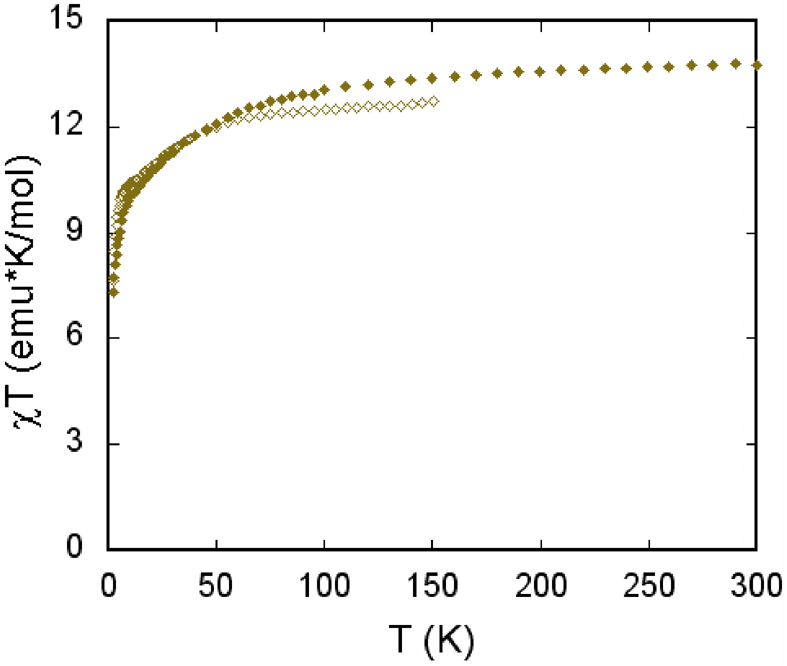

Figure 56: (a) Time dependence of the $\chi_m T$ product at 10 K of **1** upon irradiation with white light. (b) Temperature dependence of the $\chi_m T$ product of **1** at 0.5 T at a sweep rate of 1 K/min, before and after irradiation with white light (40 mW/cm^2).

transfer event. A more likely explanation for the very small increase is the slow condensation of oxygen from a small air leak in the photomagnetic attachment. Another is that the change in $\chi_m T$ is a result of a slight change in the shape, or flattening, of the sample that can occur over time from the pressure of the sample holder. (Similar responses to oxygen and/or sample shape were observed in many measurements of other TBP clusters measured at TAMU. Since the photomagnetic response was dominant in these cases, however, the response was observed merely as a small bump on the irradiated susceptibility plots at low temperatures.) Overall, based on these optical and magnetic measurements, it seems clear that there is no photo-induced charge transfer in the molecule. The most likely reason for the lack of charge transfer in the cluster, as opposed to the PB analogue, is the ligand environment of the Mn atoms. In the PB phase, the electron transfer that occurs with cooling induces a Jahn-Teller distortion to stabilize the Mn^{III} ions. In the Mn_3Fe_2 cluster, the two *cis*-chelating tmphen ligands and the rigidity of the cluster is expected to render this distortion very difficult, and therefore, the charge transfer, and any photomagnetic behavior associated with it, will be suppressed. Variable temperature Mössbauer measurements would confirm the lack of a charge transfer event and are being considered for future work.

Reflectivity and Photomagnetic Studies of Compound 12

As with the other compounds, the photo-activity of the Co_3Fe_2 cluster was tested by optical techniques. The room temperature diffuse reflectance spectrum shows one broad absorbance band around 800 nm (Figure 57a). This band falls within the expected range for metal-metal charge-transfer (MM′CT) bands and is therefore assigned to the excitation of Co^{III}-Fe^{II} pairs to Co^{II}-Fe^{III}; Co^{II} d-d transitions are also expected in this range, but the intensity of the observed band suggests that the MMCT is dominant. [103] Then, the optical reflectivity spectra were collected at various temperatures and under white light irradiation. While cooling the compound under continuous weak white light irradiation (0.05 mW/cm^2), the spectra revealed a very broad band centered at ~800 nm, the intensity of which varies significantly with temperature (Figure 57b). The reflectivity in this region (as shown for R_{800}) decreases from 290 K to 200 K and increases from 100 K to 10 K. The decrease of R_{800} (*i.e.* an increase of absorbance) between 290 K and 200 K is reminiscent of the gradual charge transfer between Co^{II} and Fe^{III} that was documented previously for this compound.[116] When the sample was further cooled to 10 K, an increase in R_{800} occurred that suggests a reverse charge-transfer from Fe^{II} to Co^{III} occurs. The similarity of the 290 K and 10 K spectra indicates that there is a photo-induced charge transfer at low temperatures which yields the same product as the thermal transition (Figure 57b); the similarity also suggests that, unlike the LIESST effect observed for Fe_3Co_2, the charge transfer occurs quite efficiently with very weak irradiation at the surface of the material. To confirm the photo-excitation process, spectra were measured for the sample at 5 K after being cooled in the absence of light and then again after 40 minutes of irradiation (Figure 58a). As expected, the dark spectrum at 10 K is very similar to the 200 and 100 K spectra, and there is a significant increase in the reflectivity after the irradiation. The temperature dependence of R_{800} suggests that a photo-induced charge transfer ($Co^{III}/Fe^{II} \rightarrow Co^{II}/Fe^{III}$) is possible at low temperatures; following this charge transfer, the excited state will thermally relax

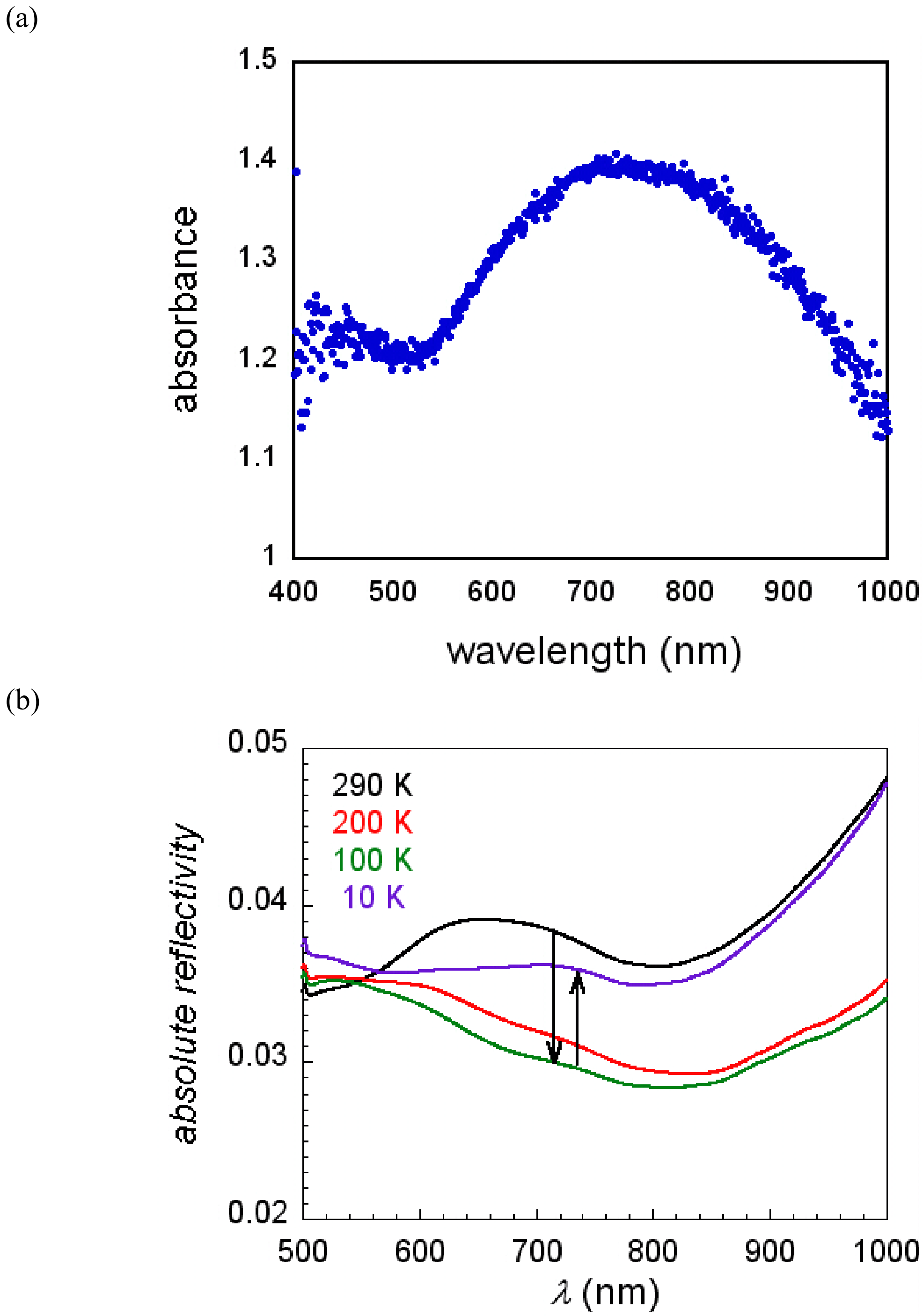

Figure 57: (a) Room temperature diffuse reflectance spectrum of **12**. (b) Variable temperature optical reflectivity spectra of **12** under continuous white light irradiation (0.05 mW/cm^2; black, 290 K; red, 200 K; green, 100 K; purple, 10 K).

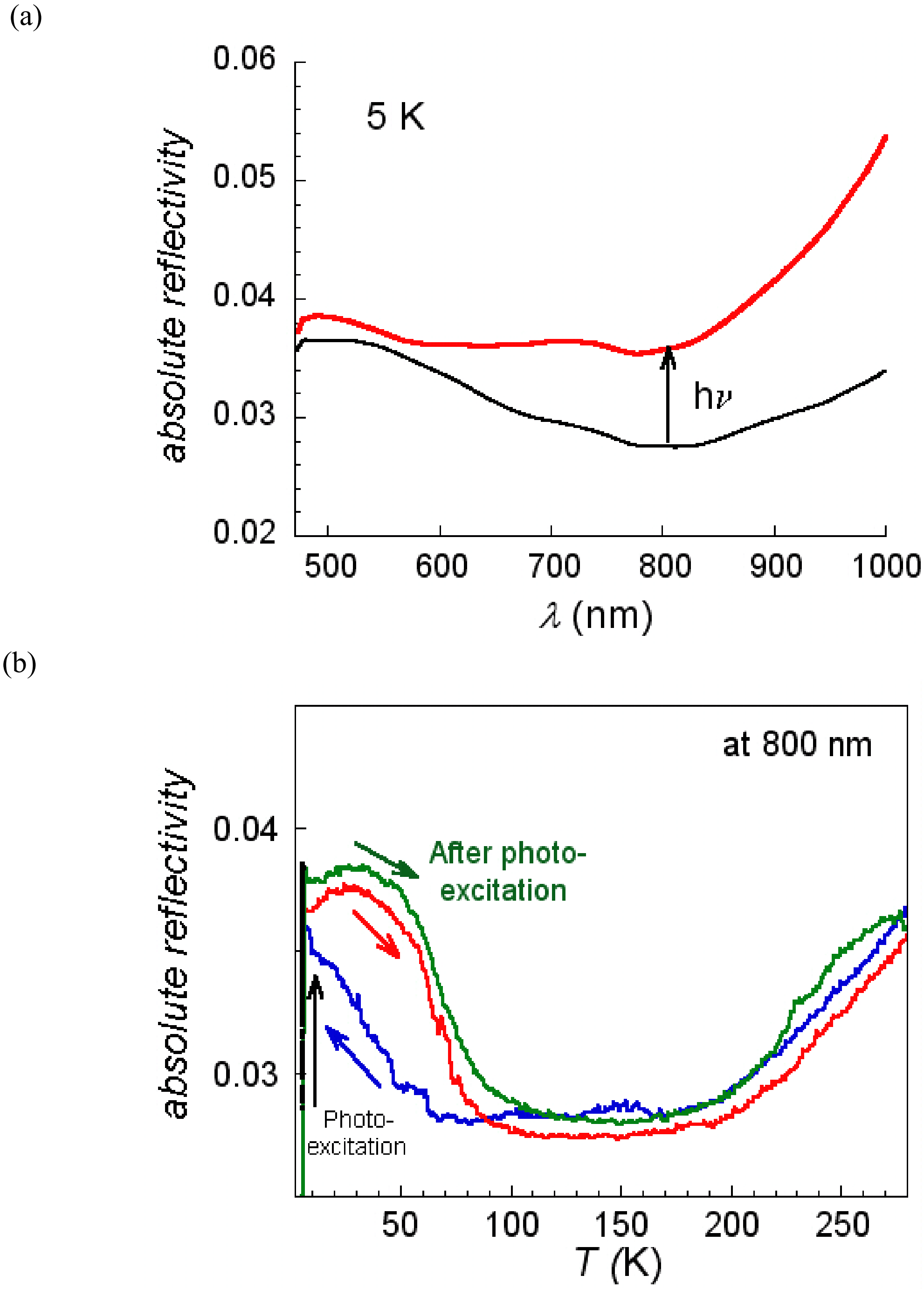

Figure 58: (a) Optical reflectivity spectra of **12** at 5 K before (black) and after (red) irradiation with white light (0.05 mW/cm^2). (b) Absolute reflectivity at 800 nm (with 0.05 mW/cm^2 white light irradiation) with cooling (blue), heating (red), and heating after 90 minutes of white light irradiation at 10 K (0.05 mW/cm^2 – green).

(Co^{II}/Fe^{III} → Co^{III}/Fe^{II}) from 50-100 K, and the previously observed thermal-induced charge transfer (Co^{III}/Fe^{II} → Co^{II}/Fe^{III}) will occur above 200 K (Figure 58b). The similarity of the spectra observed with only a short period of irradiation and with 90 minutes of irradiation indicates that the photo-induced charge transfer at the surface occurs very quickly.

The photomagnetic properties of Co_3Fe_2 were determined by magnetic susceptibility measurements, with and without irradiation. Initial experiments gave inconsistent results for the dark measurements between samples. This behavior was attributed to the influence of interstitial water molecules on the magnetic properties of **12**, similar to that previously observed for the compound by Curtis Berlinguette.[116] Variations in the photomagnetic responses were also observed, but there is currently no explanation for these differences. In order to acquire consistent measurements, it would be necessary to pre-hydrate the compound to obtain a stable compound.

It was also necessary to determine if compound **12**, like the Co-Fe Prussian blue compounds, could be excited by certain wavelengths and relaxed by others. Susceptibility over time measurements were performed on a sample (containing 24 water molecules per cluster) at various wavelengths (365-950 nm). It was observed that all tested energies of photons (Figure 59) are able to photo-induce paramagnetic Co^{II}/Fe^{III} units. Because of the different intensities of the sources, the efficiencies in photogenerating Co^{II}/Fe^{III} pairs could not be accurately compared, but it is clear that none of these wavelengths will relax these paramagnetic units at 30 K.

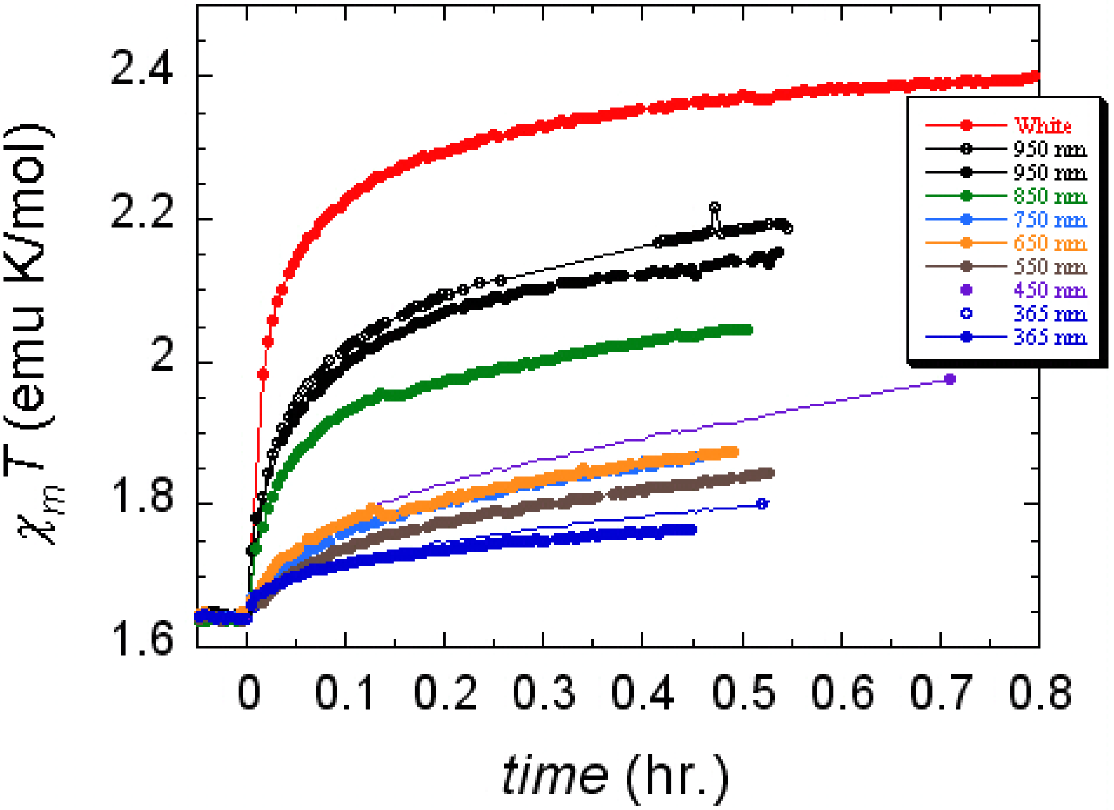

Figure 59: Time dependence of $\chi_m T$ of **12** upon irradiation (30 K) of white light (red, 5 mW/cm^2) compared with various wavelengths with filters (750 nm, 0.2 mW/cm^2, light aqua; 650 nm, 0.9 mW/cm^2, orange; 550 nm, 0.4 mW/cm^2, brown) and diode lights (950 nm, 1.25 mW/cm^2, open black; 950 nm, 1 mW/cm^2, black; 850 nm, 1 mW/cm^2, green; 365 nm, 0.15 mW/cm^2, open blue; 365 nm, 0.07 mW/cm^2, blue).

In another measurement, a stable compound (as determined by magnetic susceptibility) was obtained after exposition to humid air for several weeks (containing 23 water molecules per cluster). Irradiation of this sample at 10 K with white light (~3 mW/cm^2) indicates that, initially, the magnetic susceptibility increases quickly and begins to saturate only after 30 minutes (Figure 60 inset). Magnetic susceptibility measurements were obtained by cooling the sample in the absence of light, irradiating the sample with the white light for one hour, and then re-heating the sample without further irradiation (Figure 60). The dark measurements are in agreement with a $Co^{III}_2Co^{II}Fe^{II}_2$ configuration, with the magnetic response of the Co^{II} site being unaffected by the charge transfer process. Under a heating rate of 0.5 K/min, the photoexcited state appears to be stable up to ~ 50 K, after which temperature the susceptibility decreases until it is equivalent to the dark measurement at 75 K. The 2.94 emu·K/mol susceptibility increase observed corresponds to approximately 36% of the Co^{III}/Fe^{II} excited in Co^{II}/Fe^{III} pairs, or about a third of the clusters being converted from the $Co^{III}_2Co^{II}Fe^{II}_2$ in $Co^{II}_2Fe^{III}_2$ configurations. (The increase could also correspond to 72% of the clusters converting from $Co^{III}_2Co^{II}Fe^{II}_2$ to $Co^{III}Co^{II}_2Fe^{II}Fe^{III}$.) One possible explanation for the low efficiency of the conversion is simultaneous excitation and relaxation with the white light irradiation, similar to the behavior expected for white light irradiation of the Co-Fe Prussian blue phase,[98] which is excited with red light and relaxed with blue light. The data had previously hinted, however, that the photoexcited state is not relaxed by light. Also, as for the Fe_3Co_2 compound, the reflectivity measurements reveal a more efficient surface conversion, equivalent to the thermal

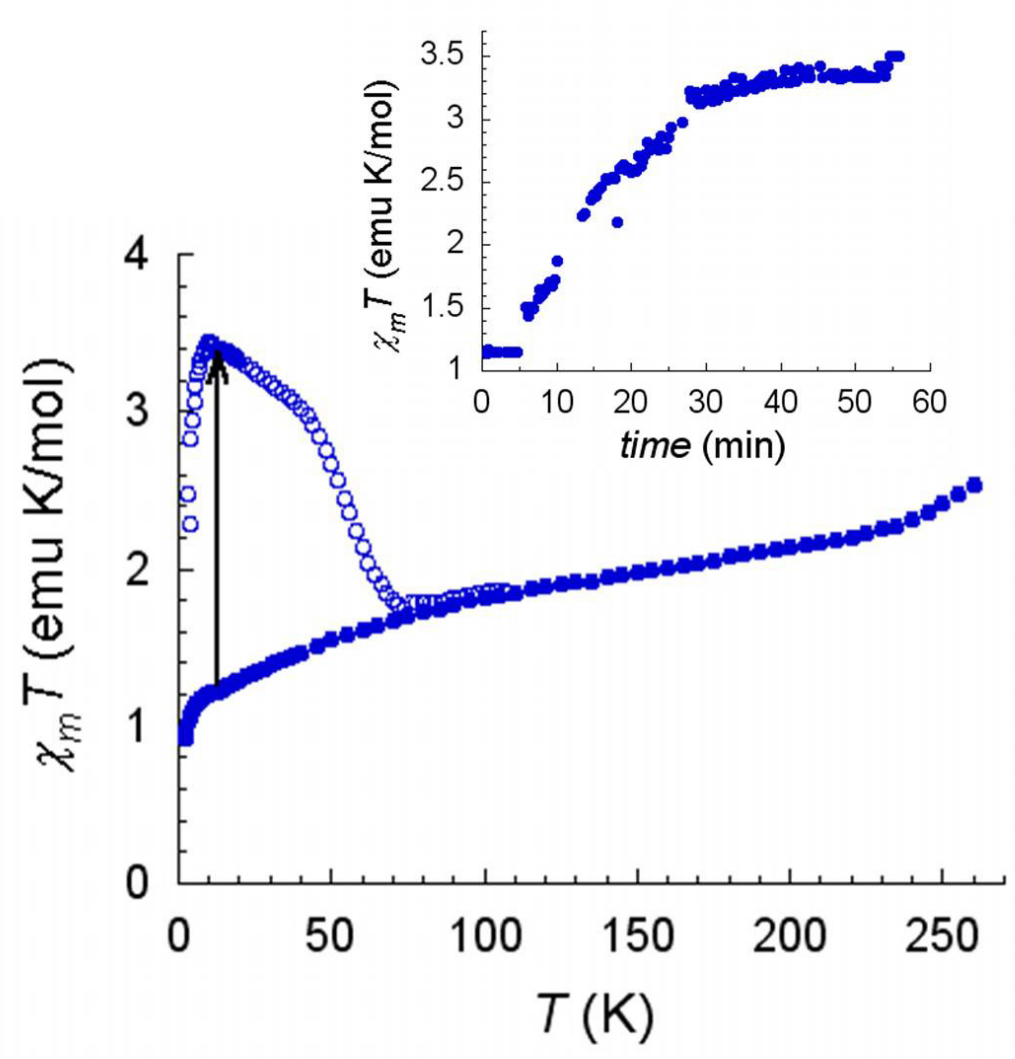

Figure 60: Temperature dependence of $\chi_m T$ of **12** at 0.1 T at a sweep rate of 0.5 K/min, before and after irradiation with white light (3 mW/cm^2). Inset: time dependence of $\chi_m T$ at 30 K of Co_3Fe_2 upon irradiation with white light.

charge transfer.[116] Therefore, a more likely explanation for the inefficiency of the photo-excitation, as well as the slow saturation, is the very dark blue color of the sample which serves to hinder light penetration.

For one sample of **12**, AC susceptibility data were acquired after the sample had been irradiated for 3 hours, but, given the lack of metal ions with strong single ion anisotropy, SMM behavior was not expected for the cluster. The data are very noisy because of the small sample size, but, surpisingly, an out-of-phase (χ'') susceptibility was observed that was frequency dependent below ~3.5 K (Figure 61a). Since the photo-excited state is presumed to contain the $Co^{II}_3Fe^{III}_2$ configuration, this behavior could be confirmed by preparing a dry sample, which is *known* to contain this configuration, and running AC susceptibility and microSQUID measurements. If SMM behavior were to be cofirmed, **12** would be the first example of a photomagnetic SMM.

Synthesis and Characterization of 14

By modifying the procedure to prepare the hydrated Co_3Fe_2 compound (**12**), a method was found to prepare and grow crystals of the same cluster using anhydrous materials – a procedure which was previously thought to be impossible based on experience. The synthesis is reproducible, but the products are often a mixture of powder and crystals, with the size and amount of crystals highly varied. Compound **14** was prepared under a nitrogen atmosphere, and it will pick up water in humid air within a few minutes.

The determination of the unit cell of one of the crystals at 110 K resulted in a monoclinic unit cell with typical parameters for a TBP compound: a = 18.840 Å, b =

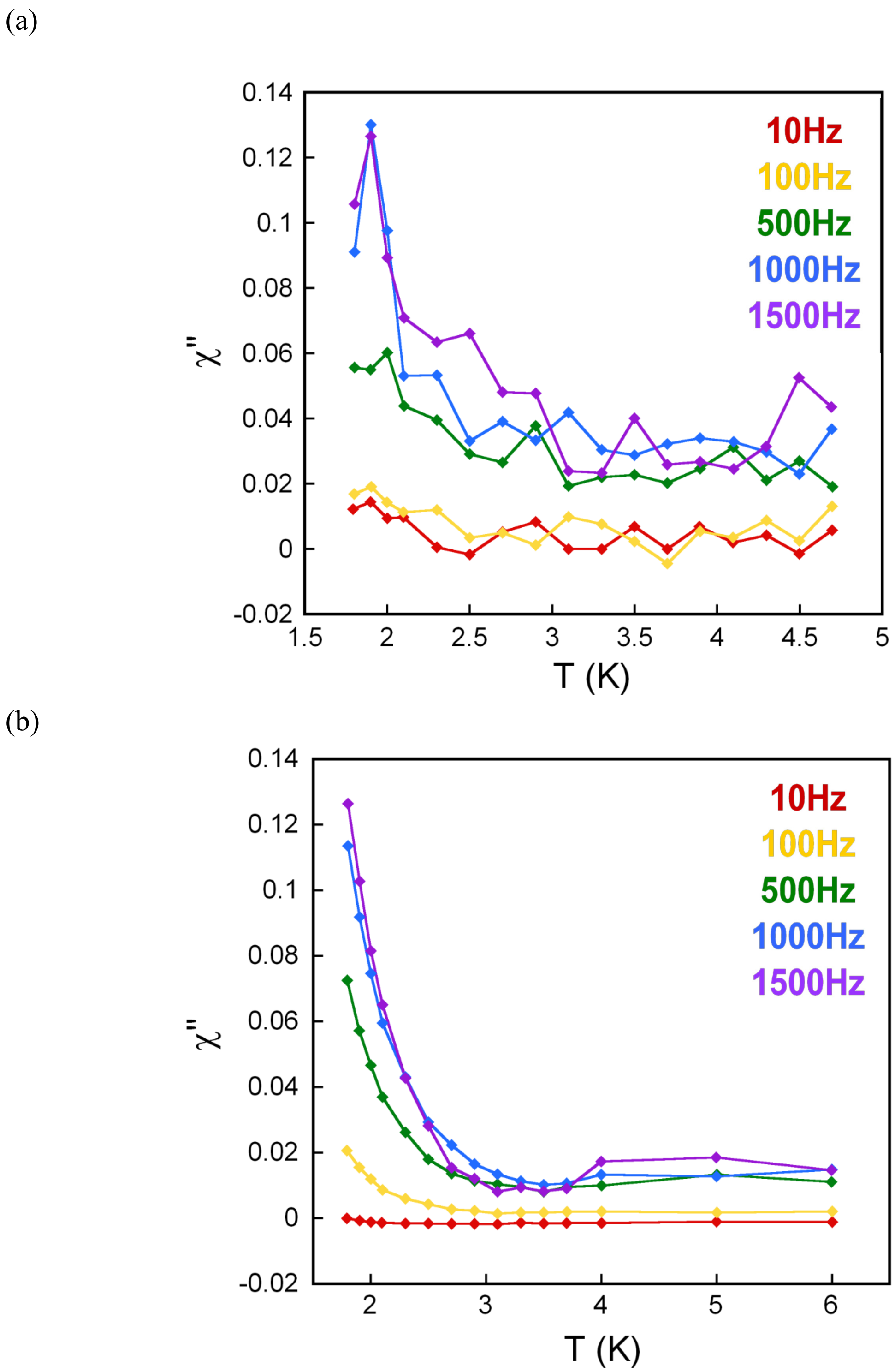

Figure 61: Frequency dependence of the χ_m'' AC susceptibility vs. T for (a) **12** after 4 hours of mW/cm^2 irradiation and (b) **14**.

24.780 Å, c = 24.384 Å, β = 97.987°. The 2114 and 2143 cm^{-1} cyanide stretching frequencies observed in the IR spectrum are very similar to the 2110 and 2140 cm^{-1} stretches observed for the Co_3Fe_2 red solid,[116] and correspond to the Fe^{III}—CN terminal mode and the Co^{II}—NC—Fe^{III} bridging mode, respectively.

Magnetic Properties of 14

The room temperature $\chi_m T$ value of **14** is 10.0 emu·K/mol (Figure 62), identical to the "5 minutes" photomagnetic measurement for **12**. This value is significantly higher than the spin-only value (6.375 emu·K/mol) for three high-spin Co^{II} (S = 3/2) and two low-spin Fe^{III} (S = 1/2) ions, but the value is reasonable for this compound since both ions have significant orbital contribution. As was noted previously for the Co_3Fe_2 red solid,[116] the decrease in $\chi_m T$ with temperature is likely the combination of the orbital contributions of the ions (particularly the Kramer's doublet population of Co^{II}_{HS}, described in Chapter II) and a partial conversion of the compound from the $Co^{II}_3Fe^{III}_2$ state to a less paramagnetic state ($Co^{II}_2Co^{III}Fe^{II}Fe^{III}$ or $Co^{III}_2Co^{II}Fe^{II}_2$).

AC susceptibility measurements were performed on **14** to compare to the observations of the photoexcited state of **12**. As predicted, a frequency dependence in χ'' was observed below ~3.5 K (Figure 61b). Although this signal is very weak, there remained potential SMM behavior in the $Co^{II}_3Fe^{III}_2$ compound. A dry crystal was submitted to Wolfgang Wernsdorfer for microSQUID measurements to check the behavior. Unfortunately, the results showed only an extremely thin "hysteresis" loop (Figure 63), which was only present at temperatures <1 K and which had no remnant

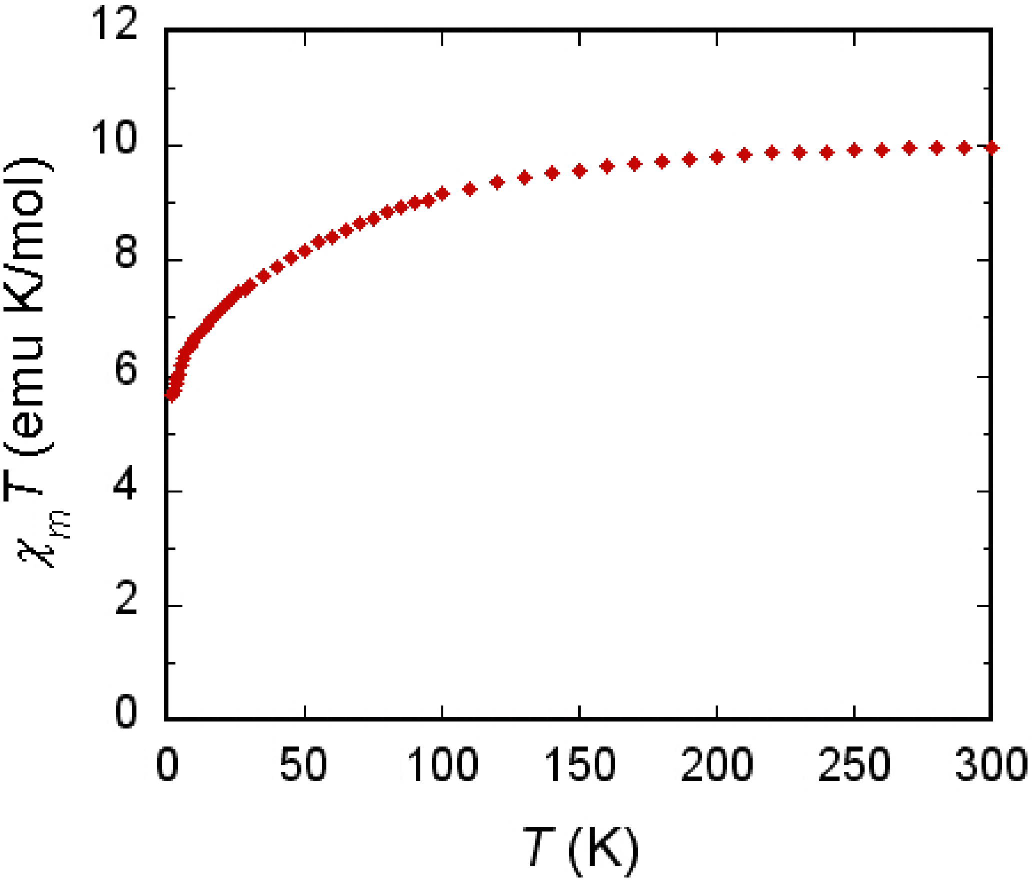

Figure 62: Thermal variation of $\chi_m T$ for compound **14**.

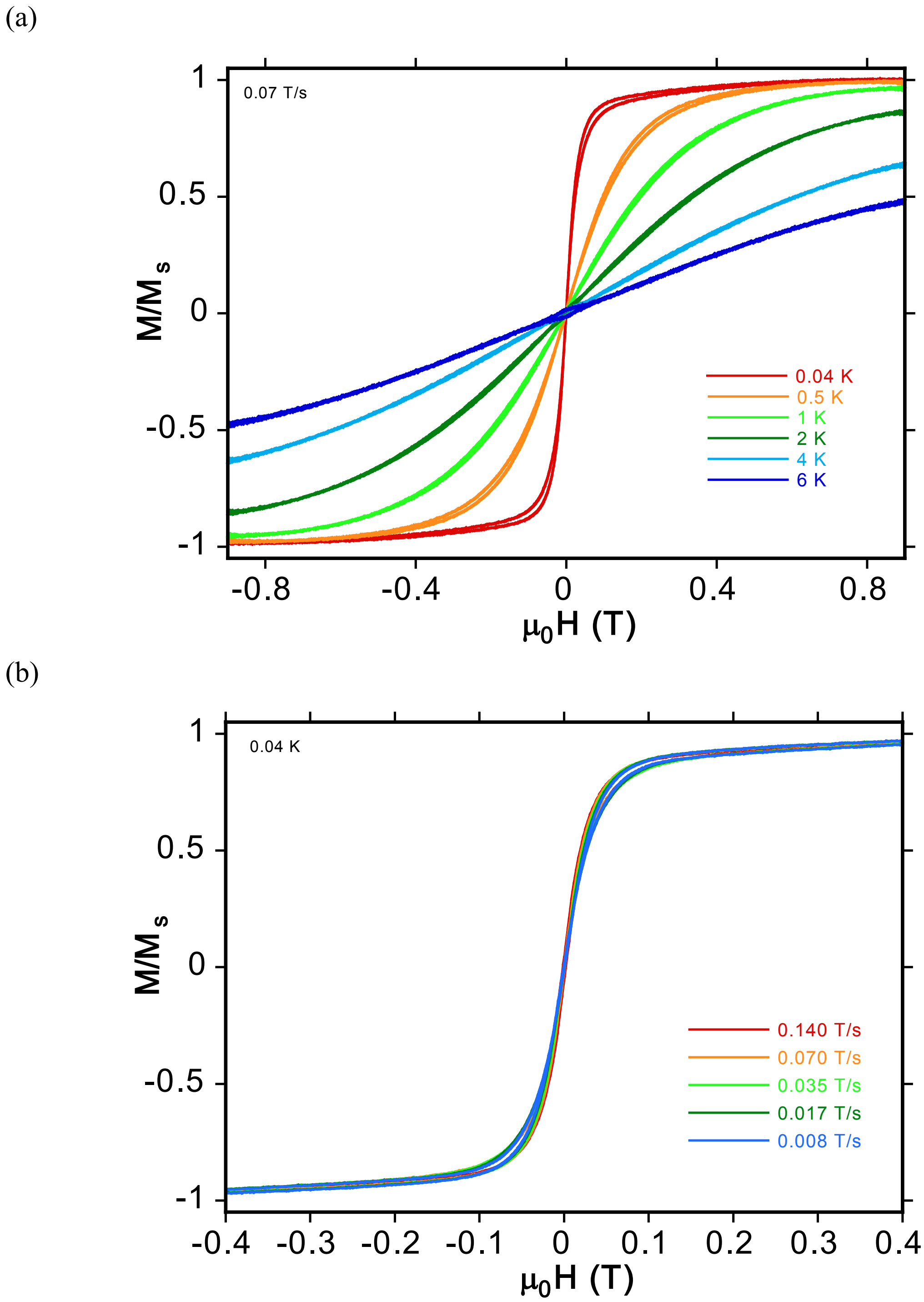

Figure 63: (a) Temperature-dependent micro-SQUID magnetization scans collected for a single crystal of **14** at 0.07 T/s. (b) Micro-SQUID magnetization scans collected at variable-field sweep rates at 0.04 K. Magnetization values are normalized to the saturation magnetization value at 1.4 T.

magnetization at zero field. It is concluded, therefore, that compound **14** is not a single molecule magnet.

CONCLUSIONS

In summary, four clusters from the family of TBP molecules under investigation in this thesis have been studied for their photo-induced optical and magnetic properties. In three of the four cases, the compounds are photosensitive. Compounds **10** and **11**, which are inspired by the Fe(diimine)$_2$(NCS)$_2$ spin crossover compounds, exhibit a light-induced spin crossover, with **10** being converted to a lesser extent. Compound **12**, a molecular analogue of the Co/Fe Prussian blues, undergoes a photo-induced charge transfer which converts Co^{III}_{LS} and Fe^{II} sites to Co^{II}_{HS} and Fe^{III} sites. In the cases of **11** and **12**, optical reflectivity measurements accurately predicted the photomagnetic behavior, and these properties were confirmed by magnetic susceptibility data. Compound **14** and the photoexcited state of **12** also showed initial evidence of single molecule magnet behavior (a frequency dependence of the out-of-phase signal), but microSQUID measurements on a single crystal of **14** revealed a negligible hysteresis. Other molecules and materials prepared in the Dunbar laboratories show potential for photomagnetic behavior. Compound **13** (described in Chapter IV) contains the same Co^{III}—NC—Fe^{II} unit as **12** and may show similar photomagnetic behavior. A photo-induced charge transfer in this compound could convert the chain from a simple paramagnet with magnetically isolated Mn^{II} centers to a coupled chain.

CHAPTER VI

CONCLUSIONS AND FUTURE OUTLOOK

The work in this dissertation focuses on the preparation, properties, and extension of a growing family of trigonal-bipyamidal cyanide clusters of the formula $[M(tmphen)_2]_3[M'(CN)_6]_2$. In Chapter II, nine new TBP compounds were prepared with the metal cores Mn_3Fe_2, Zn_3Fe_2, Mn_3Cr_2, Ni_3Cr_2, Zn_3Cr_2, Mn_3Co_2, Co_3Co_2, Ni_3Co_2, and Zn_3Co_2. The benefit of the method used to prepare these compounds is that nearly identical procedures are used to prepare all the clusters with all the different metal ion combinations in this chapter, as well as many other combinations in the work of other group members (Table 18).[117,118,178-180] The clusters were characterized and their magnetic properties studied. Six of the compounds contained one diamagnetic metal ion and could therefore be used as a "model compounds" to understand the properties of the remaining paramagnetic metal ion. By knowing the independent behavior of two paramagnetic ions in a cluster in turn one can better understand the coupling between them. Moreover, understanding the exchange interactions in the clusters can be used to enhance understanding the magnetic properties of the corresponding Prussian blue materials.

Despite the fact that we now have twenty-nine TBP clusters in the series, there is still room for the expansion to new metal ions in a quest for new properties. New chemistry of TBP's are aimed at the early transition metals, vanadium and titanium, which are intriguing because of the strong anisotropy of, for example, Ti^{III} ($3d^1$) and V^{III}

Table 18: $[M(tmphen)_2]_3[M'(CN)_6]_2$ TBP clusters prepared in the Dunbar laboratories.

		equatorial center, $[M(tmphen)_2]^{2+}$						
		V^{II}	Cr^{II}	Mn^{II}	Fe^{II}	Co^{II}	Ni^{II}	Zn^{II}
axial center, [M $_6]^{3-}$	Cr^{III}		✓	✓	✓	✓	✓	✓
	Mn^{III}			✓				
	Fe^{III}			✓	✓	✓	✓	✓
	Co^{III}			✓	✓	✓	✓	✓
	Mo^{III}	✓		✓	✓	✓	✓	
	Ru^{III}		✓	✓	✓		✓	
	Os^{III}			✓	✓		✓	

($3d^2$) ions. Another important extension is to heavier 4d and 5d metal ions which exhibit strong spin orbit coupling. Both of these ideas are directed at the search for new single molecule magnets with higher blocking temperatures and molecules that exhibit light or temperature induced bistabilty.

Chapter III presents a detailed study of the Fe_3Fe_2 and Fe_3Co_2 TBP clusters. These clusters were prepared with the expectation that the FeN_6 ligand field of the Fe^{II} ions, given the similarity to classical spin crossover compounds such as $Fe(phen)_2(NCS)_2$ would lead to a thermal LS to HS transition for these compounds. Indeed, spin crossover was observed for the clusters as evidenced by three methods. The typical S-shaped curve in the magnetic susceptibility measurements initially revealed the presence of spin transition behavior. The Mössbauer measurements, performed in the group of Catalina Achim at Carnegie Mellon University, revealed that the Fe^{II} centers in the clusters had not been oxidized to Fe^{III}, even in the air, and confirmed that they undergo a spin transition from LS Fe^{II} to HS Fe^{II} with increasing temperatures. Finally, variable temperature X-ray measurements, with great help from Michael Shatruk, on the Fe_3Co_2 cluster answered the question of whether the spin transition occurred one cluster at a time or one center at a time. The Fe^{II}—N bond lengths of the three metal centers clearly indicated the lengthening of the bonds with temperature of one center at a time as HS Fe^{II} bond distances are approximately 0.2 Å longer than for LS Fe^{II}. Ultimately, the ease of the spin transitions, or the temperature range over which they occurred, was discovered to be primarily dependent on the intermolecular π-π interactions of the tmphen ligands. To further understand the effects on the spin transition, the interstitial solvent of the clusters was exchanged with other solvents. The results to date reveal that the properties of the solvent (size, polarity, aromatic or not) have a significant effect on the completeness of the HS→LS transition of Fe(1) at low temperatures. It is also well known that π-π interactions have shown to have a great influence on the cooperativity of mononuclear spin crossover compounds.[152] Inspired by this fact, attempts were made to prepare related Fe_3Fe_2 and Fe_3Co_2 TBP clusters using the dipyrido-phenazine ligand "dmdppz" instead of tmphen in hopes of increasing the cooperativity and the abruptness of the spin transition. Unfortunately, the results observed suggested that, if the desired clusters were formed, this dmdppz ligand did not provide the right ligand field for spin crossover.

Future work on these SCO clusters will take two major directions. First, in order to properly understand the solvent effects on the spin transition, further measurements are needed. Room temperature crystal structures will reveal if the solvent influence plays a role on the Fe(1) transition only at low temperatures or if there are also effects on the other Fe centers at higher temperatures. It is also important to note that crystal structures provide a lot of information, but only at a single temperature. Therefore, it is crucial to obtain magnetic susceptibility measurements of the solvent-exchanged crystals in order to get a more general idea of the abruptness of the spin transition, as well as the possibility of the all-important hysteresis loop. The second direction of this work is the variation of the diimine ligands on the equatorial metal centers. The tmphen ligand was considered ideal for this work not only for its particular ligand field, but also because the TBP compounds with this ligand easily form crystalline products. The methyl groups of the ligand seem to provide the stability and solubility for the complexes that allows this crystallization, properties not generally observed for reactions with bpy or phen. If a ligand can be prepared which combines a phenanthroline unit with an extended aromatic system such as dppz-type ligands, "tmdppz" (Scheme 3), a strongly cooperative TBP cluster might be able to be prepared.

In Chapter IV, the focus shifted from the pursuit of TBP compounds themselves to their use as starting materials, namely the application of the next level of a building block approach. For three clusters which exhibit spin transitions, Co_3Fe_2, Fe_3Fe_2, and Fe_3Co_2, the idea of connecting these clusters into a chain or other extended structures would be an excellent way to increase the cooperativity of the transition. Two chains based on the Co_3Fe_2 cluster were prepared previously in the Dunbar group, but the method produced a mixture of two compounds under the same reaction conditions. New starting materials were sought that would direct the coordination *via* blocking ligands to form a desired product. This method was successful as a proof-of-concept method for producing a trimetallic chain of Co_3Fe_2 clusters, namely $\{[Co^{III}(tmphen)_2]_3[Fe^{II}(CN)_6]_2[Mn^{II}(MeOH)_4]\}_\infty(ClO_4)_3 \cdot xMeOH$. Unfortunately, the chain did not retain the spin transition of the original cluster and was found to exhibit magnetic properties of a simple paramagnet. All further attempts to prepare chains using the SCO TBP clusters gave inconclusive or negative results.

With twenty-nine TBP clusters and a plethora of starting materials available, the number of potential extended materials based on them as building units that one can envisage is vast. The challenge is controlling the synthesis to obtain pure, crystalline

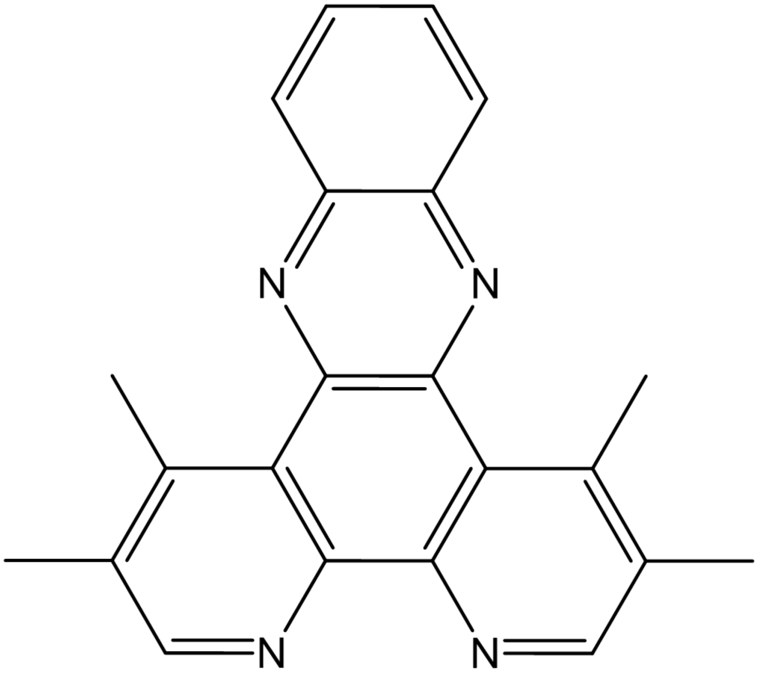

Scheme 3: The proposed “tmdppz” ligand (1,2,7,8-tetramethyldipyrido[3,2-a:2′,3′-c]phenazine).

products. It has been shown in this thesis work that reaction conditions do not translate well from one reaction to another and that solvent choice is crucial since many TBP clusters are very poorly soluble, it will be a task to find a solvent system to dissolve the clusters without decomposition. The most interesting application for these chains would be to combine two properties, such as the photo-induced single chain magnetism observed for Co/Fe chain by Sato *et al.*[181] The building block approach seems ideal for designing these multi-functional chains – obtaining one property from the TBP compound and adding a second one from the linker. For example, the thermal SCO behavior of Fe_3Fe_2 or the CTIST behavior of Co_3Fe_2 could be combined with a SMM, such as Brechin's Mn_3O or Mn_6O_2 clusters,[182-185] to create a material with a variety of properties including, possibly, coupled SMM's.

Finally, in Chapter V, photomagnetic properties were sought for previously studied clusters because of their similarities to known photomagnetic materials. A LIESST effect was observed for the Fe_3Fe_2 and Fe_3Co_2 clusters which involves the conversion of the equatorial Fe^{II} centers from LS to HS with white light. A photo-induced MMCT from Co^{III}_{LS}—NC—Fe^{II} to Co^{II}_{HS}—NC—Fe^{III} was observed for Co_3Fe_2, but the analogous transition was not observed for Mn_3Fe_2 which is not surprising given the fact that Mn^{II} is not likely to convert to Mn^{III}. The photoexcited state of the $Co^{III}_2Co^{II}Fe_2$ cluster was also observed to exhibit an out-of-phase signal, which was taken as a sign of potential single molecule magnet behavior. The observation of a comparable out-of-phase signal in an anhydrous $Co^{II}_3Fe^{II}_2$ sample confirmed the similarity between the photoexcited blue solid and the dry red solid. However, microSQUID measurements of a dry crystal revealed that neither compound is a single molecule magnet based on the lack of hysteresis at temperatures as low as 40 mK.

Future work to understand the spin transitions in the Fe_3Fe_2, Fe_3Co_2, and Co_3Fe_2 clusters will involve a temperature-trapping experiment. For some compounds, quickly cooling a room-temperature sample to liquid helium temperatures will prevent the cooling spin transition such that the room temperature spin-state is retained at low temperatures. This behavior is known as a temperature-induced spin state trapping or TIESST effect. TIESST experiments could reveal interesting properties of the high-temperature configurations, such as low temperature ordering, not visible through ordinary magnetic susceptibility measurements. While photomagnetic measurements can ideally be used for the same purpose, since these compounds all have inefficient light-induced spin transitions, the results can be masked by other factors. For the spin crossover compounds especially, a temperature-trapping experiment would likely trap a much higher portion of the high-spin states than could be created with light, giving a much better idea of the configurations' low temperature behavior.

The results reported in this dissertation constitute strong evidence for the usefulness of TBP clusters and the promise for cyanide clusters to mimic properties of Prussian Blue phases. Single molecules magnets are being discussed as possible elements in spintronics devices,[186-191] and spin crossover compounds have been used in display devices.[192] Cyanide clusters are particularly promising in these areas due to the ease in varying the metal centers and the organic ligands to tune properties such as higher blocking temperatures or more abrupt spin transitions. It is obvious that an ample knowledge of organic and inorganic synthesis combined with a thorough understanding of molecular magnetism will help researchers continue to make great strides toward a greater fundamental understanding of magnetism and, hence, future applications.

REFERENCES

1. Hysteresis figure obtained from: http://en.wikipedia.org/wiki/File:Hysteresiscurve.svg Accessed on October 1, 2010.

2. Wickman, H. H.; Trozzolo, A. M.; Williams, H. J.; Hull, G. W.; Merritt, F. R. *Phys. Rev.* **1967**, *155*, 563-566.

3. Kinoshita, M.; Turek, P.; Tamura, M.; Nozawa, K.; Shiomi, D.; Nakazawa, Y.; Ishikawa, M.; Takahashi, M.; Awaga, K.; et al. *Chem. Lett.* **1991**, 1225-1228.

4. Tamura, M.; Nakazawa, Y.; Shiomi, D.; Nozawa, K.; Hosokoshi, Y.; Ishikawa, M.; Takahashi, M.; Kinoshita, M. *Chem. Phys. Lett.* **1991**, *186*, 401-404.

5. Coronado, E.; Galán-Mascarós, J. R.; Gómez-Garcia, C. J.; Laukhin, V. *Nature* **2000**, *408*, 447-449.

6. Woodward, J. *Philos. Trans.* **1724**, *33*, 15-17.

7. Buser, H. J.; Schwarzenbach, D.; Petter, W.; Ludi, A. *Inorg. Chem.* **1977**, *16*, 2704-10.

8. Herren, F.; Fischer, P.; Ludi, A.; Hälg, W. *Inorg. Chem.* **1980**, *19*, 956-959.

9. Sano, H.; Hashimoto, F. *Bull. Chem. Soc. Jpn.* **1965**, *38*, 684-685.

10. Ito, A.; Suenaga, M.; Ôno, K. *J. Chem. Phys.* **1968**, *48*, 3597-3599.

11. Mayoh, B.; Day, P. *J. Chem. Soc., Dalton Trans.* **1976**, 1483-1486.

12. Ferlay, S.; Mallah, T.; Ouahès, R.; Veillet, P.; Verdaguer, M. *Nature* **1995**, *378*, 701-703.

13. Entley, W. R.; Girolami, G. S. *Science* **1995**, *268*, 397-400.

14. Holmes, S. M.; Girolami, G. S. *J. Am. Chem. Soc.* **1999**, *121*, 5593-5594.

15. Boxhoorn, G.; Moolhuysen, J.; Coolegem, J. G. F.; Van Santen, R. A. *J. Chem. Soc., Chem. Commun.* **1985**, 1305-1307.

16. "Prussian Blue (ferric hexacyanoferrate (II.. for Treatment of Internal Contamination with Thallium or Radioactive Cesium." http://www.fda.gov/Drugs/EmergencyPreparedness/BioterrorismandDrugPreparedness/ucm130334.htm Accessed on October 1, 2010.

17. Chapman, K. W.; Southon, P. D.; Weeks, C. L.; Kepert, C. J. *Chem. Commun.* **2005**, 3322-3324.

18. Kaye, S. S.; Long, J. R. *J. Am. Chem. Soc.* **2005**, *127*, 6506-6507.

19. Dunbar, K. R.; Heintz, R. A. *Prog. Inorg. Chem.* **1997**, *45*, 283-391.

20. Shatruk, M.; Avendaño, C.; Dunbar, K. R. *Prog. Inorg. Chem.* **2009**, *56*, 155-334.

21. Goodenough, J. B. *Phys. Rev.* **1955**, *100*, 564-573.

22. Goodenough, J. B. *J. Phys. Chem. Solids* **1958**, *6*, 287-297.

23. Kanamori, J. *Phys. Chem. Solids* **1959**, *10*, 87-98.

24. Gadet, V.; Mallah, T.; Castro, I.; Verdaguer, M.; Veillet, P. *J. Am. Chem. Soc.* **1992**, *114*, 9213-9214.

25. Entley, W. R.; Girolami, G. S. *Inorg. Chem.* **1994**, *33*, 5165-5166.

26. Néel, L. *Compt. Rend.* **1949**, *228*, 664-666.

27. Lis, T. *Acta Crystallogr., Sect. B* **1980**, *B36*, 2042-2046.

28. Sessoli, R.; Gatteschi, D.; Caneschi, A.; Novak, M. A. *Nature* **1993**, *365*, 141-143.

29. Christou, G.; Gatteschi, D.; Hendrickson, D. N.; Sessoli, R. *MRS Bull.* **2000**, *25*, 66-71.

30. Sessoli, R.; Tsai, H. L.; Schake, A. R.; Wang, S.; Vincent, J. B.; Folting, K.; Gatteschi, D.; Christou, G.; Hendrickson, D. N. *J. Am. Chem. Soc.* **1993**, *115*, 1804-1816.

31. Gatteschi, D.; Sessoli, R. *Angew. Chem., Int. Ed.* **2003**, *42*, 268-297.

32. Bagai, R.; Christou, G. *Chem. Soc. Rev.* **2009**, *38*, 1011-1026.

33. Tasiopoulos, A. J.; Wernsdorfer, W.; Abboud, K. A.; Christou, G. *Inorg. Chem.* **2005**, *44*, 6324-6338.

34. Sokol, J. J.; Hee, A. G.; Long, J. R. *J. Am. Chem. Soc.* **2002**, *124*, 7656-7657.

35. Berlinguette, C. P.; Vaughn, D.; Cañada-Vilalta, C.; Galán-Mascarós, J. R.; Dunbar, K. R. *Angew. Chem., Int. Ed.* **2003**, *42*, 1523-1526.

36. Choi, H. J.; Sokol, J. J.; Long, J. R. *Inorg. Chem.* **2004**, *43*, 1606-1608.

37. Palii, A. V.; Ostrovsky, S. M.; Klokishner, S. I.; Tsukerblat, B. S.; Berlinguette, C. P.; Dunbar, K. R.; Galán-Mascarós, J. R. *J. Am. Chem. Soc.* **2004**, *126*, 16860-16867.

38. Schelter, E. J.; Prosvirin, A. V.; Dunbar, K. R. *J. Am. Chem. Soc.* **2004**, *126*, 15004-15005.

39. Wang, S.; Zuo, J.-L.; Zhou, H.-C.; Choi, H. J.; Ke, Y.; Long, J. R.; You, X.-Z. *Angew. Chem., Int. Ed.* **2004**, *43*, 5940-5943.

40. Li, D.; Parkin, S.; Wang, G.; Yee, G. T.; Prosvirin, A. V.; Holmes, S. M. *Inorg. Chem.* **2005**, *44*, 4903-4905.

41. Song, Y.; Zhang, P.; Ren, X.-M.; Shen, X.-F.; Li, Y.-Z.; You, X.-Z. *J. Am. Chem. Soc.* **2005**, *127*, 3708-3709.

42. Tsukerblat, B. S.; Palii, A. V.; Ostrovsky, S. M.; Kunitsky, S. V.; Klokishner, S. I.; Dunbar, K. R. *J. Chem. Theor. Comp.* **2005**, *1*, 668-673.

43. Freedman, D. E.; Bennett, M. V.; Long, J. R. *Dalton Trans.* **2006**, 2829-2834.

44. Li, D.; Clérac, R.; Parkin, S.; Wang, G.; Yee, G. T.; Holmes, S. M. *Inorg. Chem.* **2006**, *45*, 5251-5253.

45. Li, D.; Parkin, S.; Wang, G.; Yee, G. T.; Clérac, R.; Wernsdorfer, W.; Holmes, S. M. *J. Am. Chem. Soc.* **2006**, *128*, 4214-4215.

46. Lim, J. H.; Yoon, J. H.; Kim, H. C.; Hong, C. S. *Angew. Chem., Int. Ed.* **2006**, *45*, 7424-7426.

47. Palii, A.; Ostrovsky, S. M.; Klokishner, S. I.; Tsukerblat, B. S.; Dunbar, K. R. *ChemPhysChem* **2006**, *7*, 871-879.

48. Rebilly, J.-N.; Mallah, T. *Struct. Bonding* **2006**, *122*, 103-131.

49. Wang, C.-F.; Zuo, J.-L.; Bartlett, B. M.; Song, Y.; Long, J. R.; You, X.-Z. *J. Am. Chem. Soc.* **2006**, *128*, 7162-7163.

50. Yoon, J. H.; Lim, J. H.; Kim, H. C.; Hong, C. S. *Inorg. Chem.* **2006**, *45*, 9613-9615.

51. Bartlett, B. M.; Harris, T. D.; Degroot, M. W.; Long, E. R. *Z. Anorg. Allg. Chem.* **2007**, *633*, 2380-2385.

52. Kim, J.; Han, S.; Lim, J. M.; Choi, K.-Y.; Nojiri, H.; Suh, B. J. *Inorg. Chim. Acta* **2007**, *360*, 2647-2652.

53. Klokishner, S. I.; Ostrovsky, S. M.; Palii, A. V.; Dunbar, K. *J. Mol. Struc.* **2007**, *838*, 144-150.

54. Li, D.; Clérac, R.; Wang, G.; Yee, G. T.; Holmes, S. M. *Eur. J. Inorg. Chem.* **2007**, 1341-1346.

55. Ni, Z.-H.; Zhang, L.-F.; Tangoulis, V.; Wernsdorfer, W.; Cui, A.-L.; Sato, O.; Kou, H.-Z. *Inorg. Chem.* **2007**, *46*, 6029-6037.

56. Ostrovsky, S. M.; Klokishner, S. I.; Palii, A. V.; Dunbar, K. R. *J. Mol. Struc.* **2007**, *838*, 138-143.

57. Palii, A. V.; Ostrovsky, S. M.; Klokishner, S. I.; Tsukerblat, B. S.; Schelter, E. J.; Prosvirin, A. V.; Dunbar, K. R. *Inorg. Chim. Acta* **2007**, *360*, 3915-3924.

58. Schelter, E. J.; Karadaş, F.; Avendaño, C.; Prosvirin, A. V.; Wernsdorfer, W.; Dunbar, K. R. *J. Am. Chem. Soc.* **2007**, *129*, 8139-8149.

59. Freedman, D. E.; Jenkins, D. M.; Iavarone, A. T.; Long, J. R. *J. Am. Chem. Soc.* **2008**, *130*, 2884-2885.

60. Funck, K. E.; Hilfiger, M. G.; Berlinguette, C. P.; Shatruk, M.; Wernsdorfer, W.; Dunbar, K. R. *Inorg. Chem.* **2009**, *48*, 3438-3452.

61. Tregenna-Piggott, P. L. W.; Sheptyakov, D.; Keller, L.; Klokishner, S. I.; Ostrovsky, S. M.; Palii, A. V.; Reu, O. S.; Bendix, J.; Nannestad, T. B.; Pedersen, K.; Weihe, H.; Mutka, H. *Inorg. Chem.* **2009**, *48*, 128-137.

62. Karadaş, F.; Avendaño, C.; Hilfiger, M. G.; Prosvirin, A. V.; Dunbar, K. R. *Dalton Trans.* **2010**, *39*, 4968-4977.

63. Wu, D.; Zhang, Y.; Huang, W.; Sato, O. *Dalton Trans* **2010**, *39*, 5500-5503.

64. Zhang, Y.; Mallik, U. P.; Rath, N.; Yee, G. T.; Clérac, R.; Holmes, S. M. *Chem. Commun.* **2010**, *46*, 4953-4955.

65. Cambi, L.; Szego, L. *Ber. Dtsch. Chem. Ges.* **1931**, *64*, 2591-2598.

66. König, E.; Madeja, K. *Chem. Commun.* **1966**, *3*, 61-62.

67. Guionneau, P.; Marchivie, M.; Bravic, G.; Létard, J.-F.; Chasseau, D. *Top. Curr. Chem.* **2004**, *234*, 97-128.

68. Vos, G.; De Graaff, R. A. G.; Haasnoot, J. G.; Van der Kraan, A. M.; De Vaal, P.; Reedijk, J. *Inorg. Chem.* **1984**, *23*, 2905-2910.

69. Schebler, P. J.; Riordan, C. G.; Liable-Sands, L.; Rheingold, A. L. *Inorg. Chim. Acta* **1998**, *270*, 543-549.

70. Breuning, E.; Ruben, M.; Lehn, J.-M.; Renz, F.; Garcia, Y.; Ksenofontov, V.; Gütlich, P.; Wegelius, E.; Rissanen, K. *Angew. Chem., Int. Ed.* **2000**, *39*, 2504-2507.

71. Garcia, Y.; Guionneau, P.; Bravic, G.; Chasseau, D.; Howard, J. A. K.; Kahn, O.; Ksenofontov, V.; Reiman, S.; Gutlich, P. *Eur. J. Inorg. Chem.* **2000**, 1531-1538.

72. Geiss, A.; Kolm, M. J.; Janiak, C.; Vahrenkamp, H. *Inorg. Chem.* **2000**, *39*, 4037-4043.

73. Nakamura, T.; Kuranuki, E.; Niwa, K.; Fujiwara, M.; Matsushita, T. *Chem. Lett.* **2000**, 248-249.

74. Hibbs, W.; Van Koningsbruggen, P. J.; Arif, A. M.; Shum, W. W.; Miller, J. S. *Inorg. Chem.* **2003**, *42*, 5645-5653.

75. Herchel, R.; Boča, R.; Gembický, M.; Kožíšek, J.; Renz, F. *Inorg. Chem.* **2004**, *43*, 4103-4105.

76. Psomas, G.; Bréfuel, N.; Dahan, F.; Tuchagues, J.-P. *Inorg. Chem.* **2004**, *43*, 4590-4594.

77. Nihei, M.; Ui, M.; Yokota, M.; Han, L.; Maeda, A.; Kishida, H.; Okamoto, H.; Oshio, H. *Angew. Chem., Int. Ed.* **2005**, *44*, 6484-6487.

78. Berezovskii, G. A.; Bushuev, M. B.; Pishchur, D. P.; Lavrenova, L. G. *J. Therm. Anal. Calorim.* **2008**, *93*, 999-1002.

79. Boldog, I.; Muñoz-Lara, F. J.; Gaspar, A. B.; Muñoz, M. C.; Seredyuk, M.; Real, J. A. *Inorg. Chem.* **2009**, *48*, 3710-3719.

80. Dîrtu, M. M.; Rotaru, A.; Gillard, D.; Linares, J.; Codjovi, E.; Tinant, B.; Garcia, Y. *Inorg. Chem.* **2009**, *48*, 7838-7852.

81. Duriska, M. B.; Neville, S. M.; Moubaraki, B.; Cashion, J. D.; Halder, G. J.; Chapman, K. W.; Balde, C.; Létard, J.-F.; Murray, K. S.; Kepert, C. J.; Batten, S. R. *Angew. Chem., Int. Ed.* **2009**, *48*, 2549-2552.

82. Nihei, M.; Ui, M.; Oshio, H. *Polyhedron* **2009**, *28*, 1718-1721.

83. Nishihara, T.; Nihei, M.; Oshio, H.; Tanaka, K. *J. Phys.: Conf. Ser.* **2009**, *148*, 012033/1-012033/4.

84. Šalitroš, I.; Boča, R.; Dlháň, L. u.; Gembický, M.; Kožíšek, J.; Linares, J.; Moncol', J.; Nemec, I.; Perašínová, L.; Renz, F.; Svoboda, I.; Fuess, H. *Eur. J. Inorg. Chem.* **2009**, 3141-3154.

85. Wu, D.-Y.; Sato, O.; Einaga, Y.; Duan, C.-Y. *Angew. Chem., Int. Ed.* **2009**, *48*, 1475-1478.

86. Gütlich, P.; Goodwin, H. A. *Top. Curr. Chem.* **2004**, *233*, 1-47.

87. McGarvey, J. J.; Lawthers, I. *J. Chem. Soc., Chem. Commun.* **1982**, 906-907.

88. Decurtins, S.; Gütlich, P.; Köhler, C. P.; Spiering, H.; Hauser, A. *Chem. Phys. Lett.* **1984**, *105*, 1-4.

89. Decurtins, S.; Gütlich, P.; Köhler, C. P.; Spiering, H. *J. Chem. Soc., Chem. Commun.* **1985**, 430-432.

90. Herber, R.; Casson, L. M. *Inorg. Chem.* **1986**, *25*, 847-52.

91. Baldenius, K. U.; Campen, A. K.; Höhnk, H. D. *J. Mol. Struc.* **1987**, *157*, 295-299.

92. Herber, R. H. *Inorg. Chem.* **1987**, *26*, 173-178.

93. Figg, D. C.; Herber, R. H.; Potenza, J. A. *Inorg. Chem.* **1992**, *31*, 2111-2117.

94. Létard, J. F.; Nguyen, O.; Soyer, H.; Mingotaud, C.; Delhaès, P.; Kahn, O. *Inorg. Chem.* **1999**, *38*, 3020-3021.

95. Suemura, N.; Ohama, M.; Kaizaki, S. *Chem. Commun.* **2001**, 1538-1539.

96. MacLean, E. J.; McGrath, C. M.; O'Connor, C. J.; Sangregorio, C.; Seddon, J. M. W.; Sinn, E.; Sowrey, F. E.; Teat, S. J.; Terry, A. E.; Vaughan, G. B. M.; Young, N. A. *Chem. Eur. J.* **2003**, *9*, 5314-5322.

97. Marchivie, M.; Guionneau, P.; Létard, J. F.; Chasseau, D. *Acta Crystallogr., Sect. B: Struct. Sci.* **2005**, *B61*, 25-28.

98. Sato, O.; Iyoda, T.; Fujishima, A.; Hashimoto, K. *Science* **1996**, *272*, 704-705.

99. Tokoro, H.; Ohkoshi, S.-i.; Hashimoto, K. *Appl. Phys. Lett.* **2003**, *82*, 1245-1247.

100. Rombaut, G.; Verelst, M.; Golhen, S.; Ouahab, L.; Mathonière, C.; Kahn, O. *Inorg. Chem.* **2001**, *40*, 1151-1159.

101. Herrera, J. M.; Marvaud, V.; Verdaguer, M.; Marrot, J.; Kalisz, M.; Mathonière, C. *Angew. Chem., Int. Ed.* **2004**, *43*, 5468-5471.

102. Mathonière, C.; Podgajny, R.; Guionneau, P.; Labrugere, C.; Sieklucka, B. *Chem. Mater.* **2005**, *17*, 442-449.

103. Li, D.; Clérac, R.; Roubeau, O.; Harté, E.; Mathonière, C.; Le Bris, R.; Holmes, S. M. *J. Am. Chem. Soc.* **2008**, *130*, 252-258.

104. Zhang, Y.; Li, D.; Clérac, R.; Kalisz, M.; Mathonière, C.; Holmes, S. M. *Angew. Chem., Int. Ed.* **2010**, *49*, 3752-3756.

105. Mathonière, C.; Kobayashi, H.; Le Bris, R.; Kaïba, A.; Bord, I. *C. R. Chimie* **2008**, *11*, 665-672.

106. Sokol, J. J.; Shores, M. P.; Long, J. R. *Inorg. Chem.* **2002**, *41*, 3052-3054.

107. Van Langenberg, K.; Batten, S. R.; Berry, K. J.; Hockless, D. C. R.; Moubaraki, B.; Murray, K. S. *Inorg. Chem.* **1997**, *36*, 5006-5015.

108. Vostrikova, K. E.; Luneau, D.; Wernsdorfer, W.; Rey, P.; Verdaguer, M. *J. Am. Chem. Soc.* **2000**, *122*, 718-719.

109. Smith, J. A.; Galán-Mascarós, J. R.; Clérac, R.; Sun, J. S.; Ouyang, X.; Dunbar, K. R. *Polyhedron* **2001**, *20*, 1727-1734.

110. Marvilliers, A.; Pei, Y.; Boquera, J. C.; Rivière, E.; Audière, J.-P.; Mallah, T. *Chem. Commun.* **1999**, 1951-1952.

111. Van Langenberg, K.; Hockless, D. C. R.; Moubaraki, B.; Murray, K. S. *Synth. Met.* **2001**, *122*, 573-580.

112. Chen, X.-Y.; Shi, W.; Xia, J.; Cheng, P.; Zhao, B.; Song, H.-B.; Wang, H.-G.; Yan, S.-P.; Liao, D.-Z.; Jiang, Z.-H. *Inorg. Chem.* **2005**, *44*, 4263-4269.

113. Gu, Z.-G.; Yang, Q.-F.; Liu, W.; Song, Y.; Li, Y.-Z.; Zuo, J.-L.; You, X.-Z. *Inorg. Chem.* **2006**, *45*, 8895-8901.

114. Berlinguette, C. P.; Galán-Mascarós, J. R.; Dunbar, K. R. *Inorg. Chem.* **2003**, *42*, 3416-3422.

115. Berlinguette, C. P.; Dragulescu-Andrasi, A.; Sieber, A.; Galán-Mascarós, J. R.; Güdel, H.-U.; Achim, C.; Dunbar, K. R. *J. Am. Chem. Soc.* **2004**, *126*, 6222-6223.

116. Berlinguette, C. P.; Dragulescu-Andrasi, A.; Sieber, A.; Güdel, H.-U.; Achim, C.; Dunbar, K. R. *J. Am. Chem. Soc.* **2005**, *127*, 6766-6779.

117. Shatruk, M.; Chambers, K. E.; Prosvirin, A. V.; Dunbar, K. R. *Inorg. Chem.* **2007**, *46*, 5155-5165.

118. Shatruk, M.; Dragulescu-Andrasi, A.; Chambers, K. E.; Stoian, S. A.; Bominaar, E. L.; Achim, C.; Dunbar, K. R. *J. Am. Chem. Soc.* **2007**, *129*, 6104-6116.

119. Avendaño, C.; Karadaş, F.; Hilfiger, M.; Shatruk, M.; Dunbar, K. R. *Inorg. Chem.* **2010**, *49*, 583-594.

120. Mironov, V. S.; Chibotaru, L. F.; Ceulemans, A. *J. Am. Chem. Soc.* **2003**, *125*, 9750-9760.

121. Marvaud, V.; Decroix, C.; Scuiller, A.; Guyard-Duhayon, C.; Vaissermann, J.; Gonnet, F.; Verdaguer, M. *Chem. Eur. J.* **2003**, *9*, 1677-1691.

122. Yang, J. Y.; Shores, M. P.; Sokol, J. J.; Long, J. R. *Inorg. Chem.* **2003**, *42*, 1403-1419.

123. Cauzzi, D. A.; Mori, G.; Predieri, G.; Tiripicchio, A.; Cavatorta, F. *Inorg. Chim. Acta* **1993**, *204*, 181-187.

124. *SMART and SAINT*; Siemens Analytical X-ray Instruments Inc.: Madison, WI, 1996.

125. Sheldrick, G. M. *SADABS*; University of Gottingen: Gottingen, Germany, 1996.

126. Sheldrick, G. M. *Acta Crystallogr., Sect. A: Found. Crystallogr.* **2008**, *A64*, 112-122.

127. Barbour, L. J. *J. Supramol. Chem.* **2003**, *1*, 189-191.

128. Spek, A. L. *J. Appl. Crystallogr.* **2003**, *36*, 7-13.

129. Bignozzi, C. A.; Argazzi, R.; Schoonover, J. R.; Gordon, K. C.; Dyer, R. B.; Scandola, F. *Inorg. Chem.* **1992**, *31*, 5260-5267.

130. Cloninger, K. K.; Callahan, R. W. *Inorg. Chem.* **1981**, *20*, 1611-1614.

131. Fernández Bertrán, J.; Blanco Pascual, J.; Reguera Ruiz, E. *Spectrochim. Acta, Part A* **1990**, *46A*, 685-689.

132. Griebler, W. D.; Babel, D. *Z. Naturforsch., B: Anorg. Chem., Org. Chem.* **1982**, *37B*, 832-837.

133. Mallah, T.; Ferlay, S.; Auberger, C.; Helary, C.; L'Hermite, F.; Ouahès, R.; Vaissermann, J.; Verdaguer, M.; Veillet, P. *Mol. Cryst. Liq. Cryst. Sci. Technol., Sect. A* **1995**, *273*, 579-589.

134. Alexander, J. J.; Gray, H. B. *J. Am. Chem. Soc.* **1968**, *90*, 4260-4271.

135. Figgis, B. N. *Trans. Faraday Soc.* **1961**, *57*, 198-203.

136. Figgis, B. N. *Trans. Faraday Soc.* **1961**, *57*, 204-209.

137. Baker, J.; Figgis, B. N. *Aust. J. Chem.* **1982**, *35*, 265-275.

138. Journaux, Y.; Sletten, J.; Kahn, O. *Inorg. Chem.* **1986**, *25*, 439-447.

139. Carlin, R. L. *Magnetochemistry*; Springer-Verlag: Berlin, Germany, 1989.

140. Chirico, R. D.; Carlin, R. L. *Inorg. Chem.* **1980**, *19*, 3031-3033.

141. Boča, R. *Coord. Chem. Rev.* **2004**, *248*, 757-815.

142. Abragam, A.; Pryce, M. H. L. *Proc. Roy. Soc., Ser. A* **1951**, *206*, 173-191.

143. Toma, L.; Lescouëzec, R.; Vaissermann, J.; Delgado, F. S.; Ruiz-Perez, C.; Carrasco, R.; Cano, J.; Lloret, F.; Julve, M. *Chem. Eur. J.* **2004**, *10*, 6130-6145.

144. Heinrich, J. L.; Sokol, J. J.; Hee, A. G.; Long, J. R. *J. Solid State Chem.* **2001**, *159*, 293-301.

145. Berseth, P. A.; Sokol, J. J.; Shores, M. P.; Heinrich, J. L.; Long, J. R. *J. Am. Chem. Soc.* **2000**, *122*, 9655-9662.

146. Dong, W.; Zhu, L.-N.; Song, H.-B.; Liao, D.-Z.; Jiang, Z.-H.; Yan, S.-P.; Cheng, P.; Gao, S. *Inorg. Chem.* **2004**, *43*, 2465-2467.

147. Néel, L. *Ann. Phys.* **1948**, *3*, 137-198.

148. Jiang, L.; Feng, X.-L.; Lu, T.-B.; Gao, S. *Inorg. Chem.* **2006**, *45*, 5018-5026.

149. Edwards, M. P.; Hoff, C. D.; Curnutte, B.; Eck, J. S.; Purcell, K. F. *Inorg. Chem.* **1984**, *23*, 2613-2619.

150. Kunkeler, P. J.; van Koningsbruggen, P. J.; Cornelissen, J. P.; van der Horst, A. N.; van der Kraan, A. M.; Spek, A. L.; Haasnoot, J. G.; Reedijk, J. *J. Am. Chem. Soc.* **1996**, *118*, 2190-2197.

151. Moliner, N.; Gaspar, A. B.; Muñoz, M. C.; Niel, V.; Cano, J.; Real, J. A. *Inorg. Chem.* **2001**, *40*, 3986-3991.

152. Murray, K. S.; Kepert, C. J. *Top. Curr. Chem.* **2004**, *233*, 195-228.

153. Real, J. A.; Gaspar, A. B.; Muñoz, M. C.; Gütlich, P.; Ksenofontov, V.; Spiering, H. *Top. Curr. Chem.* **2004**, *233*, 167-193.

154. Cotton, F. A.; Luck, R. L.; Son, K. A. *Inorg. Chim. Acta* **1991**, *179*, 11-15.

155. Kleineweischede, A.; Mattay, J. *Eur. J. Org. Chem.* **2006**, 947-957.

156. Fernández Bertrán, J.; Reguera-Ruíz, E.; Blanco Pascual, J. *Spectrochim. Acta, Part A* **1990**, *46A*, 1679-1682.

157. Reguera, E.; Bertrán, J. F.; Nuñez, L. *Polyhedron* **1994**, *13*, 1619-1624.

158. Coronado, E.; Giménez-López, M. C.; Levchenko, G.; Romero, F. M.; Garcia-Baonza, V.; Milner, A.; Paz-Pasternak, M. *J. Am. Chem. Soc.* **2005**, *127*, 4580-4581.

159. Purcell, K. F.; Yeh, S. M.; Eck, J. S. *Inorg. Chem.* **1977**, *16*, 1708-1715.

160. Ghosh, S. N. *J. Inorg. Nucl. Chem.* **1974**, *36*, 2465-2466.

161. Marchivie, M.; Guionneau, P.; Howard, J. A. K.; Chastanet, G.; Letard, J.-F.; Goeta, A. E.; Chasseau, D. *J. Am. Chem. Soc.* **2002**, *124*, 194-195.

162. Hilfiger, M. G. Ph.D. Dissertation, Texas A&M University, 2010.

163. Robin, M. B. *Inorg. Chem.* **1962**, *1*, 337-342.

164. Pavlishchuk, V. V.; Koval, I. A.; Goreshnik, E.; Addison, A. W.; Van Albada, G. A.; Reedijk, J. *Eur. J. Inorg. Chem.* **2001**, 297-301.

165. Madeja, K.; König, E. *J. Inorg. Nucl. Chem.* **1963**, *25*, 377-385.

166. Stassen, A. F.; De Vos, M.; Van Koningsbruggen, P. J.; Renz, F.; Ensling, J.; Kooijman, H.; Spek, A. L.; Haasnoot, J. G.; Gütlich, P.; Reedijk, J. *Eur. J. Inorg. Chem.* **2000**, 2231-2237.

167. Roubeau, O.; Haasnoot, J. G.; Codjovi, E.; Varret, F.; Reedijk, J. *Chem. Mater.* **2002**, *14*, 2559-2566.

168. Bonhommeau, S.; Molnár, G.; Galet, A.; Zwick, A.; Real, J.-A.; McGarvey, J. J.; Bousseksou, A. *Angew. Chem., Int. Ed.* **2005**, *44*, 4069-4073.

169. Cartledge, G. H. *J. Am. Chem. Soc.* **1952**, *74*, 6015-6018.

170. Létumier, F.; Broeker, G.; Barbe, J.-M.; Guilard, R.; Lucas, D.; Dahaoui-Gindrey, V.; Lecomte, C.; Thouin, L.; Amatore, C. *J. Chem. Soc., Dalton Trans.* **1998**, 2233-2240.

171. Bosnich, B.; Tobe, M. L.; Webb, G. A. *Inorg. Chem.* **1965**, *4*, 1109-1112.

172. Bakac, A.; Espenson, J. H. *Inorg. Chem.* **1992**, *31*, 1108-1110.

173. Berlinguette, C. P.; Dunbar, K. R. *Chem. Commun.* **2005**, 2451-2453.

174. Berlinguette, C. P. Ph.D. Dissertation, Texas A&M University, 2004.

175. Heintz, R. A.; Smith, J. A.; Szalay, P. S.; Weisgerber, A.; Dunbar, K. R.; Beck, K.; Coucouvanis, D. *Inorg. Synth.* **2002**, *33*, 75-83.

176. König, E.; Madeja, K. *Inorg. Chem.* **1967**, *6*, 48-57.

177. Létard, J.-F. *J. Mater. Chem.* **2006**, *16*, 2550-2559.

178. Hilfiger, M. G.; Chen, M.; Brinzari, T. V.; Nocera, T. M.; Shatruk, M.; Petasis, D. T.; Musfeldt, J. L.; Achim, C.; Dunbar, K. R. *Angew. Chem., Int. Ed.* **2010**, *49*, 1410-1413, S1410/1-S1410/6.

179. Wang, X.-Y.; Hilfiger, M. G.; Prosvirin, A.; Dunbar, K. R. *Chem. Commun.* **2010**, *46*, 4484-4486.

180. Hilfiger, M. G.; Shatruk, M.; Prosvirin, A.; Dunbar, K. R. *Chem. Commun.* **2008**, 5752-5754.

181. Liu, T.; Zhang, Y.-J.; Kanegawa, S.; Sato, O. *J. Am. Chem. Soc.* **2010**, *132*, 8250-8251.

182. Milios, C. J.; Inglis, R.; Vinslava, A.; Bagai, R.; Wernsdorfer, W.; Parsons, S.; Perlepes, S. P.; Christou, G.; Brechin, E. K. *J. Am. Chem. Soc.* **2007**, *129*, 12505-12511.

183. Milios, C. J.; Vinslava, A.; Wernsdorfer, W.; Moggach, S.; Parsons, S.; Perlepes, S. P.; Christou, G.; Brechin, E. K. *J. Am. Chem. Soc.* **2007**, *129*, 2754-2755.

184. Milios, C. J.; Vinslava, A.; Wernsdorfer, W.; Prescimone, A.; Wood, P. A.; Parsons, S.; Perlepes, S. P.; Christou, G.; Brechin, E. K. *J. Am. Chem. Soc.* **2007**, *129*, 6547-6561.

185. Milios, C. J.; Vinslava, A.; Wood, P. A.; Parsons, S.; Wernsdorfer, W.; Christou, G.; Perlepes, S. P.; Brechin, E. K. *J. Am. Chem. Soc.* **2007**, *129*, 8-9.

186. Wolf, S. A.; Awschalom, D. D.; Buhrman, R. A.; Daughton, J. M.; von Molnar, S.; Roukes, M. L.; Chtchelkanova, A. Y.; Treger, D. M. *Science* **2001**, *294*, 1488-1495.

187. Zutic, I.; Fabian, J.; Das Sarma, S. *Rev. Mod. Phys.* **2004**, *76*, 323-410.

188. Dagotto, E. *Science* **2005**, *309*, 257-262.

189. Bogani, L.; Wernsdorfer, W. *Inorg. Chim. Acta* **2008**, *361*, 3807-3819.

190. Bogani, L.; Wernsdorfer, W. *Nature Materials* **2008**, *7*, 179-186.

191. Winpenny, R. E. P. *Angew. Chem., Int. Ed.* **2008**, *47*, 7992-7994.

192. Létard, J.-F.; Guionneau, P.; Goux-Capes, L. *Top. Curr. Chem.* **2004**, *235*, 221-249.

193. Borrás-Almenar, J. J.; Clemente-Juan, J. M.; Coronado, E.; Tsukerblat, B. S. *J. Comput. Chem.* **2001**, *22*, 985-991.

APPENDIX

PHYSICAL METHODS

Mass Spectrometry

Electrospray mass spectrograms were acquired on a Sciex API QStar Pulsar mass spectrometer using an electrospray ionization source; nano-electrospray mass spectra were obtained using a Protana Nanospray ion source. ~50 μM solutions of the samples (~10 μM for nano-ESI) were electrosprayed, and the data were acquired in the positive-ion mode. The ion spray voltage was set at ~4800 V (900-1000V for nano-ESI), and the nozzle skimmer potential was adjusted to 10 V to minimize fragmentation. Theoretical isotope ratio calculations were performed using the program IsoPro 3.0.

Thermal Gravimeteric Analysis

The thermogravimetric analyses (TGA's) were performed on a Shimadzu TGA-50 or an Instrument Specialists Inc. TGA 1000 thermogravimetric analyzer in the temperature range up to 298-573 K at the heating rate of 5-10 K/min, under an N_2 gas flow of 20-30 L/min.

Infrared Spectroscopy

Infrared (IR) spectra of the solid compounds were measured as Nujol mulls placed between KBr plates on a Nicolet 740 FTIR spectrometer.

Ultraviolet-visible Spectroscopy

Solution UV-Vis spectra were collected on a Shimadzu UV 1601PC spectrophotometer in the 1000–200 nm range.

Diffuse Reflectance Spectroscopy

Diffuse reflectance spectra were measured on a Hitachi U-4100 UV-vis-NIR spectrophotometer with a Praying Mantis diffuse reflection accessory or a Hewlett Packard 8453 UV-vis spectrophotometer with a Labsphere RSA-HP-8453 reflectance spectroscopy accessory.

Optical Reflectivity Spectroscopy

Surface reflectivity measurements were performed on a home built system in the 10-300 K range. A tungsten-halogen light source was used (Leica CLS 150 XD, adjustable from 0.5 to 1 W/cm^2) at wavelengths between 300 and 1000 nm. All measurements were calibrated against a NIST traceable reflectance standard (sphereOptics, ref SG3054). This set-up collects the light reflected by the sample (that is the sum of direct and diffuse reflected light). The temperature heating and cooling rates were maintained at 4 K/min.

^{57}Fe Mössbauer Spectroscopy

The ^{57}Fe Mössbauer spectra were collected on constant acceleration instruments over the temperature range of 1.5-300 K, in applied external fields up to 8 T. Samples for experiments in low applied magnetic fields ($\leq$0.05 T) were prepared by placing polycrystalline solids in Mössbauer cups covered with Teflon lids. For high-field measurements, the solid materials were ground to finely divided powders and suspended in mineral oil. Samples of acetonitrile-wet crystals of **10** or **11** (Chapter III) suspended in acetonitrile were placed in a Mössbauer cup and immediately frozen for experiments between 4.2 and 220 K. A sample of acetonitrile-wet crystals of **11** was prepared in a similar fashion except that all manipulations were done in a nitrogen-containing glovebox to prevent any exposure to oxygen. Spectral simulations were generated using WMOSS (WEB Research, Edina, MN), and isomer shifts are reported relative to Fe metal foil at room temperature.

Magnetic Susceptibility Measurements

Magnetic measurements were performed on a Quantum Design SQUID MPMS-XL magnetometer. Magnetic susceptibility measurements in the direct current mode were carried out in an applied field of 0.1 T in the 2-300 K range. Magnetization data were acquired at 1.8 K, with the magnetic field varying from 0 to 7 T. Whenever appropriate, the fitting of magnetic behavior was carried out with the *MAGPACK* simulation program.[193] Magnetic data obtained for samples were corrected for diamagnetic contributions by the use of Pascal constants.[139] Because of the high content of disordered solvent in the crystals, each sample was also subjected to TGA; the molecular weight of each compound was adjusted according to the interstitial solvent content determined from the TGA. Micro-SQUID measurements were collected on samples of aligned single crystals at the temperatures indicated (Chapter V).

Some of the photomagnetic measurements (at Texas A&M University) were obtained using the Quantum Design fiber optic sample holder. Samples (1-2 mg) were sealed in clear tape and placed in a glass tube equipped with an optical fiber placed ~2 mm from the sample. The white light source used was a Thor Labs OSL1 High Intensity fiber light source (adjustable up to 0.22 W/cm^2 through a 36" fiber bundle). Due to the small sample amount, an applied field of 0.5 T was used. Susceptibility measurements were calibrated to determine sample mass by comparing to a DC measurement of a known larger mass of the same batch of sample. Other photomagnetic measurements (measured at Université Bordeaux) were performed using a mixed gas Ar-Kr laser (spectrum physics Beam Lock 2060) coupled through an optical fiber directed into the magnometer cavity or with the tungsten-halogen light source (Leica CLS 150 XD, adjustable from 0.5 to 1 W/cm^2). Samples (2-3 mg) were packed into a thermoformed SQUID straw placed about 3.5 cm from the fiber. The water content of the samples was determined by TGA before mailing, sent in a sealed container, and was assumed to remain constant.

VITA

Kristen Elise Funck
P.O. Box 30012, College Station TX 77842-3012
Phone: 979-845-1966
Email Address: kristenfunck@gmail.com

EDUCATION

Texas A&M University, College Station, TX

Ph.D. Chemistry

Dissertation: Magnetic Properties and Reactivity Studies of Families of Trigonal Bipyramidal Cyanide Clusters and Their Extended Structures.

Advisor: Prof. Kim R. Dunbar

Mississippi State University, Mississippi State, MS

B.S. Chemistry, ACS Certified (2004)

RESEARCH EXPERIENCE

Texas A&M University, College Station, TX

Research Assistant, Department of Chemistry (October 2004-August 2010)

Teaching Assistant, Department of Chemistry (2004-2009)

Texas A&M University, College Station, TX

Research Assistant (Research Experience for Undergraduates), Department of Chemistry, (May 2003-August 2003)

Mississippi State University, Mississippi State, MS

Research Assistant, Department of Chemistry (May 2001-April 2003)

AFFILIATIONS

American Chemical Society (2003-present)